Multicomponent Metal-Organic Frameworks: Tailoring Platforms for Transition Metal- and Bioelectrocatalysis

A thesis presented in partial fulfilment of the requirements of the degree of

Doctor of Philosophy

in

Chemistry

at Massey University, Manawatū, New Zealand

Bernhard Stephan Auer

2024

Abstract

MUF-77 (MUF = Massey University Framework) is a quaternary, multicomponent metal-organic framework (MOF), constructed from three topologically distinct carboxylate linkers and Zn_4O secondary building units. Multicomponent MOFs such as MUF-77, constructed from a set of ligands with different geometries, provide a valuable platform for obtaining ordered and programmable pore environments. In this context, they show great potential as recyclable and stable, heterogeneous catalysts. In this work, we looked at the typical MUF-77 synthesis conditions and investigated the formation of additional crystalline phases. Several new MOFs were discovered, including new multicomponent MOFs. We then investigated MUF-77 for the incorporation of transition metal catalysts. The work included ligand and MOF syntheses and synthetic modifications of the frameworks upon MOF formation. We also embedded a Au(III) catalyst within the MUF-77 framework and evaluated its catalytic properties upon installation into the framework. Finally, we shifted our focus to systems comprising MOF and enzyme components for their electrochemical application in layer-by-layer-grafted electrodes. The work extended our library of potential heterogeneous catalysts, showcasing the great potential of multicomponent systems.

Contributions

All the work in this thesis was completed by Bernhard Stephan Auer

Except:

- Chapter 2, SXRD data for BMUF-3 was collected by Ludwig Petters, Massey University.
- Chapter 3, ^{13}C NMR of bocaz-bpdc at 176 MHz was collected by Suraj Patel, Massey University.
- Chapter 3, the ligands 2-(diphenylphosphaneyl)terephthalic acid and 2-(diethylphosphaneyl)-terephthalic acid were generously provided by Dr Marco Ranocchiari, Laboratory for Catalysis and Sustainable Chemistry, Paul Scherrer Institute, Switzerland. The bpdc imidazolium salt ester was synthesized by Dr John Clements.
- Chapter 4, the ligand IPrAu(bpdc)Cl was generously provided by Prof F. Dean Toste, University of California, Berkeley, United States of America.
- Chapter 5, the PXRD pattern of PCN-333 synthesized in France, which was collected by Thierry Encinas (Grenoble INP Engineer) at the Université Grenoble Alpes in close discussion with Dr Andrew Gross and myself; SEM was conducted by Christine Lancelon-Pin (CERMAV institute). General findings from the collaborative work reported by Master's student, Ardeshir Dadgar Yeganeh, under the supervision of Dr Andrew Gross, were included for additional information and were labelled as such.
- High-resolution mass spectrometry data was collected by Dave Lun, Massey University.

Acknowledgments

The length of this section is no measure for the gratitude I feel towards everyone who made this journey possible, but rather an expression of how much I struggle to express my feelings. There are more people to thank for and more blessings I received than I could ever fit into writing. I am deeply grateful to everyone who was a part of this journey.

First and foremost, I would like to thank my parents for their unconditional love, their never-ending support and for making my journey possible. I am grateful for the love and support from my family and friends, who were there when things were rough and who celebrate all the good moments in life with me.

I would like to thank Prof Shane Telfer for his supervision, but more importantly for giving me the chance to learn and grow and for his support when things were difficult.

Further, I would like to thank Gareth Rowlands for his supervision and his guidance.

I want to thank Dr Andrew Gross for his guidance and support. I am grateful for the opportunity to conduct research at the Département de Chimie Moléculaire, Université Grenoble Alpes, France, and for the hospitality of the whole research group.

I would like to thank Prof F. Dean Toste and Dr Marco Ranocchiari for their collaborative work and for their generous contributions of chemicals and experience.

I would like to thank all current and former group members, whose hard work and dedication made this research possible. Especially, I would like to thank Dr John Clements, Dr Tian-You (Daniel) Zhou, Dr Adil Alkaş and Dr Seok June (Subo) Lee for their support, patience, and guidance. I would like to thank Elnaz Jangodaz for her guidance and support with gas adsorption measurements.

I wish to thank Suraj Patel for his guidance and support in the laboratory and in writing, as well as for his commitment and efforts to improve the school for students. I would also like to thank Dr. Tyson Dais for his guidance.

I wish to thank Dr Pat Edwards for providing guidance and support with NMR spectroscopy; Dave Lun for providing guidance and support with analytical methods and instruments, especially HPLC, and other laboratory equipment, for making sure the laboratory runs smoothly and for the collection of high-resolution mass spectrometry data; the Manawatū Microscopy and Imaging Centre for providing guidance and support with, and access to EDX, SEM and microscopy.

Publications and Thesis Structure

Publications relevant to this thesis

1. B. Auer, S. G. Telfer, A. J. Gross, *Electroanalysis* **2023**, *35*, 1–10.

2. T.-Y. Zhou, B. Auer, S. J. Lee, S. G. Telfer, *J. Am. Chem. Soc.* **2019**, *141*, 1577–1582.
   Contributions: Synthesis of MOFs following the established procedure and preparing a sample for SXRD and gas adsorption measurements. Characterization for one MOF after synthesis and for all MOFs after catalysis by NMR and PXRD. Running some catalytic experiments and conducting all catalytic control experiments.

Table of Contents

Abbreviations

Aq	Aqueous
Ar	Aryl
az	Azepine
BA	Benzoic acid
bdc	Benzene-1,4-dicarboxylic acid
BINAP	(2,2′-Bis(diphenylphosphino)-1,1′-binaphthyl)
BINOL	1,1′-Bi-2-naphthol
BIPY	2,2'-Bipyridine or 2,2'-bipyridine-5,5'-dicarboxylic acid
Boc	*tert*-Butyloxycarbonyl
Boc2O	Di-*tert*-butyl dicarbonate
BODIPY	4,4-Difluoro-4-bora-3a,4a-diaza-*s*-indacene
BOx	Billirubin oxidase
bpdc	Biphenyl-4,4′-dicarboxylic acid
btb	1,3,5-Tris(4-carboxyphenyl)benzene
btc	Benzene-1,3,5-tricarboxylate
bte	4,4′,4″-[Benzene-1,3,5- triyl-tris(ethyne-2,1-diyl)]tribenzoate
bttv	Benzo-tris-thiophene carboxylic acid
Cat	Catalase
CNT	Carbon Nanotube
CV	Cyclic voltammetry
cyt c	Cytochrome c
d	Doublet
dd	Doublet of doublets
ddd	Doublet of doublet of doublets
DEF	Diethylformamide
DEPT	Distortionless enhancement by polarization transfer
DET	Direct electron transfer
DI	Deionized water
DIC	*N,N*′-Diisopropylcarbodiimide
Dipp	2,6-Diisopropylphenyl
DMAP	4-Dimethylaminopyridine
DMF	Dimethylformamide
DMSO	Dimethyl sulfoxide
EDTA	Ethylenediaminetetraacetic acid

EDX	Energy-dispersive X-ray spectroscopy
ee	Enantiomeric excess
eq.	Equivalents
FTIR	Fourier transformed infrared
GC	Glassy Carbon
HKUST	Hong Kong University of Science and Technology
HMQC	Heteronuclear multiple quantum coherence
hmtt	5,5′,10,10′,15,15′-Hexamethyltruxene-2,7,12-tricarboxylic acid
HPLC	High-performance liquid chromatography
HRP	Horseradish peroxidase
HSAB	Hard and soft acids and bases
im	Imidazole
IPr	[1,3-Bis(2,6-diisopropylphenyl) imidazole-2-ylidene]
IRMOF	Isoreticular metal-organic framework
J	Coupling constant
L	Ligand
LSK-1	German acronym of the Laboratory for Catalysis and Sustainable Chemistry
m	Multiplet
m/z	Mass to charge ratio
mam	2-((Methylamino)methyl)
Me	Methyl
Me2SAuCl	Chloro(dimethyl sulfide)gold(I)
MIL	Matériaux de l′Institut Lavoisier
MOF	Metal-organic framework
mol %	mole percent
MP-11	Microperoxidase-11
MUF	Massey University Framework
MWCNT	Multi-walled carbon nanotube
NAC	Nitrogen acyclic carbene
ndc	2,6-Napthalenedicarboxylate
NHC	N-heterocyclic carbene
NMR	Nuclear magnetic resonance
NU	Northwestern University
P(NMe2)3	*N,N,N′,N′,N″,N″*-Hexamethylphosphanetriamine
PB	Phosphate buffer
PBS	Phosphate buffered saline

PCN	Porous coordination network
Ph	Phenyl
PSE	Post-synthetic ligand exchange
PSM	Post-synthetic modification
PXRD	Powder X-ray diffraction
s	Singlet
SBU	Secondary building unit
SCE	Saturated calomel electrode
SOD	Superoxide dismutase
SPhos	2-Dicyclohexylphosphino-2′,6′-dimethoxybiphenyl
SXRD	Single-crystal X-ray diffraction
t	Triplet
tatb	4,4',4''-*s*-Triazine-2,4,6-triyl-tribenzoic acid
TGA	Thermogravimetric analysis
THF	Tetrahydrofuran
tht	Tetrahydrothiophene
TLC	Thin layer chromatography
TM	Transition metal
TON	Turnover Number
Tris	Tris(hydroxymethyl)aminomethane
Tris HCl	Tris(hydroxymethyl)aminomethane hydrochloride
TSM	Trimethylsilyl
UiO-67	Universitetet i Oslo
UV	Ultraviolet
ZIF	Zeolitic imidazolate frameworks

Chapter 1 Introduction

1.1 Metal-Organic Frameworks: A Promising Class of Porous Materials

Materials such as zeolites,[1] mesoporous silica,[2] covalent or hydrogen-bonded organic frameworks (HOFs or COFs)[3,4] and metal-organic frameworks (MOFs)[5,6] are exciting classes of materials due to their high porosity. Their modular assembly and synthetic access to a vast variety of structures (Figure 1-1), and the oftentimes good stability and crystallinity make MOFs promising candidates in various areas. MOFs have been widely used for gas storage and separation,[7–10] toxin removal,[11–13] sensing,[14,15] drug delivery,[16,17] catalysis[18–23] and many others.

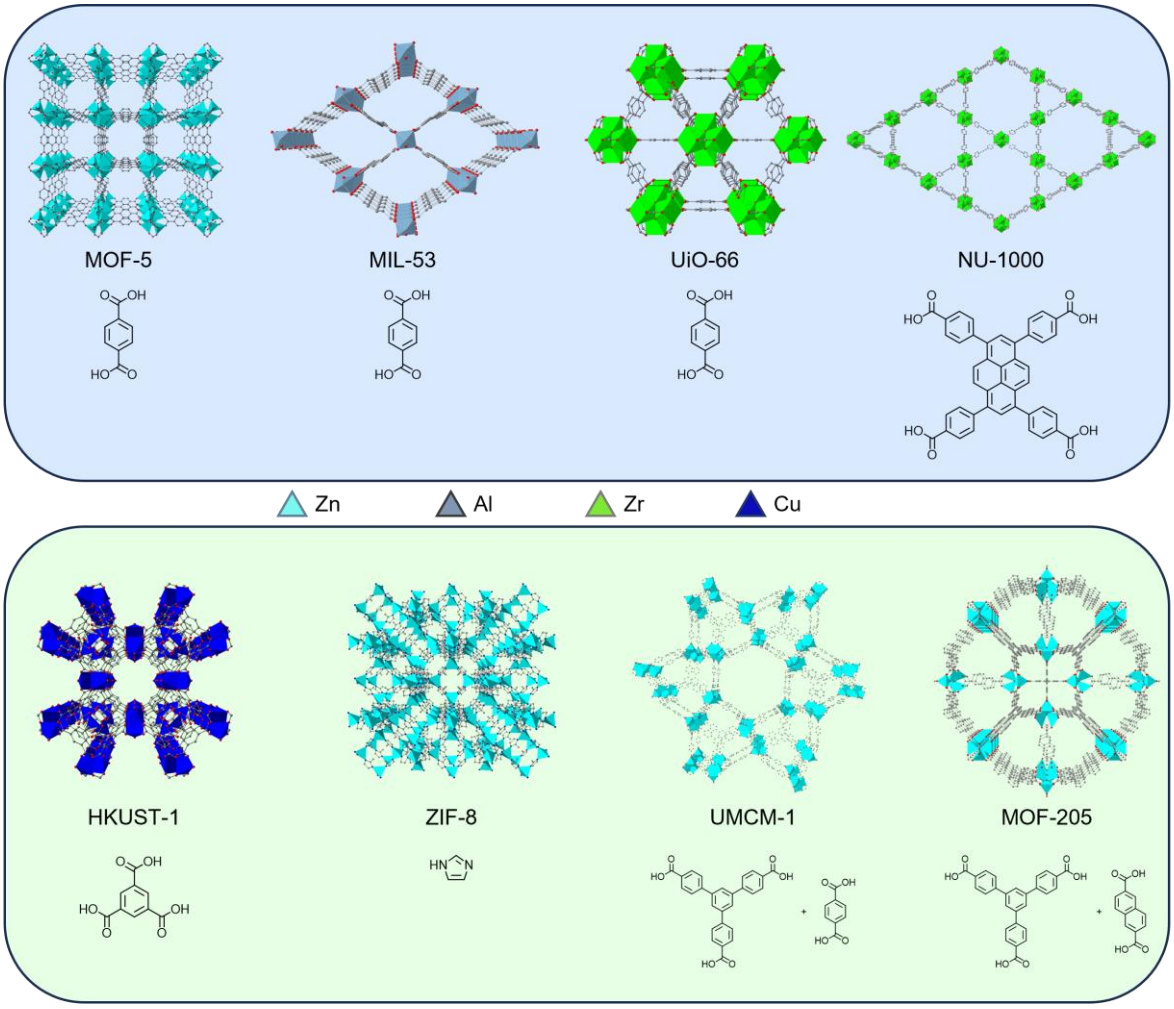

Figure 1-1 Overview of different well-established MOFs, their organic linkers, and typical or exemplary metal secondary building units (SBUs).

Following the IUPAC (International Union of Pure and Applied Chemistry) recommendation a metal-organic framework is "a coordination network with organic ligands containing potential voids".[24] As a relatively young field of research, which gained immensely in popularity over the last two decades, it is not surprising that much of the terminology and classifications is still a topic of discussion. Although the term MOF is predominantly used today, individual reports prefer to use different terminologies, describing this class of

materials as porous coordination polymers (PCP), porous coordination networks (PCN), and microporous coordination polymers (MCPs) amongst others. After the advent of MOF chemistry in the early 1990s, the popularity of the field rose drastically with Yaghi's discovery of MOF-5 in 1999.[25,26] The framework with the formula $Zn_4O(bdc)_3 \cdot (DMF)_8(C_6H_5Cl)$ (bdc = terephthalate, 1,4-benzenedicarboxylate) showed increased stability, a surface area of 2,900 m^2g^{-1} and retained porosity after guest removal (Figure 1-2)

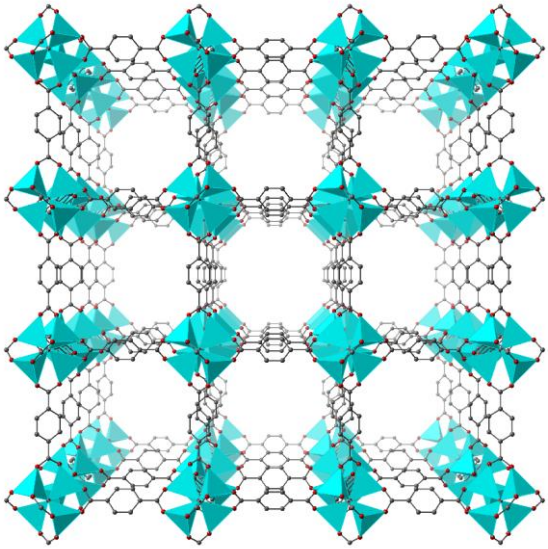

Figure 1-2 Structure of MOF-5. Carbon atoms are shown in grey, oxygen is shown in red, and zinc is shown in turquoise. Hydrogen atoms and solvent molecules are omitted for clarity.

MOF-5 was quickly identified as a potential hydrogen storage material.[27,28] Framework design allows the physicochemical properties of pores and channels to be tuned to achieve the separation of various gases, a process that still requires extensive distillation setups for industrial scales today.[29] In 2002 the same group optimized the synthetic procedure for MOF-5 and reported a series of related MOFs with different organic linkers.[30] The new synthetic procedure for the IRMOF series was drastically simplified compared to the original MOF-5 synthesis and only involved heating the organic linker and zinc nitrate in *N*,*N*-diethylformamide (DEF). This general method is still widely applied for the development of new MOFs. This elegant approach takes advantage of the instability of dialkylformamides to decompose to formic acid/formate and a dialkylamine, which *in situ* deprotonates the carboxylic acid groups of the organic ligands (Figure 1-3).[31] As this process can be acid/base catalysed, the presence and amount of water in the reaction medium are often critical for the synthesis outcome.[32]

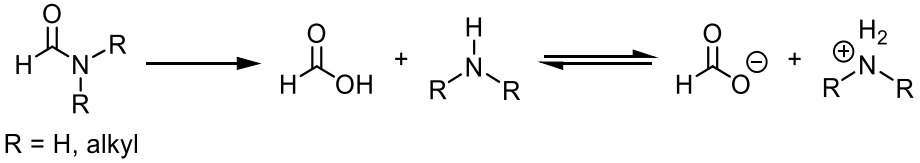

Figure 1-3 Decomposition pathway of dialkylamines.

Contemporaneous with Yaghi's MOF-5, the Williams group reported HKUST-1 (Hong Kong University of Science and Technology, Figure 1-4).[33] The framework with the formula $[Cu_3(TMA)_2(H_2O)_3]_n$ (TMA or BTC = benzene-1,3,5-tricarboxylate) is based on secondary building units (SBUs) containing Cu_2 dimers at the six

vertices of a cube and four organic linkers tetrahedrally. In this work, they also reported the replacement of the terminal axial water ligands with pyridine. This idea of ligand exchange in MOFs has later been extended and utilized in various publications, a concept today commonly used under the name of post-synthetic modification (PSM) which will be discussed further in Chapter 1.2.2.

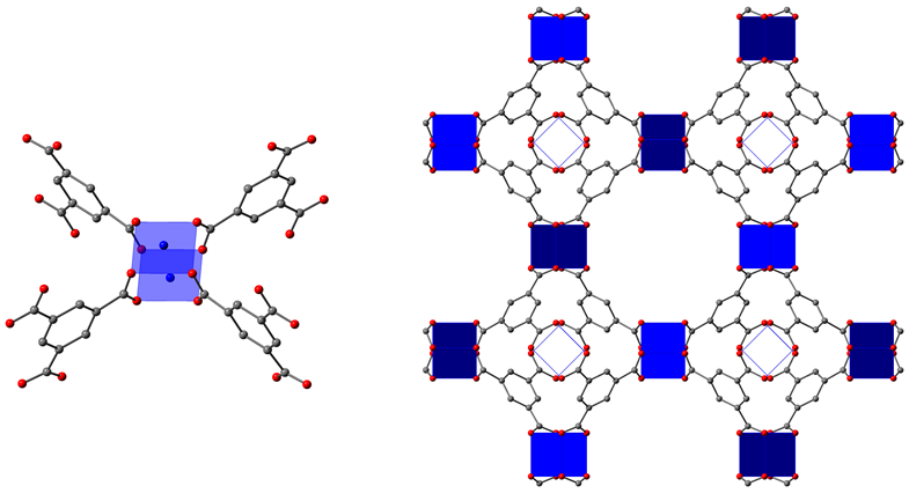

Figure 1-4 Structure of HKUST-1. Carbon atoms are shown in grey, oxygen is shown in red, and copper is shown in dark blue. Hydrogen atoms and solvent molecules are omitted for clarity.

Another milestone in the relatively young history of MOFs was the synthesis of UiO-66 (Universitetet i Oslo). Many of the MOFs before lacked stability under harsher conditions, caused by the lability of the metal-linker interactions, MOF-5 being the most prominent example. In 2008, the group of Lillerud presented UiO-66 and UiO-67, frameworks built from bdc or bpdc linkers, each connected by $Zr_6O_4(OH)_4(CO_2)_{12}$ clusters (Figure 1-5). Group 4 metals show a high affinity towards oxygen, making the zirconium-carboxylate bonds in this framework extremely stable. The framework was intact after immersing in water and showed high thermal stability.

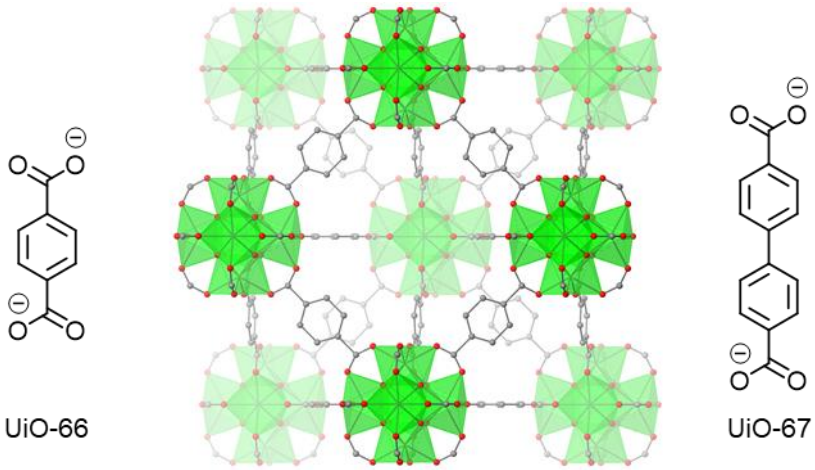

Figure 1-5 Structure of UiO-66. Carbon atoms are shown in grey, oxygen is shown in red, and zirconium in green. Hydrogen atoms are omitted for clarity.

1.2 Advantages of the Building Block Design — Tuneability of MOFs

1.2.1 Isoreticular Principle

The beauty of MOF chemistry lies within the plentiful possibilities to chemically alter the individual building blocks or the composition of the framework without compromising the structural integrity. The Yaghi group reported a series of MOF frameworks derived from the parent MOF-5 (Figure 1-6).[30] Each MOF was designed by connecting the tetrahedral Zn_4O clusters with organic dicarboxylic acid derivatives. Each MOF followed the parent structure despite the original organic linker being exchanged for functionalized or extended analogues. A series of different MOFs was obtained and as each followed the parent architecture, they were termed isoreticular MOFs. Thus, the pore size could be designed for a specific application, for example, IRMOF-6 (organic linker: bicyclo[4.2.0]octa-1,3,5-triene-2,5-dicarboxylate) showed high methane storage capacity. The isoreticular concept offers many possibilities in MOF chemistry. Thus the framework properties can be directly adjusted by changing the properties of the organic linkers, while the original structure is maintained.

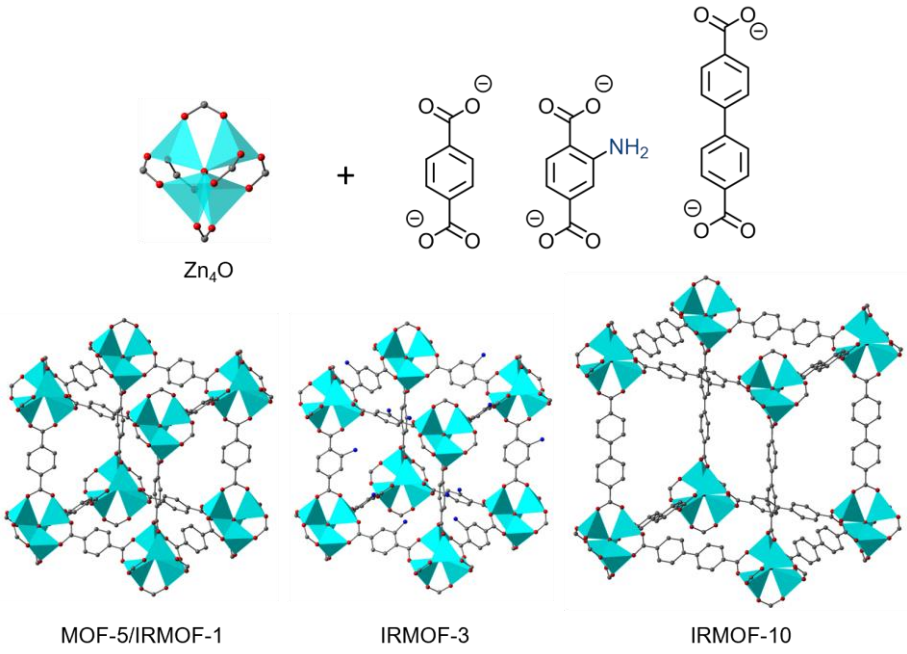

Figure 1-6 Examples of MOFs within the IRMOF series and depiction of their building blocks.

In 2015, PCN-333 (Porous Coordination Network) was reported as a single-protein encapsulating MOF.[34] This MOF beautifully represents the possibilities of specifically designing a framework tailored to a certain task by isoreticular chemistry. Protein encapsulation requires frameworks with high porosity and large cavities, which are stable under aqueous conditions. For this purpose, the highly stable mesoporous MIL-100 (Materials of Institut Lavoisier)[35] was used as a template. The strong carboxylate-metal interactions in those trivalent metal species (Al^{3+}, Fe^{3+}, Cr^{3+}, V^{3+}, Sc^{3+}) provide the MOF with good stability in aqueous media. The high porosity and large cavities offered an ideal starting point for the design of new MOFs. The pore sizes were systematically enlarged by replacing the 1,3,5-benzene tricarboxylic acid (btc) with benzo-tris-thiophene carboxylic acid (bttc) or 4,4',4''-*s*-triazine-2,4,6-triyl-tribenzoic acid (tatb) to give PCN-332 and PCN-333, respectively. The size of the largest pore could systematically be increased from

29 Å (MIL-100) to 45 Å (PCN-332) and 55 Å (PCN-333) while retaining the high porosity and stability of the frameworks (Figure 1-7).

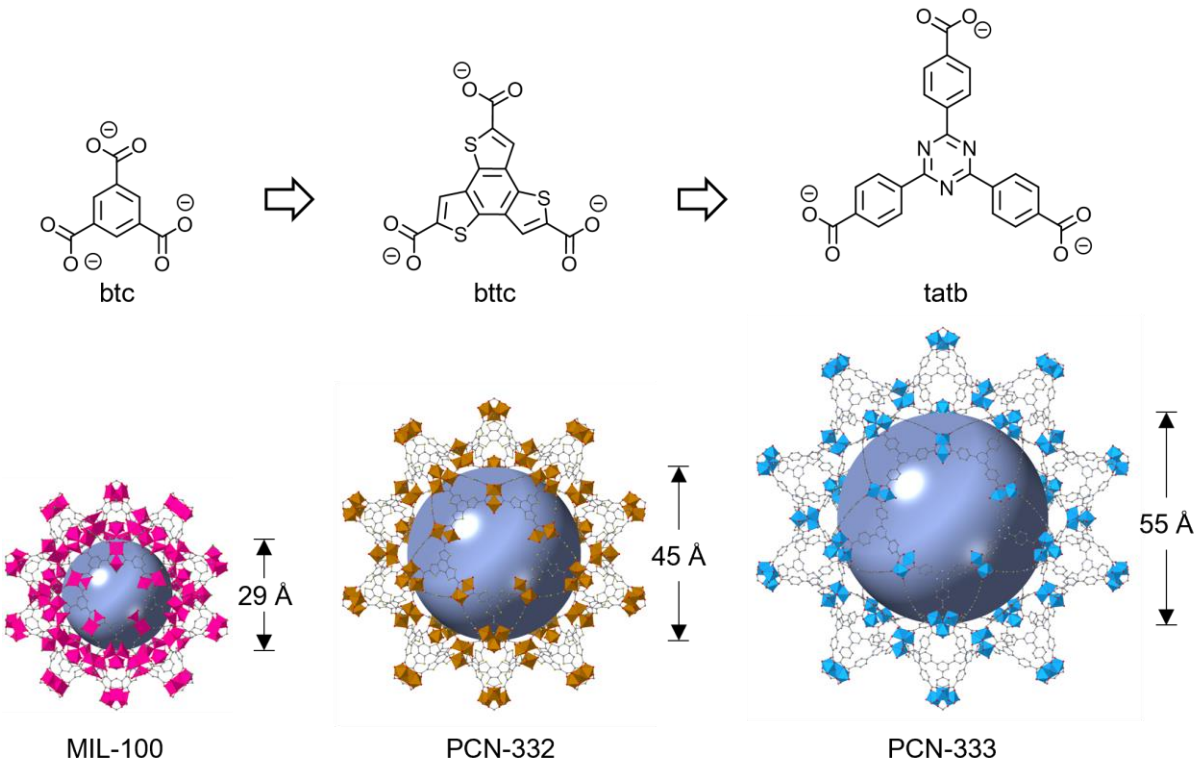

Figure 1-7 Isoreticular structures of MIL-100, PCN-332, and PCN-333 and their respective organic linkers.

1.2.2 Framework Functionalization by Post-Synthetic Modification

1.2.2.1 Non-Covalent Interactions

The large internal surface area of many MOFs makes them an excellent target as host for guest encapsulation. However, the incorporation of guest molecules can be as much of a challenge as it can be exploited for MOF chemistry. While MOFs are usually relatively stable while immersed in the right solvent, forceful removal of the solvent molecules coordinated to the framework can lead to a collapse of the structure. To prevent structural collapse, synthetic procedures often include a step to replace the often polar, high boiling point solvents like dialkylformamides with less polar and more volatile solvents like acetone or DCM before drying the material.[36–38] Removal of guest molecules from the MOF can lead to interesting new properties, as shown by the Yaghi group with the selective absorption of aromatic molecules in their 2D Co(II) BTC-based MOF upon removal of pyridine. Without the guest the MOF showed good selectivity in adsorbing aromatic molecules such as benzene, nitrobenzene, cyanobenzene, and chlorobenzene, but not acetonitrile, nitromethane, or dichloroethane.[39] Some MOFs even experience structural flexibility upon guest removal or exchange.[40] The phenomenon of 'breathing' frameworks opened access to new exciting applications. The dynamic pore environment allows selective gas[41,42] or other guest adsorption[43,44] and the design of advanced materials like breathing porous liquids.[45] The adsorption or incorporation of guests through non-covalent interactions allows the usage of MOFs in a variety of additional applications. The installation of metal nanoparticles enables the design of advanced hybrid materials with properties that can exceed those of the individual components.[46,47] The catalytic scope of

those nanoparticle/MOF hybrid materials includes photocatalysis,[48,49] quantification and bioimaging of reactive oxygen species[50], photosensitizer,[51] or regioselective carboxylations[52].

1.2.2.2 Post-Synthetic Covalent Bond Formations

The building block-based design of MOFs gave scientists various handles to tune the overall framework properties by modifying the individual building blocks. Post-synthetic modification (PSM) of MOFs quickly arose as a powerful tool to increase the scope of framework functionalizations.[53–56] If the formed framework shows sufficient stability, covalent bond manipulations can be conducted upon MOF synthesis. This enables the introduction of functionality without impacting crystal growth or risking an alteration of the functional group under harsher MOF synthesis conditions. The Cohen group first presented the post-synthetic modification of IRMOF-3, an isoreticular framework to MOF-5 functionalized with an amine group. Upon installation of the linker, the amine was readily converted using acetic and alkyl anhydrides or isocyanates (Figure 1-8).[57–59] The universal use of this approach was demonstrated by extending the scope of modified MOFs.[60] Today PSM is a widely applied tool for the functionalisation of MOFs.

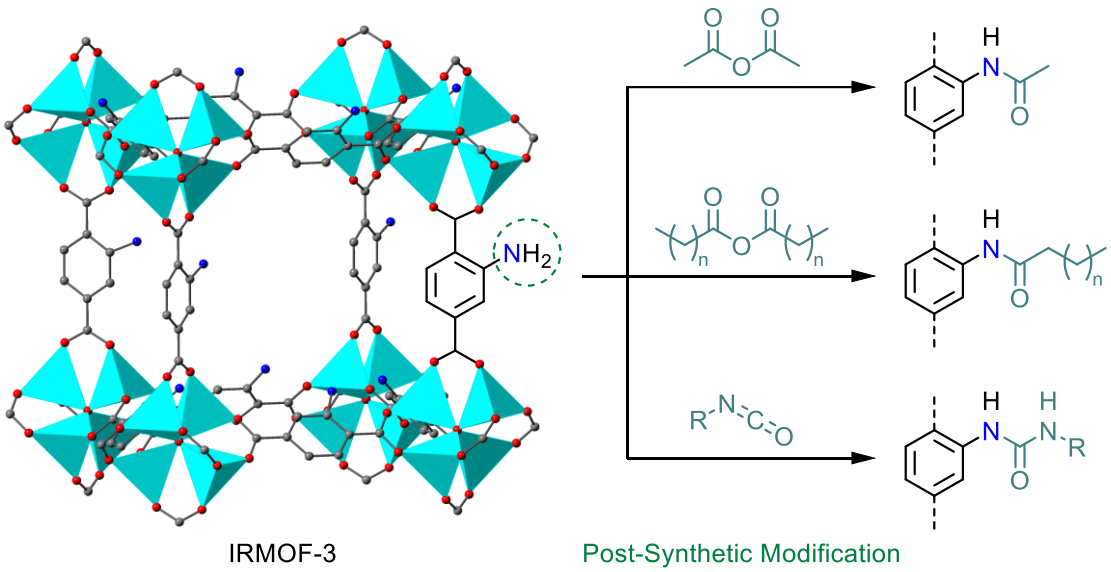

Figure 1-8 Post-synthetic modification of IRMOF-3 with different substrates as an example of MOF functionalization through covalent bond formation.

In the case of MOFs based on Zn_4O building blocks the introduction of secondary amine functionalities can be challenging. The incorporation of the amine catalyst, following traditional solvothermal synthesis, might lead to (de)protonation of the functional group, or coordination to the metal ions might interfere with catalytic activity or crystal growth. Our group developed a strategy to protect the amino functionality with a thermolabile *tert*-butyloxycarbonyl (Boc) to successfully form IRMOF-type crystals.[61] The free amino group was generated following MOF synthesis via the thermal removal of the Boc protecting group at elevated temperatures under vacuum. The framework was stable under the deprotection conditions and the catalyst retained catalytic activity. The MOF successfully promoted asymmetric aldol reactions, showcasing the viability of this post-synthetic modification protocol.

Another important consideration is the incorporation of linkers with additional metal-coordinating functional groups, which are not required for the framework formation and might interfere with crystal

growth. Post-synthetic modification elegantly overcomes the limitations by introducing the additional functionalities once the framework has already formed, avoiding competing coordination sites. A beautiful example of combining different such sites within one organic MOF linker was reported by the Lin group.[62] The 1,1′-bi-2-naphthol (BINOL) backbone was equipped with pyridine groups for coordination to Cd(II) ions during MOF synthesis to yield a framework with the formula $[Cd_3Cl_6L_3]\cdot 4DMF\cdot 6MeOH\cdot 3H_2O$ (L = (*R*)-6,6′-dichloro-2,2′-dihydroxy-1,1′-binaphthyl-4,4′-bipyridine) (Figure 1-9). The BINOL hydroxyl groups remained available for metal coordination upon MOF formation. This was exploited to combine the MOF with titanium(IV) isopropoxide to form the BINOL-titanium catalytic complex *in situ*. The MOF catalyst showed excellent enantioselectivity with up to 93 % enantiomeric excess (ee) and full conversion for several substrates in $ZnEt_2$ addition reactions to aromatic aldehydes.

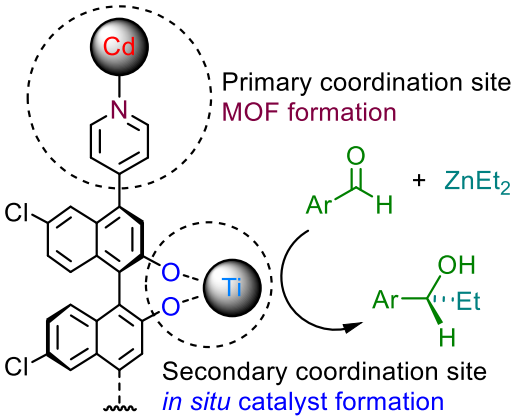

Figure 1-9 Two independent coordination sites on one MOF linker. The pyridine functionality (red) was necessary for MOF formation, while the hydroxy groups were employed *in situ* for asymmetric titanium(IV) catalysis.

1.3 MOFs as Catalysts

Their porous nature and accessibility of a large variety of building blocks make MOFs a great platform for catalytic processes and the heterogeneous nature of the catalysts allows for easy recyclability.

1.3.1 MOFs as Hosts for Enzyme Encapsulation

Despite the drive to enlarge the portfolio of synthetic catalysts and their important role in many industrial processes, the true masterclass of catalysts, especially in biochemical fields, is formed by enzymes. The complex systems have been perfected by evolution and are often the catalyst of choice for biochemical processes. However, the high specificity towards the substrates and the good performance often come with the price of low structural stability under other than perfect conditions.

MOFs with high inner surface areas are predestined for enzyme encapsulation, creating a porous shield that allows substrate diffusion while improving enzyme stability. ZIF-8, due to its good stability,[63] high bioavailability,[64] negligible cytotoxicity, and the choice of different synthetic procedures[65,66] has been widely explored for enzyme encapsulation. Yet, due to a pore diameter of 11.6 Å[67] the MOF is used primarily to form a composite material with enzymes by forming the MOFs around the guests, such as co-precipitation or biomineralization,[68] rather than utilizing the MOF pores for host-guest interactions. Integrating the enzymes during the framework synthesis into MOF nanoparticles requires conditions mild enough to avoid

enzyme denaturation. A post-synthetic, direct encapsulation of an enzyme within a MOF pore of suitable size not only mitigates those limitations during synthesis but enables fine-tuning the host-guest interactions. As described in Chapter 1.2.1, the Zhou group enlarged the pore volume of MIL-100 by substituting the pristine ligand for tatb.[34] The obtained PCN-333 is predestined for enzyme encapsulation as it offered sufficiently large pores and was stable in water, which was required to ensure enzyme stability. PCN-333 was suitable to encapsulate the enzymes horseradish peroxidase (HRP), cytochrome *c* (cyt *c*), and microperoxidase-11 (MP-11). The quick encapsulation of the enzymes and the high stability of those composites were attributed to the favourable affinity of the enzymes to the MOF cages. In buffer, the encapsulated enzymes showed a decreased turnover number, but increased substrate affinity, resulting in an overall similar activity compared to the free enzymes. In aqueous media, however, the PCN-333/cyt-*c* composite exhibited around 29-fold higher specific activity compared to the free enzymes (Figure 1-10). Denaturing and agglomeration of the enzymes upon changing reaction conditions such as solvent, pH, or temperature is a common problem, however, the host environment seemed to mitigate those influences. PCN-333/HRP showed maintained specific activity in water. In organic solvents, conditions relatively harsh for enzyme catalysis, the specific activity was increased compared to the free enzymes. The smaller MP-11 showed decreased activity in water, which was attributed to the encapsulation of multiple enzyme units per pore instead of a single enzyme encapsulation ascribed to the cyt *c* and HRP composites. The MOF/enzyme composites showed almost no leaching during the catalysis and were recyclable. Its large pores and good stability make PCN-333 an interesting target for other catalytically active enzymes to be encapsulated.

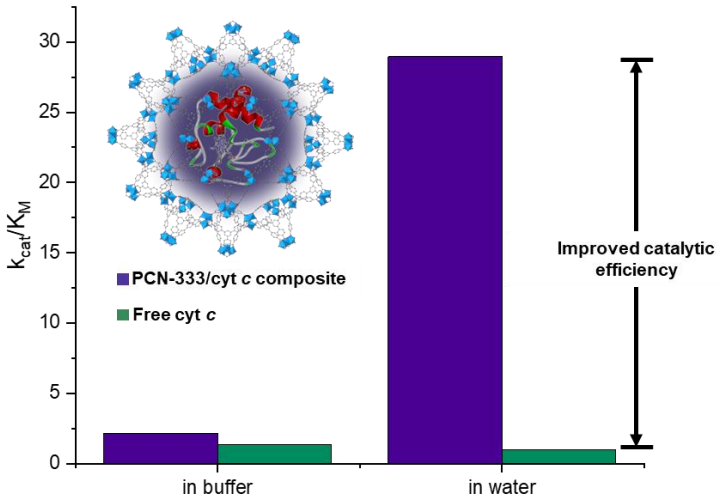

Figure 1-10 PCN-333 encapsulated cyt *c* showed improved catalytic efficiency compared to the free ligand in water.[34]

1.3.2 MOFs as Organocatalysts

Due to their modular structural arrangements and generally high porosity, MOFs are ideal materials for applications in heterogeneous catalysis.[69,70] By confining the catalytic active site within the MOF pores the catalytic performance can be significantly improved[21] or synergistic effects[71,72] can be exploited. Through post-synthetic modification, Luan *et al.* installed a thiourea catalyst within the IRMOF-3 pores (Figure 1-11). The catalyst showed good performance for acetalization and Morita–Baylis–Hillman reactions. Homogeneous thiourea catalytic systems often suffer from self-aggregation of the catalyst, an undesired

side effect of the same propensity for hydrogen bonding exploited for the catalytic applications, negatively impacting the catalytic performance.[73–75] By isolating the catalyst within the different MOF pores the turnover number (TON) was improved up to five-fold. Similarly, a thiourea-functionalized MIL-101 was later exploited for Friedel-Crafts alkylation and Biginelli reactions.[76]

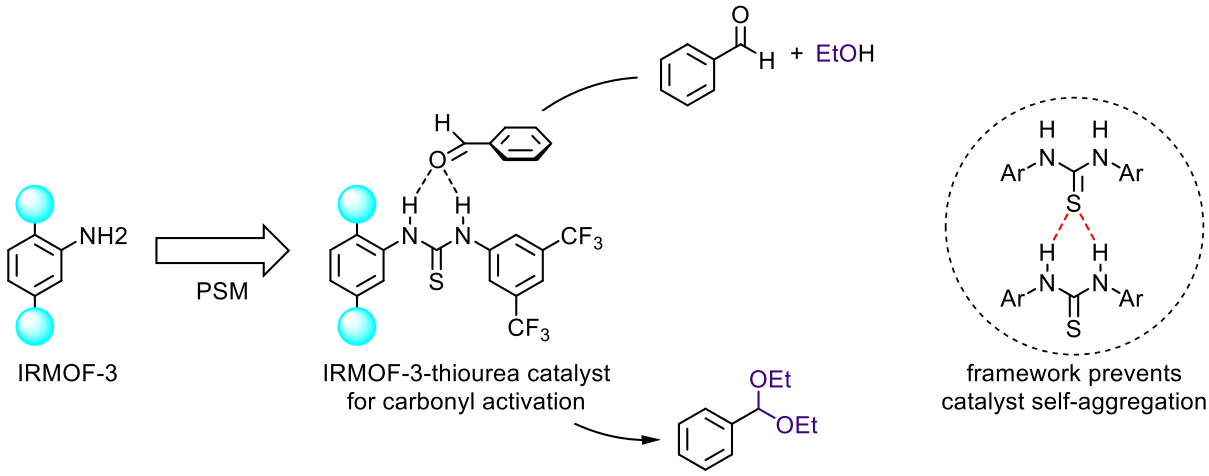

Figure 1-11 Post-synthetic incorporation of a thiourea catalyst within IRMUF-3 as a catalyst for organocatalytic reactions.

Other examples of organocatalytic reactions promoted by MOFs include Knoevenagel condensation reactions[77–79] and the ring opening of epoxides by amines.[80] The potential for MOFs as catalysts is not limited to the functionalization of the organic linkers. Designing and exploiting catalytically active metal SBUs is only one example of how versatile MOFs are as platforms for catalysis.[81–83]

1.3.3 Transition Metal Catalysts Within MOFs

The beauty of MOF synthesis lies in the versatility of possible approaches.[84] In many cases, MOFs can be synthesized directly from the linkers and the metal salts.[85,86] If this direct approach is not suitable, the organic linkers (or the inorganic nodes) can often be functionalized upon framework formation through post-synthetic modification.[87] In their pioneering work on post-synthetic modifications, the Cohen group showed that amine-functionalized linkers in IRMOF-3 could be further modified upon MOF synthesis.[57] Soon after, this principle was exploited by the functionalization of the amine groups in IRMOF-3 with salicylaldehyde to introduce free half-salen upon MOF synthesis. Salen ligands are widely used in transition metal chemistry.[88,89] Prominent examples include the commercially available Jacobsen's catalyst, a Mn-Salen complex used in the asymmetric epoxidation of unfunctionalized olefins.[90,91] Half-salen ligands are the bidentate equivalent. Their straightforward synthesis quickly brought them attention as potential transition metal catalysts for MOFs. The half-salen ligands were then successfully employed to stabilize a vanadium complex in solution. The obtained MOF was catalytically active in the oxidation of cyclohexene with ^{t}BuOOH.[92] A similar approach was chosen to stabilize palladium complexes within the framework pores.[93] Sun *et al.* adapted this post-synthetic modification strategy for the design of UiO-66 and UiO-67 frameworks (in UiO-67 the ligand is a biphenyl dicarboxylic acid analogue instead of terephthalic acid).[94] The linkers were sequentially modified upon MOF synthesis to anchor the catalytically active palladium complex (Figure 1-12a). The optimized UiO-67 catalyst with a Pd content of 0.27 mmol g^{-1} showed a

conversion of up to 95 % for Suzuki coupling and 93 % for the Heck reaction with an *E*-selectivity of 100 % (Figure 1-12b). The heterogeneous catalyst showed superior activity and selectivity compared to the homogeneous controls.

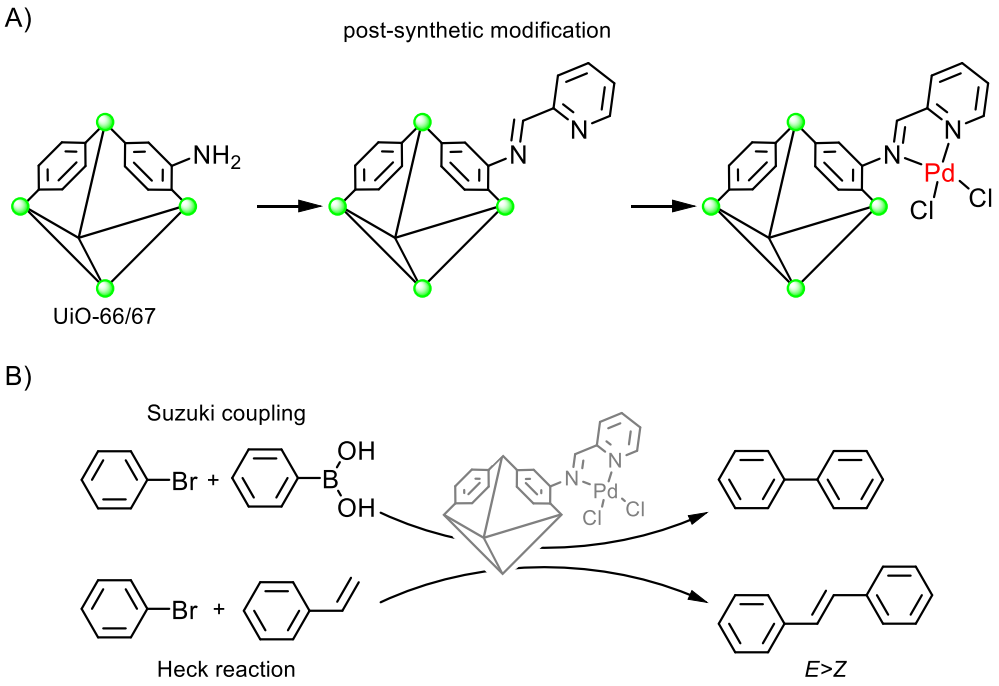

Figure 1-12 a) Incorporation of the catalytic group into the MOF by post-synthetic modification. b) The UiO-66 and UiO-67 analogues were catalytically active in palladium-catalysed C–C coupling reactions.

Zirconium-based MOFs, like the before-mentioned UiO-66, are popular platforms for catalysis due to the chemical and thermal stability of the zirconium-oxygen bonds, providing a robust framework for the integration of well-known ligands like NacNacs (β-Diketimines)[95] or salicylaldimines.[96,97] CO_2 was hydrogenated to formic acid/formate catalysed by a Ir(III)-functionalized Zr(IV) MOF.[98] To obtain this MOF the traditional biphenyl linker was replaced with a [2,2'-bipyridine]-5,5'-dicarboxylic acid (Figure 1-13). Upon coordination of the catalytically active iridium species, the catalyst reached a turnover number of 6149±50 in 15 h and a turnover frequency of 410±3 h^{-1} under atmospheric pressure at 85 °C. The heterogeneous nature of the catalyst allowed to create a dynamic gas/liquid interface at the catalytic site, enhancing the contact of CO_2, H_2, and H_2O.

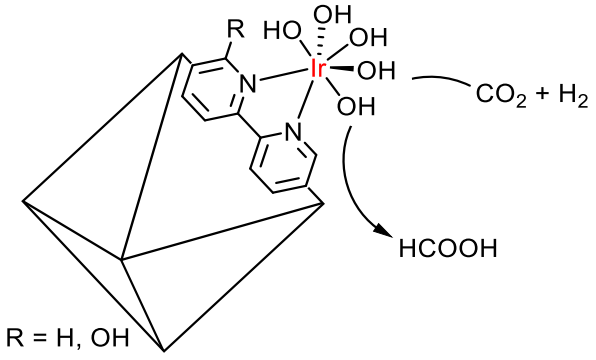

Figure 1-13 An Ir(III)-functionalized UiO-type MOF catalyst for the hydrogenation of CO_2.

A different approach was chosen for the synthesis of a phosphine-based MOF catalyst. Instead of leaning on an existing structure, 4,4′,4′′-phosphinetriyltribenzoic acid was selected as a linker in combination with a zirconium metal source to form LSK-1 (German acronym of the Laboratory for Catalysis and Sustainable Chemistry) (Figure 1-14).[99] The LSK-1-Au-Cl pre-catalyst was obtained after the post-synthetic addition of chloro(tetrahydrothiophene)gold(I). Formation of the gold-alkyne species led to the catalytically active complex. This elegant method avoided activation with silver salts, commonly used in homogeneous catalysis,[100,101] which leads to the precipitation of AgCl and thus complicates the recovery of the heterogeneous catalyst from solution. This catalyst successfully promoted the hydration of phenylacetylene and cyclization of *N*-(prop-2-yn-1-yl)benzamide exceeding homogeneous catalytic activity for the latter.

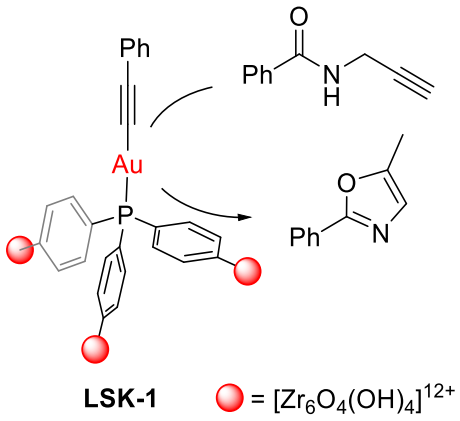

Figure 1-14 LSK-1, a MOF with triphenylphosphine groups as organic linkers to anchor the catalytically active gold complex.

The Lin group beautifully showcased the potential of MOF organocatalysis by extending the scope of reactions to asymmetric catalysis. New Cu-based chiral MOFs were designed from 4,4′,6,6′-substituted 1,1′-bi-2-naphthol (BINOL) ligands. Upon combination with Ti(O^iPr)$_4$ the MOF/catalyst system successfully promoted the additions of diethylzinc and ethyl(phenylalkynyl)zinc to aromatic aldehydes to yield chiral secondary alcohols.[102]

1.3.3.1 Architectural Stabilisation of the Catalyst

The true potential of MOFs, however, can only be reached by exploiting the entirety of the framework. The groups of Toste and Yaghi followed this multidisciplinary approach to improve the stability of a homogeneous gold(III) catalyst.[103] The homogeneous catalyst IPrAu(III)(biphenyl)X (where IPr is 1,3-Bis(2,6-diisopropylphenyl)-1,3-dihydro-2H-imidazol-2-ylidene) and X^- a non-coordinating counter anion) is known to undergo an unimolecular decomposition *via* reductive elimination (Figure 1-15). By confining the linear molecular geometry into a rigid framework, such as IRMOF-10 and bio-MOF-100, decomposition could be suppressed, and catalytic activity was retained, whereas the homogeneous catalyst suffered from decomposition over time.

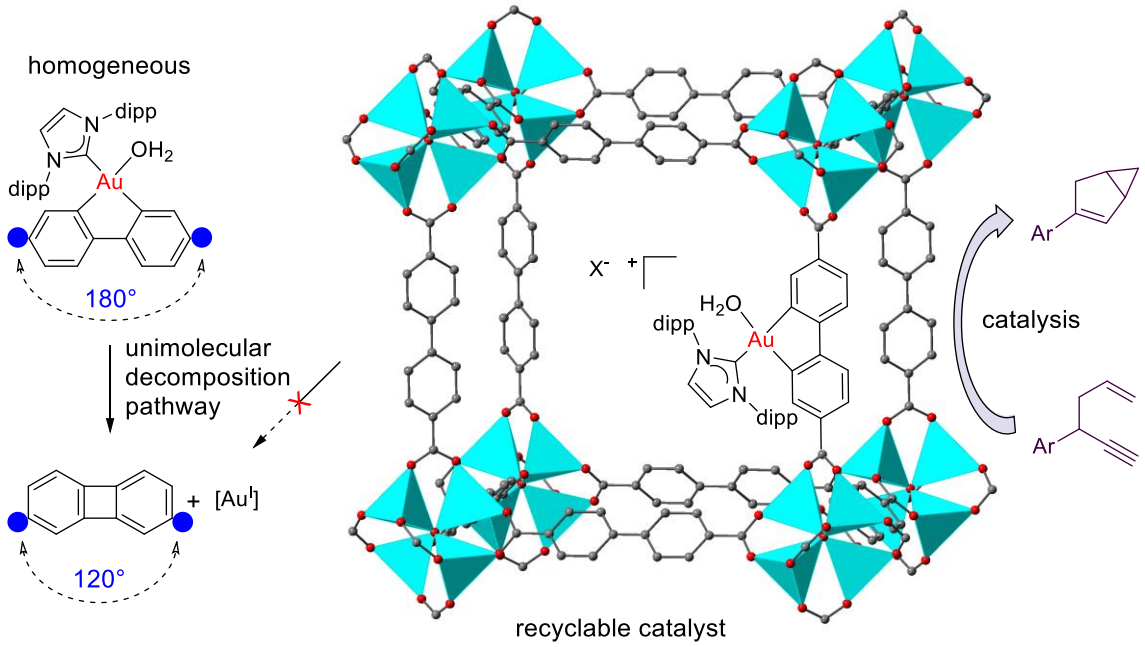

Figure 1-15 Architectural stabilization of an Au(III) catalyst in MOFs. The incorporation into the rigid framework hindered the unimolecular decomposition that is observed for the homogeneous catalyst.

In the same manner, monophosphine ligands were locked into a rigid framework, minimizing disproportionation and ligand exchange reactions at the metal centres (Rh, Ir) which would lead to a decrease in catalytic performance.[104] The recyclable catalysts showed superior performance in the hydrosilylation of ketones and alkenes, the hydrogenation of alkenes, and the C–H borylation of arenes compared to the homogeneous controls.

1.3.3.2 Cooperative Catalysis

MOF synthesis is not limited to one organic linker or one metal centre but also allows the incorporation of multiple linkers of different lengths and connectivity.[105] This opens the door for cooperative catalysis, where a combination of catalysts improves the catalytic performance. Utilizing two linkers that promote different reactions allows to target sequential or stepwise reaction cascades. Recently, LIFM-28 (Lehn Institute of Functional Materials) was reported as a platform to install a variety of catalytically active linkers for Knoevenagel condensation, alcohol oxidation, acetal-, click- and Baylis-Hillman reactions (Figure 1-16).[106,107] The multi-ligand MOFs incorporated multiple catalysts into the same framework for stepwise or sequential reactions. In this example, copper(I) sites promote the aerobic alcohol oxidation and the click reaction to form the triazole. Upon workup, the amine-functionalized linker was utilized for Knoevenagel condensation.

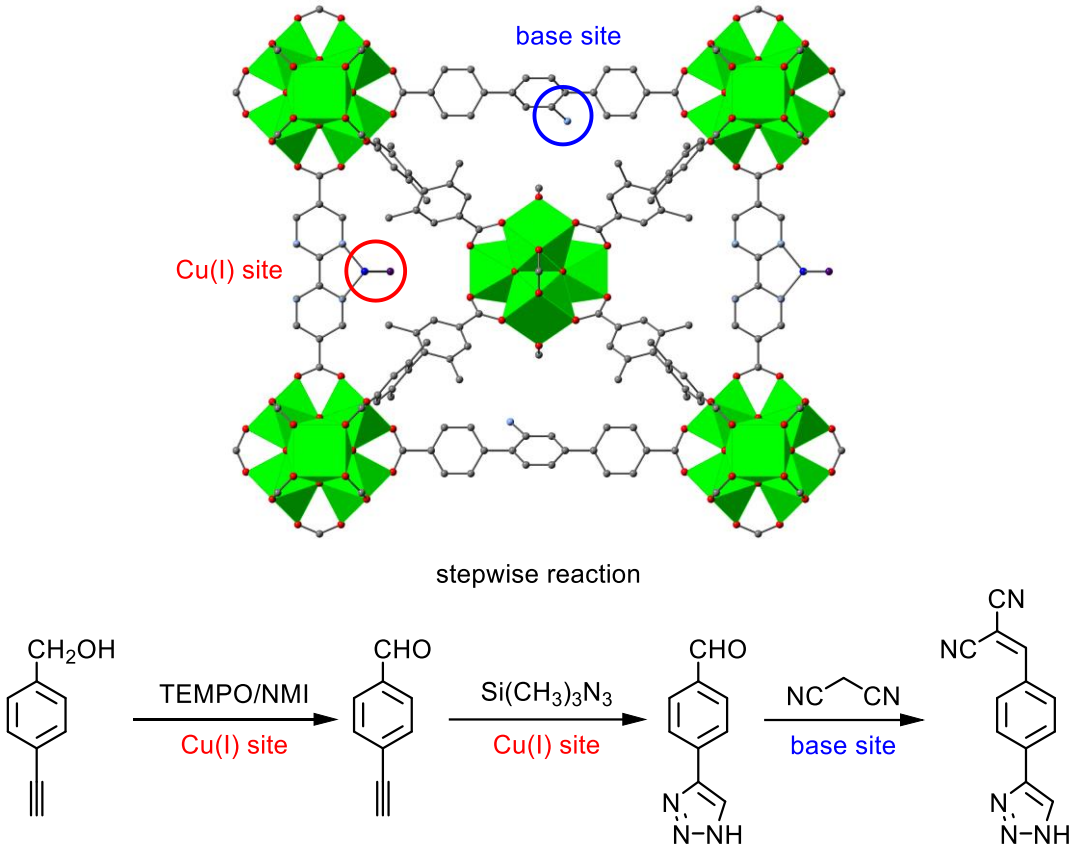

Figure 1-16 Synergistic catalysis in LIFM-28, a MOF incorporating multiple catalytic centres.

The Cui group reported the synthesis of isoreticular UiO-68 frameworks by post-synthetic introduction of metal-salen (Cr, Cu, Fe, Mn, V) linkers.[96] The MOFs were employed as enantioselective catalysts for the asymmetric cyanosilylation of aldehydes, ring-opening of epoxides, oxidative kinetic resolution of secondary alcohols, and aminolysis of stilbene oxide. The combination of Mn- and Cr-coordinated ligands in the framework allowed to subsequently promote epoxidation of 2,2-dimethyl-2H-chromene with 2-*tert*-butylsulfonyliodosobenzen as oxidant followed by a ring-opening reaction with anilines in 80-85 % yield and up to 99.5 % ee.

Through framework design, it is also possible to achieve cooperative effects by installing catalytically active metal centres in proximity to each other. For example, chiral salen-VO MOFs showed advanced stereoselectivity for the cyanation of aldehydes compared to the homogeneous counterpart while maintaining the catalytic activity.[86] Control experiments indicated that the improved selectivity of up to >99% ee was due to the proximity of VO units in the MOF pores, leading to cooperative activation of the substrates. In another example, copper-coordinated Schiff base ligands were employed for Friedel–Crafts and Henry reactions.[85] The framework also showed increased activity compared to homogeneous catalysis, due to the cooperative effects of the bimetallic catalytic centres.

1.3.3.3 Ligands for Transition Metal Catalysis Within MOFs

The range of transition metal catalysts incorporated into MOFs is extensive.[108,109] The assembly of new MOFs and the improvement of synthetic procedures allowed the insertion of more and more complex systems. Bipyridine (bipy) ligands are prominently featured in the world of homogeneous transition metal

catalysis. Ni and Ir-coordinated bipy derivatives were essential in their roles as transition metal catalysts for promoting the selective sp^3 C–H alkylation of the α-C–H of amines, ethers, and sulfides.[110] Re-bipy complexes have been widely explored as catalysts for water oxidation[111,112] and $[Fe(bpy)_3]^{2+}$ was employed as a photocatalyst for the enantioselective alkylation of aldehydes.[113] Their geometric similarity to the popular ditopic ligand bpdc makes bipy ligands a promising target for incorporation into MOFs. Bipyridine ligands of different lengths were successfully integrated into UiO-type frameworks. The transition metal catalysts were introduced by post-synthetic metalation of bipy-based linkers with Pd or Ir precursors.[114] The new bpy-UiO-Pd catalysts were tested in the palladium-promoted aerobic oxidation of cyclohexanone to phenol (Figure 1-17).[114,115] The recyclable MOF catalysts exhibited improved catalytic activity and stability compared to their homogeneous counterparts.

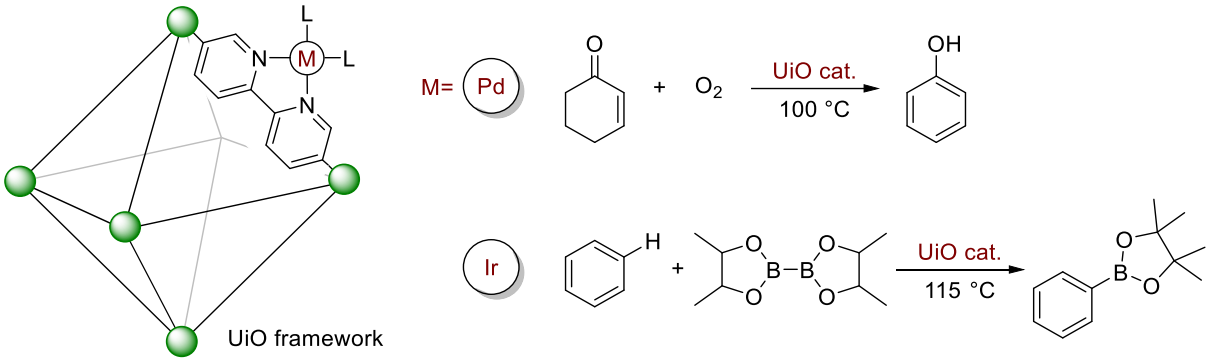

Figure 1-17 Bipy-functionalized UiO frameworks as transition metal catalysts for the oxidation of cyclohexanone and arene C–H borylation.

The respective bpy-UiO-Ir was obtained after metalation with $[Ir(COD)(OMe)]_2$. Isoreticular UiO-bipy-Ir catalysts produced by the insertion of elongated bipy linkers and post-synthetic metallation.[116] The MOF catalysts successfully promoted borylation of aromatic C–H bonds and the tandem hydrosilylation of aryl ketones and dehydrogenative ortho-silylation of benzylic silyl ethers. The activity for the *ortho*-silylation of benzylic silyl ethers was increased at least three-fold compared to the homogeneous control. Another class of archetypic ligands for Pd-catalysed cross-coupling reactions are phosphine ligands. Buchwald ligands, dialkylbiarylphosphine ligands like SPhos, are prominently featured in promoting cross-coupling reactions[117–119] and the Buchwald–Hartwig amination.[120] The ligand design strongly influences the activity and stability of the respective transition metal catalysts. The related 2,2′-bis(diphenylphosphino)-1,1′-binaphthyl (BINAP)[121] ligands represent another class of phosphine ligands. The axial chirality, due to the restricted rotation of the individual naphthalene groups along the C_2 axis, creates a chiral environment for a potential coordinated metal centre, making them excellent ligand candidates for asymmetric catalysis.[122–124] The Lin group beautifully illustrated two different approaches for the incorporation of phosphine-transition metal complexes into MOFs as catalysts. A triarylphosphine-derived tricarboxylate linker was used for the MOF synthesis, exploiting the affinity of the carboxylate groups towards coordination with the zirconium SBUs.[125] The soft phosphine coordination sites were less compatible with the Zr ions and no interference with framework formation was observed. The phosphine groups remained available for coordination with Rh or Ir transition metal complexes upon MOF synthesis (Figure 1-18 A). The obtained Rh- and Ir-functionalized MOF catalysts successfully promoted hydrosilylation,

hydrogenation, and borylation reactions. Following a different approach, an extended BINAP-type linker was incorporated into a framework of UiO-66 topology.[126] Upon MOF synthesis the phosphine groups were successfully metalated to form the respective Ru or Rh complexes within the framework. Due to the chiral nature of the ligand, the functionalized MOFs successfully catalysed asymmetric hydrogenation reactions and the addition of arylboronic acids and trimethylaluminium to α,β-unsaturated ketones (Figure 1-18 B).

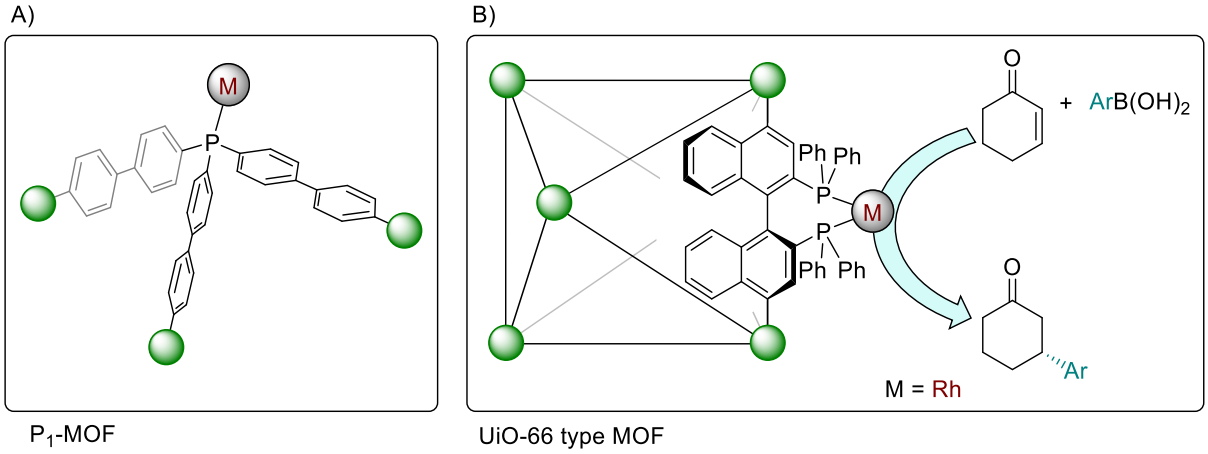

Figure 1-18 Two phosphine functionalized frameworks as transition metal catalysts. The Zr-based MOFs were obtained by new framework design (A) or incorporation into a well-studied existing framework topology (B).

Ligands structurally derived from 1,1′-bi-2-naphthol (BINOL) can be similarly used for application in asymmetric catalysis. Prominent examples of such a ligand class are phosphoramidites. Phosphoramidites are suitable to support a variety of transition metal catalysts and substitution at the amine functionality allows easy influence on the catalytic properties of the transition metal complexes.[127] Examples of asymmetric catalytic reactions promoted by phosphoramidite transition metal complexes include Rh-catalysed asymmetric hydrogenation reactions,[128] Au-catalysed diastereo- and enantioselective cycloadditions of allenenes,[129] Ru-catalysed Diels-Alder reactions,[130] Ir-catalysed regio- and enantioselective allylation reactions[131] and hydrosilylation reactions (Figure 1-19).[132] Reports of phosphoramidite ligands within MOFs, despite their formidable predisposition as ligands for transition metal catalysts, are rather scarce. Jiang *et al.* installed the phosphoramidite ligand through post-synthetic modification, reasoning that the lability of the P–O bond under solvothermal MOF synthesis conditions or acidic conditions interfered with a direct MOF synthesis approach.[133] Upon successful addition of the Ir-catalyst, the MOF was active in the enantioselective hydrogenation of α-dehydroamino acid esters.

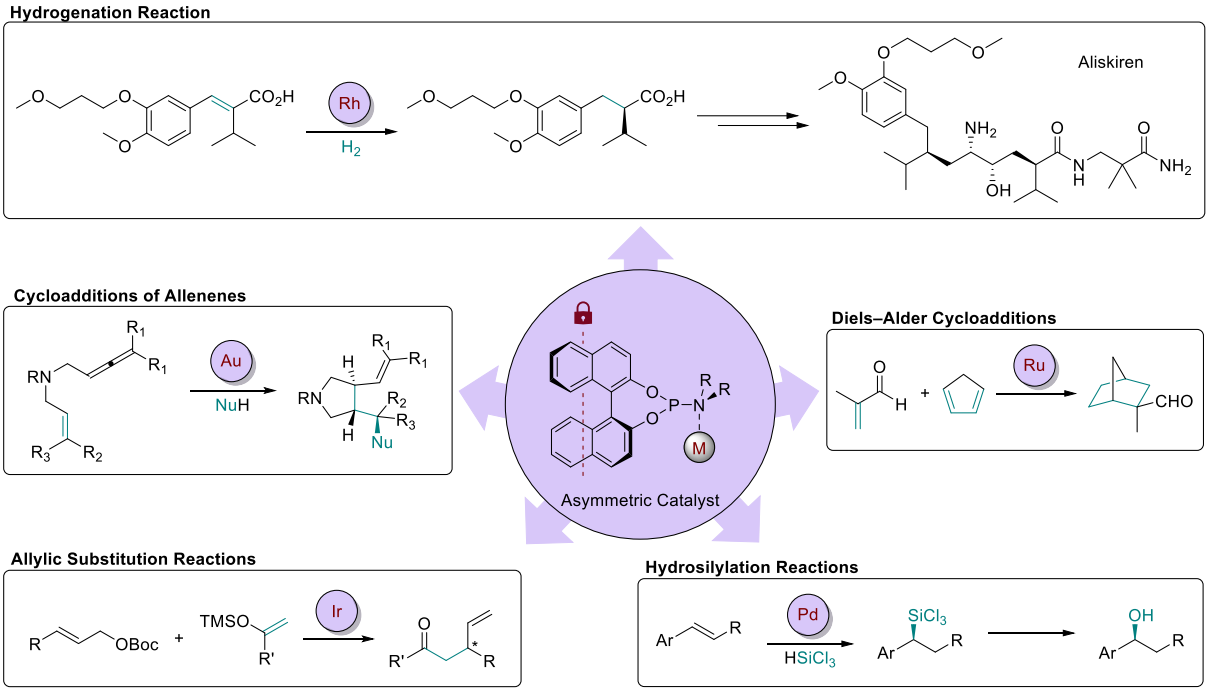

Figure 1-19 Schematic overview of different exemplary reactions catalysed by phosphoramidite transition metal catalysts.

Since Arduengo *et al.* first reported the isolation of a stable carbene in 1991[134] N-heterocyclic carbenes (NHCs) became a staple of transition metal catalysis. The combination of stability and tunability made them the ligand of choice for many transition metal catalysts.[135–137] The structure of the NHCs enables easy modification of the ligand to influence the space surrounding the coordinated metal, shaping the catalytic side for the desired outcome.[138] A bent 1,1′-methylenebis-(3-(4-carboxy-2-methylphenyl)-1H-imidazol-3-ium ligand was used to construct a Zn-based metal-organic nanotube (Figure 1-20).[139] The imidazolium ligands were readily deprotonated by palladium acetate in tetrahydrofuran as solvent to form a catalytically active Pd-NHC complex within the nanotube. The functionalized metal-organic nanotubes successfully promoted Suzuki–Miyaura and Heck coupling reactions, as well as hydrogenation reactions, and were recyclable for at least seven cycles.

Following the isoreticular principle, an NHC-functionalized ligand was incorporated into a framework of UiO-type through a mixed linker approach.[140] BPDC and bi-NHC-functionalized Au- and Pd complexes were combined with zirconium chloride to yield the functionalized UiO-67 framework. The new material was successfully tested as a dual catalyst for the alkyne hydration–Suzuki coupling reaction. In a similar approach, an Ir-NHC-functionalized UiO-type framework was synthesized through direct mixed linker synthesis.[141] The authors showed that through the alternative post-synthetic introduction of the Ir-NHC-functionalized linker higher metal loadings were achieved within the MOFs. On a normalized catalytic loading, the catalytic performance of both materials was similar.

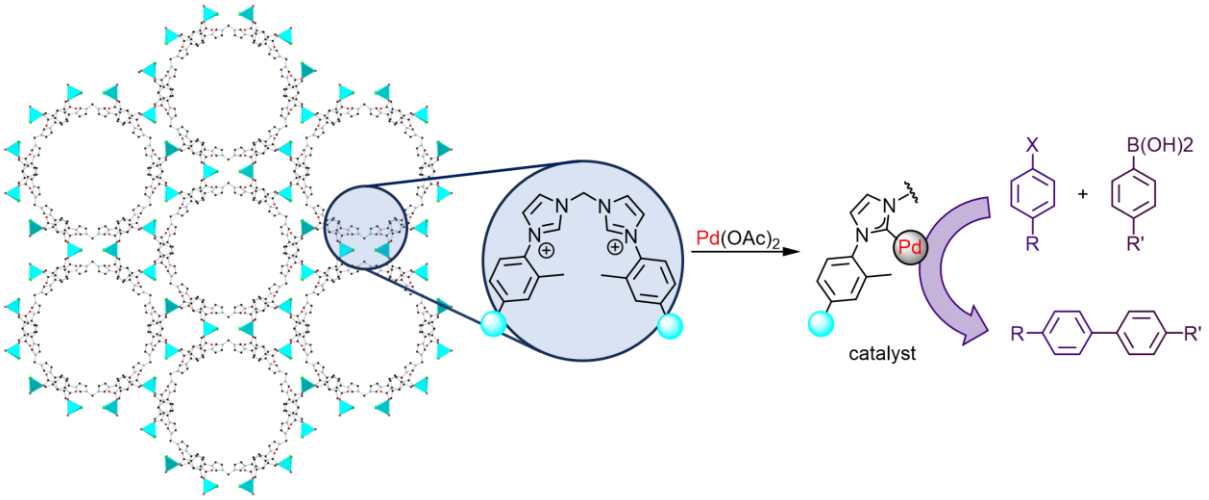

Figure 1-20 Post-synthetic modification of an imidazolium functionalized-metal-organic nanotube and successful promotion of the Suzuki–Miyaura coupling reaction of phenyl halides and phenylboronic acids.

1.4 MUF-77 — a Multicomponent MOF With a Tuneable Pore Environment

Multicomponent metal-organic frameworks, which are constructed from a set of several ligands with different geometries, provide a powerful platform for obtaining ordered, elaborate, and programmable pores. MUF-77 (MUF = Massey University Framework) materials are quaternary MOFs, constructed from three topologically distinct carboxylate linkers and Zn_4O secondary building units. MUF-77 is outstanding in the wide realm of Zn-based MOFs for it is formed by three distinct organic linkers. When the ligand bears catalytically-active groups, the frameworks act as effective, recyclable and stable heterogeneous catalysts.[142] By introducing functional groups to the ligands, the pore-environment in the framework can be tuned. In turn, this allows the catalytic properties to be modulated.[143]

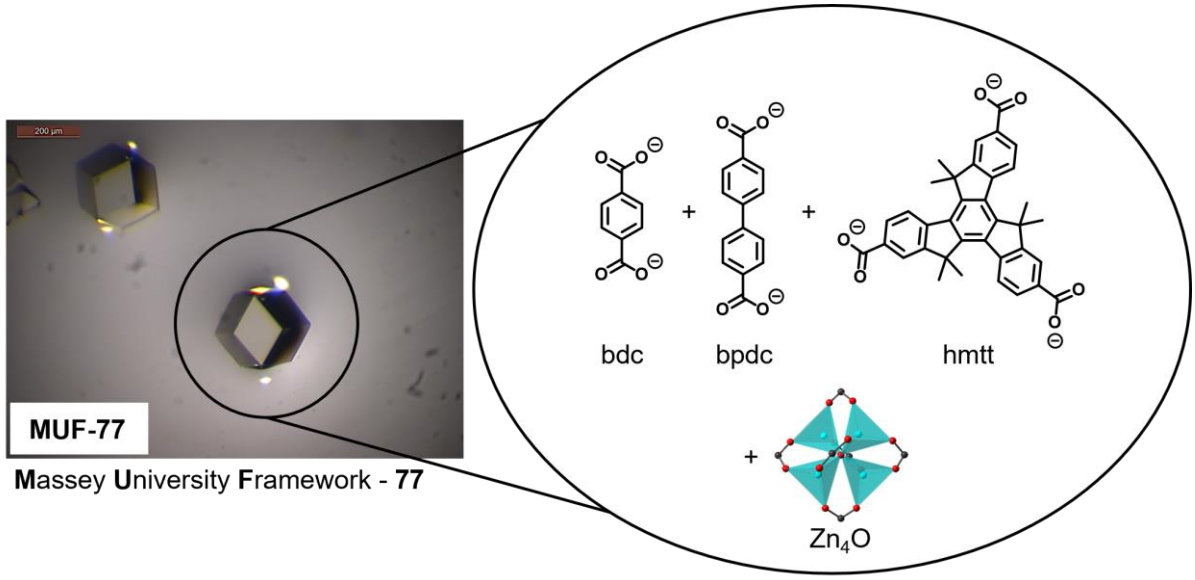

Figure 1-21 MUF-77, a multicomponent MOF assembled from the organic linkers bdc, bdpc, and hmtt in combination with Zn_4O SBUs.[142]

1.4.1 Synthesis of MUF-77

Our group developed two main synthetic pathways to obtain MUF-77, described by the formula $[Zn_4O(hxtt)_{4/3}(bpdc)_{1/2}(bdc)_{1/2}]$, where x is the substituent on the methine bridges of the truxene tricarboxylic acid linker (for MUF-77 most commonly alkyl groups, with 'm' for methyl, 'e' for ethyl, *et cetera*), a solvothermal synthesis and a room temperature synthesis. The methods are sensitive to the ratios of ligands used in the synthesis, as well as other reaction conditions, like the choice of solvent or additives. As described earlier, bdc and bpdc ligands have been utilized as ligands for the IRMOF series, and truxene-derived ligands are also known to independently form MOFs.[144–146] Moreover, the combination of tritopic and ditopic linkers under the right conditions is known to form MOFs like UMCM-1.[147] It is thus remarkable, that the formation of MUF-77 with the three distinct ligands is preferred under the right conditions. Both synthesis methods yield crystalline MUF-77, however, crystals in sizes suitable for single-crystal X-ray diffraction can so far only be obtained through solvothermal synthesis (Figure 1-22).

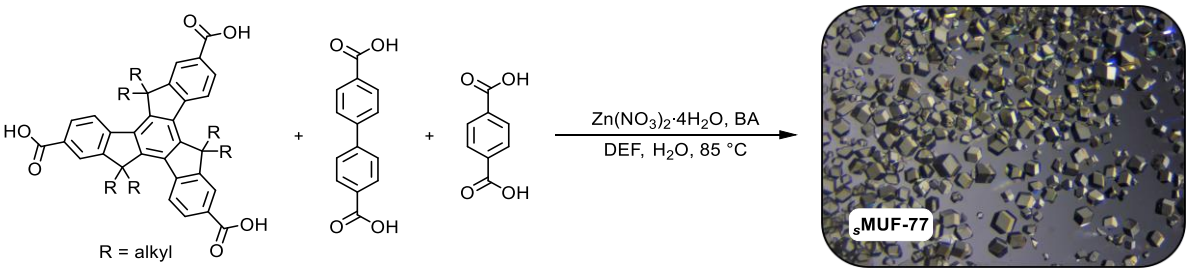

Figure 1-22 General solvothermal synthesis procedure for $_s$MUF-77.

An optimized synthetic solvothermal protocol produces uniform single crystals of up to 0.5 mm in size. The crystals are usually obtained as truncated-dodecahedrons. As seen with other MOFs, MUF-77 crystals are transparent and often turn opaque upon loss of crystallinity. Variations in synthesis temperature and amount of benzoic acid (BA) as a crystal-growth modulator can lead to changes in the nucleation time. Crystal formation at more elevated temperatures can be observed within hours, while slower crystal growth can be achieved at lower temperatures. However, the most reliable and reproducible results are usually obtained at 85 °C after around 24 h, making it the preferred synthesis protocol in many use cases.

The synthetic procedure at room temperature requires zinc acetate instead of zinc nitrate used for solvothermal procedures (Figure 1-23). The increasing basic nature of the metal source allows the formation of nanometer-sized MUF-77 ($_{rt}$MUF-77) crystals, around 500 µm in size.[148] $_{rt}$MUF-77 can usually be obtained within minutes of mixing a solution of ligands with the zinc salt.

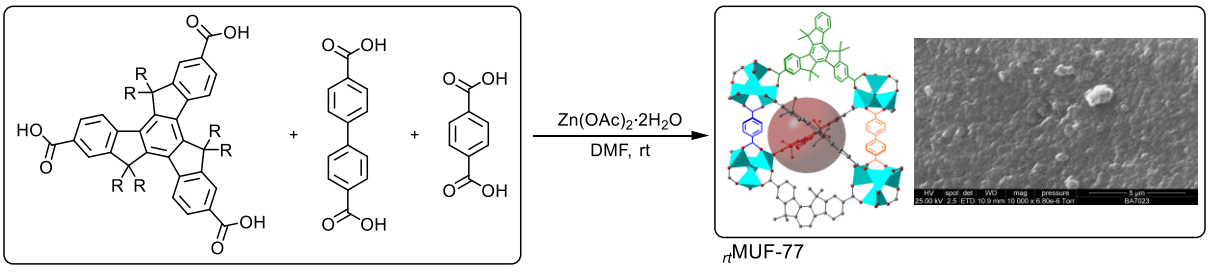

Figure 1-23 General solvothermal synthesis procedure for $_{rt}$MUF-77.

MUF-77 is built by the three ligands and Zn_4O SBUs falling perfectly into place to form the framework structure, each ligand in its distinct crystallographic position. MUF-77 crystalizes in the cubic space group $Pm\bar{3}$ and the framework lattice topology can be described as *ith-d*. At each Zn_4O SBU, four tritopic ligands are positioned equatorially, while the axial sites are filled by one bpdc and one bdc ligand. The linker and SBUs are arranged to form two mesopores and one smaller micropore. The diameter of the mesopores was estimated around 22 Å and 24 Å (calculated from the crystal structure using CrystalMaker® 10, allowing for van der Waals radii of the framework atoms) while the micropore is roughly 10 Å in diameter in size.

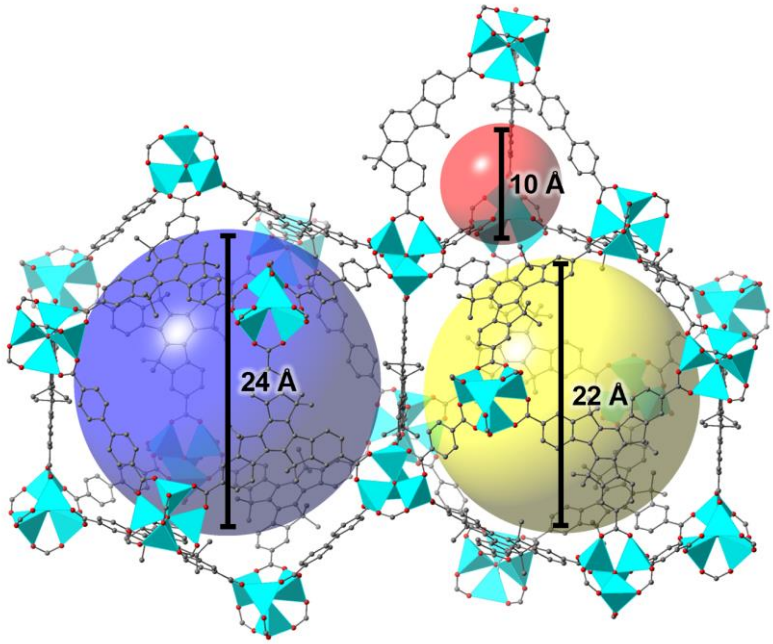

Figure 1-24 The three distinct pores within MUF-77 as illustrated by the crystal structure of $[Zn_4O(hmtt)_{3/4}(bpdc)_{1/2}(bdc)_{1/2}]$. The three distinct linkers arrange during MOF synthesis to form two mesopores and one micropore.

Those cavities illustrate beautifully the highly porous nature of MUF-77. MUF-77 from hmtt (hexamethyl truxene tricarboxylic acid, 5,5′,10,10′,15,15′-hexamethyltruxene-2,7,12-tricarboxylate), bpdc and bdc showed a BET surface area of 3600 g^2/m.[142] Naturally, the porosity is a function of linker functionalisation and the uptake of space of each functional group introduced into the pores. Extending the alkyl chain from hexamethyl- to the hexahexyl- and hexadecyltruxene ligands was accompanied by a decrease in BET surface area to 2170 and 1170 g^2/m, respectively. That porosity lays the foundation for the application of MUF-77 in various fields where easy diffusion of small molecules through the framework is critical. The isoreticular principle, as discussed in Chapter 1.2.1, can also be applied to MUF-77 and the organic linkers in many cases exchanged with linkers of similar size and geometry. Compared to other zinc-carboxylate MOFs, MUF-77 is very stable in solvent and upon solvent removal, even at elevated temperatures. Yet, the ligand-metal coordination bond is weaker than in the zirconium-carboxylate bonds in UiO-66 or the zeolite-type framework ZIF-8, which is formed by zinc-imidazolate coordination. Those frameworks are versatile skeletons for simple incorporation of functional groups and their application under harsh conditions. MUF-77, however, is the MOF of choice when modulation of the pore sites is required. The well-defined arrangement of the three different ligands allows us to fine-tune the pore environment by independently

functionalizing each ligand. This provides us with three levers to shape the pore to the desired application. This is only possible due to the unique locations of each ligand within the structure. This well-defined framework of several organic linkers is commonly described as a multi-component MOF. It is important to emphasize the difference to multivariate (MTV) MOFs, frameworks also built from several different linkers, but with the linkers randomly filling the available positions (Figure 1-25). The terms multicomponent and multivariate are sometimes used interchangeably in literature. However, a more precise definition is essential as both framework types are inherently different. A comparison of MUF-77 with MTV-MOF-5 (multivariate MOF-5) visualizes the difference in the incorporation of multiple ligands within the framework. In MUF-77 each ligand is unique in its geometry and length, forcing them into ligand-specific locations during the framework formation (Figure 1-25). MTV-MOF-5 is constructed from ligands very similar in geometry and length, thus all ligands are theoretically able to fill all available locations. The ligand locations can be merely predicted as statistical distributions within the framework. Of course, the incorporation of several, very similar ligands is not unique to MOF-5 and it is easy to imagine that multivariate versions- at least theoretically- exist for a large number of MOFs. For a multicomponent MOF, such as MUF-77, multivariate analogues can be obtained by introducing several similar ligands for each component of the MOF.

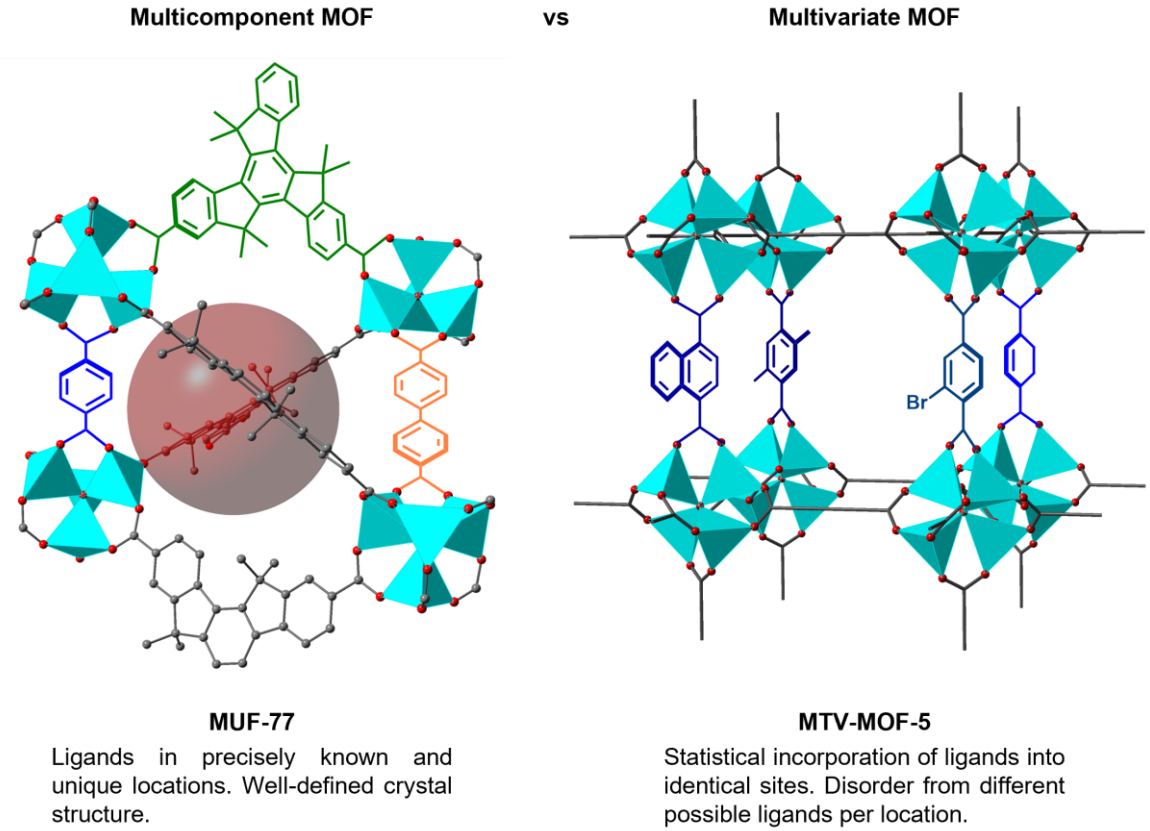

Figure 1-25 Comparison of the multicomponent MOF MUF-77 with a multivariate MOF like MTV-MOF-5.

Those structural differences also have important implications for the properties of each MOF family. MTV-MOFs are easy to synthesize, due to the great similarities in the ligands' coordination behaviours. The properties of the resulting MOFs can easily be modified by the introduction and combination of several different ligands. Alterations in MTV-MOF-5 thus led to major changes in the gas uptake behaviour of the

MOF. However, those modulations are limited to the statistical incorporation and distribution of the ligands. It is impossible to design and predict individual pores. This becomes a significant obstacle when trying to arrange less-compatible ligands within the pores. In this case, the naturally preferred ligand arrangement for each pore might lead to unwanted aggregation of certain ligand types at different framework locations to avoid steric or physiochemical repulsion of ligands within the pore. The synthesis of multicomponent MOFs is more challenging, as it requires favourable crystallization conditions for ligands with different geometries and properties. The synthetic procedures also need to favour the multicomponent MOF over the possible frameworks formed by each component. However, once obtained, multicomponent MOFs like MUF-77 allow for precise modulation of the framework pores, enabling the combination of ligands with very different properties in a highly predictable manner.

1.4.2 Modularity of MUF-77

The modular of MUF-77 was demonstrated by our group in the work on tuning the luminescent output of the MOF.[148] Incorporation of different fluorophores into MUF-77 allowed to finely tune the emission spectra of the whole framework as a combination of the individual emission spectrum (Figure 1-26). The different tritopic truxene linkers showed maximum emission around 430 to 445 nm, using an excitation wavelength of 390 nm. That yielded a blue colour of the framework under UV light exposure. Functionalization of the parent ditopic bpdc linker with a guanidine group shifted the emission maximum to 570 nm. Upon incorporation into MUF-77, the framework produced a yellow emission band. A similar influence in emission on the framework was observed when the ditopic bdc ligand was functionalized with an amino group, yielding a linker with a strong blue emission, leading to a deep-blue emission band of the frameworks. Combining both linkers with a suitable truxene-based linker gave access to MUF-77 with white emission. In additional experiments, the yellow contribution to the overall emission was finely modified by diluting the fluorophoric guanidine-functionalized bpdc with essentially non-emissive parent bpdc linkers. This work beautifully highlighted the isoreticular chemistry possible within MUF-77 and the potential of multicomponent MOFs for tuning desired applications by linker combination and pore design.

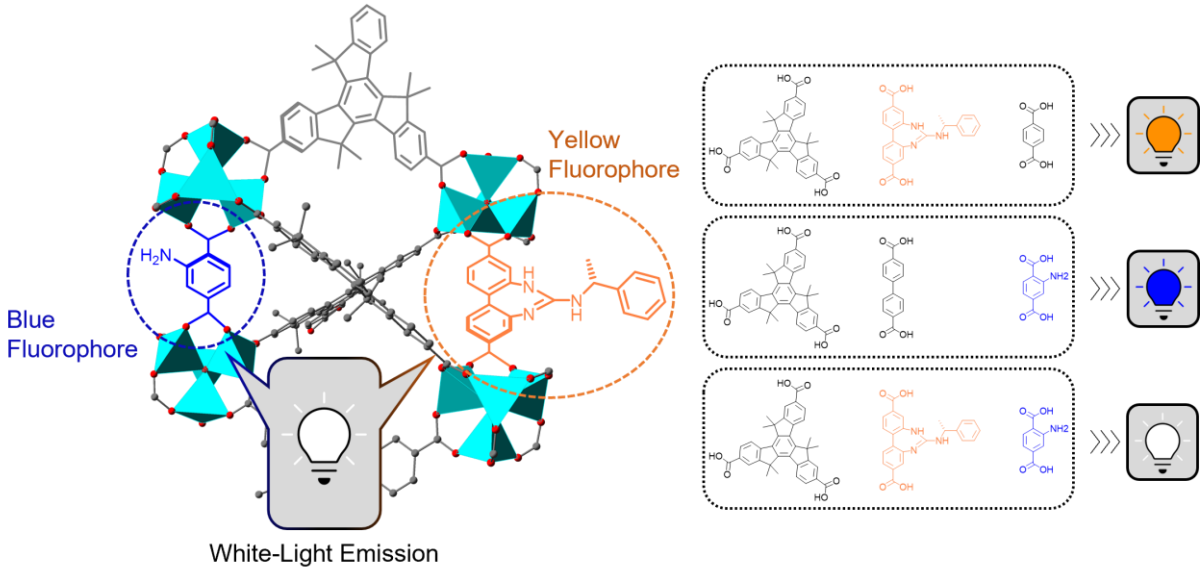

Figure 1-26 The combination of different fluorophoric linkers within MUF-77 allowed to finely tune the emission spectra of the framework as a complex combination of the individual emission profiles.

1.4.3 Pore Modulation in MUF-77 for Tuning Catalysis

The challenge in the design of novel catalytic systems arises from the limitations of tuning the catalyst properties for specific, demanding reactions. This can be often observed in the synthesis of fine chemicals where catalyst selectivity is essential for obtaining the desired product. Enzymes are well known for achieving high selectivity by providing favourable pore environments for certain substrates. However, altering those enzyme catalysts in a controlled manner is challenging and due to their structural complexity, the stability is often limited to very specific and often mild conditions. Traditional molecular catalysts were employed to close the gap and widen the scope of catalysts. Their design relies on traditional synthesis and is thus easily altered. A large variety can be relatively easily designed and screened. However, due to their limited structural complexity, they are often limited in the extent of controlling the substrate environment. While more complex molecular systems can be obtained, their syntheses become more challenging and the structural arrangement in solution is often hard to predict. Multicomponent MOFs like MUF-77 are valuable scaffoldings for selective catalytic applications. Through isoreticular chemistry, the linkers are easily replaced with known molecular catalysts. Adjusting the remaining linkers to the desired reaction allows the creation of a unique and highly specific pore environment.

Proline is a well-known organocatalyst and its successful application as a chiral catalyst defined a milestone in asymmetric organocatalysis.[149–152] The potential for catalytic applications of proline was reported in the early 1970s and the reaction was coined Hajos–Parrish–Eder–Sauer–Wiechert after the researchers involved.[153,154] While the scope of catalytic applications was quickly broadened, including Mannich reactions[155], α-amination of aldehydes[156] and Michael additions,[157] aldol reactions remained among the most prominently featured reactions successfully promoted by proline with great enantioselectivity.[158] Our group successfully installed a proline functional group within the MUF-77 framework (Figure 1-27).[143] Adapting the protocol[61] presented earlier (Chapter 1.2.2.2) the ditopic bpdc and bdc linkers were functionalized with a Boc-protected proline group. The functionalized linkers were then used in the synthesis of MUF-77 with the unaltered ditopic counterpart, tritopic hmtt linkers, and zinc nitrate

tetrahydrate in diethylformamide (DEF) as solvent. The MUF-77 crystals with the formulas $[Zn_4O(hmtt)_{4/3}(bpdc\text{-}Pro\text{-}Boc)_{1/2}(bdc)_{1/2}]$ or $[Zn_4O(hmtt)_{4/3}(bpdc)_{1/2}(bdc\text{-}Pro\text{-}Boc)_{1/2}]$ were then exposed to high temperature under vacuum to cleave off the thermolabile Boc protection group. The obtained proline-functionalized MUF-77 crystals were active catalysts for the aldol reaction of acetone and *p*-nitrobenzaldehyde. The proline group retained its catalytic activity within the MOF pores and the heterogeneous nature of the catalyst allowed for easy recyclability. The advantage of multicomponent MOFs was demonstrated by adjusting the pore environment around the catalytic side. Adjusting the length of the alkyl chain of the truxene linkers improved the activity, while functionalization of the bdc linker increased the selectivity of the proline catalyst for the tested aldol and Henry reactions.

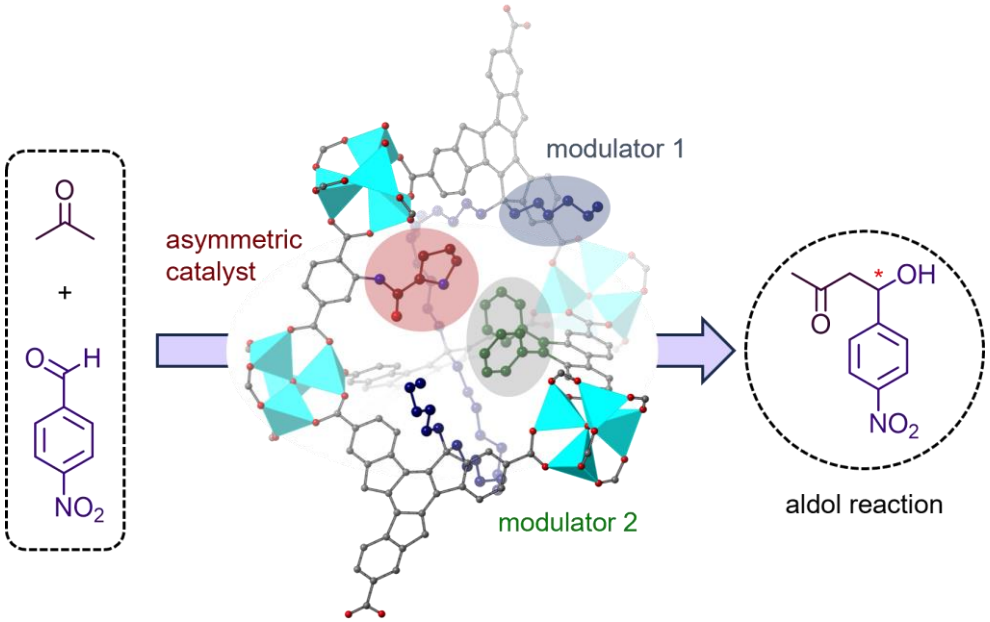

Figure 1-27 Schematic representation of pore modulation strategies within MUF-77.

1.5 Research Aims and Objectives

To expand the scope of potential applications for MUF-77, the incorporation of functionalized linkers is of great importance. While the synthesis of MUF-77 has been well understood for previously reported linker combinations, incorporating new linker systems is not trivial and often leads to the formation of unknown phases, rather than the desired MUF-77 product. Competing formation of other multicomponent or single-ligand-MOF systems from the same set of linkers often interferes with MUF-77 synthesis in favour of the formation of unknown crystalline phases. This work is aimed at deepening our understanding of the competing MOF formations. By systematically adjusting individual parameters of the standard MUF-77 synthesis conditions, we can monitor the impact on MOF composition. In our experience, linker ratios and linker functionalization are crucial parameters for the successful MUF-77 synthesis and thus provided a promising starting point for this analysis. The findings would not only shed light on the different synthetic parameters for successfully and reliably obtaining MUF-77 but investigating the new crystalline phases would allow us to identify potential new MOF systems with unique characteristics and properties. Chapter 2 of this work is focused on the discussion of novel MOFs obtained from traditional MUF-77 building blocks.

As described in the previous chapter, MUF-77 was successfully employed as a scaffold for proline-catalyzed reactions. We envision broadening the scope of MUF-77 catalytic systems towards the implementation of transition metal complexes as active catalysts. We outlined a broad range of possible catalysts and transformations that such systems would allow access to. We hypothesize that pore modulation, similar to the reported organocatalytic MUF-77 examples, would enable us to access catalyst performances surpassing those achievable through traditional homogeneous catalysts, paired with easy recyclability inherent to heterogeneous materials. The functionalization of known MOFs with catalytically active transition metal catalysts has its unique challenges. The design of MUF-77-compatible linkers needs to take MOF and linker properties, like stability and steric demand, into account. To identify suitable transition metal catalysts, we aim to employ traditional MUF-77 linkers and introduce functionalities suitable for the stabilization of transition metal complexes. The examples of transition metal complexes and catalysts described in the introduction to this work include, in our eyes, the most promising starting candidates for this exploration due to their structural resemblance to traditional MUF-77 linkers. MUF-77-compatible linkers shall be synthesized and further investigated for the incorporation into MUF-77. Upon successful installation of a transition metal complex within the MUF-77 scaffold, the catalytic activity should be evaluated based on well-established protocols for similar homogeneous systems. Once satisfying catalytic activity is achieved, pore modulation by functionalization of the adjacent linkers with catalytically inert moieties should be employed to tune the catalytic performance. The findings of this approach are discussed in Chapters 3 and 4.

MOFs like PCN-333 provide powerful platforms for the encapsulation of enzymes. We envision that similar interactions with bioelectrocatalytic electrodes could improve electrode performance and stability. However, bioelectrode preparation and application often include the use of aqueous buffers to ensure enzyme stability, conditions detrimental to the stability of many MOFs. Thus, the stability and behavior of PCN-333 under those conditions need to be understood. Subsequently, the impact of MOF modifications on bioelectrode stability and performance should be evaluated. Our investigations on this topic are presented in Chapter 5.

In addition to traditional characterisation techniques employed in organic chemistry, such as ^{13}C NMR and ^{1}H NMR spectroscopy, which are used to confirm the organic linker synthesis, additional standard methods are available for MOF characterisation. The molecular arrangement and structure of the new materials can be confirmed by X-ray diffraction analysis of well-ordered and sufficiently large single crystals. Here, the detected diffractions are used to model the crystal's unit cell dimensions, the positions of all atoms within the unit cell, and the bond lengths and angles between them. Bulk properties of the material are often determined by powder X-ray diffraction, as this method can be employed to quickly gather information about the crystallinity and composition of bulk samples. Similar to single-crystal X-ray diffraction, the incident X-ray beam is diffracted at specific angles by the crystalline structure. A detector measures the intensity of these diffracted X-rays as a function of the diffraction angle (2θ), creating a unique "fingerprint" pattern for the material. Additionally, the MOF composition can be determined by NMR spectroscopy. Where solid-state NMR is not available or applicable, the solid samples are usually digested and dissolved, often described as “digested”, in a suitable deuterated solvent before the solutions are subjected to the analysis. The information obtained includes the ratio of ligands within the solid material and the chemical

nature of the linkers upon exposure to the MOF synthesis conditions. Additionally, measuring the adsorption of different gases provides insights into the surface area, pore size distribution, and the interaction of the new materials with gases. The enzyme activity of bioelectrodes can be established by cyclic voltammetry. Cyclic voltammetry (CV) is used to study electron transfer processes involving enzyme catalysts. By sweeping the electrode's potential and measuring the resulting current, CV provides insights into the redox activity of the biocatalyst. Stability of the electrodes can be further analysed by chronoamperometry (CA), an electrochemical technique where a constant potential is applied to an electrode, and the resulting current is measured as a function of time.

Chapter 2 New MOFs From MUF-77 Building Blocks

2.1 Overview

The synthesis of multicomponent MOFs is challenging due to the various combination possibilities of linkers and metal nodes. This is also true for MUF-77. The synthesis of MUF-77 from new organic ligands often requires adjustments of the synthetic conditions to account for differences in the ligands' properties. Different solubilities or electrochemical properties can influence the coordination behavior of each ligand and thus have a detrimental impact on the nucleation and crystallization of the desired MOF. It is not surprising that during new synthesis attempts of isoreticular MUF-77 systems, second phases of unknown origin can be observed (Figure 2-1). To this point our understanding of the formation of those secondary phases and their structures was very limited. Deeper insights into these systems would enable us to fine-tune synthetic conditions for MUF-77, leading to more successful and consistent outcomes. Additionally, it may reveal new applications if the resulting MOFs exhibit promising properties.

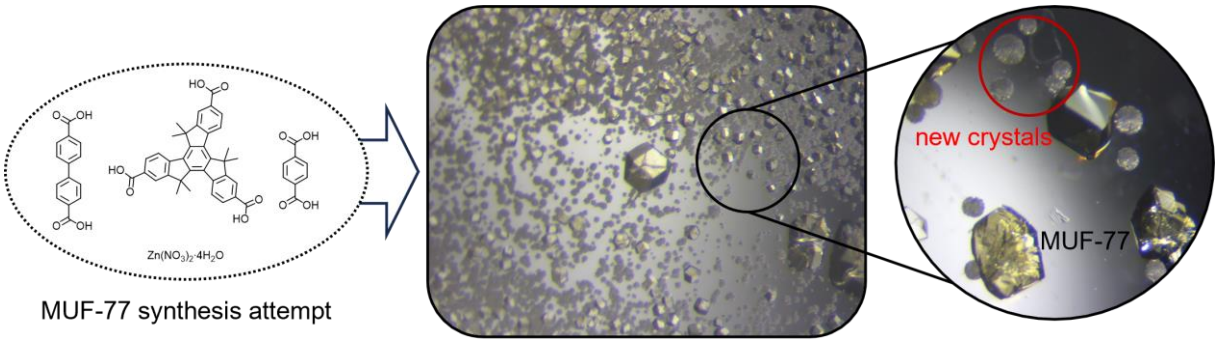

Figure 2-1 MUF-77 synthesis attempts leading to the formation of a second, novel, and crystalline phase.

Small changes in the reaction conditions can have a large impact on the MOF formation. An example was shown by the Matzger group, where the combination of a ditopic bdc and a tritopic 1,3,5-tris(4-carboxyphenyl)benzene (btb) linker with a Zn^{2+} source led to the formation of new MOFs (Figure 2-2).[159] Under otherwise identical reaction conditions, an excess of bdc led primarily to the formation of MOF-5. Increasing the amount of tbt in the synthetic procedure led to a mixture of products. Besides MOF-5 a second framework was identified and denoted as UMCM-1. The framework with the molecular formula $Zn_4O(bdc)(btb)_{4/3}$ is constructed from both, ditopic and tritopic ligands. Optimizing the molar ratios allowed to tweak the product formation towards a pure UMCM-1 phase. Further increases in the molar btb:bdc ratio led to a new mixture of MOF materials, UMCM-1 and MOF-177,[160] a MOF formed solely by btb ligands and metal SBUs. Increasing the amount further led to the uniform formation of MOF-177.

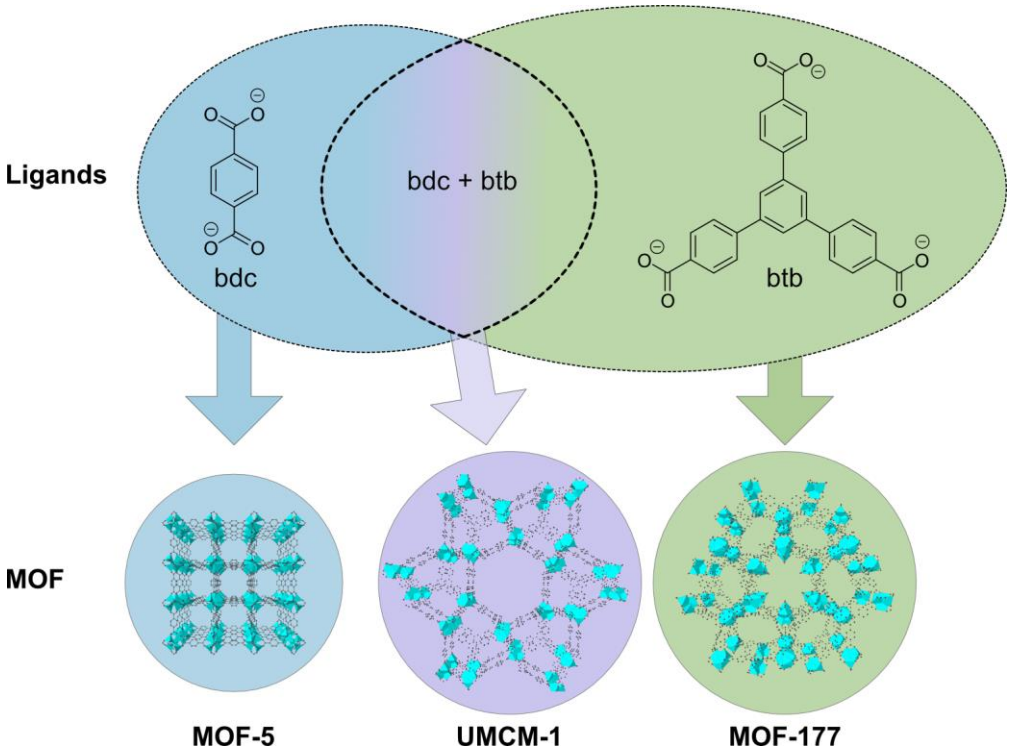

Figure 2-2 The combination of bdc and btb linkers with zinc nitrate in *N,N*-diethylformamide under the same conditions yielded three different MOFs, MOF-5, UMCM-1, and MOF-177, depending on the linker stoichiometry.[159]

This versatility was exploited for the formation of new structures. The Yaghi group utilized extended tritopic ligands to synthesize new MOFs with high porosity (Figure 2-3). The combination of btb with a 2,6-napthalenedicarboxylate (ndc) ditopic ligand successfully formed a new framework, MOF-205. A combination of btb and bpdc was long believed to not lead to a MOF formation.[161] Only after extension of the btb linker, the new 4,4′,4″-[benzene-1,3,5-triyl-tris(ethyne-2,1-diyl)]tribenzoate (bte) linker was successfully combined with bpdc in the synthesis of MOF-210.[162] The similarity of ligands and reaction conditions to the ones applied for the MUF-77 synthesis was striking. Thus, it is not surprising, that during synthesis attempts of new MUF-77 analogues the formation of different crystals is often observed, either as a secondary phase or as the main product.

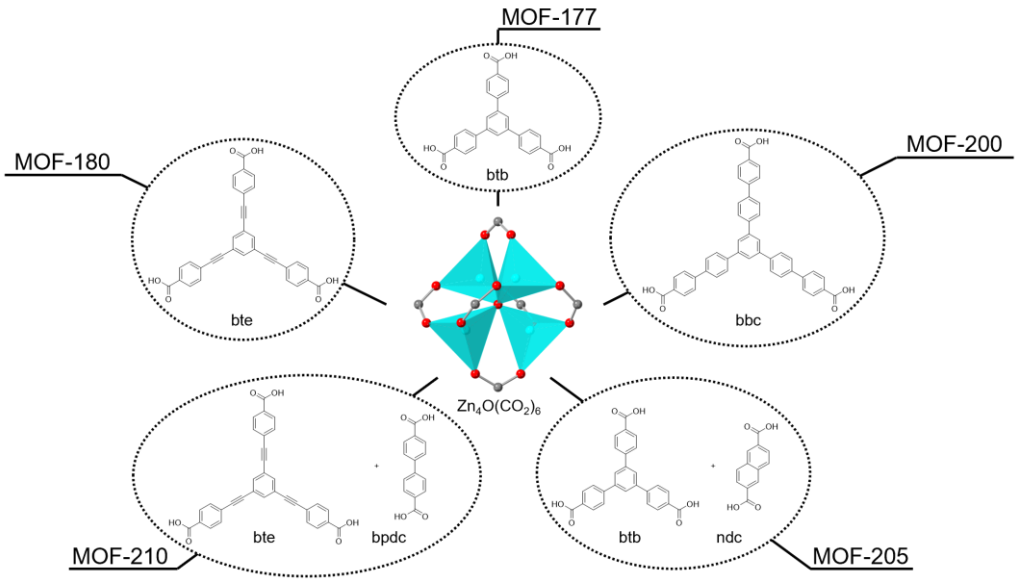

Figure 2-3 Overview of the different MOFs reported by the Yaghi group.[161] The MOFs were based on tritopic linkers, either used individually or in combination with ditopic linkers.

2.2 Results and Discussion

To investigate the formation of new crystal phases, we adjusted the typical MUF-77 synthesis procedures by systematically adjusted linker composition and reagent ratios as outlined in the following chapters. During our investigations, we found at least six reoccurring crystalline products (Figure 2-4). We denoted the new phases as BMUFs as we first noticed them as byproducts during MUF-77 synthesis.

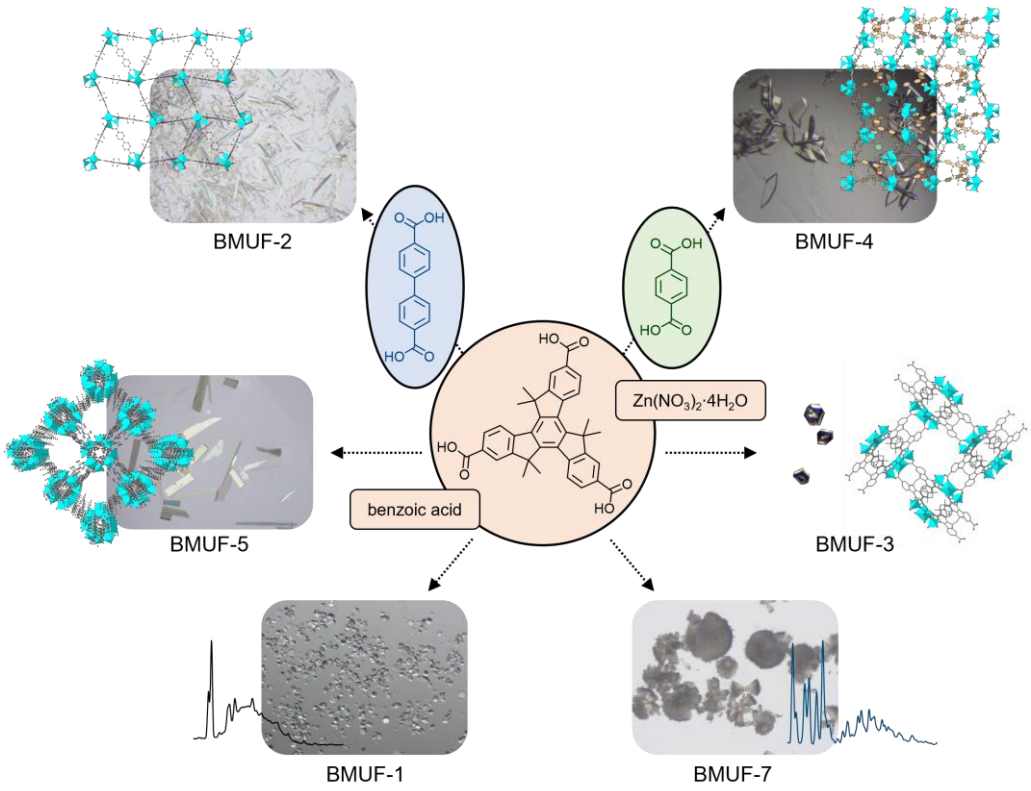

Figure 2-4 Overview of the crystalline phases obtained from hmtt, benzoic acid (BA) and zinc nitrate tetrahydrate in DMF or DEF.

2.2.1 Synthesis and Characterization of M[$Zn_4O(hmtt)_2(bpdc)_{0.5}$]

MUF-77 synthesis is often accompanied by the formation of a second phase of distinct crystalline solids, regularly observed as spherical clusters. For many ligand combinations, we found those clusters as the main product of the attempted MUF-77 synthesis. Removal of those clusters by hand is cumbersome and adjustments to the reaction conditions were only sometimes successful. Thus, we decided to investigate the formation of this byproduct. During our investigations, we found that the novel multicomponent framework was comprised of hmtt and bpdc ligands. A synthetic procedure was developed to produce the MOF with phase purity. Combining hmtt with bpdc zinc nitrate in DMF yielded uniform colourless crystals of a new multicomponent MOF, which was coined BMUF-2.

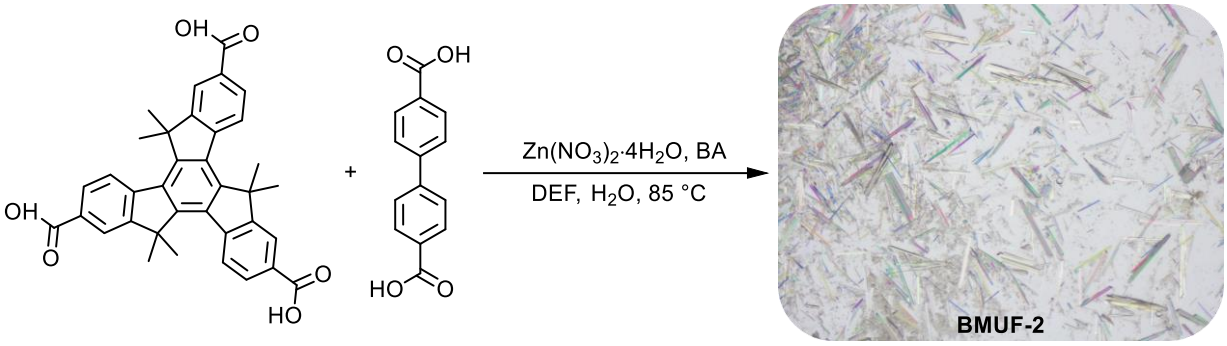

Scheme 1 Synthesis of BMUF-2 from hmtt, bpdc, benzoic acid (BA) and zinc nitrate tetrahydrate.

From the integration of the ^{1}H NMR spectrum of the digested MOF in a mixture of DMSO-d_6 and DCl we determined the ligand ratio of hmtt to bpdc as 1:0.25.

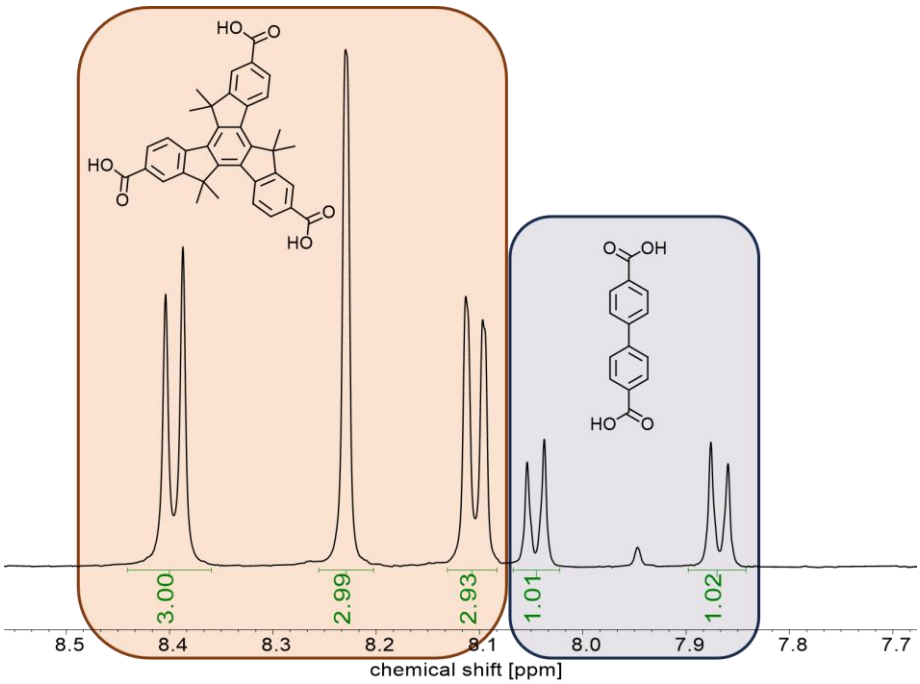

Figure 2-5 ^{1}H NMR of the digested BMUF-2 in a mixture of DMSO-d_6 and DCl. Only the aromatic region is shown for clarity.

SXRD data confirmed the formation of a framework with the formula M[$Zn_4O(hmtt)_2(bpdc)_{0.5}$], where M is a monovalent, cationic species (Figure 2-6). In BMUF-2, hmtt linkers form a honeycomb-like framework

with bpdc ligands inserted into alternating channels creating octahedral pores. The rhombohedral channels span approximately 18 Å x 11 Å in diameter and pores can house a sphere with a diameter of 13 Å (determined with CrystalMaker® 10 from the crystal structure, considering the calculated van-der-Waals surface). A monovalent cation must be present in the MOF pore to ensure a formal charge balance. This was supported by significant unresolved electron density. The cation could not be identified due to the high amount of disorder in the pore.

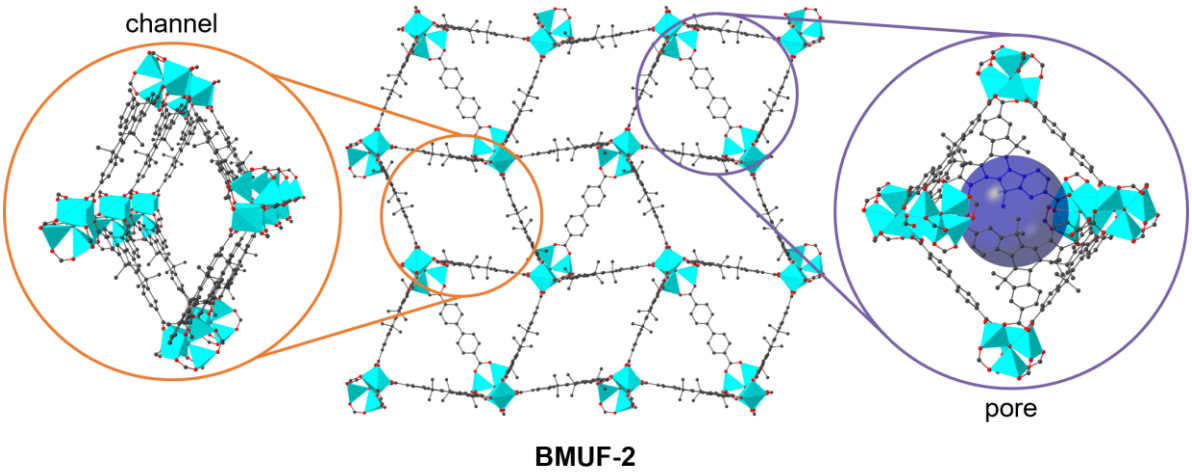

Figure 2-6 Crystal structure of BMUF-2. Carbon atoms are depicted in grey, oxygen in red, nitrogen in blue, and zinc in turquoise. Hydrogen atoms are omitted for clarity.

PXRD data confirmed the phase purity of the sample and was in good agreement with the simulated data (Figure 2-7).

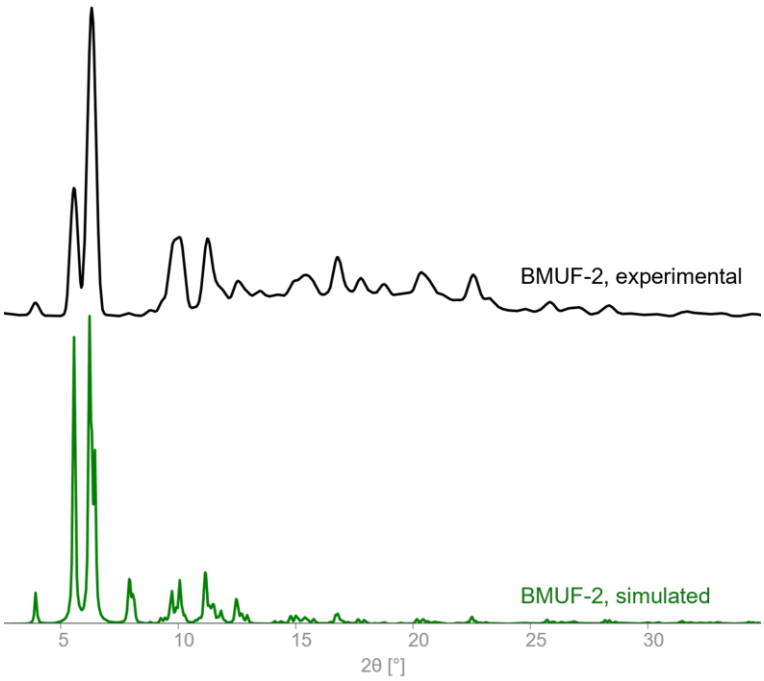

Figure 2-7 Experimental PXRD pattern of BMUF-2 (top, black) in comparison with the simulated PXRD pattern (bottom, green).

As mentioned in the previous chapter, a multicomponent MOF containing bpdc ligand and a tritopic btb type ligand was long considered not possible.[161] However, recent reports showed that reducing the symmetry of the tritopic ligand allowed the combination with bpdc to successfully form frameworks with new topologies. Duan *et al.* synthesized a framework with *hww* topology from tritopic linkers with C_{2v} symmetry.[163] They theorized that reducing the symmetry of the ligand avoided the preferred average coordination of six ligands, as usually observed for btb, around the cluster, creating coordination sites for terminal ligands. They were able to adjust the pore volume, sizes, and shape of the MOF by systematically altering the size of ditopic and tritopic ligands. Hmtt and similar truxene-derived tritopic ligands are of C_{3h} symmetry. While the symmetry is lowered compared to btb, the coordination geometry of hmtt can also be depicted as a planar triangle with similar dimensions (Figure 2-8).

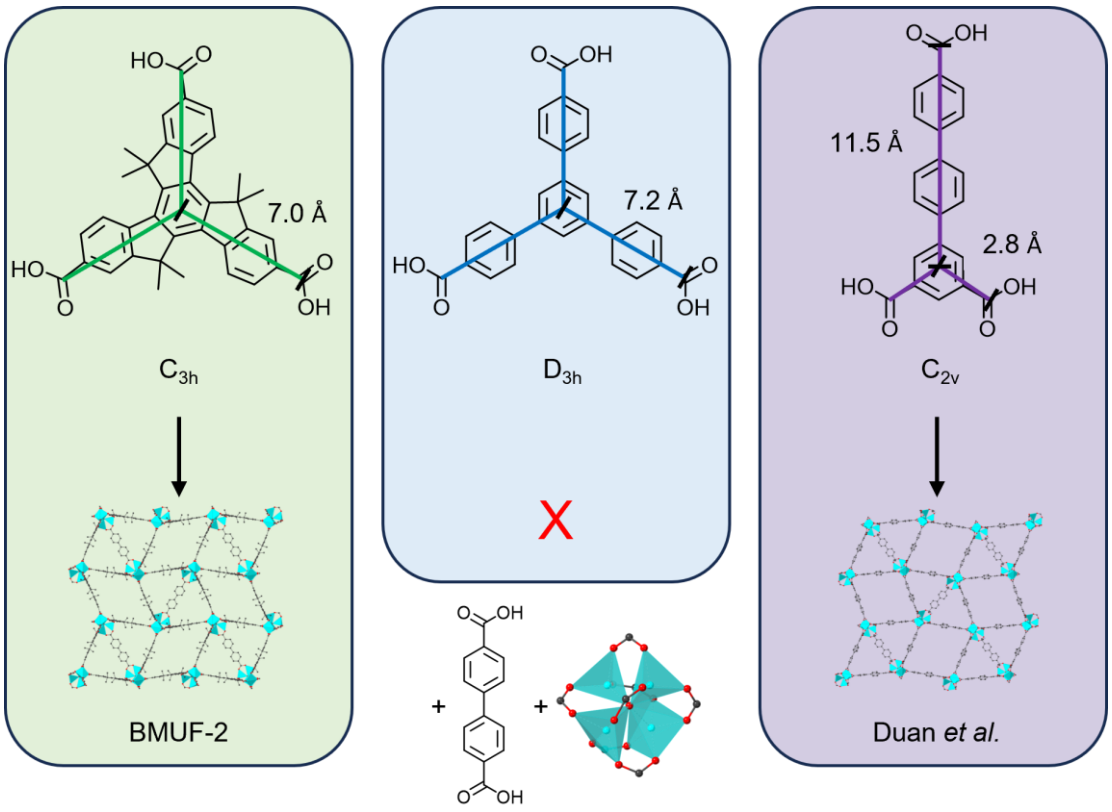

Figure 2-8 Comparison of tritopic ligands with different symmetries and sizes in the synthesis of new multicomponent MOFs. Atom-to-atom distances were calculated from structural models of the ligands. The ligand geometry was optimized using the software Avogadro 1.20[164] employing a MMFF94 forcefield.

It is mainly the lower symmetry that sets hmtt and btb apart, breaking up the preferred coordination uniformity and allowing for the incorporation of the ditopic bpdc ligands. Compared to the terphenyl-type tritopic ligands employed by Duan *et al.* hmtt is in close resemblance to btb, highlighting the importance of the symmetry-derived coordination preferences of the ligands as opposed to length or shape differences, which could also explain the different behaviour of btb compared to the terphenyl-type ligands. We observed this kind of framework for a number of different additional ligands and found the typical crystals in many other MUF-77 synthesis attempts, indicating the tolerance of the framework towards different organic linkers.

Typically for many Zn-based MOFs, BMUF-2 showed good stability in different solvents. After drying the crystals from acetone or dichloromethane the PXRD changed significantly. The overall signal-to-noise ratio was decreased, indicating a partial structural collapse. Only two broadened peaks around 2θ = 6.0° and 10.4° indicated some retained crystallinity. In our experience, many Zn-SBU-containing MOFs often require elevated temperatures under vacuum to fully remove *n*-octane from the MOF pores. We theorized that trapped *n*-octane within the pore could lead to partial structural support of the MOF during the desolvation process. A sample in *n*-octane was mounted and the solvent was slowly allowed to evaporate over of 30 min. During the desolvation process, we observed retained crystallinity, but distinct changes within the PXRD pattern (Figure 2-9). Most notably the peaks around 2θ = 3.9° and 8.0° gained in relative intensity while the characteristic peaks around 2θ = 5.6° and 6.3° decreased in intensity with continued solvent evaporation. Upon full solvent removal under vacuum at 150 °C for 20 h the material's PXRD pattern resembled those observed from drying in more volatile solvents. The structural change was irreversible. A partial structural collapse was supported by the calculated BET surface area from N_2 adsorption isotherms at 77 K of only 170 m^2/g, a very low value for MOFs and for the porosity expected from the SXRD data.

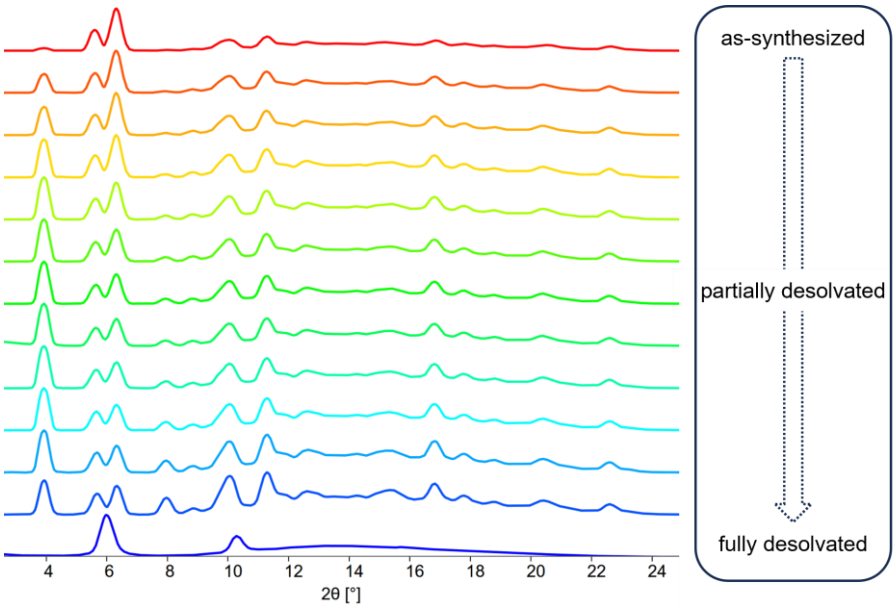

Figure 2-9 PXRD pattern of BMUF-2 during slow solvent evaporation and after complete solvent removal.

2.2.2 Synthesis and Characterization of M[Zn_4Ohmtt)$_2$(bdc)$_{0.5}$]

Inspired by the new MOF variants discussed in the previous chapter, we decided to investigate a possible combination of tritopic truxene-derived ligand and a shorter ditopic ligand such as bdc. We expected that the combination of hmtt and bdc would not yield BMUF-2, as bdc was not long enough to replace bpdc in the framework. We were curious if this new combination would lead to a new multicomponent MOF or if single-ligand MOFs were preferred under those conditions. A new multicomponent MOF from those ligands would also allow us to shed more light on the synthesis of MUF-77 and the potential competing reactions.

Hmtt and bdc were heated in a solvothermal oven with zinc nitrate in a solution of DMF and benzoic acid (BA) as crystal growth modulator to yield phase-pure crystals of a new MOF, which we denoted as BMUF-4

(Figure 2-10). The crystals were washed with DMF to remove excess reagents before being analyzed by PXRD, SXRD, and ^{1}H NMR spectroscopy.

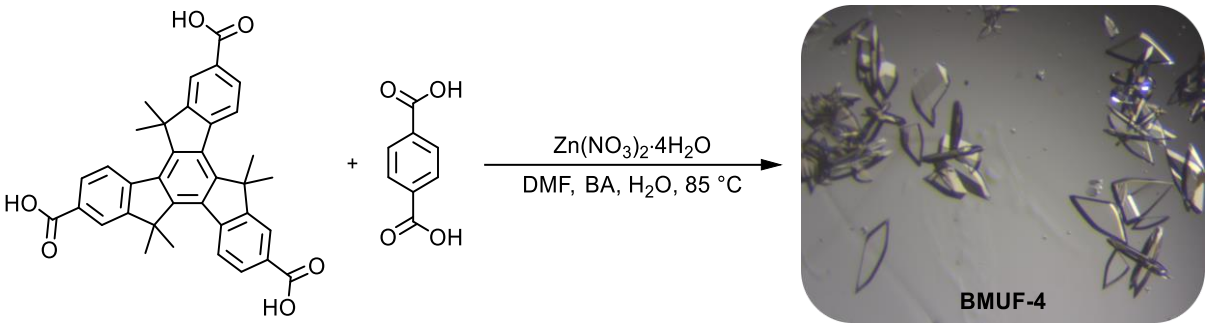

Figure 2-10 Synthesis of BMUF-4 from hmtt, bdc and zinc nitrate tetrahydrate.

The ^{1}H NMR spectrum of the digested MOF showed a ligand ratio of four hmtt linkers for each bdc linker (Figure 2-11).

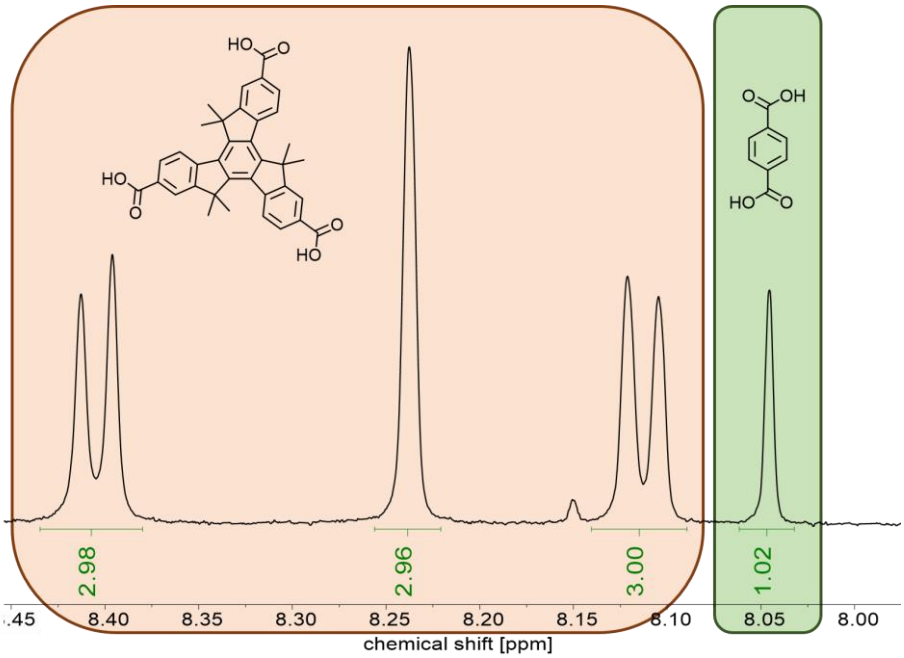

Figure 2-11 ^{1}H NMR spectrum of BMUF-4 upon digestion in DMSO-d_6/DCl. Only the aromatic region is shown for clarity.

The crystals were stable while solvated, but lost crystallinity within minutes when exposed to air upon desolvation. Samples were handled solvated where possible. SXRD analysis of the crystals revealed a new framework with the formula $M[Zn_4O(hmtt)_2(bdc)_{0.5}]$, where M is a monovalent, cationic species (Figure 2-12).

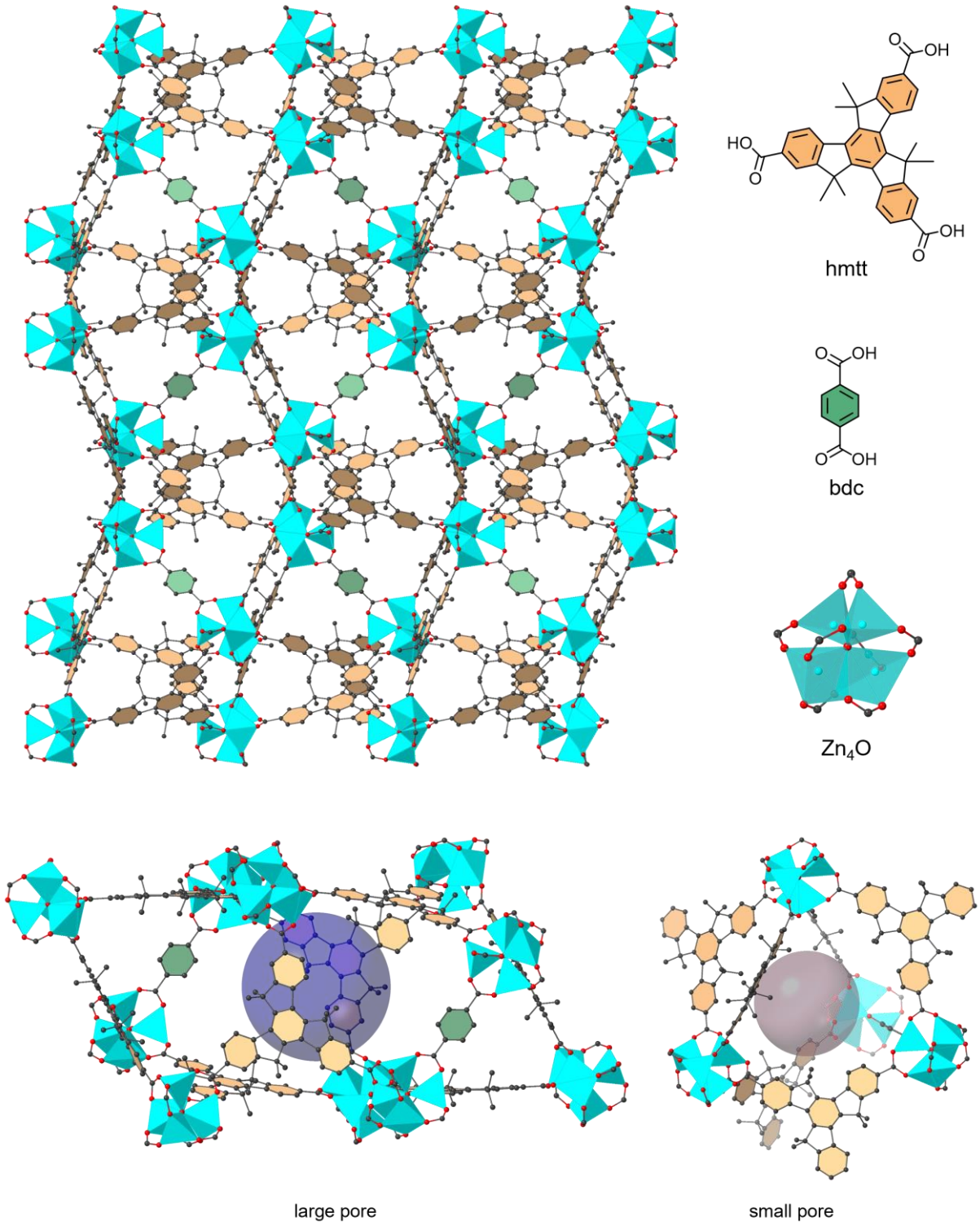

Figure 2-12 Crystal structure of BMUF-4, $M[Zn_4O(hmtt)_2(bdc)_{0.5}]$. Carbon atoms are depicted in grey, oxygen in red, and zinc in turquoise. Hydrogen atoms were omitted for clarity.

The large pore can be best described as a gyroelongated square pyramid that can fit a sphere with a diameter of 14 Å (determined with crystal maker from the crystal structure, considering the calculated van-der-Waals surface) but offers additional pore volume due to its elongated nature. The smaller pore can fit a sphere with a radius of 11 Å. Attempts to determine the topology with CrystalNets[165] and TopCryst[166] did not match a known topology. The pores incorporate both ligand types, hmtt and bdc. Zn_4O clusters were

observed for BMUF-4 and consisted of two tetragonal and two distorted trigonal bipyramidal coordinated zinc atoms. This cluster arrangement is very similar to the ones observed in BMUF-2 and in Duan's reported isoreticular MOF.[163] However, it stands in contrast with the SBUs observed for MOF-210 and MUF-77, which are solely comprised of only tetragonal coordinated zinc atoms (Figure 2-13). To ensure the formal charge balance between ligands and Zn SBUs a cationic species must be present within the BMUF-4 pore, which was supported by significant unresolved electron density within the MOF pore. The high degree of disorder did not allow for an identification. While MUF-77 is stable under air for prolonged periods, exposure to excess water quickly leads to the decomposition of the SBUs and the framework. The lability towards water is pronounced in BMUF-2 and BMUF-4 and exposure of the dried samples to moisture, as in ambient air, quickly leads to the decomposition of the frameworks.

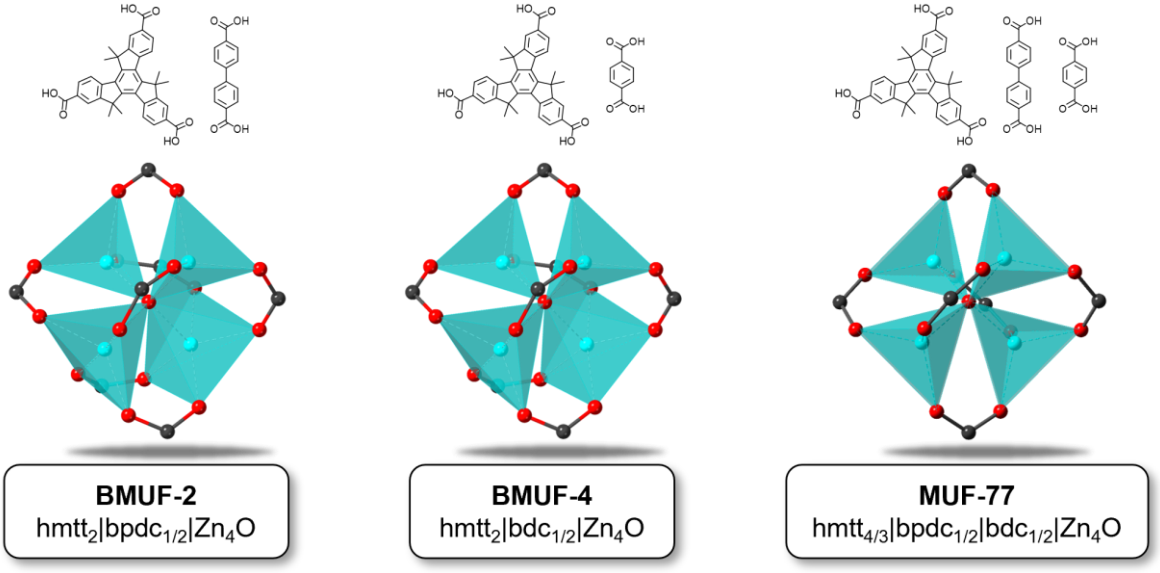

Figure 2-13 The Zn_4O-clusters of BMUF-2 (left), BMUF-4 (middle) and MUF-77 (right) in comparison.

PXRD patterns of the samples were in good agreement with the simulated data and indicated the phase-purity of the sample (Figure 2-14). For removal of the solvent, the crystals were first washed with acetone before being washed with *n*-octane. The tendency of *n*-octane to maintain within the MOF pores was exploited to allow safe handling and removal of excess solvent before the samples were heated at 150 °C under vacuum and kept under an inert atmosphere. BMUF-4 showed the MOF-typical high porosity even after activation, supported by an estimated BET surface area of 2180 m^2/g calculated from nitrogen adsorption isotherms at 77 K. BMUF-4 could also be obtained through a room-temperature synthesis protocol, similar to MUF-77. However, the PXRD pattern and ^1H NMR spectrum indicated that the sample was not phase pure. Further experiments to optimize the room temperature synthesis protocol are necessary.

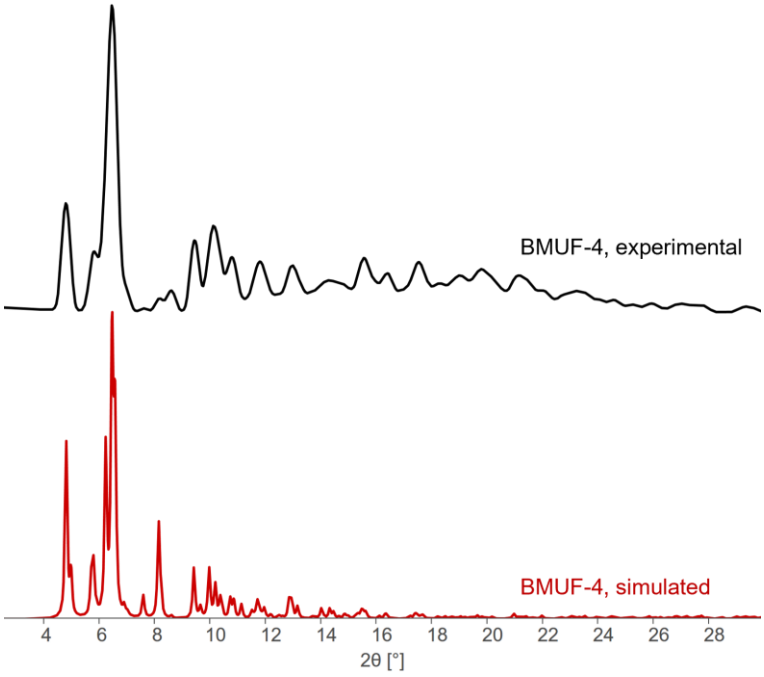

Figure 2-14 Experimental PXRD pattern of BMUF-4 (top, black) in comparison with the simulated PXRD pattern (bottom, red).

2.2.3 Hmtt-Single-Linker MOFs

While multicomponent MOFs seemed to be prevalent under synthesis conditions employing different ligand-types, we sometimes observed the formation of additional crystalline phases. MOF-5, IRMOF-9 and MOF-177 are archetypal MOFs based on Zn_4O SBUs, thus we expected to identify those MOFs in crystalline byproducts. However, the typical PXRD pattern of those MOFs were hardly observed. To shed more light onto the issue we further investigated the products formed from only the tritopic hmtt ligand under conditions similar to the synthesis of MUF-77. MUF-77 can be synthesized in DMF or DEF with varying amounts of benzoic acid as crystal growth modulator and the synthesis often tolerates variations in the ligand ratios. We found that the combination of hmtt with zinc nitrate tetrahydrate in DMF or DEF with different amounts of added water or crystal growth modulator benzoic acid led to the formation of several different crystalline phases. We investigated the product outcome more thoroughly with DMF as solvent. We identified four major crystalline phases that formed either as sole product or combination of different phases (Figure 2-15).

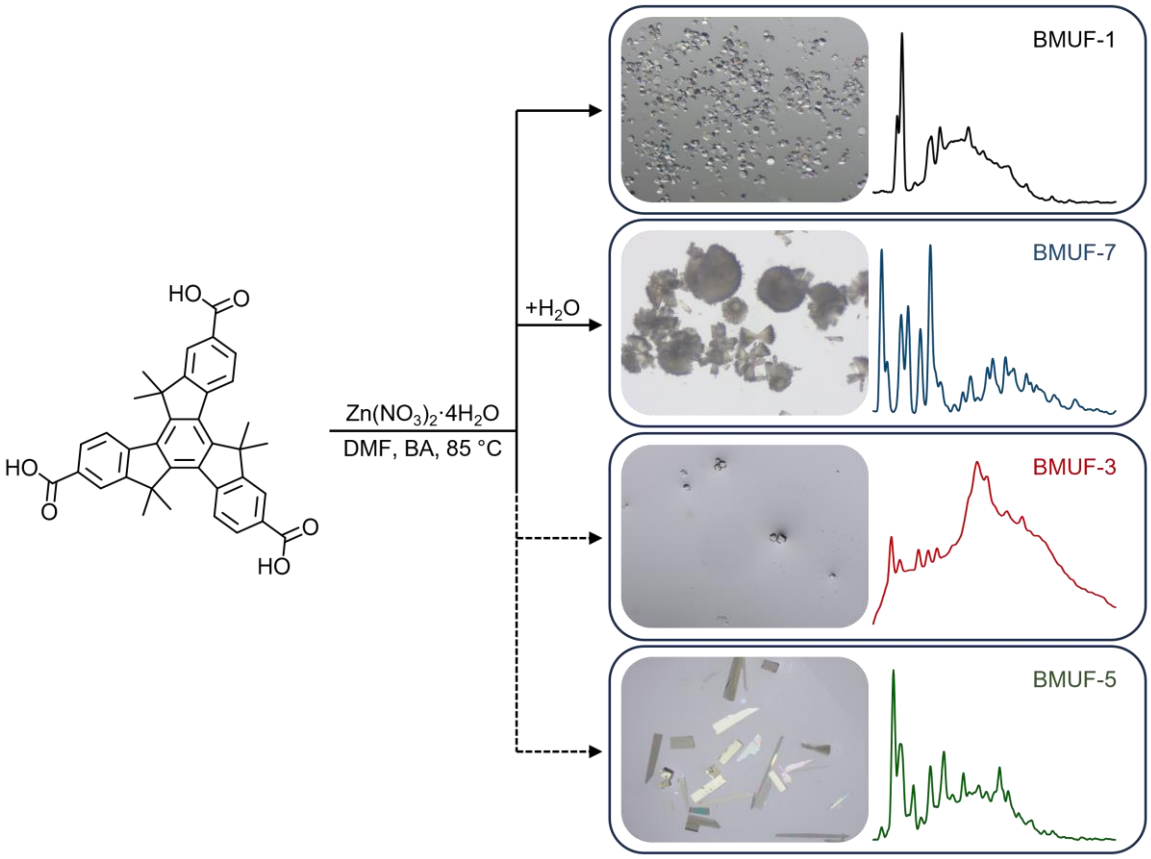

Figure 2-15 Overview of different crystalline phases observed from hmtt and zinc nitrate tetrahydrate in DMF with different modulators.

Which phase formed was mostly dictated by the amount of water added and seemed unaffected by the amount of benzoic acid. For both phases phase-pure synthetic conditions were successfully established. With the addition of water to the reaction mixture, a distinct crystalline phase, which we named BMUF-7, was predominant. The intergrown crystals were not suitable for single-crystal X-ray analysis. Without the addition of water, a new MOF, which we coined BMUF-1, was the predominant synthesis product. For the phase-pure synthesis of BMUF-1, hmtt was combined with zinc nitrate tetrahydrate and benzoic acid as growth modulator in dimethylformamide and heated in a solvothermal oven at 85 °C for 48 h. The MOF was obtained as colorless hexagonal plates, with crystals often being truncated. An alternative room-temperature synthesis protocol with zinc acetate as metal source was also developed, leading to the formation of a fine crystalline powder. Interestingly, the collected PXRD pattern of the MOFs showed great similarity with the experimental and simulated PXRD pattern of BMUF-2 (Figure 2-16). The resemblance of the characteristic peaks around 2θ = 15.8, 13.9, 11.0, 8.8, 7.7, 5.8, and 4.3 Å to the BMUF-2 pattern indicated a similar structural arrangement of the MOFs. While phase-pure samples were successfully synthesized, the obtained crystals were not suitable for SXRD analysis. Despite different attempts to shield the sample from solvent evaporation and ensure MOF stability, for example by snap freezing in liquid nitrogen or covering in a solvent-filled sleeve, the observed diffraction was insufficient to allow for an accurate crystallographic model. Both BMUF-1 and BMUF-7, showed traces of trapped benzoic acid in the ^{1}H NMR spectrum upon digestion of the MOFs despite washing the MOFs with solvent over a prolonged time.

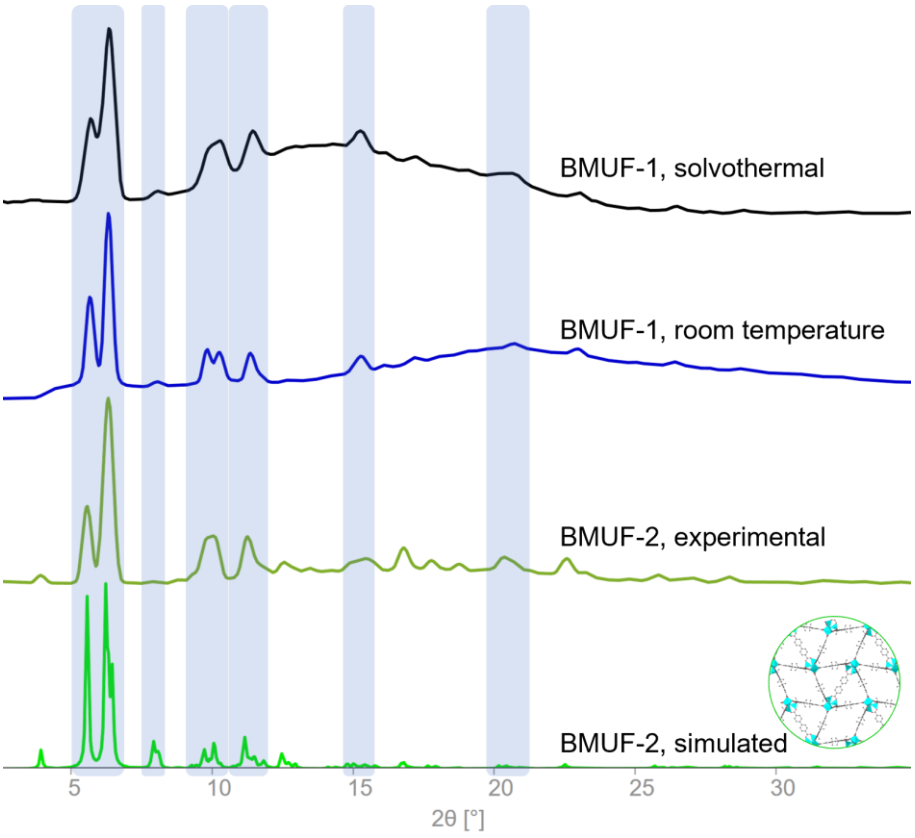

Figure 2-16 PXRD pattern of BMUF-1 (black, top) in comparison to the experimental (dark green, middle) and simulated PXRD pattern of BMUF-2 (bottom, light green).

We observed two rarer MOF byproducts during our synthetic experiments. They were coined BMUF-3 and BMUF-6. Attempts to establish reproducible, phase pure synthesis conditions were not fruitful. The difficulties underlined the complexities of MOF synthesis, even with only a single organic linker, and showcased that the crystal formation can be dictated by parameters beyond ligand and modulator ratios. BMUF-3 is isoreticular to the truxene MOFs reported by our group previously.[167] SXRD data showed the framework was comprised of two channels, a larger trigonal channel, with a window size of around 10.3 Å, and a smaller, helical channel with a window size of 9.6 Å can be described (Figure 2-17). The hmtt ligands are arranged into ligand pairs in a gauche confirmation. Three ligand pairs are assembled in a threefold paddlewheel-like structure around the Zn SBUs. Three zinc-oxygen clusters line up to form the SBUs, capped by one water molecule each. The central cluster shows an octahedral arrangement, whereas the two wing-side zinc clusters show a trigonal-pyramidal geometry. This arrangement is slightly distorted from a classic tetrahedral coordination.

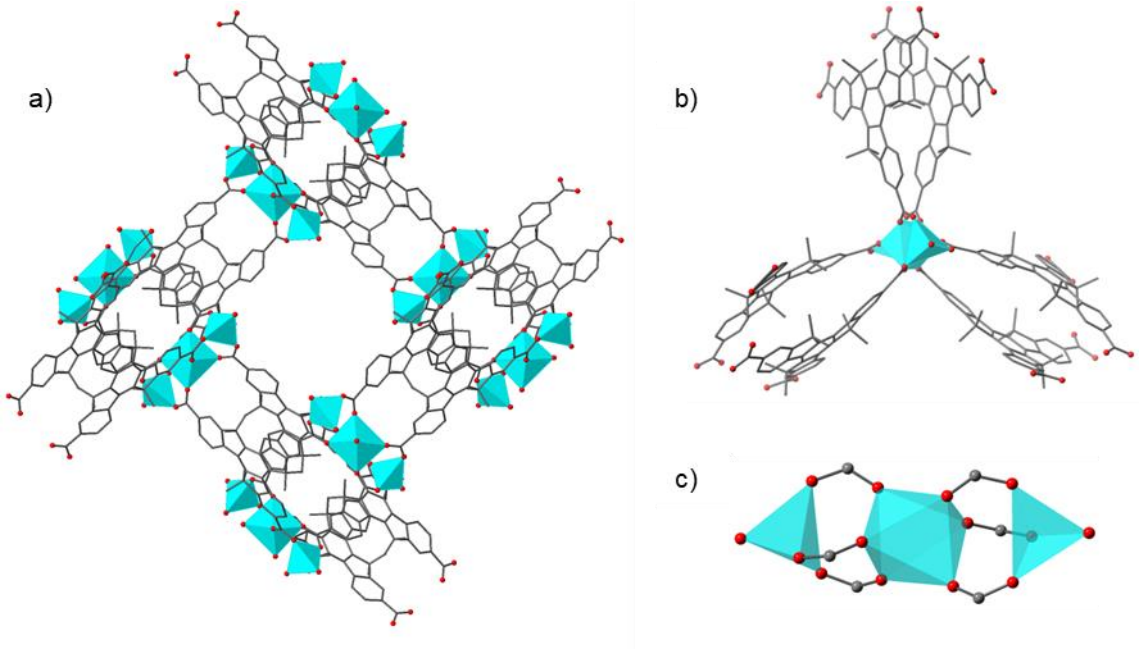

Figure 2-17 Crystal structure of BMUF-3. The smaller, helical channel is shown in a). The paddlewheel structure of the pair-wise arranged ligands is shown in b), and c) depicts the zinc SBU. Carbon atoms are depicted in grey, oxygen in red, and zinc in turquoise. Hydrogen atoms have been omitted for clarity.

BMUF-5 was found in several reactions as a side product. SXRD data of the crystals revealed a structure dictated by open channels with around 7.1 Å in diameter accessible (the void space was calculated with the software CrystalMaker® 11). According to our model, the zinc SBUs were stabilized by the coordination of several solvent molecules. We expected this more unusual arrangement to be the reason for the propensity of other MOFs to be formed in the synthesis procedures, as we expected the coordination of the organic linker to be relatively stronger and thus preferred over solvent coordination. The Zn SBUs were arranged in wave-like layers, interconnected by hmtt linkers.

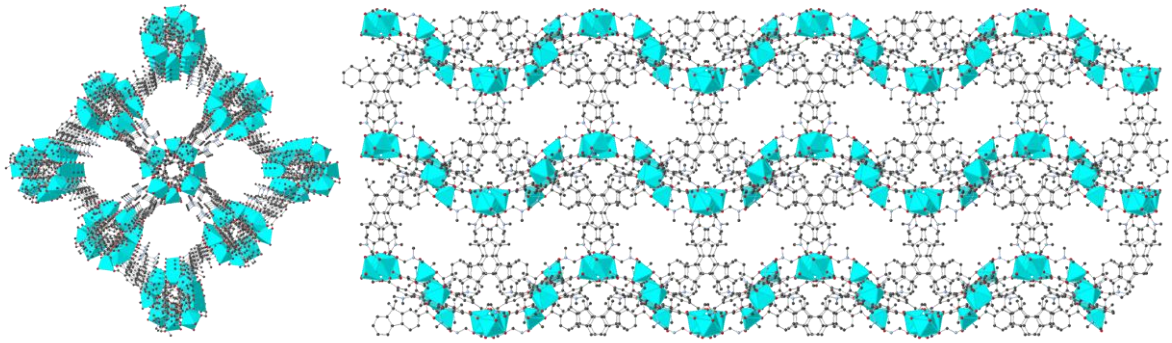

Figure 2-18 Crystal structure of BMUF-5, depicting the characteristic channels (left) and a sideview showing the layered arrangement of clusters (right). Carbon atoms are depicted in grey, oxygen in red, nitrogen in blue and zinc in turquoise. Hydrogen atoms have been omitted for clarity.

2.3 Conclusion

Our experiments were another proof of the vast possibilities of MOF synthesis. Using similar conditions to traditional MUF-77 procedures we observed more than six different possible MOFs, four single linker hmtt MOFs and two multicomponent MOFs incorporating hmtt and either bpdc or bdc. The MOFs showed

unusual structural arrangements, which we attributed to the reduced symmetry of hmtt compared to simpler trigonal linkers such as btb. The synthesis and characterization of new multicomponent frameworks allow us to expand our scope of potential multicomponent MOF catalysts in future experiments. For example, linker functionalized with catalytically active species can be incorporated. The multicomponent nature of the novel materials promises unique and easily tunable pore environments for embedding potential catalysts.

2.4 Experimental

All starting materials and solvents were used as received from commercial sources without further purification. NMR spectra were recorded at 25 °C (unless otherwise noted) on Bruker-400 and Bruker-500 Avance instruments, with the use of the solvent proton as an internal standard. Low-pressure gas adsorption isotherms were measured by a volumetric method using a Quantachrome Autosorb iQ2 instrument. All adsorption measurements used ultra-high purity gases. X-ray diffraction measurements were carried out on either Rigaku Spider or Bruker D8 Venture.

2.4.1 MOF Synthesis

BMUF-1, solvothermal synthesis Hmtt (1.9 mg, 3.4 μmol, 1 eq.), benzoic acid (4.2 mg, 34 μmol, 10 eq.) and a 0.478 M zinc nitrate tetrahydrate solution in DMF (100 μL) were combined in DMF (900 μL). The solution was placed in an isothermal oven at 85 °C for 48 h to yield colorless, hexagonal crystals. The solvent was replenished with fresh DMF (5x).

BMUF-1, room temperature synthesis Hmtt (6.0 mg, 10.7 μmol, 1 eq.) was dissolved in DMF (0.3 mL). While stirring, a solution of zinc acetate dihydrate (9.1 mg, 0.415 mmol, 39 eq.) in DMF (0.2 mL) and water (10 μL) was added. Immediate precipitation of solids was observed. The reaction was stirred at room temperature for 60 min before the solids were isolated by centrifugation and washed with DMF (3x).

BMUF-2, M[$Zn_4O(hmtt)_2(bpdc)_{0.5}$] Hmtt (10.2 mg, 18.3 μmol, 1 eq.), bpdc (7.5 mg, 31 μmol, 1.7 eq.), benzoic acid (100 mg, 0.819 mmol, 45 eq.) and zinc nitrate tetrahydrate (62.5 mg, 0.239 mmol) were combined in DEF (5 mL) and water (250 μL). The solution was sonicated for 10 min and placed in an isothermal oven at 85 °C for 48 h to yield golden, rectangular plates. The solvent was replenished with fresh DMF (5x).

BMUF-4, M[$Zn_4O(hmtt)_2(bdc)_{0.5}$] Hmtt (10.0 mg, 17.9 μmol, 1 eq.), bdc (5.5 mg, 33 μmol, 1.9 eq.), benzoic acid (60 mg, 0.819 mmol, 45 eq.) and a 0.478 M zinc nitrate tetrahydrate solution in DMF (1 mL) were combined in DMF (5 mL) and water (250 μL). The suspension was sonicated for 10 min and placed in an isothermal oven at 85 °C for 48 h to yield colourless plates. The solvent was replenished with fresh DMF (5x).

BMUF-7 Hmtt (1.9 mg, 3.4 μmol, 1 eq.), benzoic acid (12.0 mg, 98.3 μmol, 29 eq.) and a 0.478 M zinc nitrate tetrahydrate solution in DMF (100 μL) were combined in DMF (900 μL) and water (100 μL). The solution was placed in an isothermal oven at 85 °C for 24 h to yield colourless, fan-like crystal clusters. The solvent was replenished with fresh DMF (5x).

2.4.2 NMR Spectroscopy

Solvated crystals in DMF were washed with acetone (5x) before being dried under vacuum. For ^1H NMR spectroscopy, the desolvated crystals were digested using the following protocol: 23 μL of a 35% DCl solution in D_2O was mixed with 1 mL of DMSO-d_6 to give a DCl/DMSO-d_6 stock solution. The sample was digested in 150 μL of this stock solution together with 450 μL of DMSO-d_6. Spectra were acquired immediately following dissolution.

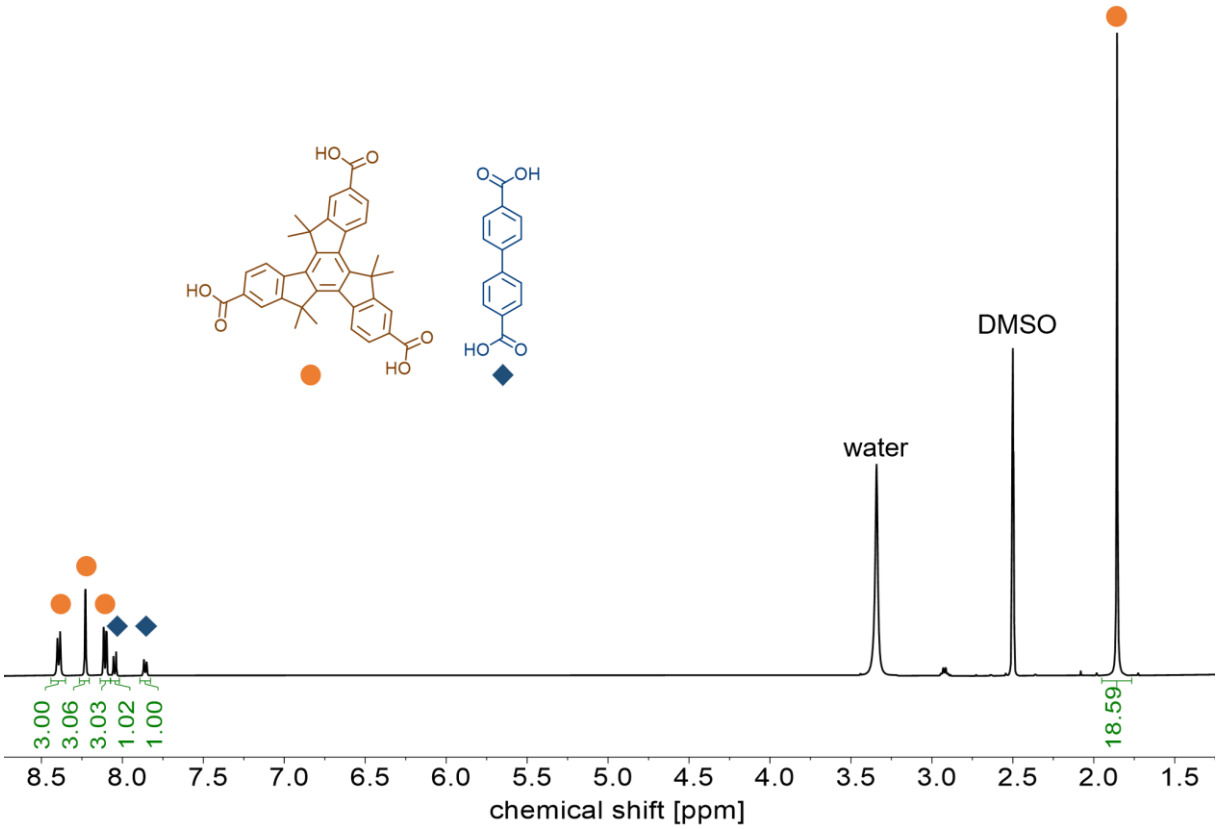

Figure 2-19 ^{1}H NMR spectrum of BMUF-2 upon digestion in DMSO-d_6/DCl.

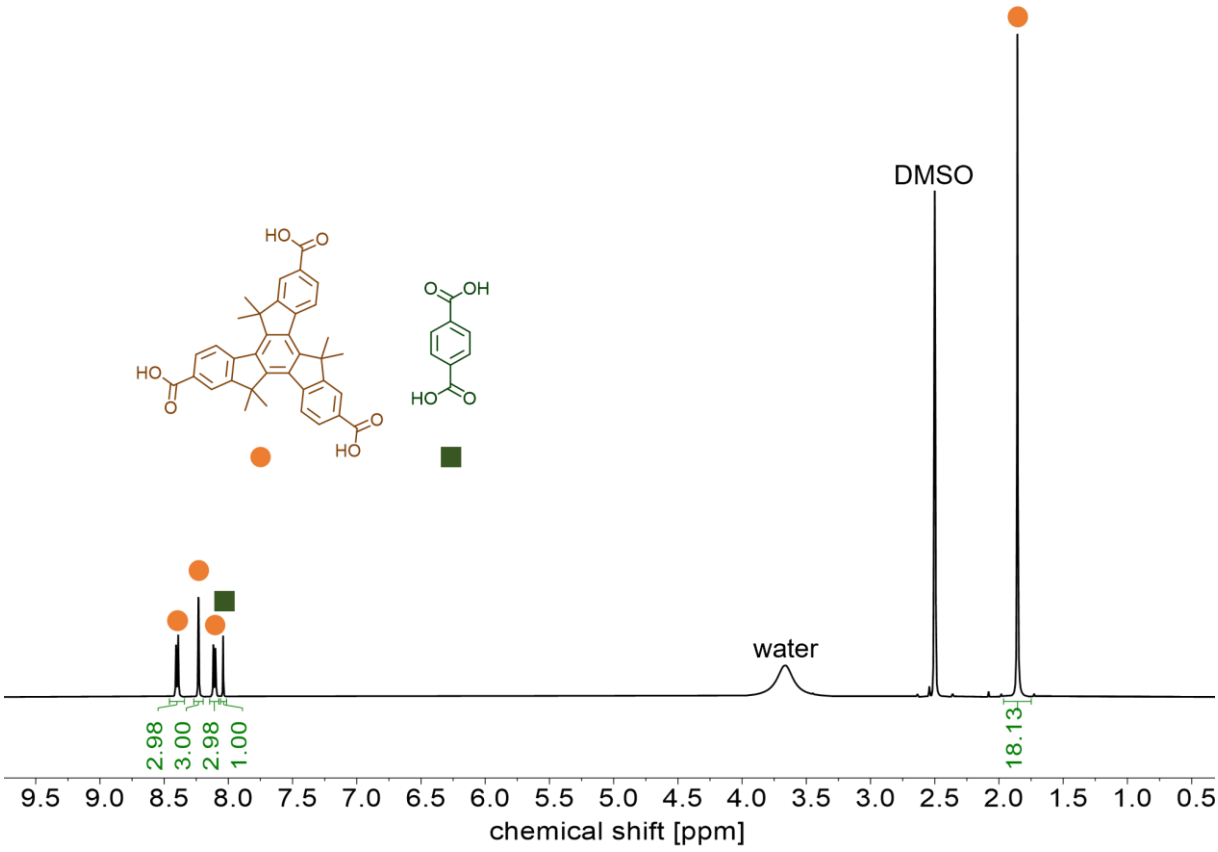

Figure 2-20 ^{1}H NMR spectrum of BMUF-4 upon digestion in DMSO-d_6/DCl.

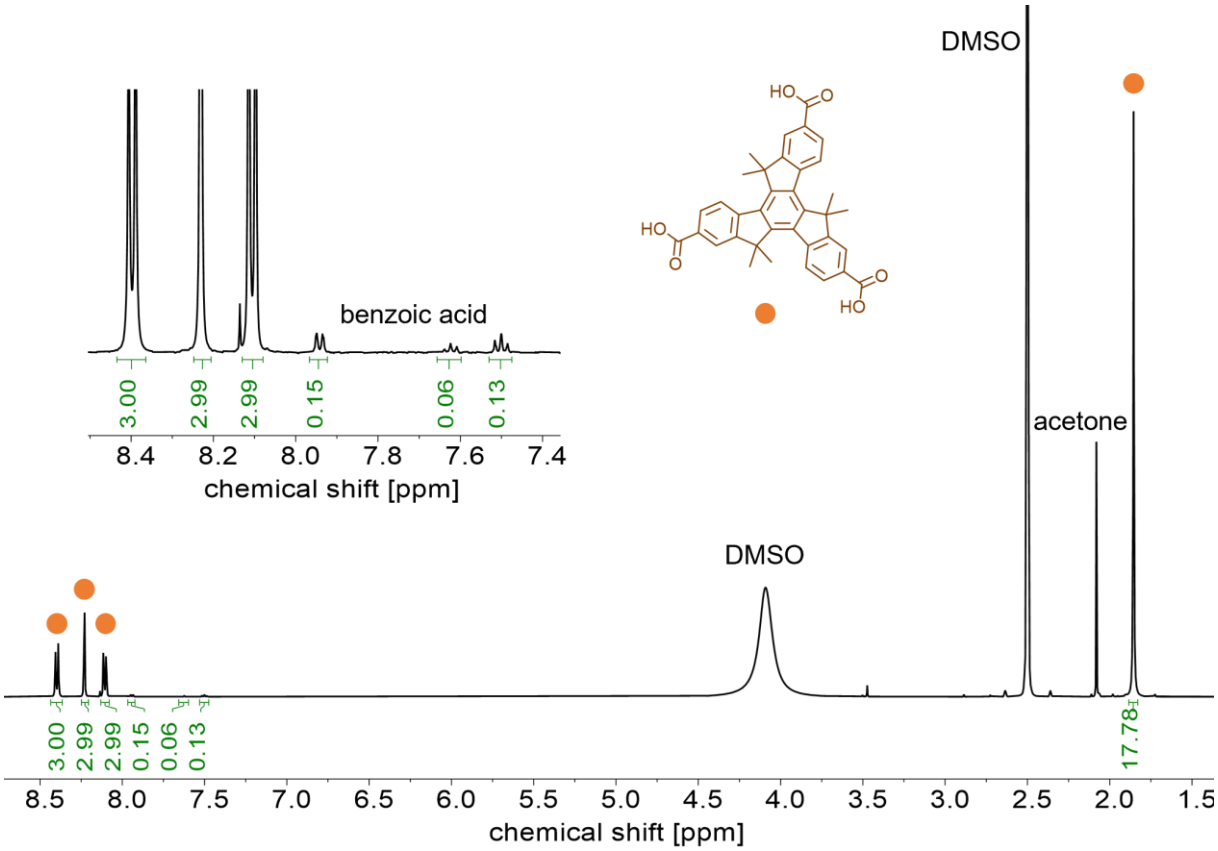

Figure 2-21 ^{1}H NMR spectrum of BMUF-1 upon digestion in DMSO-d_6/DCl.

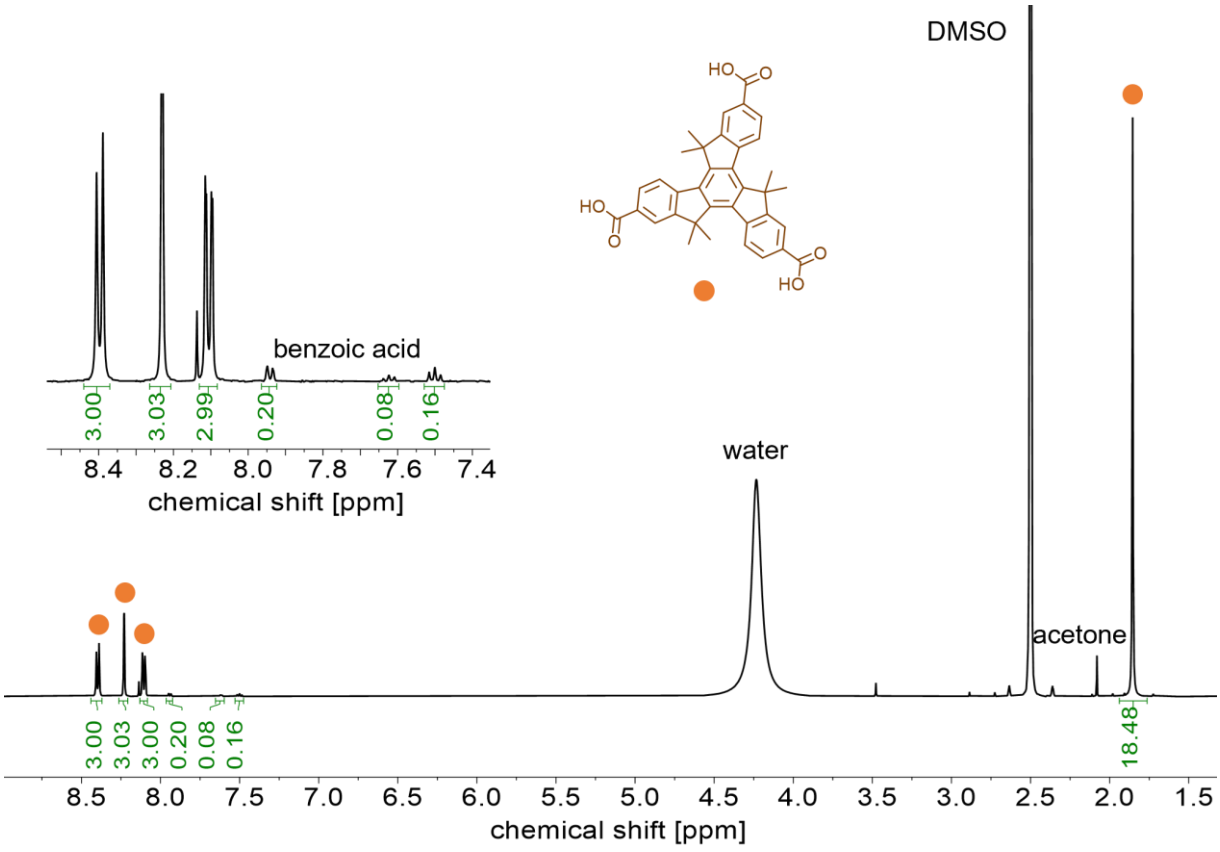

Figure 2-22 ^{1}H NMR spectrum of BMUF-7 upon digestion in DMSO-d_6/DCl.

2.4.3 PXRD Patterns

All powder X-ray diffraction measurements were carried out on either Rigaku Spider or Bruker D8 Venture. Rigaku Spider X-ray diffractometer is equipped with CuKα radiation (Rigaku MM007 microfocus rotating-anode generator), monochromated and focused with high-flux Osmic multilayer mirror optics and a curved image plate detector. Bruker D8 Venture diffractometer is equipped with CuKα radiation with a diamond microfocus X-ray source and a Photon III 28 detector. The two-dimensional images of the Debye rings were integrated with 2DP or Diffract Eva to give 2θ vs I diffractograms. Predicted powder patterns were generated from single-crystal structures using Mercury.

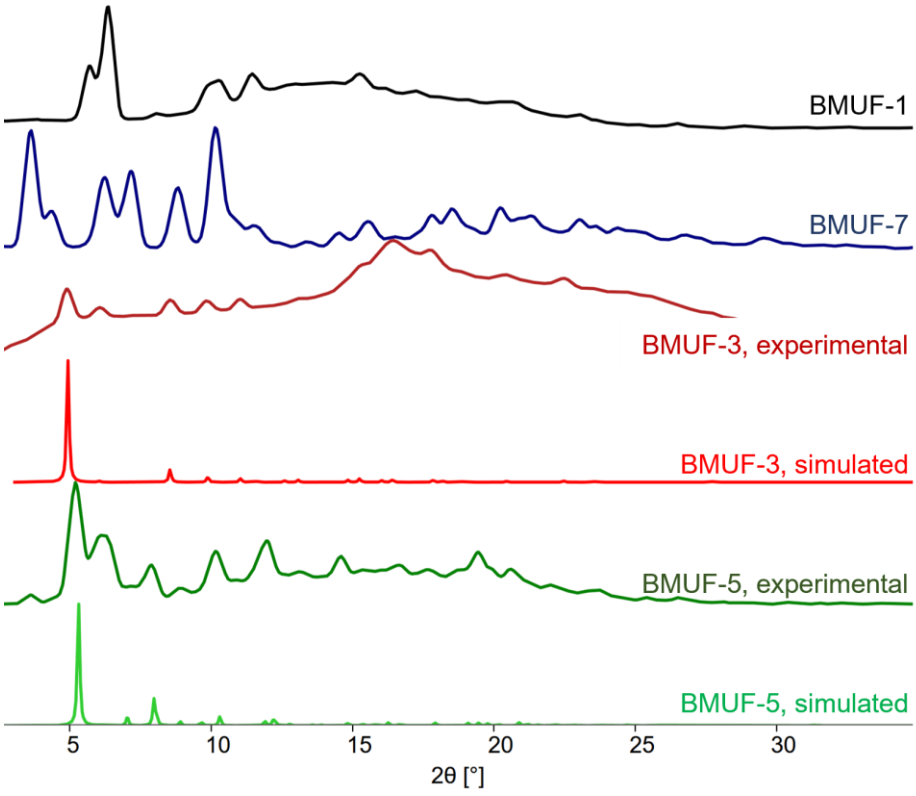

2.4.4 SXRD Measurements

All single-crystal X-ray diffraction measurements were carried out on Bruker D8 Venture, and the measurement temperature was controlled using Oxford Cryostream if required. Bruker APEX 3 was used to collect and process data, and the structure was solved and refined using the Shelx package[168,169] under Olex2.[170]

Table 2-1 Summary of X-ray crystallography data for the BMUF series.

Name	**BMUF-2**	**BMUF-4**	**BMUF-3**	**BMUF-5***
Empirical formula	$C_{79}H_{58}O_{15}Zn_4$	$C_{76}H_{56}O_{15}Zn_4$	$C_{72}H_{58}O_{14}Zn_3$	$C_{45}H_{50}N_3O_{11}Zn_2$
Formula weight	1508.73	1470.68	1343.29	939.62
Temperature/K	294	294	294	100
Crystal system	monoclinic	orthorhombic	cubic	tetragonal
Space group	$P2_1/n$	Pbca	$P4_332$	$P4_32_12$
a/Å	17.5358(12)	29.8345(7)	25.3199(11)	23.5031(6)
b/Å	31.802(2)	30.8553(7)	25.3199(11)	23.5031(6)
c/Å	31.621(2)	35.3960(8)	25.3199(11)	29.6809(12)
α/°	90	90	90	90
β/°	91.695(3)	90	90	90
γ/°	90	90	90	90
Volume/Å^3	17627(2)	32583.9(13)	16233(2)	16395.6(11)
Z	4	8	4	8
ρ_{calc}g/cm^3	0.569	0.6	0.55	0.761
μ/mm^{-1}	0.836	0.898	0.73	1.001
F(000)	3088	6016	2768	3912
Crystal size/mm^3	0.2 × 0.1 × 0.6	0.3 × 0.1 x 0.5	0.2×0.2×0.2	0.2×0.2×0.3
Radiation	CuKα (λ = 1.54178)	CuKα (λ = 1.54178)	CuKα (λ = 1.54178)	CuKα (λ = 1.54178)
2Θ range for data collection/°	3.942 to 153.618	4.818 to 153.032	26.34 to 152.306	4.796 to 152.854
Index ranges	-21 ≤ h ≤ 21 -37 ≤ k ≤ 39 -39 ≤ l ≤ 39	-33 ≤ h ≤ 33 -33 ≤ k ≤ 37 -40 ≤ l ≤ 44	-31 ≤ h ≤ 23 -18 ≤ k ≤ 22 -31 ≤ l ≤ 26	-29 ≤ h ≤ 29 -29 ≤ k ≤ 28 -35 ≤ l ≤ 36
Reflections collected	307229	393448	39614	243973
Independent reflections	3659 R_{int} = 0.0475 R_{sigma} = 0.0258	32605 R_{int} = 0.0675 R_{sigma} = 0.0371	5558 R_{int} = 0.1088 R_{sigma} = 0.0769	17119 R_{int} = 0.0412 R_{sigma} = 0.0181
Data/restraints/ parameters	36592/58/ 931	32605/0/ 868	5558/0/ 134	17119/156/ 544
Goodness-of-fit on F^2	1.174	1.46	1.096	1.031
Final R indexes [I>=2σ (I)]	R_1 = 0.1262 wR_2 = 0.3595	R_1 = 0.1041 wR_2 = 0.3331	R_1 = 0.1246, wR_2 = 0.3094	R_1 = 0.0686 wR_2 = 0.2059
Final R indexes [all data]	R_1 = 0.1282 wR_2 = 0.3607	R_1 = 0.1343 wR_2 = 0.3654	R_1 = 0.1724, wR_2 = 0.3410	R_1 = 0.0761 wR_2 = 0.2217
Largest diff. peak/hole / e Å^{-3}	2.44/-1.03	1.09/-1.11	0.41/-1.17	0.39/-0.71
Flack parameter			-0.11(3)	0.13(3)

* A solvent mask was used.

2.4.5 Gas Adsorption Measurements

N_2 adsorption isotherms were measured by a volumetric method using a Quantachrome Autosorb iQ2 instrument. Before the initial measurements, as-synthesized samples were washed with acetone (5x) and *n*-octane (5x) and activated under dynamic vacuum at 150 °C for 20 h. BET surface areas were calculated from N_2 adsorption isotherms at 77 K according to the following procedures[171]:

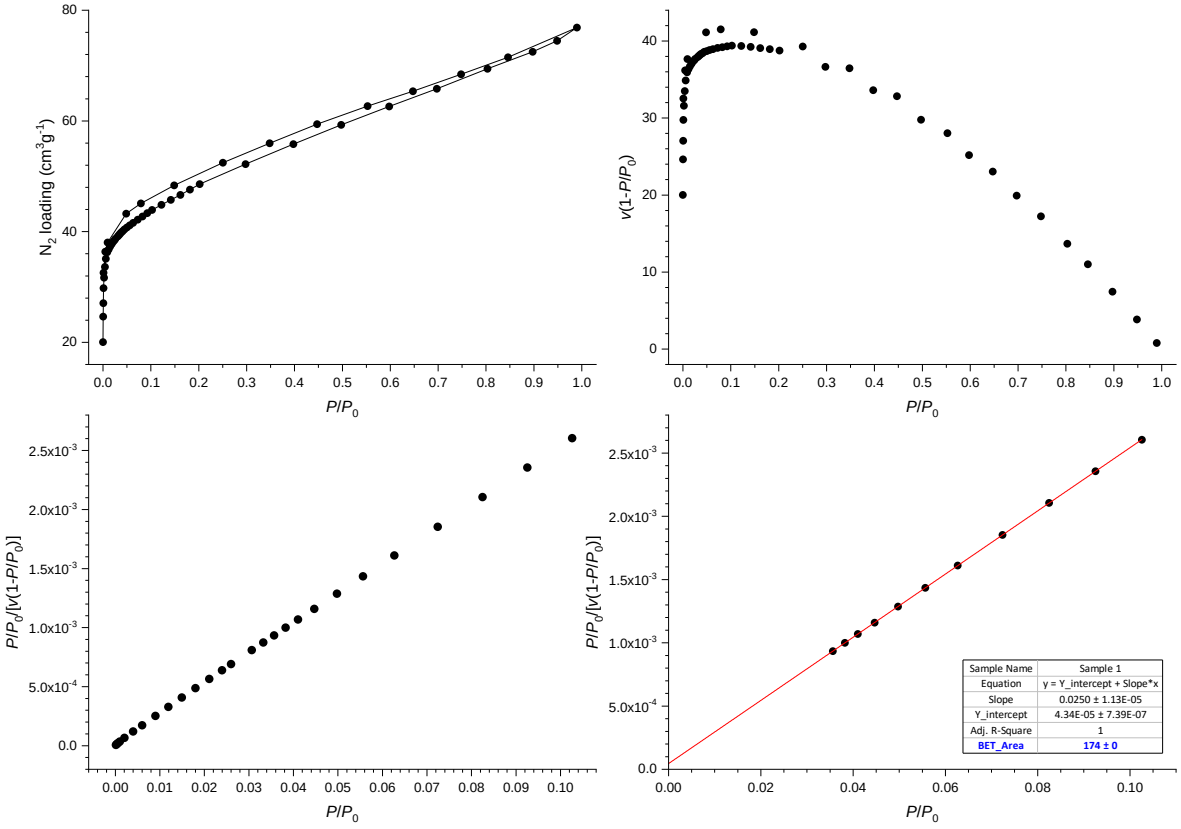

Figure 2-23 Nitrogen adsorption isotherm at 77 K and BET surface area plots for BMUF-2.

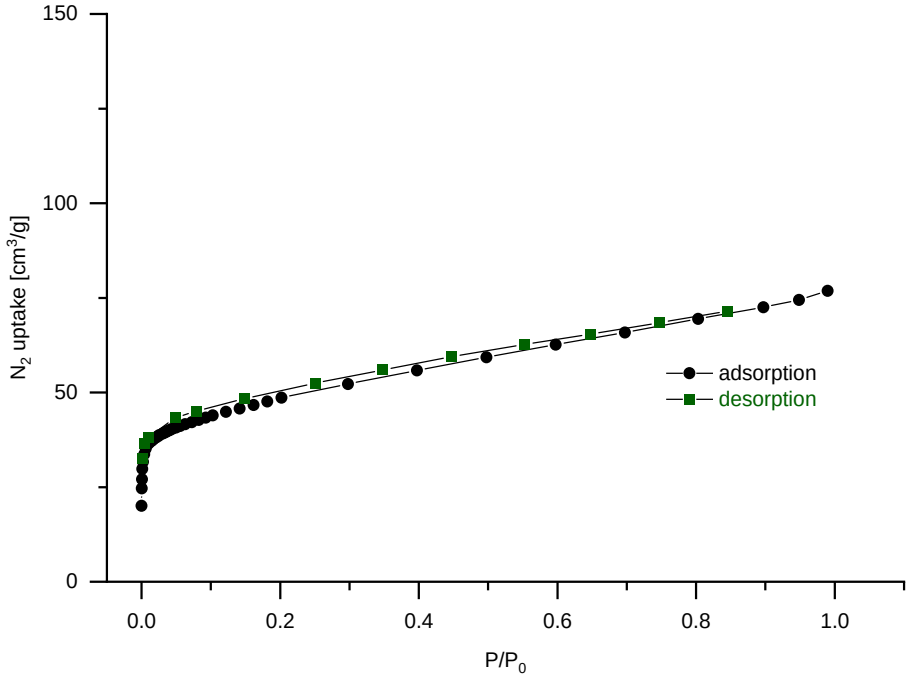

Figure 2-24 Nitrogen adsorption isotherm of BMUF-2 at 77 K.

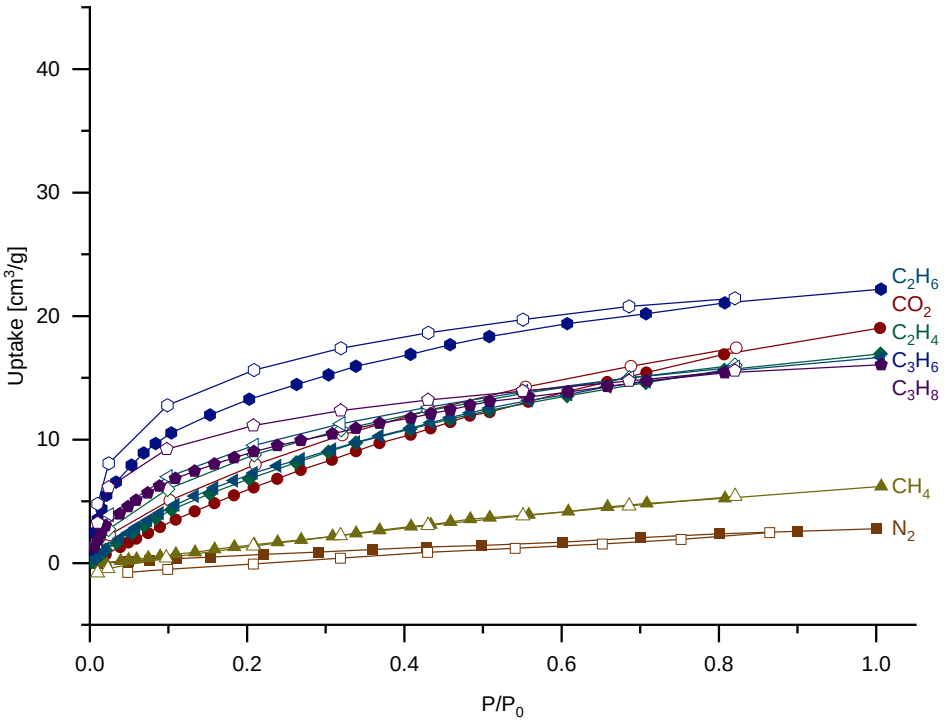

Figure 2-25 Gas adsorption isotherms of BMUF-2 at 293 K.

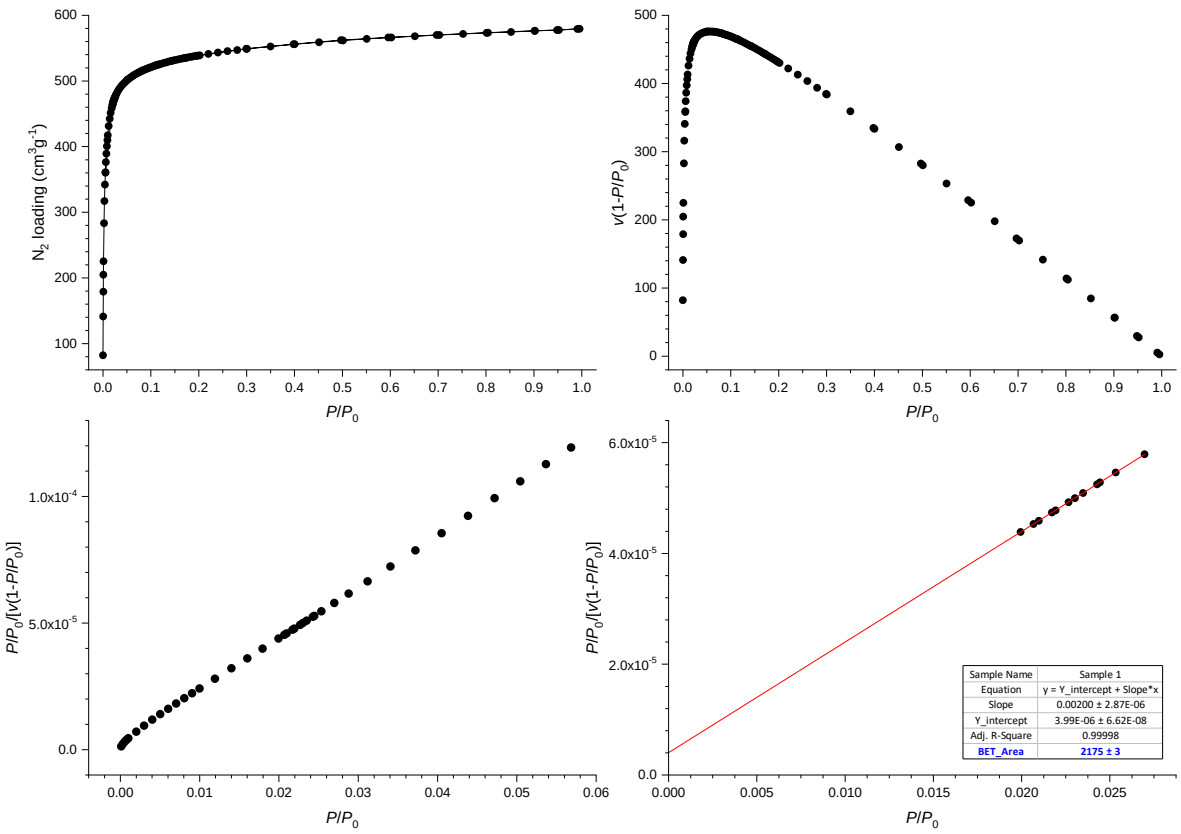

Figure 2-26 Nitrogen adsorption isotherm at 77 K and BET surface area plots for BMUF-4.

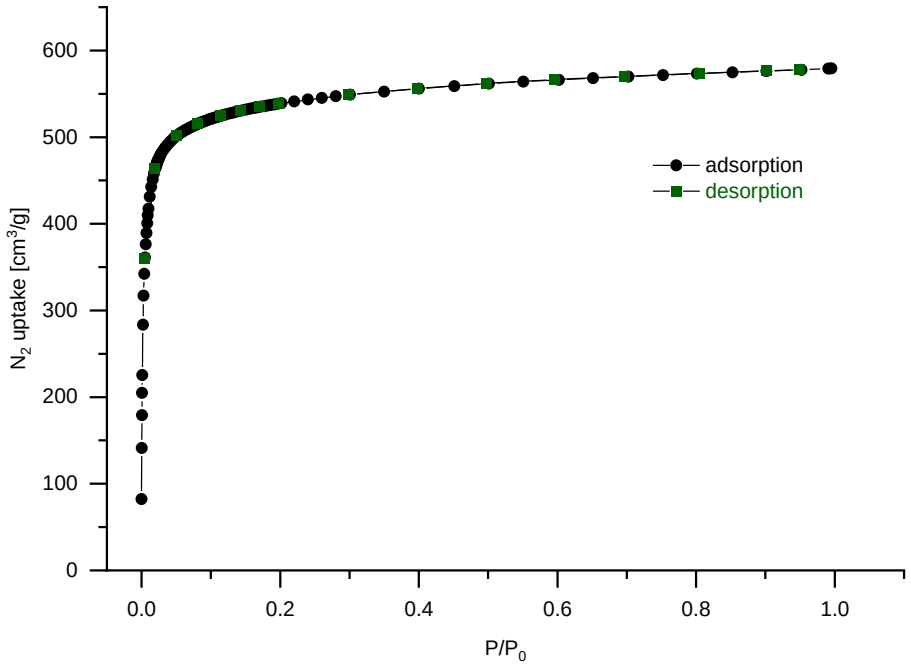

Figure 2-27 Nitrogen adsorption isotherm of BMUF-4 at 77 K.

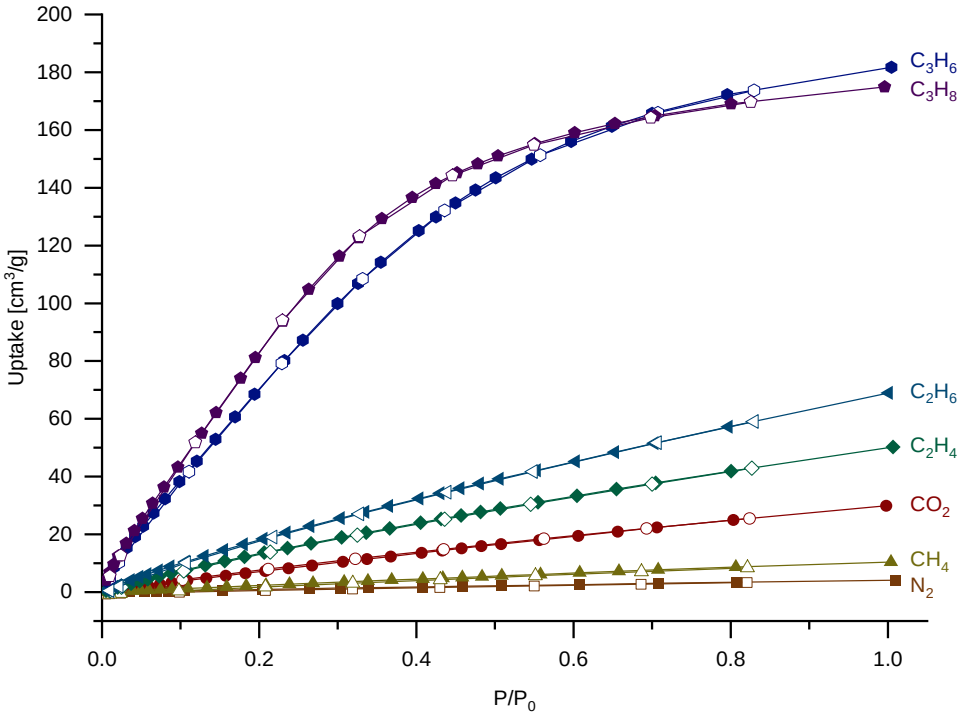

Figure 2-28 Gas adsorption isotherms of BMUF-4 at 293 K.

2.4.6 Pore Size Distribution

The pore size distribution was calculated with VersaWin™ from N_2 isotherms at 77 K using a DFT method. The selected parameters were: N_2 at 77K on carbon (slit/cylindr./sphere pores, QSDFT); adsorbat: nitrogen at 77K; adsorbent: carbon.

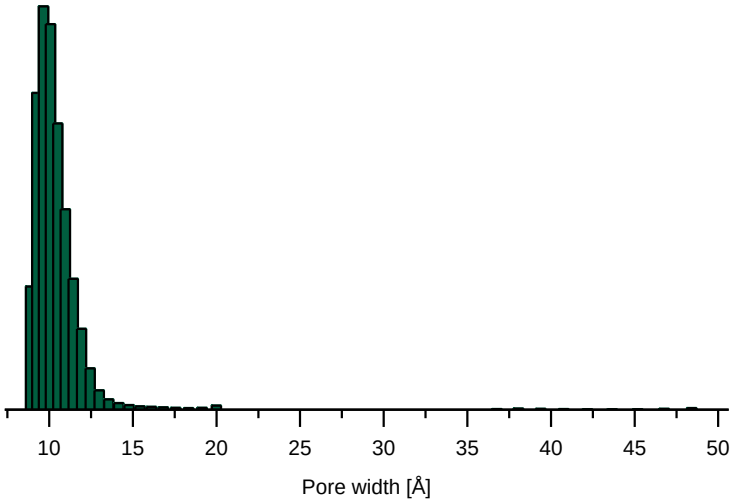

Figure 2-29 Calculated pore size distribution of BMUF-4.

Chapter 3 Incorporation of Transition Metal Catalysts Into MUF-77

3.1 Opportunities and Challenges in the Integration of Metal Catalysts in MUF-77

Molecular transition metal complexes are an important class of homogeneous catalysts. C–C bond formation reactions like the Sonogashira,[172] Suzuki[173–175] or Heck[176] reactions are only some of the prominent examples that have made it into chemistry laboratories around the globe. Today, the periodic table is widely exploited for different synthetic applications. From earth-abundant catalysts for hydrosilylations and hydroborations,[177] nickel catalysts for asymmetric reactions[178,179] to heavy transition metals like gold for activating multiple C–C bonds.[180–182] Often the improvement of those homogeneous catalysts relies heavily on the design of new functional ligands to create highly specialized coordination environments around the active metal centre. Specific ligand design can lead to improved catalytic activity and stabilization of the catalyst (Figure 3-1).[183–186]

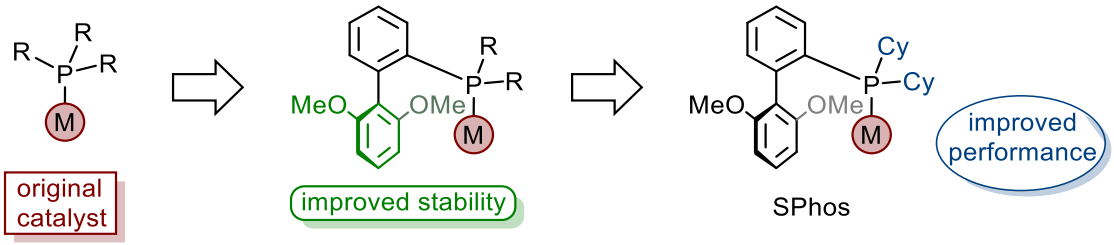

Figure 3-1 The evolution of ligand design for homogeneous catalysis, illustrated by SPhos[186], an example of a commercially available Buchwald ligand. By adjusting the steric and electronic properties of the ligand it is possible to stabilize the catalyst and improve its performance.

The prominent role of transition metal (TM) complexes in traditional homogeneous catalysis quickly drew the interest of researchers in the MOF community. While the incorporation of those systems first simply served as examples in post-synthetic ligand exchange reactions,[92,93] their true potential was quickly uncovered when the recyclability and stability of MOFs as scaffolding were exploited. The challenges in synthesizing a MOF/TM-catalyst hybrid are obvious when considering that MOFs themselves are coordination complexes. Ligands employed for the synthesis of the MOF scaffold and ligands stabilizing the transition metal catalyst can potentially compete for the same metal ions. This can lead to decomposition of the catalyst and problems for the MOF formation. Two strategies are commonly followed for the incorporation of a transition metal catalyst in MOF. If the transition metal complex is sufficiently stable under MOF synthesis conditions, the complex-bearing linker can be synthesized beforehand and then used in the traditional MOF synthesis procedure. However, for less stabile systems, a post-synthetic functionalization is often the preferred approach. Here the free ligand is used for the framework synthesis. After MOF formation, the ligand is then metalated in a second step under milder conditions.[187] If the metal chosen as a transition metal catalyst is sufficiently different from the metal nodes forming the MOF, the stabilizing ligands often contrast enough from the MOF linkers to avoid any interference. The HSAB theory (HSAB = Hard and Soft Acids and Bases)[188] is a useful indication for outlining possible combinations of ligand/metal pairs.[189] The strong interactions between zirconium ions and

carboxylate-based linkers, a typical case of interactions between a hard acid and a hard base, are demonstrated in the chemical stability of UiO-66, UiO-67, and isoreticular frameworks (Figure 3-2). This allowed the incorporation of 2,2'-bipyridine-5,5'-dicarboxylic acid (bipy; the abbreviation is usually used for 2,2'-bipyridine but is commonly adapted in the MOF context to refer to the dicarboxylic acid ligand) within the framework without any interference during the MOF synthesis.[114,190,191]

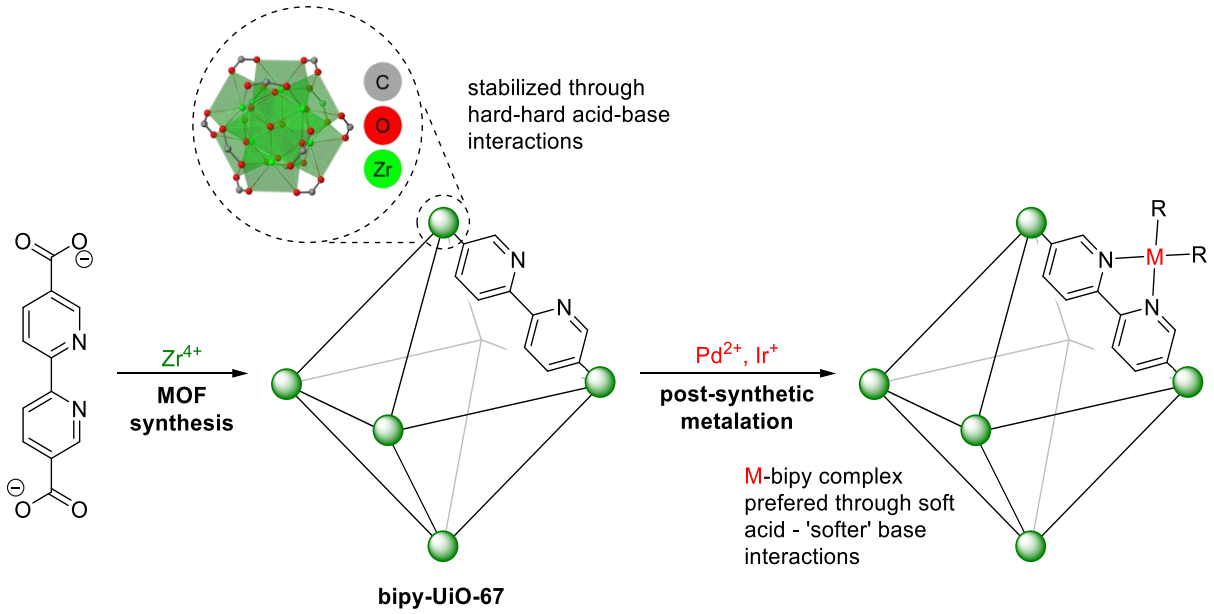

Figure 3-2 Synthesis of bipy-UiO-67 and the post-synthetic metalation with heavy transition metals. The stepwise synthesis exploited the difference in affinity of carboxylate and pyridine ligands towards harder or softer metals according to the HSAB concept, avoiding interference of the two potential coordination sites during MOF synthesis.

The carboxylate groups of the bipy ligand firmly anchored the linker to the framework $Zr_6O_4(OH)_4$ SBUs, while comparably softer pyridyl donors (according to the HSAB theory) did not interfere with the UiO-67 formation. Those free coordination sites were then employed to bind soft transition metal ions like Pd^{2+} and Ir^{+}. The introduced metal complexes were active catalysts for the C–H borylation of arenes, intramolecular *ortho*-silylation of benzylicsilyl ethers to benzoxasiloles, and the dehydrogenation of substituted cyclohexenones to phenols. The MOF catalysts showed improved catalytic activity, stability, and recyclability compared to the homogeneous counterparts.[190]

MUF-77 provides an excellent scaffold for the incorporation of transition metal catalysts since the functionalisation of the three linkers does not perturb framework assembly except in very rare cases. Yet, the choice of potential transition metal catalysts and thus of linkers appended with coordinating motifs is limited to complexes that will compete for the zinc(II) ions with the carboxyl groups involved in MOF formation. A secondary interaction with the zinc ions in solution would lead to undesired coordination or polymerisation during MOF synthesis. The ligand choices are further dictated by geometric restrictions due to the structural specifications of MUF-77. The incorporation of existing homogeneous catalysts allows us to lean on their well-studied mechanisms and the principle understanding of such systems while evolving the catalysts beyond the limits of homogeneous catalysis. Synthetic chemistry has done a wonderful job in developing ligand systems large enough to create catalytic pockets and modulate the substrate binding sites

of catalysts. Yet, the design of new ligands for homogeneous catalysts becomes more challenging with possible unpredictable interactions in homogeneous reaction mixtures. Replacing those complicated ligand systems through the incorporation of the parent catalyst into a MOF pore with tuneable properties allows for modulation of the substrate environment beyond the possibilities of homogeneous systems. It is noteworthy, that in the following discussion about transition metal complexes within MUF-77 the focus solely lies on the functionalization of the organic linkers with potential catalytically active species. While the metal clusters necessary for MOF assembly can be altered[192–194] and exploited for catalytic purposes[195] it was not part of our strategy for MUF-77.

3.2 Results and Discussion

3.2.1 Bipyridine Linkers for the Incorporation into MUF-77

As discussed in the previous chapters, bipy was successfully used to produce transition metal catalysts within UiO-67-type frameworks. The linear geometry 2,2'-bipyridine-5,5'-dicarboxylic acid and its similarity to bpdc, traditionally used for the MUF-77 synthesis, made this an interesting target. This would lead to a useful intermediate for subsequent post-synthetic metalation steps to obtain a catalytically active transition metal complex within the MUF-77 framework. We hypothesized that the milder room-temperature conditions might be advantageous for a successful MUF-77 synthesis. We followed the original procedure for the synthesis of $_{rt}$MUF-77, while replacing bpdc with 2,2'-bipyridine-5,5'-dicarboxylic acid (Route A, Figure 3-3) or a pre-metalated analogue (Route B, Figure 3-3). The organic ligands were dissolved in DMF or DEF prior to the addition of zinc acetate, which immediately led to precipitation of a crystalline material. However, no MUF-77 was formed. Control experiments indicated that the bipy ligand was prone to quickly forming an amorphous precipitate with zinc acetate. Similar complexation reactions were previously described in the literature.[196–198] The PXRD pattern of the crystalline solids showed the typical peaks for BMUF-1 or BMUF-2 and a set of additional peaks, indicating a second unknown species. We moved to focus on combining the bipy ligand with a suitable metal precursor to form a metal complex that would occupy the bipyridine coordination sites during the subsequent MOF synthesis. Due to the catalytic versatility of bipyridine-nickel complexes,[199–202] we attempted to incorporate the respective nickel(II)-coordinated bipy ligand into MUF-77 (Figure 3-3, M = Ni). We screened different ligand ratios for the synthesis of bipy-MUF-77. While precipitation of a crystalline solid was observed, none of the PXRDs indicated successful formation of the MUF-77 framework. Instead, PXRD indicated the formation of BMUF-1 or BMUF-2 and other unknown crystalline products. FT-IR and energy-dispersive X-ray spectroscopy (EDX) of the crystalline material, indicated that the Ni-complex retained stability during the MOF synthesis. The formation of other crystalline species under conditions that otherwise favour $_{rt}$MUF-77 formation indicated that the Ni-bipy complex was not suitable for incorporation into a MUF-77 framework. We expanded our trials to a $PdCl_2$-coordinated bipyridine ligand to see if the nature of the metal centre influenced the MUF-77 formation. Homogeneous $PdCl_2$-bipy complexes are known to promote C-C coupling reactions[203–206] and thus offer good potential as a proof-of-concept for the incorporation of catalytically active transition metal complexes into MUF-77. While a crystalline material was obtained, the PXRD pattern of the trials indicated the same product formation as observed in the previous experiments with free bipy ligands and $NiCl_2$-complexated ligands, but no MUF-77 crystals. ^{1}H NMR spectroscopy indicated that the palladium complex

retained stability throughout the experiment. The affinity of the ligand to form other MOF species and not MUF-77, even when the coordination site was occupied with stable metal complexes during the MOF synthesis, ruled out Route B as a viable synthetic method.

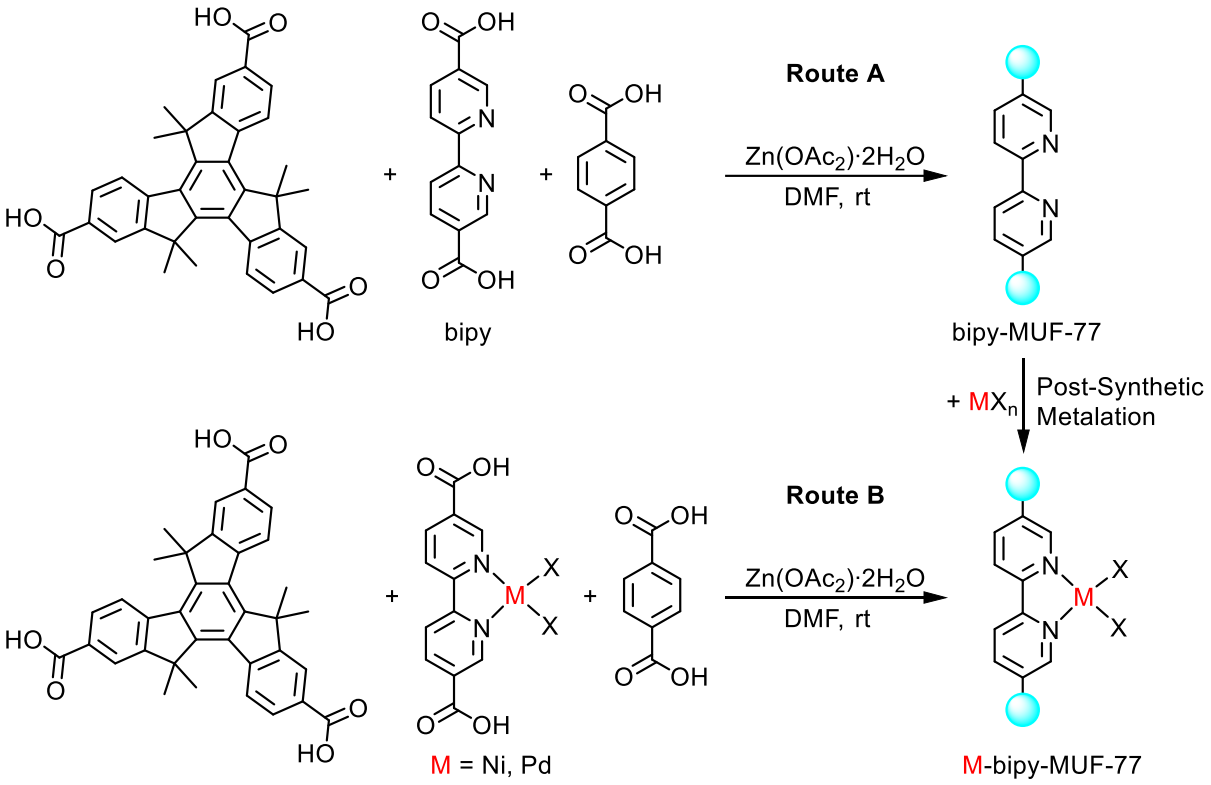

Figure 3-3 Reaction scheme for the attempted synthesis of M-bipy-MUF-77.

3.2.2 Phosphine-functionalized MUF-77 and Respective Gold(I) Complexes

Tertiary phosphines are an important class of ligands in transition metal catalysis.[207–209] A diphenylphosphine-functionalized bdc (PPh_2-bdc) was previously used for incorporation into MOF-5 and MIL-101 analogues.[210] We envisioned, that by embedding PPh_2-bdc or similar tertiary phosphine linkers within the MUF-77 framework, metalation of the ligand would give access to a transition metal catalyst within the MUF-77 pore (Figure 3-4).[211]

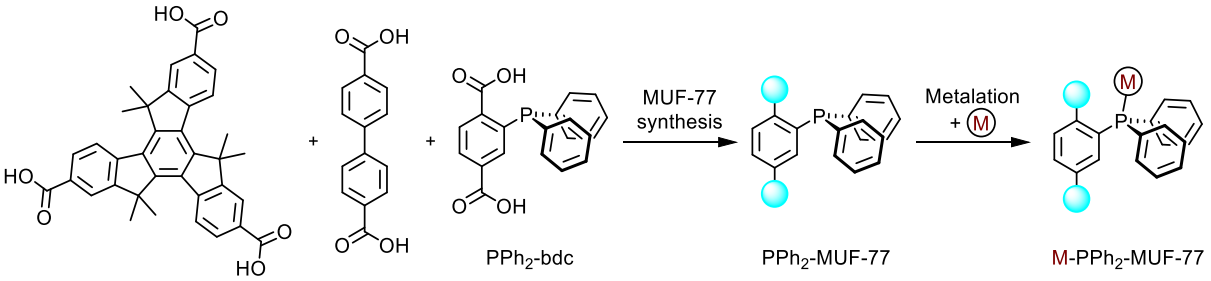

Figure 3-4 General strategy for the incorporation of a phosphine-stabilized transition metal catalyst within MUF-77.

3.2.2.1 Ligand Stability

One disadvantage of phosphine-appended ligands is that they are prone to oxidation to phosphine oxides during MOF synthesis[212] or following MOF synthesis if they are not stored in dry, degassed solvents. To

verify we could handle the PPh_2-bdc linker under ambient conditions during our MOF preparation we conducted a series of stability tests. The ^1H NMR spectrum of the phosphine ligand exposed to air for an hour did not differ from a freshly prepared sample. Partial oxidation was observed in both samples, indicated by minor additional signals in the ^1H NMR spectra and the presence of a peak around 29 ppm in the $^{31}P\{^1H\}$ NMR spectra, matching the reported spectra for the phosphine ligand upon oxidation (Figure 3-5).[212] This was attributed to the ligand sample we received being either partially oxidized or oxidation occurring due to using standard NMR solvent. We did not expect limited oxidation to be troublesome, as it was reported that, while the oxidation of the phosphine linker reduced the amount of available coordination sites, it did not adversely affect the framework.[212] Upon the addition of excess DCl complete oxidation of the ligand was observed. The experiments indicated that the ligand could be handled without significant oxidation under ambient conditions but was prone to oxidation at harsher conditions.

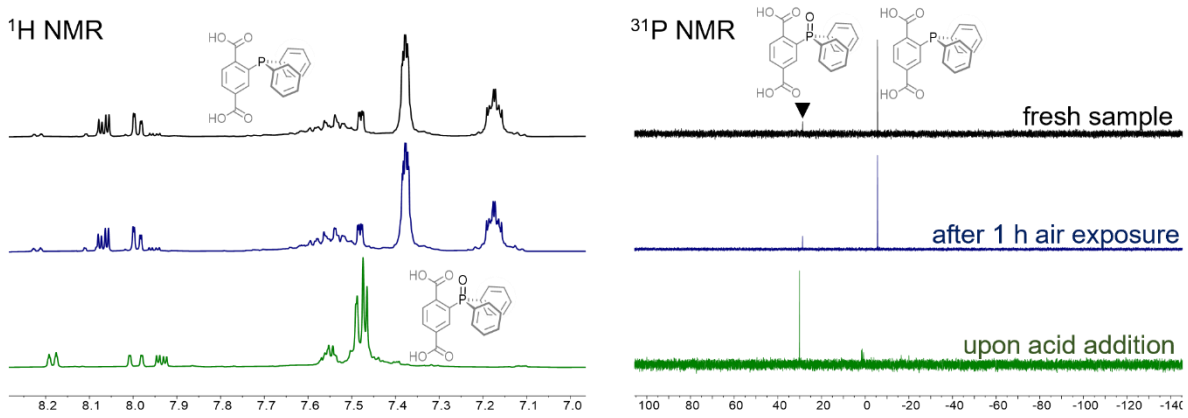

Figure 3-5 ^1H NMR spectrum (right) and $^{31}P\{^1H\}$ NMR spectrum (right) in DMSO-d_6 of a freshly prepared sample of PPh_2-bdc (top, black), a dry sample exposed to air for 1 h, (middle, blue) and after the addition of excess DCl to the NMR sample (bottom, green).

3.2.2.2 Diphenyl Phosphine-functionalized MUF-77

To limit oxidation, we combined the ligands in oven-dried vials in degassed solvent and under an inert atmosphere. Upon successful MOF formation, the crystals were handled under an inert atmosphere and kept in degassed solvent. PPh_2-MUF-77 was synthesized using two different protocols. A solvothermal synthesis was conducted at 85 °C in diethyl formamide as solvent (Figure 3-6, route A) and a milder room temperature synthesis protocol was employed (Figure 3-6, route B), yielding a nanocrystalline material in DMF. Both synthetic methods led to the successful formation of PPh_2-MUF-77.

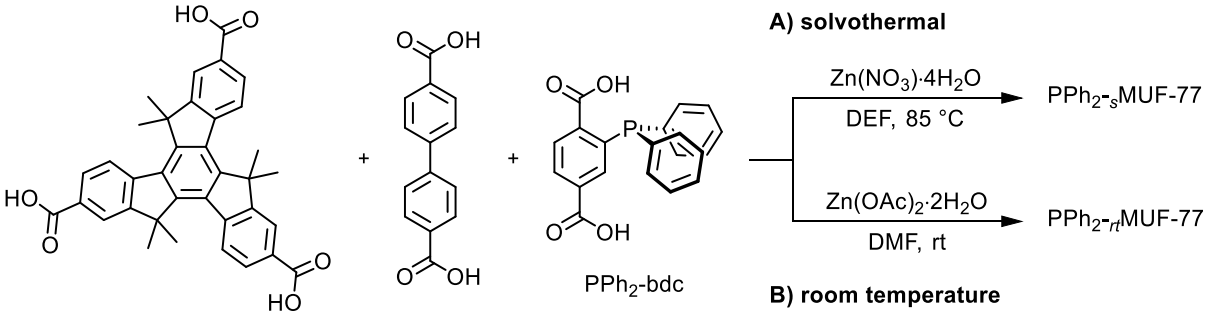

Figure 3-6 Reaction scheme for the synthesis of PPh_2-*s*MUF-77 and PPh_2-*rt*MUF-77.

The PXRD pattern of PPh_2-*s*MUF-77 was in good agreement with its simulated pattern (Figure 3-7, A). SXRD was obtained from a desolvated sample (Figure 3-7, B). As seen before for other MUF-77 analogues, the three linkers occupy distinct spaces in the crystal lattice. The SXRD data showed the successful incorporation of the PPh_2-bdc into the MUF-77 pore. The phosphine group is disordered over four equivalent positions, facing into the smallest, tetrahedral pocket. This arrangement is advantageous for our envisioned pore-modulation of the catalyst environment. The phenyl groups attached to the phosphorous could not be determined from the crystal structure due to the high degree of disorder. For a better understanding of the pore environment, we modelled the phenyl groups in representative positions. Our structural model of PPh_2-*s*MUF-77 only indicated minor oxidation during MOF synthesis.

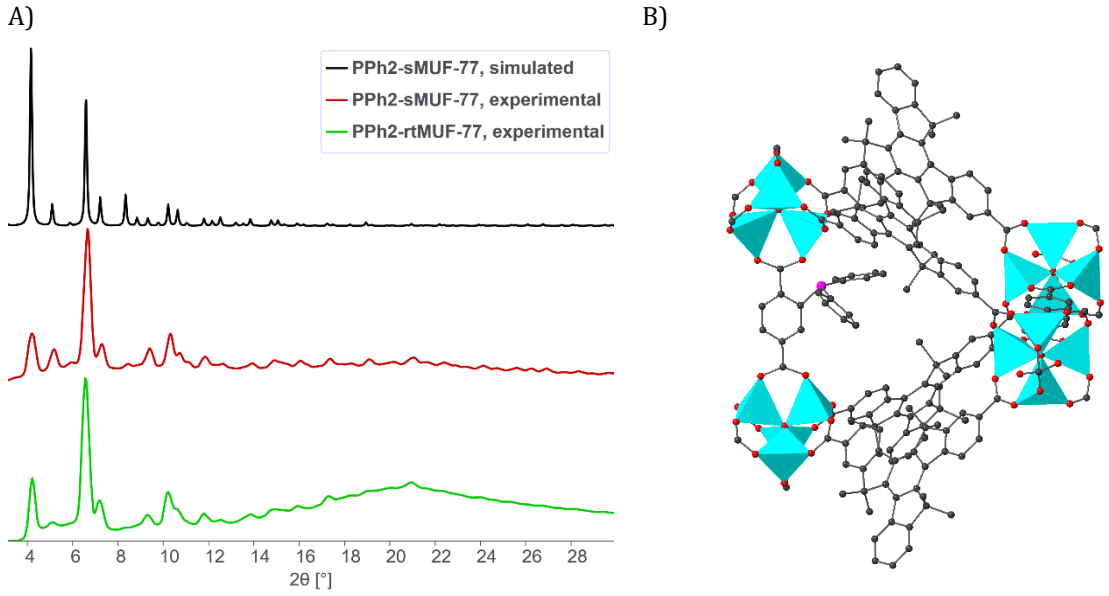

Figure 3-7 A) Simulated PXRD pattern for PPh_2-*s*MUF-77 (top, black) and experimental PXRD pattern for PPh_2-*s*MUF-77 (middle, red) and PPh_2-*rt*MUF-77 (bottom, green). B) SXRD model of the small pore in PPh_2-*s*MUF-77. Carbon atoms are shown in grey, phosphorus in pink, oxygen in red, and zinc as cyan polyhedra. Positions of phenyl groups attached to the phosphorous could not be determined from the structure but were later modelled in representative positions. Hydrogen atoms are omitted for clarity.

To obtain nanocrystalline PPh_2-*rt*MUF-77, zinc acetate was added to a stirring solution of H_2bpdc, H_2pbdc, and H_3hmtt in DMF to yield PPh_2-*rt*MUF-77 as a pale-yellow powder (Figure 3-6, route B). The successful formation of PPh_2-*rt*MUF-77 was confirmed by PXRD, ^{1}H NMR spectroscopy of a digested sample, and ^{31}P NMR spectroscopic data (Figure 3-8). The obtained PXRD data from the nanocrystalline samples were in good agreement with the simulated powder pattern from the crystal structure (Figure 3-7, A). ^{1}H and ^{31}P NMR data indicated ligand oxidation of around 45 %. As the standard digestion procedures for MUF-77 required either acidic or basic conditions, partial oxidation of the ligand could not be avoided during sample preparation. This made an accurate determination of the actual oxidation in the MOF difficult since some oxidation may have occurred during MOF digestion and analysis.

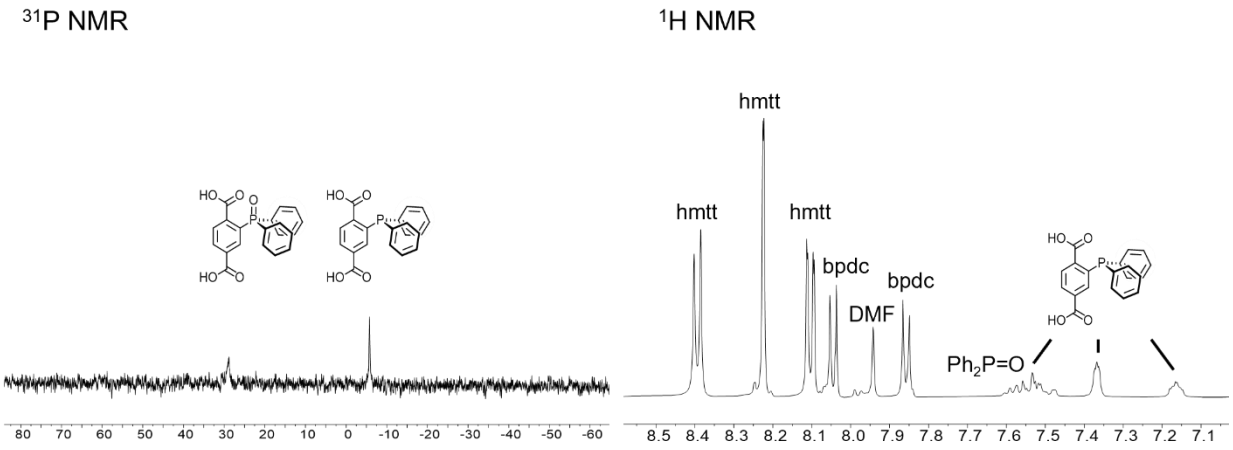

Figure 3-8 $^{31}P\{^{1}H\}$ NMR spectrum (left) and ^{1}H NMR spectrum (right) upon digestion of PPh_2-*rt*MUF-77 in a mixture of DMSO-d_6 and DCl.

3.2.2.3 Diethyl Phosphine-functionalized MUF-77

The stability and catalytic performance of phosphine-stabilized transition metal complexes depend on the functional groups used to stabilize the phosphine.[183–186] Aryl-phosphines often offer the best compromise of stability and activity. However, as our crystallographic models of PPh_2-bdc within the MUF-77 framework indicated substantial steric limitations within the pore, we were interested in additional alkyl-substituted phosphine ligands to reduce the steric pressure within the pore.

PEt_2-bdc was used as HCl salt. Unfortunately, employing the ligand in salt form under standard conditions for MUF-77 synthesis was not successful, but rather led to the formation of BMUF-1 or BMUF-2 and a second phase. We expected that the protonation of the PEt_2-bdc ligand prevented it from being available for the zinc cluster formation and that the addition of a base might avert that issue. We chose triethylamine as a suitable base as we knew that MUF-77 was stable in its presence. The addition of excess triethylamine to the solvothermal synthesis led to the successful formation of PEt_2-*s*MUF-77 crystals (Figure 3-9).

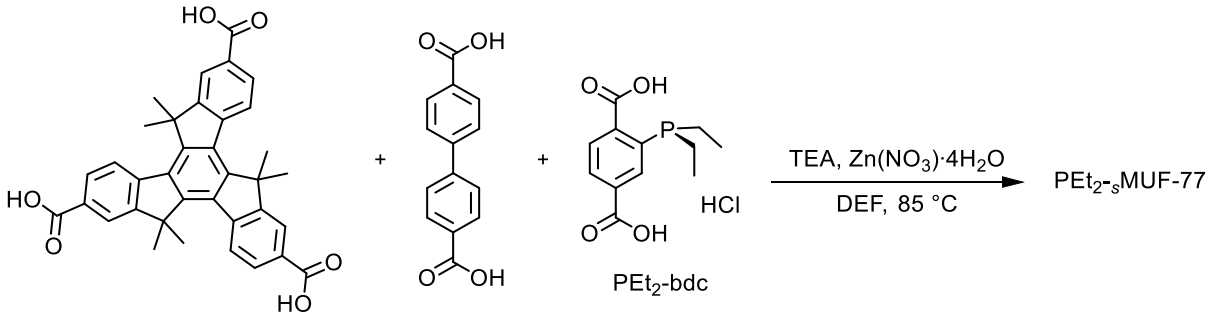

Figure 3-9 Synthesis attempts of PEt_2-MUF-77 under solvothermal and room-temperature synthesis conditions.

SXRD data of the crystals obtained from the solvothermal synthesis indicated the successful incorporation of PEt_2-bdc into MUF-77 (Figure 3-10 A). The model displayed the typical MUF-77 structure. The bdc-appended phosphine group pointed into the small, tetrahedral pore of MUF-77, which is desired from a catalytic application standpoint. The ethyl groups attached to the phosphorous were modelled in representative positions due to the high degree of disorder. The SXRD data did not indicate ligand oxidation.

While the synthesis was not phase-pure, MUF-77 crystals were readily isolated by hand, as shown by the PXRD pattern of the isolated phase and its similarity of characteristic peaks with the simulated pattern (Figure 3-10 B).

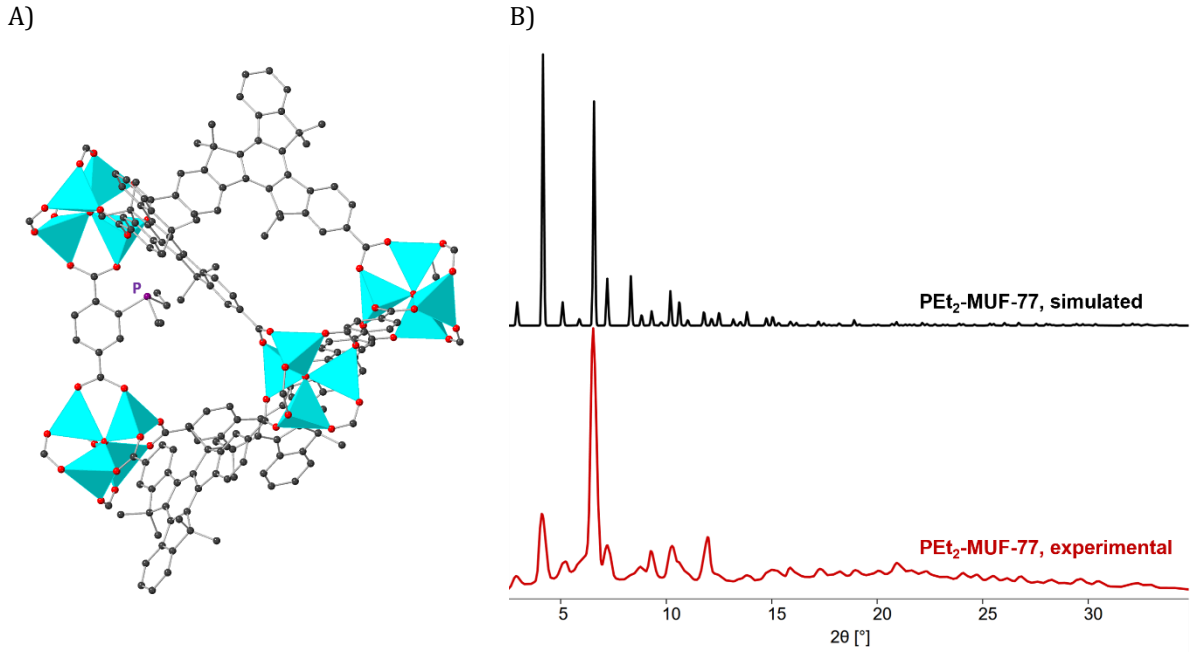

Figure 3-10 A) SXRD model of the small pore in PEt_2-$_s$MUF-77. Carbon atoms are shown in grey, phosphorus in pink, oxygen in red, and zinc as cyan polyhedra. Ethyl-groups attached to the phosphorous were modelled in representative positions due to disorder. Hydrogen atoms are omitted for clarity. B) Simulated PXRD spectrum of PEt_2-$_s$MUF-77 (top, black) and experimental PXRD spectra of as-synthesized PEt_2-$_s$MUF-77 (bottom, red)

^{1}H NMR analysis of the mixed sample confirmed the presence of all three ligands (Figure 3-11). The shifts correlated to the PEt_2-bdc ligand showed identical chemical shifts compared to the original ligand NMR spectrum, indicating that the synthetic conditions for the MUF-77 formation and the addition of triethylamine did not lead to undesired oxidation of the ligand. Due to the different additional crystalline species within the sample, the ligand ratios for hmtt and bpdc were higher than expected from a phase-pure MUF-77 synthesis.

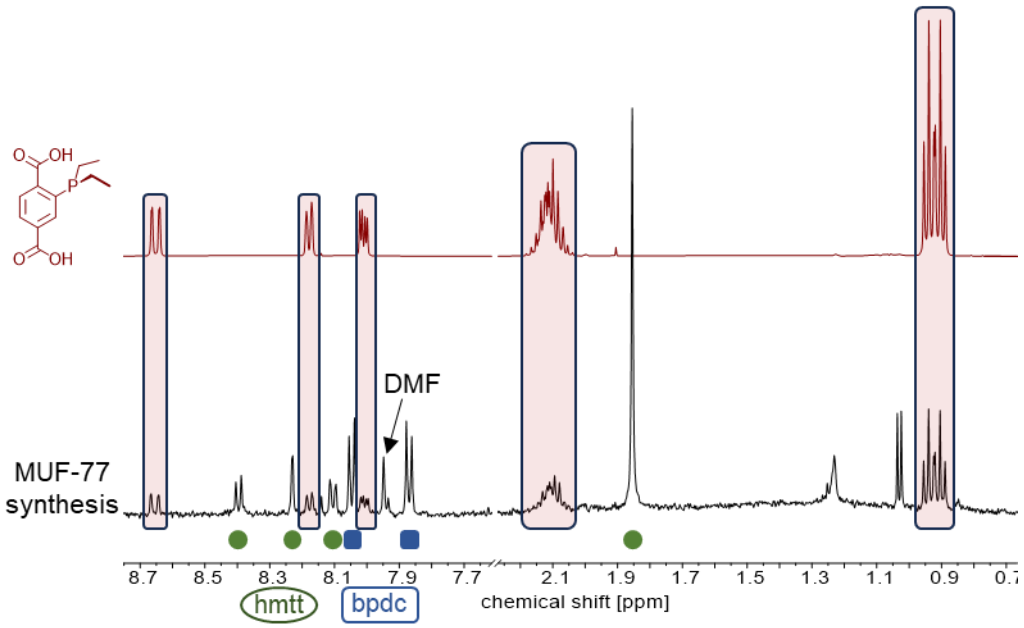

Figure 3-11 ^{1}H NMR spectra of PEt_2-bdc·HCl (top, red) and digested PEt_2-*s*MUF-77 (bottom, black). The good agreement of both NMR spectra indicated the successful incorporation of the ligand into MUF-77.

3.2.2.4 Metalation of PPh_2-MUF-77

With the diphenylphosphine-functionalized MUF-77 in hand, the focus was on introducing a suitable pre-catalyst to the framework. In homogeneous catalysis, this can be achieved by reacting the free diphenyl phosphine ligand with a suitable gold chloride precursor.[100,101] Usually, the gold is stabilized with an easily displaceable ligand, allowing for quick ligand exchange. Gold(I) chloride complexes are excellent catalysts upon halide abstraction.[129,213–215] Following this methodology, we combined freshly synthesized PPh_2-MUF-77 with chloro(dimethylsulfide)gold(I), $(Me_2S)AuCl$, in dichloromethane at room temperature (Figure 3-12). To avoid the formation of gold nanoparticles the samples were protected from light.

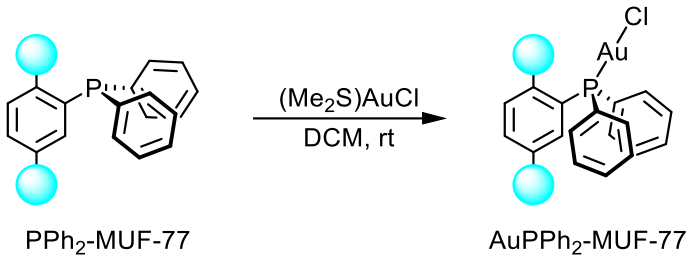

Figure 3-12 General procedure for the metalation of PPh_2-*s*MUF-77.

When the van Bokhoven group employed a similar strategy for the synthesis of LSK-1, they found that the reaction time was crucial for maintaining single atom sites. Reaction of the MOF for 4 h with the gold reagent gave the complex with 16 % catalyst loading, while nanoparticles were observed during reaction times of several days.[216]

3.2.2.4.1 Metalation of PPh_2-*rt*MUF-77

With PPh_2-*rt*MUF-77 at room temperature, we did not observe a time dependence, however, the ratio of gold precursor to MOF was essential for avoiding the formation of elemental gold. The MOF samples retained

crystallinity after the reaction as shown by PXRD (Figure 3-13, a). No diffraction peaks related to gold nanoparticles were observed. The successful coordination of the gold pre-catalyst was confirmed by EDX and NMR (Figure 3-13, b and c). The observed peak in the $^{31}P\{^{1}H\}$ NMR at 35.6 ppm was in good agreement with the reported data for triphenylphosphine gold complexes (triphenylphosphine gold chloride: 34.19 ppm, [(4,5-dicyano-imidazolyl-1yl)-(triphenylphosphane)-gold(I)]: 32.04 ppm).[217,218] EDX data showed the existence of gold in the sample, while no signals for gold were found in control experiments with the parent MUF-77 under similar metalation conditions.

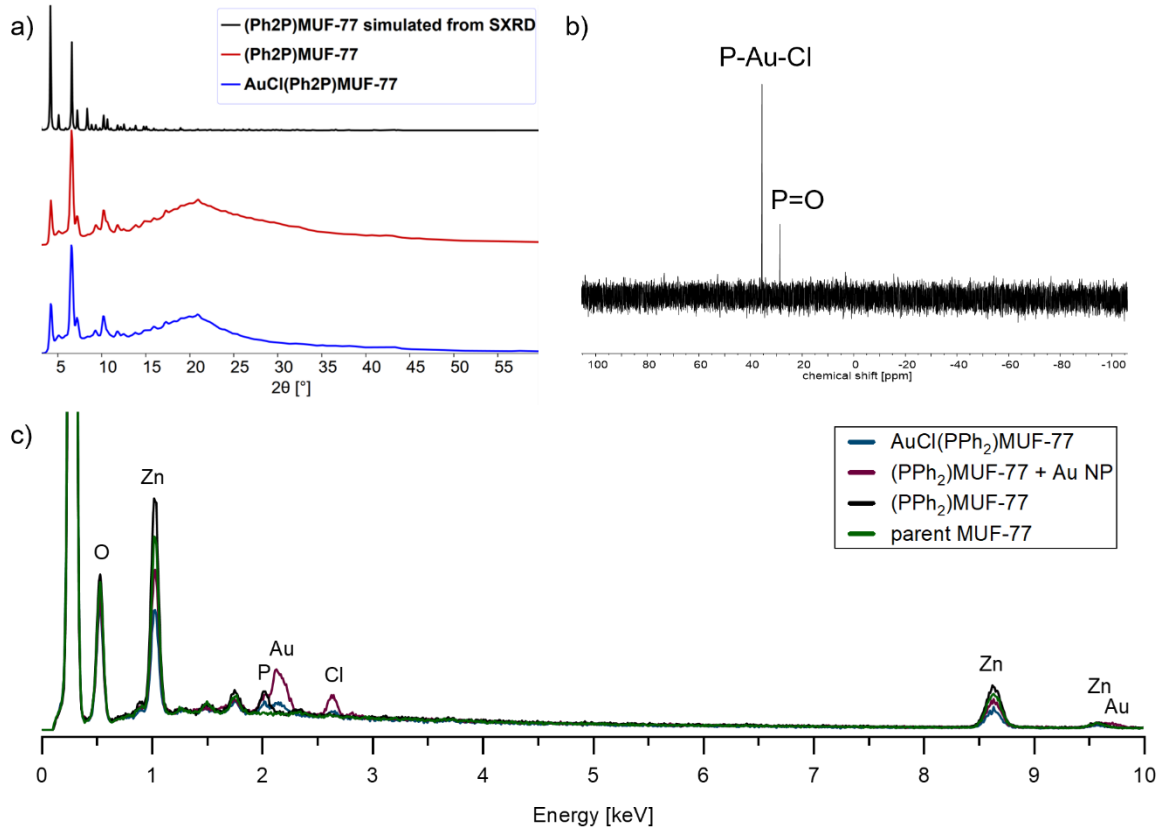

Figure 3-13 Characterization of $AuPPh_2$-MUF-77 by a) PXRD, b) $^{31}P\{^{1}H\}$ NMR in DMSO-d_6/DCl and c) EDX.

3.2.2.4.2 Attempted Metalation of PPh_2-$_s$MUF-77

Encouraged by the results we attempted to repeat the metalation experiments with $_s$MUF-77 from solvothermal synthesis. The larger crystal sizes allowed for further investigation of the coordination through SXRD experiments. Crystals of PPh_2-$_s$MUF-77 were reacted with Me_2SAuCl in dichloromethane at room temperature. As observed with the nanocrystalline MUF-77 variant, excess gold precursor (in comparison to the estimated amount of phosphine linker) quickly led to nanoparticle formation as indicated by the appearance of purple colouration. In contrast to our expectations, SXRD data of PPh_2-$_s$MUF-77 did not indicate the successful complex formation. Instead, SXRD data indicated a partial oxidation of the phosphine group (Figure 3-14). While the experiments with nanocrystalline samples were promising, indicating the formation of the desired complex, the attempted metalation within the crystals derived from solvothermal synthesis did not lead to complex formation, but oxidation of the ligands was observed.

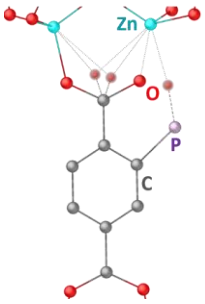

Figure 3-14 Structural model from SXRD data of the distortion arising from the oxidation of the phosphine functionality at the bdc linker within the MUF-77 pore.

3.2.3 Phosphoramidite-functionalized MUF-77

We further focused our efforts on the functionalization of the bpdc ligand with a phosphoramidite group, another promising ligand for transition metal catalysis.[127] We envisioned that functionalization of the diphenyl backbone would move the steric bulk further into the MOF pore. That would lead to fewer steric constraints and stabilize our target transition metal complexes.

3.2.3.1 Attempted Synthesis of a Ditopic Phosphoramidite Ligand

Following the procedure by Bartels *et al.,* the 2,2'-dihydroxy bpdc ester was refluxed in toluene with *N,N,N',N',N'',N''*-hexamethylphosphanetriamine, $P(NMe_2)_3$, to yield the desired phosphoramidite ligand ester **1** (Figure 3-15).[219,220] In our hands, the bpdc phosphoramidite ester slowly decomposed in solution over time, which was not surprising, as many phosphoramidites are susceptible to hydrolysis, especially under acidic conditions.[127,221–223] We directly commenced with the metalation step, expecting the complexation would stabilize the functional group.[224] Slow addition of the bpdc ligand to a solution of Me_2SAuCl in dichloromethane afforded the respective transition metal complex **2**.[214] The successful metal complex formation was supported by ^{31}P NMR spectroscopy, showing a shift of the signal from 149.9 ppm, a value typical for the related BINOL-derived phosphoramidites (^{31}P NMR for BINOL-$P(N(Me_2))$ = 148.8 ppm; biphenyl-$P(N(Me_2))$ = 149.7 ppm)[214,225], to 129.1 ppm. For comparison, the ^{31}P NMR chemical shift for the BINOL-derived phosphoramidite gold complex was reported at 128.2 ppm.[214] While we successfully synthesized the desired Au(I)-complex as the bpdc-ester, attempts to obtain the final ligand (**3**) through hydrolysis of the ester groups led to the decomposition of the phosphoramidite. A direct reaction of $(OH)_2$-bpdc with $P(NMe_2)_3$ did not yield the desired product but the respective carboxamide.

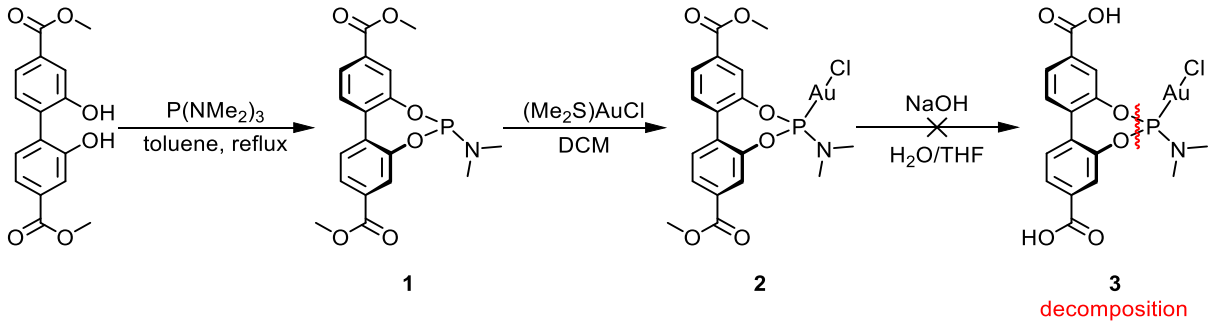

Figure 3-15 Attempted functionalization of the bpdc linker with a phosphoramidite-derived gold-complex for incorporation into MUF-77.

3.2.3.2 Post-Synthetic Modification of MUF-77

As an alternative approach, we investigated the post-synthetic modification of MUF-77. We hoped this strategy would reduce the chances of ligand hydrolysis during MOF and ligand synthesis. The challenge in this approach was to ensure the phosphoramidite formation would not come at the expense of framework stability. As MUF-77 showed good stability in toluene we adapted the homogeneous synthesis conditions. $(OH)_2$-MUF-77 was successfully synthesized through a solvothermal synthesis approach (Figure 3-16).

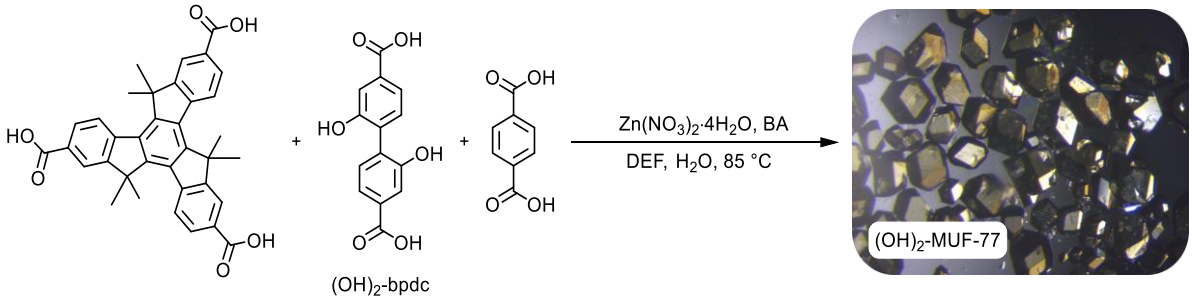

Figure 3-16 Solvothermal synthesis of $(OH)_2$-$_s$MUF-77.

A solution of hmtt, $(OH)_2$-bpdc, bdc and zinc nitrate hexahydrate in DMF with benzoic acid as crystal growth modulator was heated in an isothermal oven at 85 °C for 24 hours. The morphology of the obtained MUF-77 crystals was unusually sensitive to the ligand ratios employed in the synthesis until the ideal ratio was found. The good agreement of the PXRD data with that of parent MUF-77 confirmed the synthesis of crystalline $(OH)_2$-MUF-77 (Figure 3-17). ^{1}H NMR data of the digested MOF supported the successful incorporation of $(OH)_2$-bpdc into the MUF-77 framework. The ligand ratios matched the expected ratios $hmtt_{1.33}|(OH)_2\text{-}bpdc_{0.5}|bdc_{0.5}$ for $(OH)_2$-MUF-77 with the formula $\{Zn_4O(hmtt)_{4/3}[(OH)_2\text{-}bpdc)]_{1/2}(bdc)_{1/2}\}$.

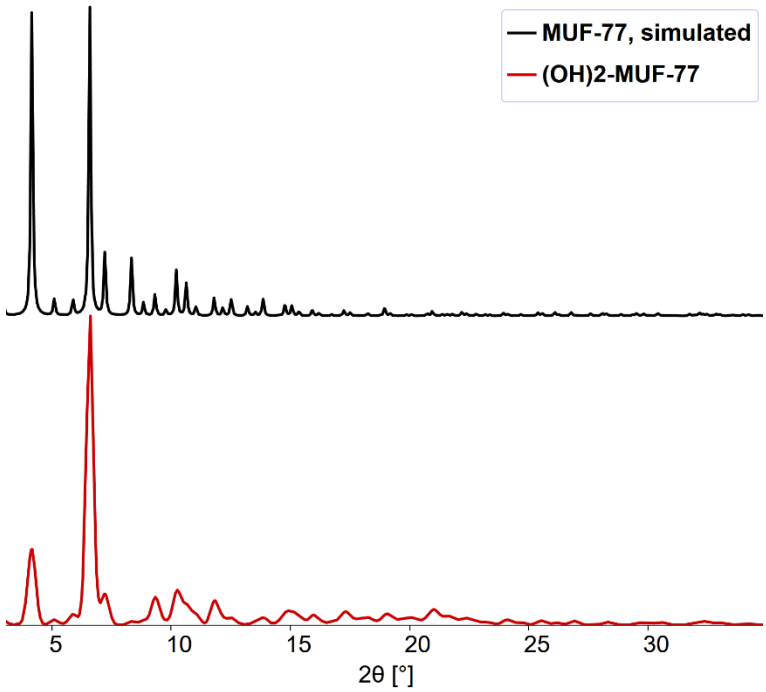

Figure 3-17 Simulated PXRD pattern of parent MUF-77 (black, top) and experimental PXRD pattern of $(OH)_2$-MUF-77 (red, bottom).

The MOF was subsequently refluxed under argon in toluene with $P(NMe_3)$ to synthesize $(Me_2N)PO_2$-MUF-77 (Figure 3-18).

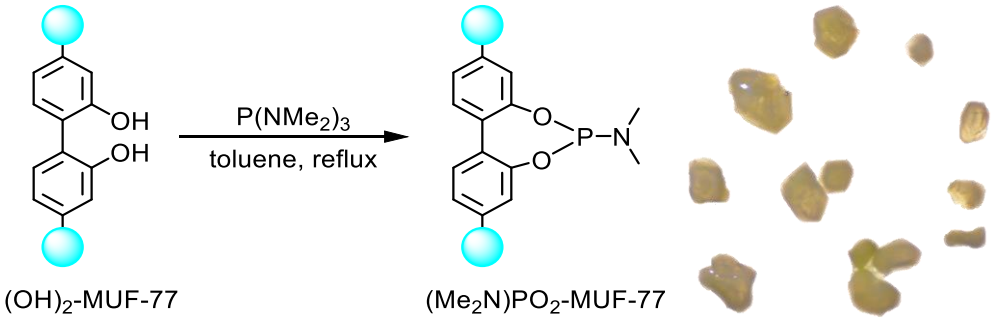

Figure 3-18 Synthesis of $(Me_2N)PO_2$-MUF-77.

While the MOF showed clear signs of stress, indicated by increased opacity of the crystals under visual inspection, PXRD analysis indicated the framework maintained its crystallinity (Figure 3-19 A). SXRD analysis of the single crystals indicated the successful post-synthetic formation of the phosphoramidite (Figure 3-19 B). The disorder arising from the different possible locations for the dimethylamino group impaired its modelling. While incomplete, the observed geometry matched the usually observed pseudo tetrahedral structure of phosphoramidites and respective bond lengths. At 1.64 Å, the P-O bond length is in good agreement with reported BINOL-derived structures (1.62 Å for the reported bis(1-phenylethyl)phosphoramidite).[226]

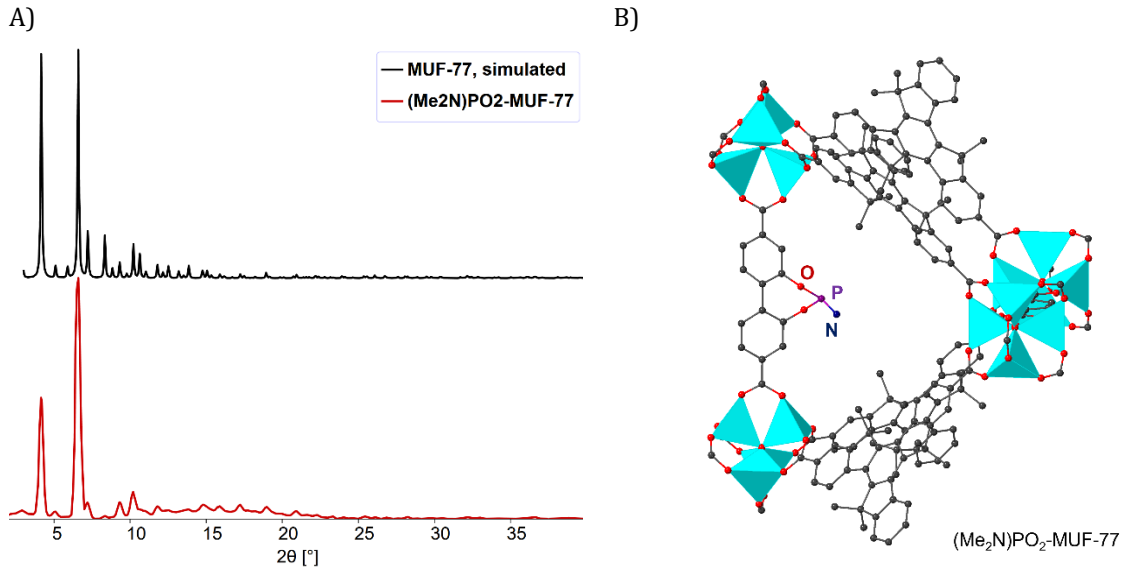

Figure 3-19 A) Simulated PXRD pattern for parent MUF-77 (black, top) and experimental PXRD pattern of $(Me_2N)PO_2$-MUF-77. B) SXRD model of the small pore in $(Me_2N)PO_2$-MUF-77. Carbon atoms are shown in grey, phosphorus in pink, oxygen in red, and zinc as cyan polyhedra. Hydrogen atoms are omitted for clarity. The high degree of disorder interfered with modelling of the dimethylamino functional group.

To support our model and to understand the degree of any functionalization, several NMR experiments were conducted. As expected from our experiments with the molecular phosphoramidite esters, the phosphoramidite was prone to hydrolysis under our standard basic MOF digestion conditions. The ^{1}H NMR spectrum from the digestion in 0.1 M NaOD in D_2O indicated the presence of dihydroxy bpdc. While this could stem from unreacted ligand, it was likely to result from decomposed phosphoramidite systems. We thus explored additional digestion methods. Different metal binding reagents were used to cleave the Zn–O metal-ligand bonds within MUF-77. Due to the hygroscopic nature of sodium sulfide and because of practical limitations working with H_2S gas, the most suitable alternatives to acidic or basic digestion were found to be the use of acetamide or ethylenediaminetetraacetic acid (EDTA) in DMSO-d_6. Both reagents successfully digested parent $(OH)_2$-MUF-77 but let to the decomposition of the phosphoramidite functional group. Following the same strategy as for the ligand synthesis, we attempted to stabilize the phosphoramidite by reacting it with Me_2SAuCl in dichloromethane to yield the respective complex (Figure 3-20).

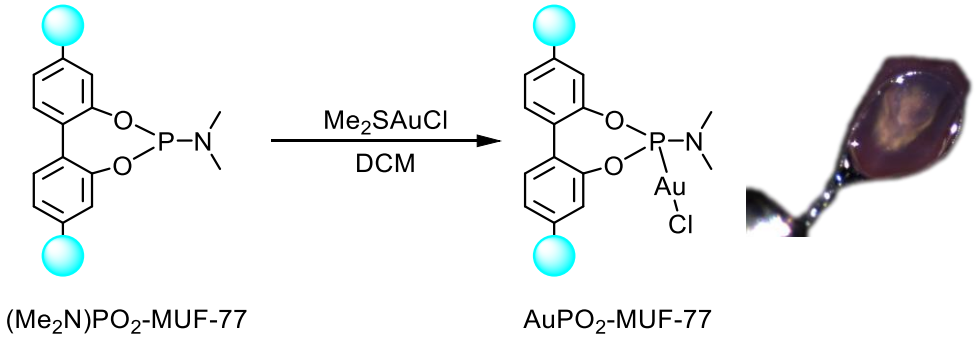

Figure 3-20 Attempted metalation of $(Me_2N)PO_2$-MUF-77 with Me_2SAuCl to yield the respective gold(I) complex within MUF-77.

The reaction accompanied a change of colour for the $AuPO_2$-MUF-77 crystals from a golden colour to a deep purple. We observed this coloration several times as an indication of the formation of gold

nanoparticles,[227,228] being visible by eye or microscope before the concentration reached the threshold necessary for confirmation by our PXRD setup. SXRD data was inconclusive. The reduced stability of the phosphoramidite ligand restricted our standard MOF digestion protocols and NMR analysis. Therefore, we shifted our focus to alternative transition metal complexes within MUF-77.

3.2.4 N-Heterocyclic Carbene-Transition Metal Complexes in MUF-77

3.2.4.1 Synthesis of a Gold(I)-NHC-Functionalized Linker for MUF-77

Gold-NHC complexes are accessible through several different metalation routes.[229] Many NHC complexes can be obtained by directly reacting a suitable gold source with the free NHC. Due to limitations in suitable substrates and the requirement for glove box techniques, alternative methods were quickly introduced.[230] The reported procedures include the synthesis from isonitrile-gold complexes[231,232] and imidazolium salts as substrates,[233] often in the presence of weak bases.[234] Commonly, the complexes are obtained through a transmetalation route. Imidazolium halide salts were readily converted to the respective silver complexes. Transmetalation with a gold source led to the desired gold complex.[230,235] For the synthesis of our NHC-bpdc ligand (**7**), we adapted this popular method, as it did not require the use of a glovebox, other specialized equipment, or uncommon reagents (Figure 3-21). The bpdc imidazolium salt ester (**4**) was reacted with silver oxide in dichloromethane under inert conditions and protected from light to give the respective Ag(I)-NHC complex (**5**) *in situ*. After removing unreacted solids, (Me_2S)AuCl was added, and the stirring was continued. Solids were again filtered off and upon solvent removal, the NHC-gold(I) complex of the bpdc ester (**6**) was obtained. Hydrolysis of the ester gave the desired ligand, Au(I)-NHC-bpdc (**7**).

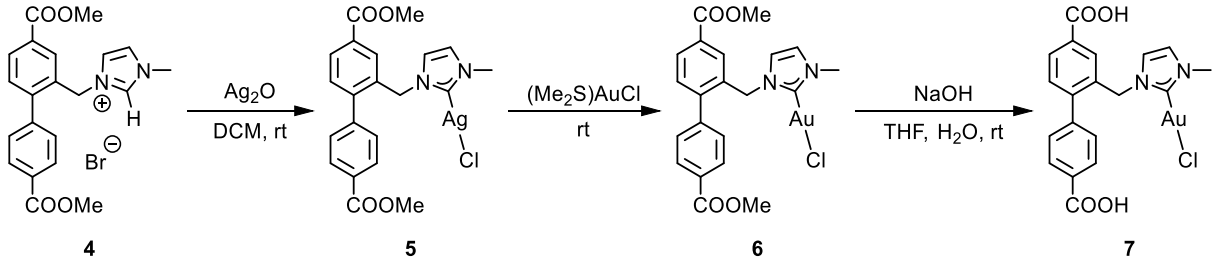

Figure 3-21 Synthesis of a NHC gold(I) complex-bearing bpdc linker for the incorporation into MUF-77.

3.2.4.2 Attempted Solvothermal Synthesis of Au(I)NHC-$_s$MUF-77

With the pre-catalyst in hand, we attempted the direct solvothermal synthesis of Au(I)NHC-$_s$MUF-77 (Figure 3-22). The ligands were combined in diethylformamide in the presence of benzoic acid as a crystal growth modulator and heated in an isothermal oven at 85 °C for 16-24 h. The reaction yielded crystals of typical MUF-77 morphology, however, a purple powder formed on the walls of the glass vial, and the crystals themselves showed the purple coloration indicative of gold nanoparticle formation.

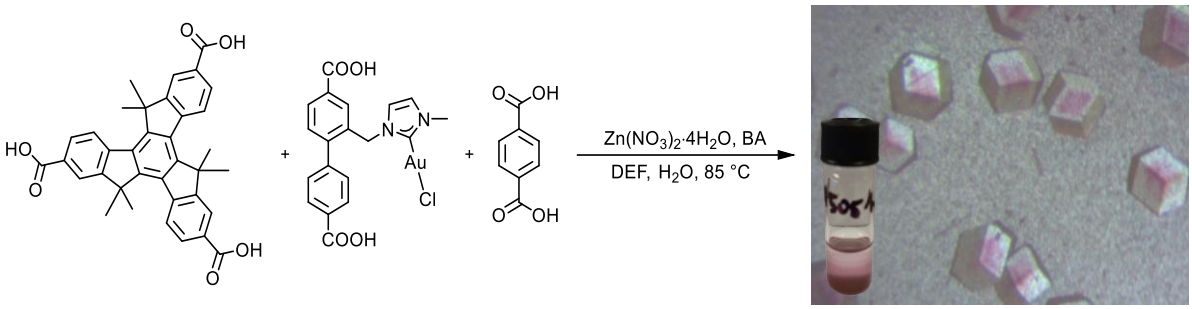

Figure 3-22 Attempted solvothermal synthesis of Au(I)NHC-$_s$MUF-77.

Indeed, PXRD of the sample indicated the formation of gold nanoparticles besides the desired MUF-77 framework (Figure 3-23). The typical diffraction peaks for MUF-77 were observed, however, peaks at high angles around 38, 65, and 78 Å indicated the formation of gold nanoparticles.[236,237] The ^{1}H NMR spectrum of the digested MOF confirmed the NHC ligand decomposes during MOF synthesis. Analysis by SXRD did not deliver further insights. The disorder of the functional group in the pore complicated any suggestions for a structural model. Due to the limited stability of the Au(I)NHC-bpdc complex during ligand and MOF synthesis, we moved on to alternative synthesis conditions.

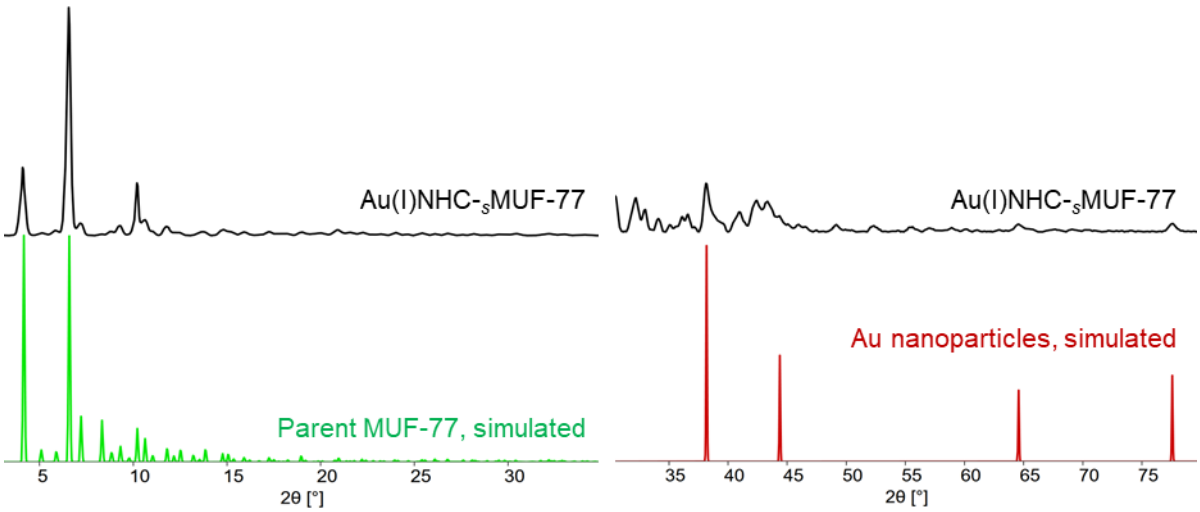

Figure 3-23 Experimental PXRD pattern of Au(I)NHC-$_s$MUF-77 (top, black) and the simulated PXRD pattern of parent MUF-77 (left bottom, green) and gold nanoparticles (bottom right, red).

3.2.4.3 Room-Temperature Synthesis of Au(I)NHC-$_{rt}$MUF-77

To avoid the decomposition of the metal complex we shifted our approach to utilize milder synthesis conditions with the already metalated NHC-bpdc linker. Following our standard room-temperature MUF-77 conditions, adjusted for ligand ratios, and limiting additional water, the ligands were dissolved in DMF. A solution of zinc nitrate dihydrate in DMF was added under stirring. MOF formation was indicated by the immediate formation of a precipitate. After 45 min the off-white solid was isolated by centrifugation and washed with fresh DMF five times (Figure 3-24).

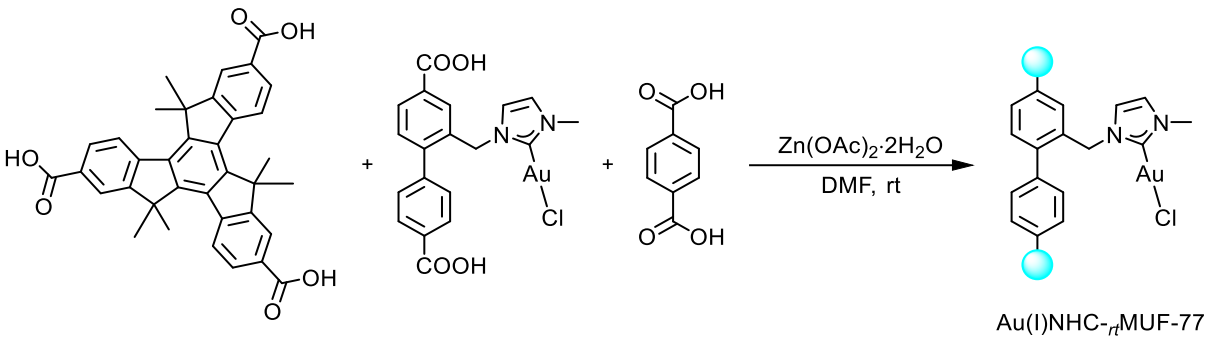

Figure 3-24 Room-temperature synthesis of Au(I)NHC-*rt*MUF-77.

The PXRD pattern of the synthesized material confirmed the successful formation of Au(I)NHC-*rt*MUF-77 crystals. The pattern was in good agreement with the simulated pattern for parent MUF-77 crystals. Signals indicating the formation of elemental gold, an indication of the decomposition of the gold-linker complex, were absent (Figure 3-25). The broad peak around 2θ =21° is caused by the oil used to mounting the sample during the PXRD experiment. The intensity of the peak depends on the amount of oil in ratio to substrate. As MOFs typically lead to characteristic diffractions at lower angles, the peaks attributed to oil are usually not interfering with the characterisation of the material.

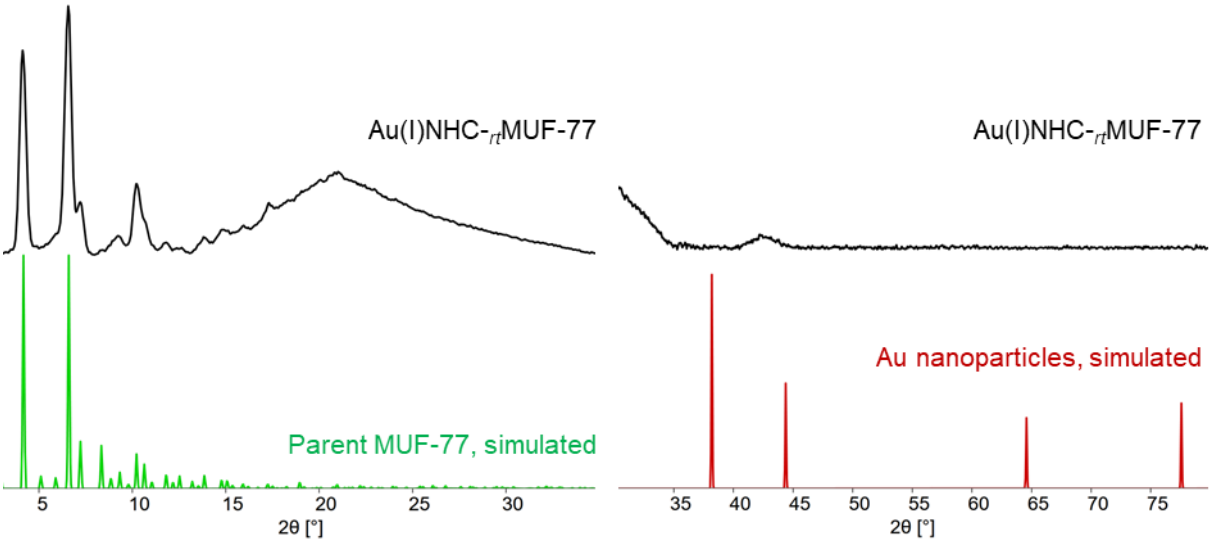

Figure 3-25 Experimental PXRD pattern of Au(I)NHC-*rt*MUF-77 (top, black) and the simulated PXRD pattern of parent MUF-77 (left bottom, green) and gold nanoparticles (bottom right, red).

The ^{1}H NMR spectrum of the digested MOF supported that finding (Figure 3-26). All ligand signals were found to match those of the parent samples, supporting the conclusion that decomposition of the complex was avoided through the milder conditions and by using the already metalated linker. The ligand ratios matched the expected ratios $hmtt_{1.33}$|Au(I)NHC-$bpdc_{0.5}$|$bdc_{0.5}$ for Au(I)NHC-MUF-77 with the formula $[Zn_4O(hmtt)_{4/3}((Au(I)NHC\text{-}bpdc)_{1/2}(bdc)_{1/2}]$. Mass spectrometry of the NMR sample further supported the presence of intact Au(I)-NHC-bpdc after synthesis, with an calculated m/z of 567.038 and a found m/z of 567.039. Unexpectedly, after 12 h the off-white solid in DMF changed colour to dark grey, and purple spots were observed after seven days. The colour change was a good indication of gold nanoparticle formation in previous experiments. Storing the crystals in dichloromethane did not improve the ligand stability. The

reactivity and stability of transition metal-NHC complexes are influenced greatly by the choice of the *N,N'*-functionalisation. The electronic properties of the NHC ligand and the steric bulk around the metal centre are crucial factors in synthesising stable NHC complexes.[138] Stable complexes are often obtained by employing NHC ligands with bulky, aryl-N,N'-substituents like the popular 1,3-Bis(2,6-diisopropylphenyl)-1,3-dihydro-2H-imidazol-2-ylidene, IPr. Due to the size limitations within the MUF-77 pore, we compromised on the functionalization the bpdc linker with a less bulky methyl substituent, which showed only limited stability under the MUF-77 synthesis conditions.

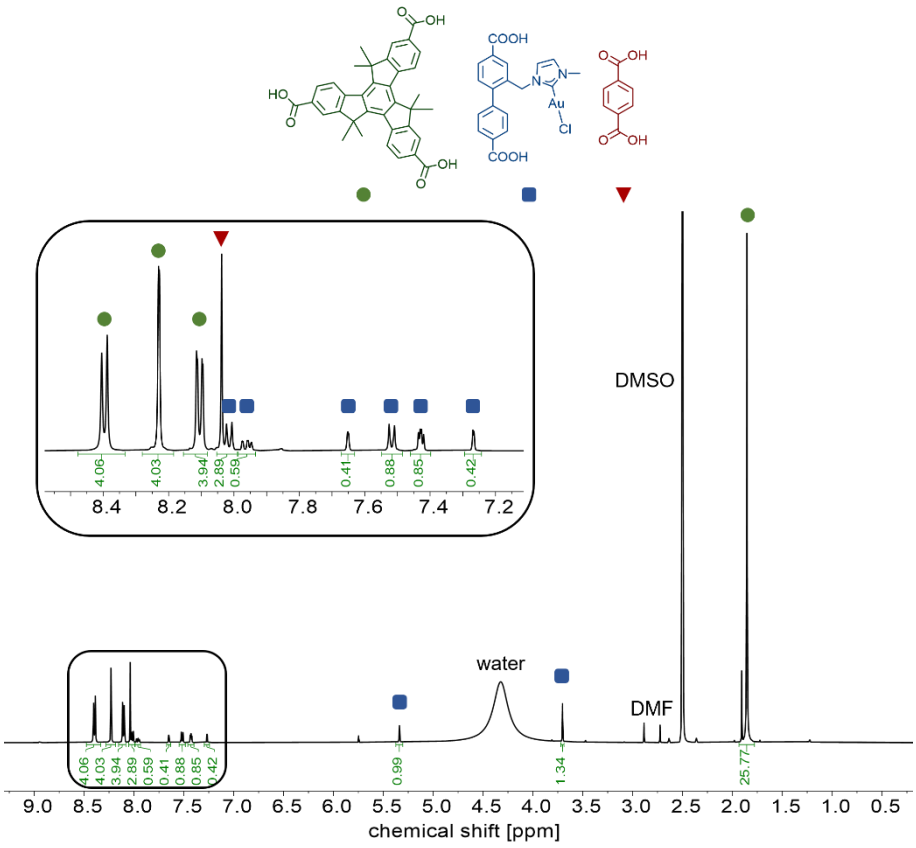

Figure 3-26 The ^{1}H NMR spectrum of Au(I)NHC-$_{rt}$MUF-77 upon digestion in a mixture of DCl and DMSO-d$_6$.

3.2.4.4 Attempted Post-Synthetic-Metalation of Imidazole-Functionalized MUF-77

3.2.4.4.1 Solvothermal Synthesis of Imidazole-Functionalized MUF-77

As an alternative route to avoid the decomposition of the transition metal ligand complex during synthesis we attempted to introduce the transition metal complex after successfully synthesizing the imidazole-functionalized MUF-77 framework, im-$_s$MUF-77 (Figure 3-27). Ligands, zinc nitrate, and the crystal growth modulator benzoic acid were combined in diethylformamide and heated in an isothermal oven at 85 °C for 16-24 h to yield colourless im-$_s$MUF-77crystals with the typical MUF-77 morphology.

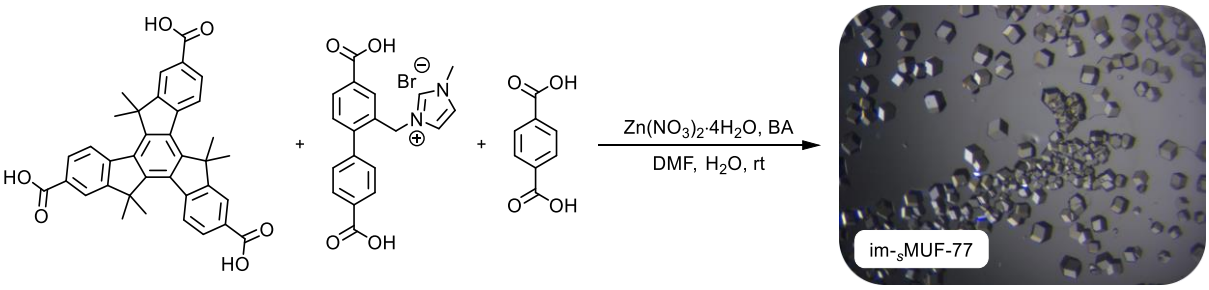

Figure 3-27 Solvothermal synthesis of im-$_s$MUF-77.

PXRD analysis of the synthesized crystals indicated the successful formation of the MUF-77 framework. The PXRD peak pattern was in good agreement with the simulated pattern of parent MUF-77 (Figure 3-28).

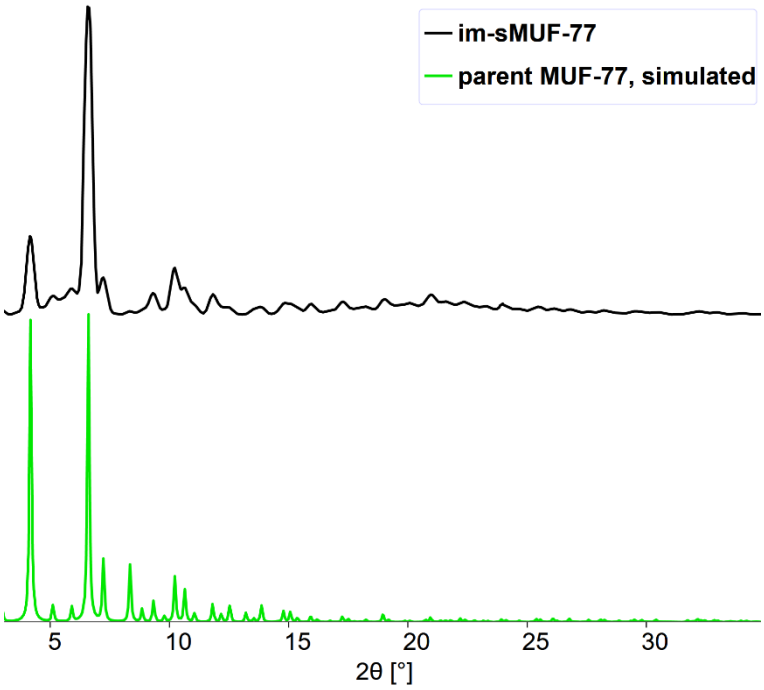

Figure 3-28 Experimental PXRD pattern of im-$_s$MUF-77 (top, black) and simulated PXRD pattern of parent MUF-77.

The ^{1}H NMR spectrum of the digested MOF further supported the successful formation of im-$_s$MUF-77. The determined ligand ratios matched the expected ratios hmtt$_{1.33}$|im-bpdc$_{0.5}$|bdc$_{0.5}$ for MUF-77, [Zn$_4$O(hmtt)$_{4/3}$((im-bpdc)$_{1/2}$(bdc)$_{1/2}$]. Signals of im-bpdc were present as expected, indicating the stability of the ligand under the solvothermal MUF-77 synthesis conditions.

3.2.4.4.2 Attempted Post-Synthetic-Metalation of im-$_s$MUF-77

With the imidazole-functionalized MUF-77 in hand, we attempted the post-synthetic metalation to yield the respective transition metal MUF-77 catalyst (Figure 3-29). Different conditions and metals were tested, with a focus on systems familiar to us through previous experiments. While transmetalation reactions, most prominently involving silver complexes, are commonly used to prepare homogeneous catalysts, we feared the resulting insoluble metal salts would be difficult to separate from the MOF crystals and complicate catalytic studies. Following Clauberg *et al.*, we attempted to post-synthetically form a nickel-NHC complex through the 'free-carbene' route (Figure 3-29, route A).[238] We attempted the post-synthetic metalation of

freshly synthesized im-$_s$MUF-77 with potassium *tert*-butoxide as a base for the *in situ* formation of the free-carbene $NiBr_2(PPh_3)_2$ as nickel precursor, but no reaction was observed. The Yaghi group followed a similar route for the metalation of a ditopic, imidazole-functionalized MOF-linker to form a stable palladium complex.[239] We attempted the metalation with $Pd(OAc)_2$ in potassium *tert*-butoxide and in the presence of KBr, but ^{1}H NMR analysis of the digested crystals only showed signals corresponding to the unaltered ligand.

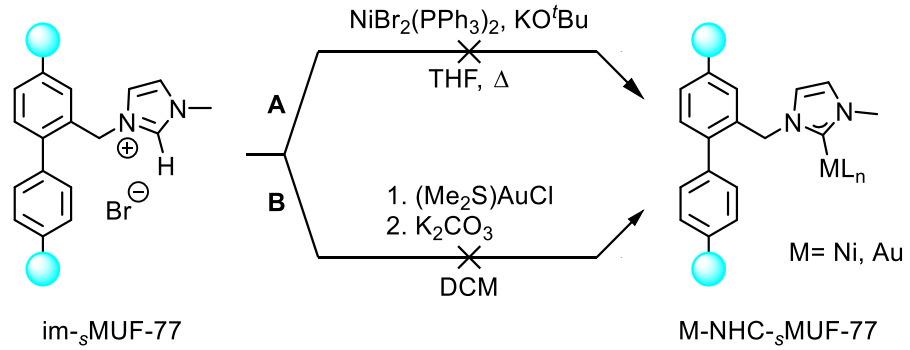

Figure 3-29 Different general synthetic approaches for the post-synthetic metalation of im-$_s$MUF-77.

While we achieved the metalation for the linker itself through transmetalation, the same route was not desirable due to the concerns mentioned earlier about insoluble silver halide salts that might hinder the isolation of the MOF. We thus pursued a protocol reported by Visbal *et al.* that involves the *in situ* formation of a $[NHC–H]^+[AuCl_2]$ and subsequent deprotonation with a mild base (Figure 3-29, route B).[234] Using a mild base was vital for the successful complex formation, as stronger bases led to the decomposition to metallic gold. We observed the formation of the imidazolium salt, $[NHC–H]^+[AuCl_2]$, during the development of the MOF linker synthesis, supporting the viability of our post-synthetic strategy. However, when we exposed im-$_s$MUF-77 to Me_2AuCl we quickly observed the originally colourless MUF-77 crystals turning purple. No precipitate or colouration was observed besides the MOF crystals (Figure 3-30).

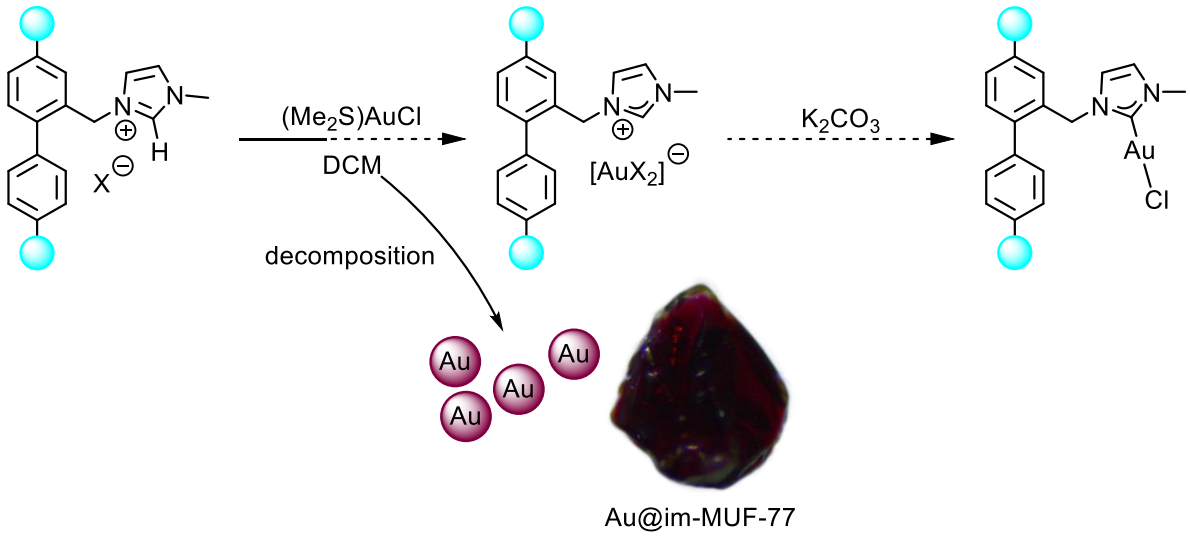

Figure 3-30 Attempted post-synthetic metalation of im-$_s$MUF-77 leading to the formation of gold nanoparticles within the MUF-77 crystal, Au@im-MUF-77.

The formation of gold nanoparticles within the MOF pores was supported by PXRD. Our hypothesis that residual solvent in the MUF-77 pore might have promoted the decomposition was disproved when a control experiment with unfunctionalized parent-MUF-77 under similar conditions did not lead to the unambiguous colour change of the MOF crystals. The challenges synthesising the desired gold complex might stem from the limited steric bulk around the coordination site.

3.2.4.5 Gold Nanoparticles in MUF-77: A Byproduct with Catalytic Potential

While the decomposition to gold nanoparticles during the solvothermal MUF-77 synthesis was problematic in achieving our primary goal of obtaining the ligand-metal-complex within MUF-77, the strict localization of the nanoparticle formation within the MUF-77 crystals woke our interest. The size-control of transition metal nanoparticles is often a main focus and MOF pores were previously used as templates for the synthesis of nanoparticles to limit aggregating and uncontrolled growth.[240] Hu *et al.* reported the formation of a conceptually similar TiO_2@UiO-68 after exposing a NHC-functionalized UiO-68 framework to $Ti(OPri)_4$.[241] The bifunctional catalyst successfully promoted the one-pot Morita–Baylis–Hillman reaction from benzylic alcohols to benzaldehydes. The reaction was initiated by the photocatalytic oxidation of benzyl alcohol through the incorporated TiO_2, while the chiral imidazolium functionalized linker promoted the Morita–Baylis–Hillman reaction. The oxidation of benzyl alcohol was also reported to be promoted by gold nanoparticle-MOF composites.[242,243] The fabrication of such nanoparticles within MOFs can be challenging and often requires additional measures to limit the crystal growth to the MOF pores.[244] To assess our system for its potential for similar applications, we tested the Au@im-MUF-77 crystals for the catalytic oxidation of benzyl alcohol (Figure 3-31).

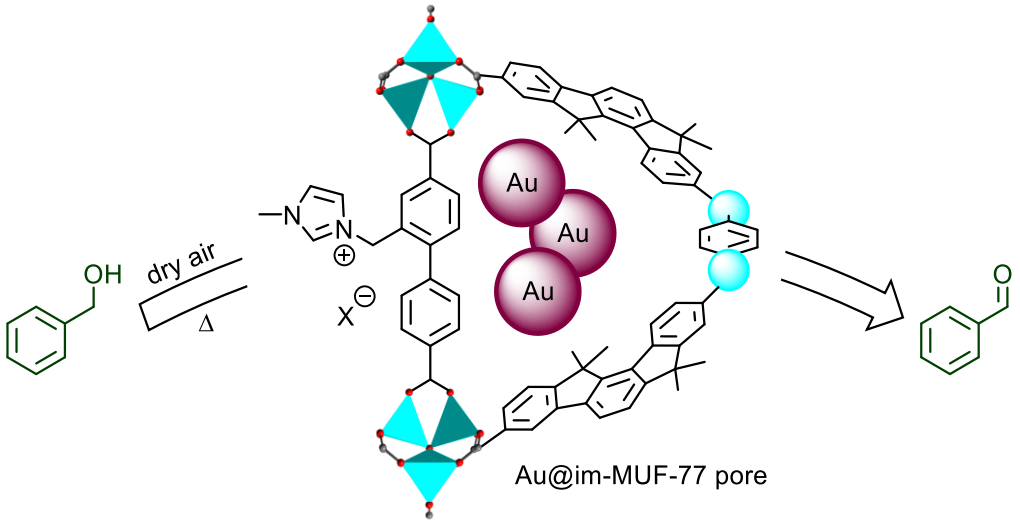

Figure 3-31 Schematic representation of the catalytic oxidation of benzyl alcohol by Au@im-MUF-77.

The MOF crystals were carefully washed with toluene and were kept in toluene during the reaction. Benzyl alcohol was added, and the reaction was heated to 90 °C. The reaction was followed by TLC and product formation was observed after two hours and confirmed by ^{1}H NMR spectroscopy after 24 h. While the preliminary nature of the experiment did not allow for quantification, the successful production of benzaldehyde showed that catalytically active gold nanoparticles were present in the im-$_s$MUF-77 crystals.

The catalytic loading was difficult to estimate without further investigations of the nanoparticle formation, but less than 2 wt.% of im-MUF-77 were used for the Au@im-MUF-77 formation. The catalysis was successful using dried air and no purified oxygen gas was required, further highlighting the catalytic potential of this hybrid material. These preliminary results showed that im-MUF-77 could be exploited in the future to direct nanoparticle growth within the MUF to form catalytically active NP@MUF-77 composites.

3.2.5 Attempted Synthesis of Acyclic Gold(I)-Carbene-Complexes as Catalysts in MUF-77

3.2.5.1 Attempted Synthesis of an Acyclic Gold(I)-Carbene-Functionalized Ligand

Nitrogen acyclic carbene (NAC)-complexes provided an interesting alternative route for us to install a stable transition metal catalyst within MUF-77 as their synthesis does not rely on metalation of an imidazolium-type precursor but shows more resemblance with traditional click-chemistry in organic synthesis. Acyclic gold carbene complexes are accessible through the reaction of primary or secondary amines with a gold(I) isonitrile complex.[231,232,245] Following this procedure, we reacted 2-[(methylamino)methyl)]-functionalized bpdc ester with the isonitrile complex in dichloromethane at room temperature to form the respective AuNAC-functionalized bpdc ester (**8**) (Figure 3-32). The complex (**8**) was obtained by combining the 2-((methylamino)methyl)-bpdc methyl ester with *tert*-butylisocyanogold(I) chloride in dichloromethane at room temperature. The product was isolated by preparative thin-layer chromatography and characterized by ^{1}H NMR and ^{13}C NMR spectroscopy. The gold(I)-NAC coordination was most prominently depicted by a characteristic ^{13}C NMR peak at 193.1 ppm which was in good agreement with literature values for similar compounds.[231] While we successfully obtained the desired Au(I)-NAC compound, the subsequent hydrolysis to form the final MUF-77 linker (**9**) led to the decomposition of the complex and the formation of the urea-type decomposition product (**10**). The decomposition of the gold(I) complex during basic hydrolysis has been seen previously for NHC-bpdc compounds. The limited stability under those conditions raised concerns that this system would also lack stability during the basic MUF-77 synthesis procedure, even if the gold(I) functionalized linker was successfully isolated.

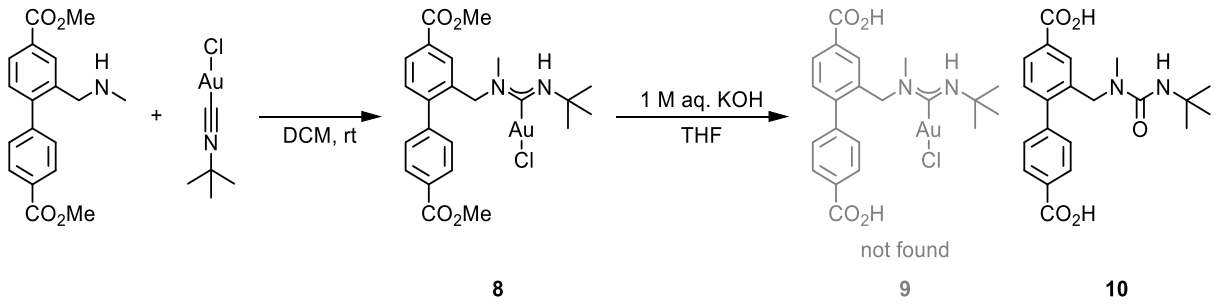

Figure 3-32 Attempted synthesis of an NAC-bpdc ligand for the incorporation into MUF-77. The gold(I) complex was successfully synthesized but suffered from decomposition during hydrolysis to obtain the final MUF-77 linker.

3.2.5.2 Synthesis of Amino-Functionalized MUF-77 as Precursors

To limit the exposure of the gold(I) complex to basic conditions we attempted to install it through post-synthetic modification of a suitable amino-functionalized MUF-77 system (Figure 3-33). We targeted two systems: 2-((methylamino)methyl)-bpdc (mam) and azepine-bpdc (az).

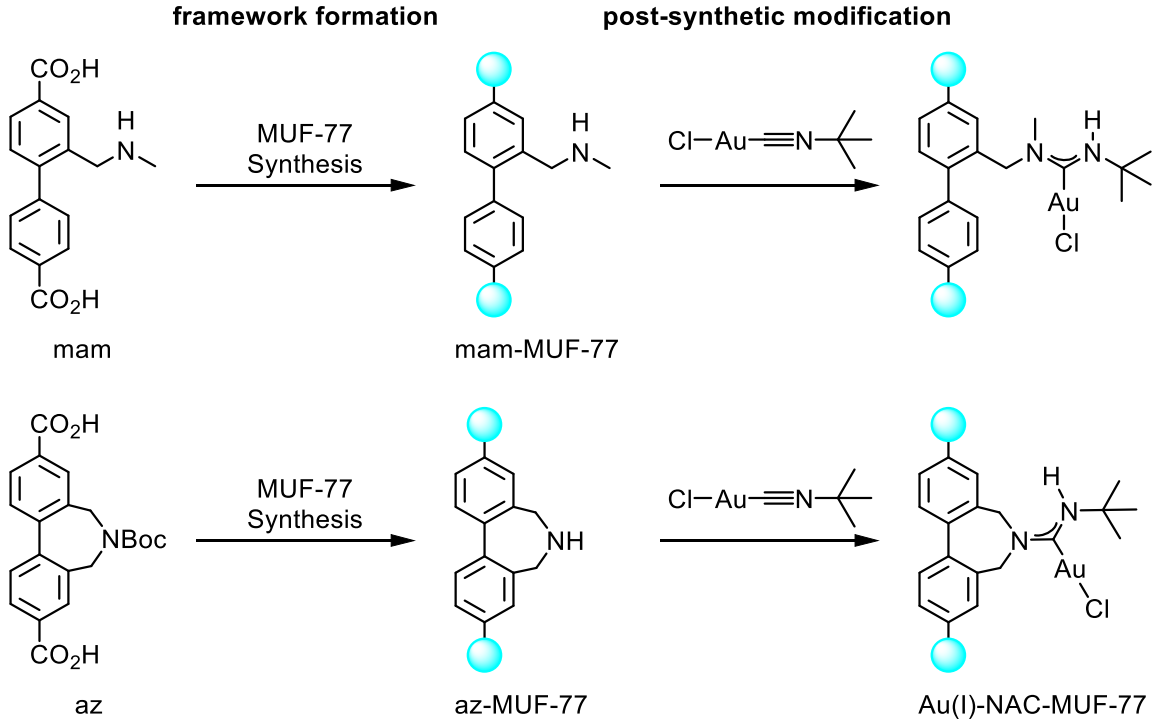

Figure 3-33 General synthetic routes to amino-functionalized MUF-77 for the post-synthetic reaction with a gold(I) isonitrile to form an Au(I)-NAC complex within the MUF-77 pore.

While the solvothermal synthesis with hmtt, 2-((methylamino)methyl)-bpdc and bdc yielded the typical MUF-77 crystals, ^{1}H NMR analysis of the digested sample indicated the undesired reaction of the amine sidechain under solvothermal MOF synthesis conditions (Figure 3-34). The potential of DMF to act as a reagent is well-documented[246] and we observed the side reaction on several occasions when amine-functionalized ligands were exposed to the dialkyl formamide solvents at elevated temperatures.

Our room-temperature protocol, which requires milder conditions and yields nano-sized crystals, successfully yielded the respective MUF-77 framework, mam-*rt*MUF-77, without any noticeable alteration of the bpdc linker. The crystalline material quickly formed after combining solutions of ligand and zinc acetate at room temperature in DMF.

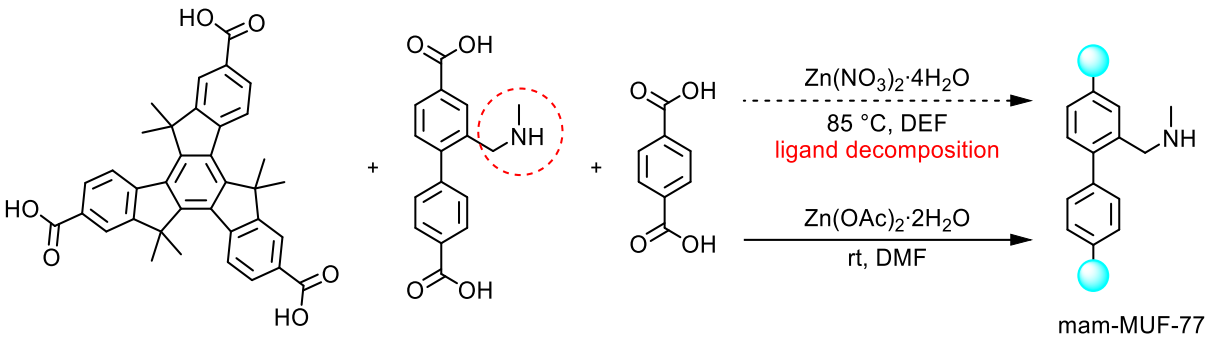

Figure 3-34 Synthesis of mam-MUF-77. Ligand decomposition was observed during solvothermal synthesis. A milder, room-temperature synthesis approach led to successful formation of the respective MUF-77.

PXRD analysis confirmed the successful MUF-77 formation (Figure 3-35). ^{1}H NMR spectroscopy of the digested MOF supported product formation without noticeable side-reaction involving the 2-((methylamino)methyl)-bpdc linker. The ligand ratios matched the expected ratios $hmtt_{1.33}$|mam-$bpdc_{0.5}$|$bdc_{0.5}$ for mam-MUF-77 with the formula $[Zn_4O(hmtt)_{4/3}((mam\text{-}bpdc)_{1/2}(bdc)_{1/2}$.

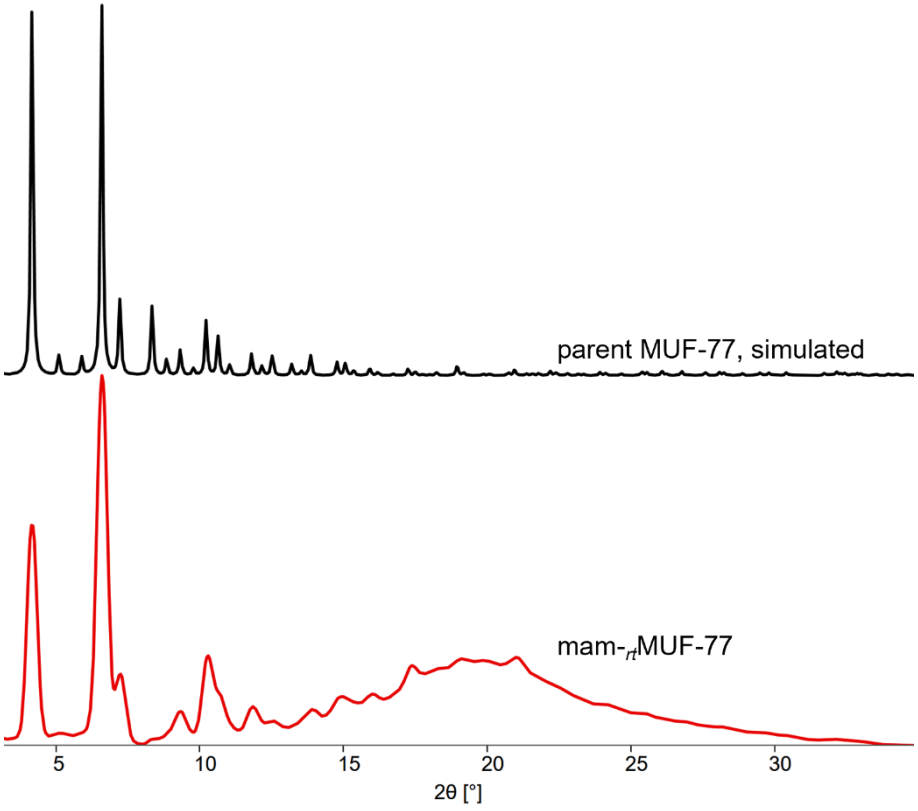

Figure 3-35 PXRD pattern of mam-$_{rt}$MUF-77 (bottom, red) in comparison with the simulated pattern for MUF-77 (top, black).

For the successful incorporation of azepine-bpdc into MUF-77 through solvothermal synthesis we protected the amine functionality with a *tert*-butyloxycarbonyl (Boc) group. The thermolability of the protecting group was previously exploited by our group for the incorporation of amine-functionalized linker into MUF-77 where a direct synthesis approach failed.[61,143] After successful MUF-77 synthesis, deprotection of the Boc-protected amine functionalities at elevated temperatures was well tolerated by MUF-77. The ligand

was synthesized from 2,2'-di(bromomethyl)bpdc methyl ester (**11**). The reaction with allylamine led to the formation of the azepine-type N-heterocycle functionalized bpdc ester (**12**). Different attempts to form the desired Boc-protected azepine-type bpdc ester (**14**) directly were not successful. Upon deallylation with a Pd(0) catalyst in the presence of 1,3-dimethylbarbituric acid as allyl group scavenger the desired azepine bpdc ester (**13**). The Boc protection group was introduced through reaction with di-tert-butyl dicarbonate (Boc_2O) in *tert*-butanol. Hydrolysis of methyl esters yielded the final MUF-77 ligand, bocaz-bpdc (Figure 3-36).

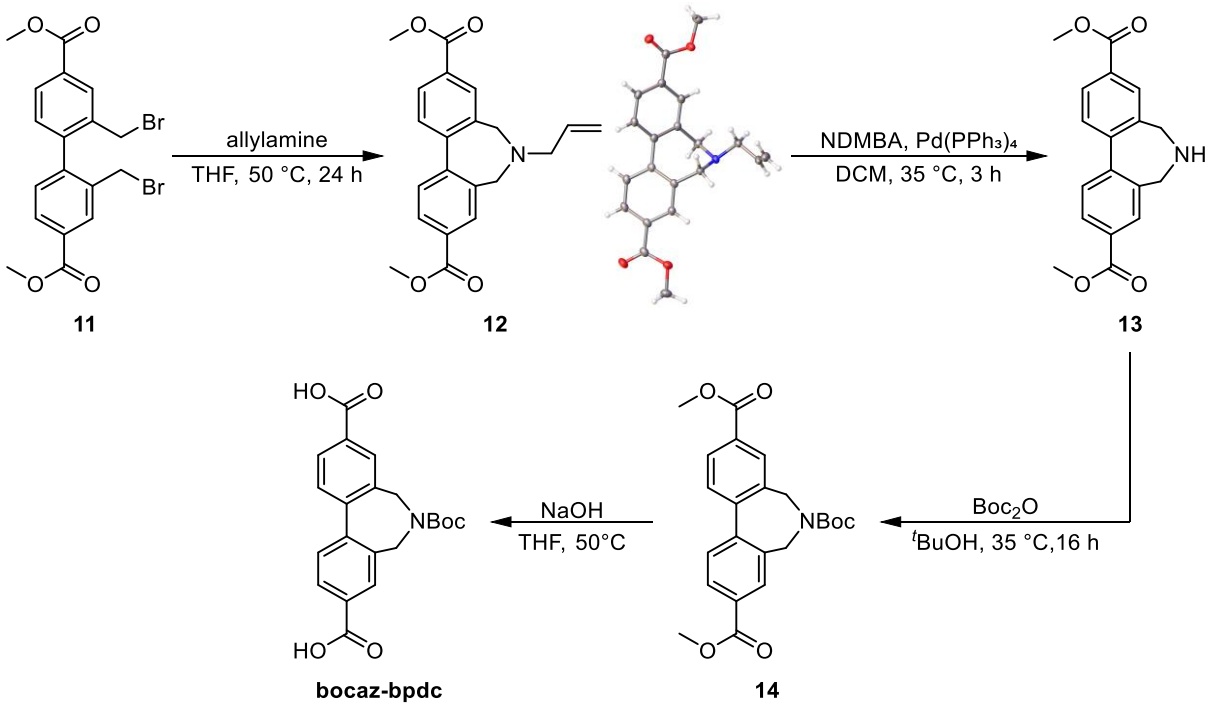

Figure 3-36 Synthesis of bocaz-bpdc.

With the ligand in hand, az-$_s$MUF-77 was synthesized following the solvothermal synthesis protocol. Hmtt, bocaz-bpdc, and bdc were combined with zinc nitrate tetrahydrate and benzoic acid as crystal growth modulator in diethyl formamide and water. The reaction was heated in an isothermal oven for 24 h. The obtained crystals were washed with dimethyl formamide and dichloromethane before the deprotection was conducted (Figure 3-37).

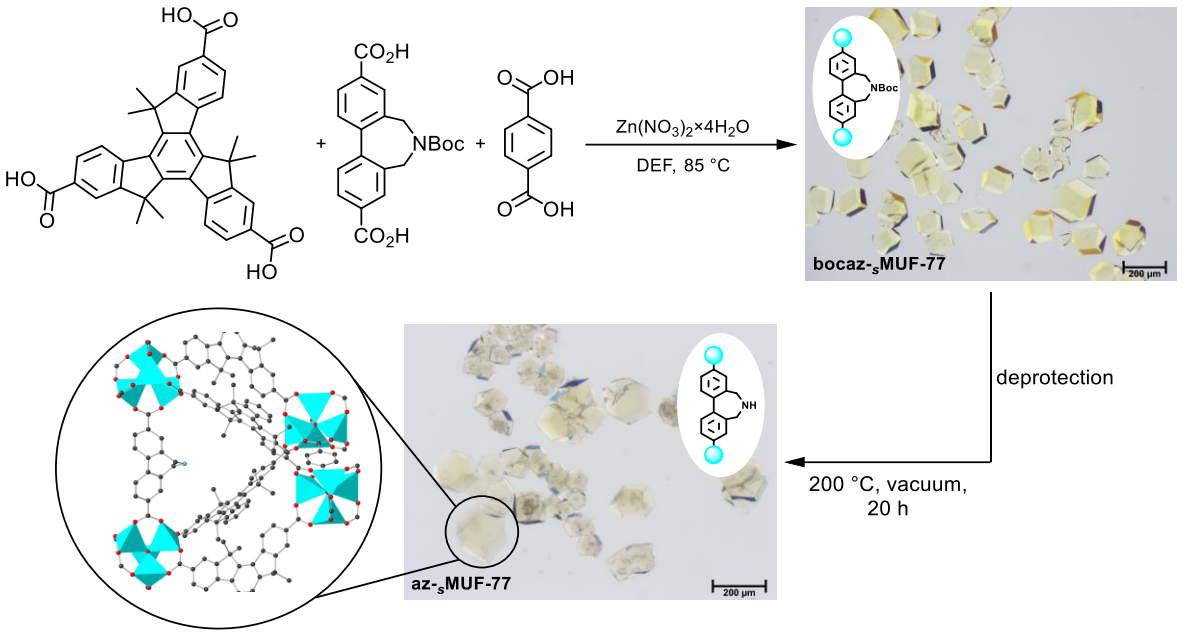

Figure 3-37 Synthesis of az-$_s$MUF-77.

For the deprotection, a reported methodology was adapted.[61,143] The Boc-protected az-$_s$MUF-77 was activated using the outgasser function at the activation port at 200 °C for 20 h. Time and temperature required for a successful deprotection were established by TGA experiments (Figure 3-38). Under TGA conditions, first indications of weight loss attributed to the removal of the Boc-protection group were observed around 190 °C. The onset of MUF-77 decomposition was around 380 °C. Holding the sample at 200 °C the deprotection was complete around 13 h.

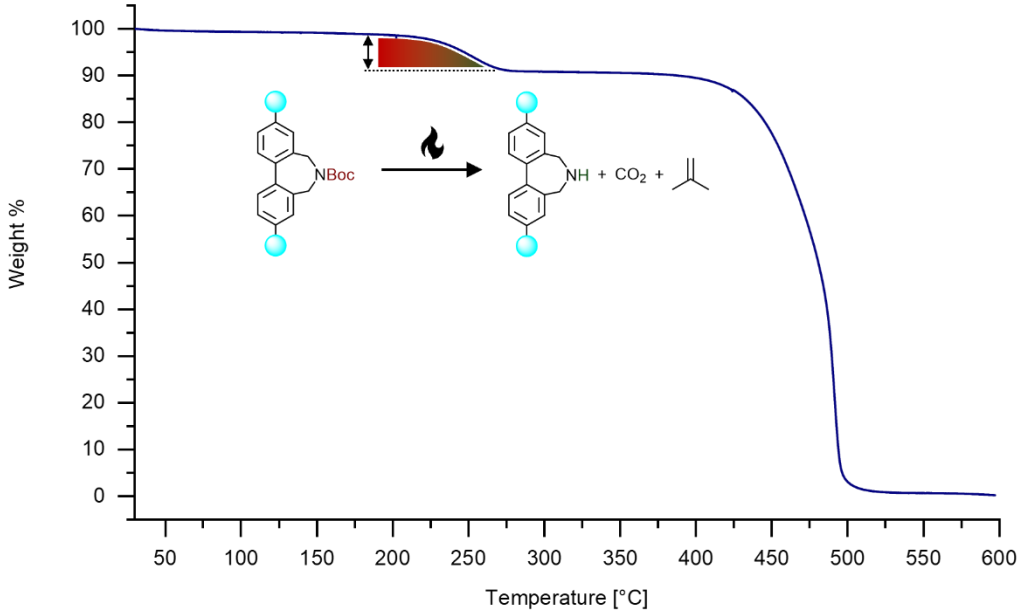

Figure 3-38 Thermogravimetric analysis of Boc-protected az-$_s$MUF-77 to establish the required deprotection parameters. The data was collected with a ramp rate of 5.00 °C/min of a carefully desolvated sample.

The successful conservation and deprotection of the amino functionality were confirmed by ^{1}H NMR spectroscopy (Figure 3-39). The ligand ratios were in good agreement with the the expected ratios

hmtt$_{1.33}$|az-bpdc$_{0.5}$|bdc$_{0.5}$ for az-$_s$MUF-77 with the formula [Zn$_4$O(hmtt)$_{4/3}$((az-bpdc)$_{1/2}$(bdc)$_{1/2}$]. The successful removal of the Boc-protection group in az-$_s$MUF-77 was shown by the absence of the characteristic signal around 1.50 ppm, corresponding to the Boc-group.

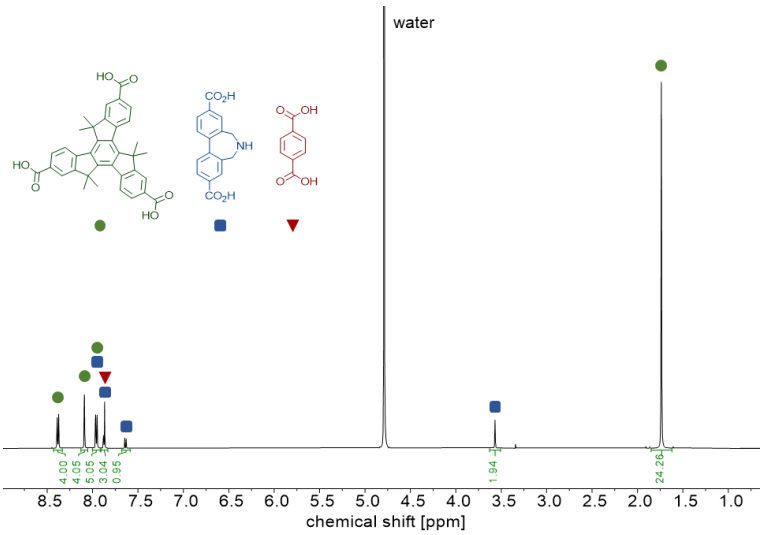

Figure 3-39 ^{1}H NMR spectrum of az-$_s$MUF-77 upon deprotection. The sample was collected upon digestion in 0.1 M NaOD.

PXRD supported the successful formation of az-MUF-77, and that crystallinity was retained throughout the deprotection procedure (Figure 3-40).

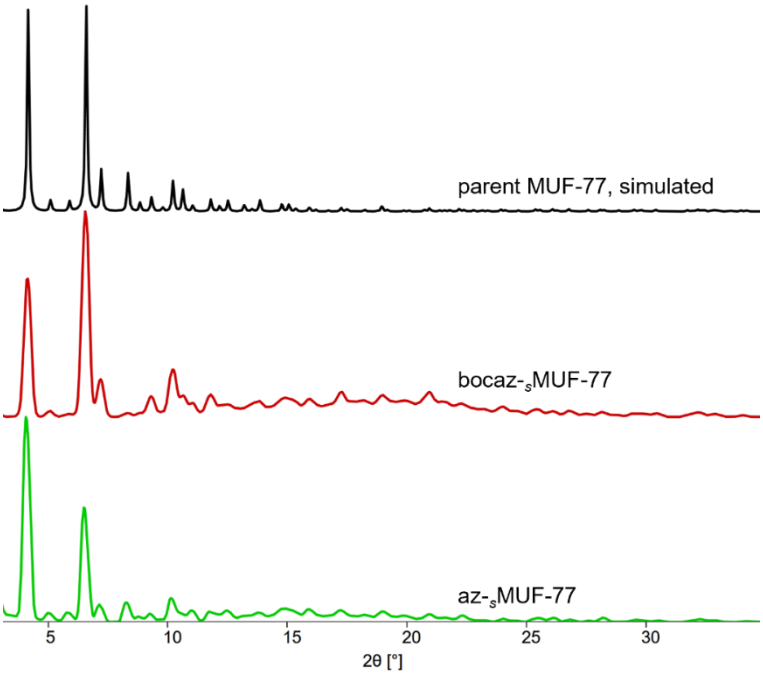

Figure 3-40 Simulated PXRD pattern of parent MUF-77 (top, black) and experimental PXRD pattern of bocaz-$_s$MUF-77 (middle, red) and az-$_s$MUF-77 (bottom, green).

3.2.5.3 Attempted Post-Synthetic-Synthesis of an Acyclic Gold Carbene-MUF-77

Following the procedure for the single molecule Au(I)NAC ligand synthesis, we exposed the amine-functionalized MUF-77 frameworks mam-$_{rt}$MUF-77 and az-$_s$MUF-77 to the gold(I) nitrile complex at room

temperature (Figure 3-41). No reaction was observed even with the addition of excess reagent. Gentle heating to 40 °C did not promote the reaction but led to the decomposition of the reagents indicated by the precipitation of metallic gold.

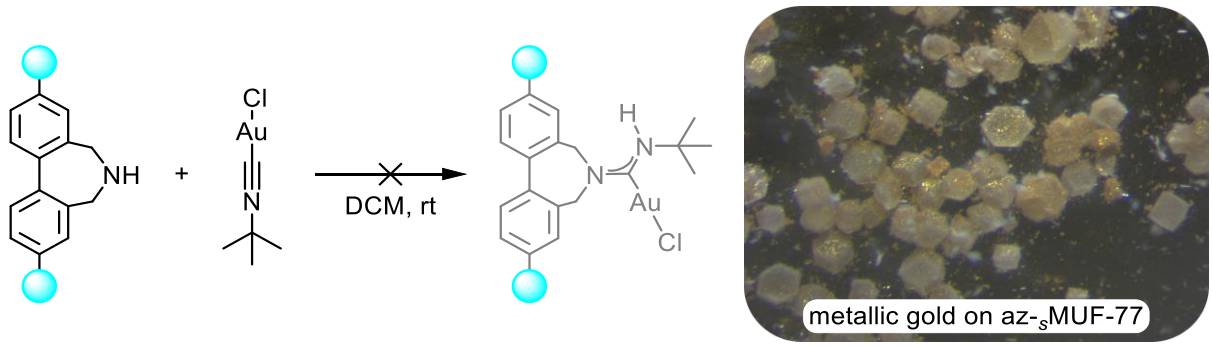

Figure 3-41 Attempted post-synthetic modification of amine-functionalized MUF-77 with a gold(I) nitrile complex. The example of az-$_s$MUF-77 is shown. No reaction was observed but the precipitation of elemental gold indicated the decomposition of reagent upon gentle heating.

The ^{1}H NMR spectrum of the digested samples showed hmtt, bdc, and unaltered mam/az-bpdc, indicating that the post-synthetic modification of the framework was not successful. SXRD data of the crystals also showed no signs of a successful post-synthetic modification.

3.3 Conclusion

We reported the successful incorporation of phosphine-, phosphoramidite- and NHC-functionalized linkers into the MUF-77 framework. Those ligands are prominently featured in traditional, homogeneous transition metal catalysis. The integration of bipyridine linkers into MUF-77 was not successful. Integration of metalated ligands directly or through post-synthetic metalation upon MUF-77 synthesis faced several challenges due to the partially limited stability of the metal complexes. Milder MUF-77 synthesis conditions were often necessary to stabilize the MOF linker and transition metal complexes. We focused our ligand design on smaller functionalities to limit steric stress within the MUF-77 pore, however, that likely led to insufficient stabilization of the transition metal complexes. Homogeneous gold(I)-NAC complexes suffered from limited stability and post-synthetic modification of amine-functionalized MUF-77 was unsuccessful. Gold(I) phosphine and -NHC complexes were successfully introduced into MUF-77 but showed limited stability. Gold nanoparticles crafted within MUF-77 during the attempted incorporation of a gold(I)-NHC linker showed promising catalytic activity. While further characterization of the nanoparticle-MOF hybrid is necessary, those findings are promising for the development of size-controlled nanoparticles and the potential to influence the catalytic properties through the MUF-77 environment. Future experiments are necessary to improve ligand design to stabilize the metal complexes while maintaining a footprint suitable for incorporation into MUF-77. Transition metal-functionalized MUF-77 materials remain very promising candidates for evaluating their catalytic potential and the influence of the MUF-77 environment on the catalytic performance.

3.4 Experimental

3.4.1 General Procedures

All starting materials and solvents were used as received from commercial sources without further purification unless otherwise noted. Triethylamine was purified by distillation prior to usage. Sensitive reactions were carried out under an inert atmosphere in glassware that was heated under vacuum prior to usage. Where this was not suitable, glassware was oven-dried prior to use. Solvents were degassed prior to usage by at least 10 cycles of sonication under half vacuum and under an inert atmosphere. Reactions including sensitive reagents were carried protected from light exposure. High-resolution mass spectrometry was performed using a ThermoScientific Q Exactive Focus Hybrid Quadrupole-Orbitrap Mass Spectrometer.

3.4.2 NMR Spectroscopy

Crystals in high-boiling point solvents were washed with acetone or DCM (5x) and dried under vacuum. Desolvated crystals were dissolved using the denotated reagents. For the digestion in DMSO-d_6/DCl the following protocol was followed: 23 µL of a 35% DCl solution in D_2O was mixed with 1 mL of DMSO-d_6 to give a DCl/DMSO-d_6 stock solution. The sample was digested in 150 µL of this stock solution together with 450 µL of DMSO-d_6. Spectra were acquired immediately following dissolution. NMR spectra were recorded at room temperature on Bruker-400, Bruker-500 and Bruker-700 Avance instruments, with the use of the solvent proton as an internal standard.

3.4.3 X-ray Crystallography

All powder X-ray diffraction measurements were carried out on either a Rigaku Spider or Bruker D8 Venture instrument. Rigaku Spider X-ray diffractometer is equipped with CuKα radiation (Rigaku MM007 microfocus rotating-anode generator), monochromated and focused with high-flux Osmic multilayer mirror optics and a curved image plate detector. Bruker D8 Venture diffractometer is equipped with CuKα radiation with a diamond microfocus X-ray source and a Photon III 28 detector. The two-dimensional images of the Debye rings were integrated with 2DP or Diffract Eva to give 2θ vs I diffractograms. Predicted powder patterns were generated from single-crystal structures using Mercury. Samples were mounted using Fomblin® Y oil or dialkyl formamide solvents.

All single-crystal X-ray diffraction measurements were carried out on Bruker D8 Venture, and the measurement temperature was controlled using Oxford Cryostream if required. Bruker APEX 3 was used to collect and process data, and the structure was solved and refined using the Shelx package[168,169] under Olex2[170]

Table 3-1 Summary of X-ray crystallography data for PPh_2-*s*MUF-77, PEt_2-*s*MUF-77 and $(Me_2N)PO_2$-*s*MUF-77.

Name	PPh_2-*s*MUF-77[a]	PEt_2-*s*MUF-77	$(Me_2N)PO_2$-*s*MUF-77[b]
Empirical formula	$C_{59}H_{40}O_{13}P_{0.5}Zn_4$	$C_{61}H_{45}O_{13}P_{0.5}Zn_4$	$C_{59}H_{42}N_{0.5}O_{14}P_{0.5}Zn_4$
Formula weight	1233.87	1262.93	1258.89
Temperature/K	101	293	293
Crystal system	cubic	cubic	cubic
Space group	Pm-3	Pm-3	Pm-3
a/Å	29.9306(11)	30.0017(3)	29.9790(15)
b/Å	29.9306(11)	30.0017(3)	29.9790(15)
c/Å	29.9306(11)	30.0017(3)	29.9790(15)
α/°	90	90	90
β/°	90	90	90
γ/°	90	90	90
Volume/Å^3	26813(3)	27004.6(8)	26943(4)
Z	6	6	6
ρ_{calc}g/cm^3	0.458	0.466	0.466
μ/mm^{-1}	0.814	0.812	0.819
F(000)	3753	3855	3834
Crystal size/mm^3	0.3 × 0.3 × 0.3	0.3 × 0.3 × 0.3	0.5 × 0.5 × 0.5
Radiation	CuKα (λ = 1.54178)	CuKα (λ = 1.54178)	CuKα (λ = 1.54178)
2Θ range for data collection/°	4.174 to 152.45	4.164 to 144.13	4.168 to 152.516
Index ranges	-37 ≤ h ≤ 32 -36 ≤ k ≤ 30 -35 ≤ l ≤ 34	-24 ≤ h ≤ 31 -32 ≤ k ≤ 35 -37 ≤ l ≤ 26	-36 ≤ h ≤ 34 -32 ≤ k ≤ 24 -20 ≤ l ≤ 36
Reflections collected	236080	116507	68752
Independent reflections	9859 [R_{int} = 0.0445 R_{sigma} = 0.0162]	9391 [R_{int} = 0.0680 R_{sigma} = 0.0478]	9820 [R_{int} = 0.0470 R_{sigma} = 0.0193]
Data/restraints/ parameters	9859/0/ 202	9391/76/ 225	9820/7/ 224
Goodness-of-fit on F^2	2.17	1.387	1.099
Final R indexes [I>=2σ (I)]	R_1 = 0.1304 wR_2 = 0.4184	R_1 = 0.1418 wR_2 = 0.3800	R_1 = 0.0528 wR_2 = 0.1558
Final R indexes [all data]	R_1 = 0.1375 wR_2 = 0.4298	R_1 = 0.1856 wR_2 = 0.4110	R_1 = 0.0564 wR_2 = 0.1601
Largest diff. peak/hole / e Å^{-3}	3.03/-1.1	0.85/-0.76	1.03/-0.48

a) Phosphine-appended phenyl moieties could not be modelled.
b) A solvent mask was used. Nitrogen-appended methyl groups could not be modelled.

Table 3-2 Summary of X-ray crystallography data for bocaz-MUF-77 and az-MUF-77.

Name	bocaz-MUF-77*	az-MUF-77
Empirical formula	$C_{60}H_{40}N_{0.5}O_{13}Zn_4$	$C_{60}H_{42}N_{0.5}O_{13}Zn_4$
Formula weight	1237.4	1239.42
Temperature/K	101	101
Crystal system	cubic	cubic
Space group	Pm-3	Pm-3
a/Å	29.8772(5)	30.0226(6)
b/Å	29.8772(5)	30.0226(6)
c/Å	29.8772(5)	30.0226(6)
α/°	90	90
β/°	90	90
γ/°	90	90
Volume/Å^3	26669.8(13)	27061.1(16)
Z	6	6
ρ_{calc}g/cm^3	0.462	0.456
μ/mm^{-1}	0.779	0.768
F(000)	3765	3777
Crystal size/mm^3	0.5 × 0.4 × 0.4	0.4 × 0.4 × 0.4
Radiation	CuKα (λ = 1.54178)	CuKα (λ = 1.54178)
2Θ range for data collection/°	4.182 to 152.628	4.162 to 152.328
Index ranges	-35 ≤ h ≤ 16 -31 ≤ k ≤ 28 -36 ≤ l ≤ 35	-35 ≤ h ≤ 17 -34 ≤ k ≤ 37 -24 ≤ l ≤ 36
Reflections collected	69565	71422
Independent reflections	9785 [R_{int} = 0.0393, R_{sigma} = 0.0218]	9915 [R_{int} = 0.0296, R_{sigma} = 0.0130]
Data/restraints/ parameters	9785/0/ 214	9915/0/ 214
Goodness-of-fit on F^2	1.133	2.179
Final R indexes [I>=2σ (I)]	R_1 = 0.0723, wR_2 = 0.2320	R_1 = 0.1112, wR_2 = 0.4189
Final R indexes [all data]	R_1 = 0.0753, wR_2 = 0.2363	R_1 = 0.1119, wR_2 = 0.4202
Largest diff. peak/hole / e Å^{-3}	1.28/-1.03	4.03/-0.78

*Boc groups could not be modelled.

3.4.4 Phosphines

PPh_2-*s*MUF-77 An oven-dried and argon-purged 4.5 mL vial was charged with hmtt (2.2 mg, 3.9 µmol, 1.0 eq), PPh_2-bdc (1.9 mg, 5.4 µmol, 1.4 eq), bpdc (1.3 mg, 5.4 µmol, 1.4 eq), $Zn(NO_3)_2{\cdot}4H_2O$ (16.8 mg, 64.3 µmol, 16.4 eq) and benzoic acid (7.6 mg, 62 µmol, 15.8 eq). Degassed DEF (1 mL) and water (50 µL) were added, and the vial was purged with argon. The suspension was sonicated for 10 minutes and was placed in an 85 °C isothermal oven for 48 h. The hot solvent was replaced with fresh, degassed DMF (5x).

Alternatively, the reaction vessel was heated in a metal heating block with an argon-filled balloon attached for 24 h to yield MUF-77 crystals.

For solvent removal, the crystals were washed with degassed, anhydrous DCM (5x) before the crystals were dried under vacuum. The crystals were activated at 80 °C for 2h at a ramping rate of 1 °C/min using the outgasser function at the activation port.

PEt_2-*s*MUF-77 An oven-dried and argon-purged 4.5 mL vial was charged with hmtt (1.9 mg, 3.4 µmol, 1.0 eq), PEt_2-bdc·HCl (2.2 mg, 7.6 µmol, 2.2 eq), bpdc (1.4 mg, 5.8 µmol, 1.7 eq), $Zn(NO_3)_2{\cdot}4H_2O$ (17.1 mg, 65.4 µmol, 19.2 eq) and benzoic acid (8.6 mg, 62 µmol, 18.3 eq). Triethylamine was added where noted. Degassed DEF (1 mL) and water (50 µL) were added, and the vial was purged with argon. The suspension was sonicated for five minutes and was placed in an 85 °C isothermal oven for 48 h. The hot solvent was replaced with fresh, degassed DMF (5x). The MUF-77 phase was isolated by hand from additional phases.

PPh_2-*rt*MUF-77 In a standard experiment an oven-dried, argon-purged 4.5 mL vial was charged with hmtt (12.0 mg, 21.5 µmol, 2.6 eq), PPh_2-bdc (2.9 mg, 8.3 µmol, 1.0 eq) and bpdc (2.0 mg, 8.3 µmol, 1.0 eq). The ligands were dissolved in degassed DMF (1 mL). A solution of $Zn(OAc)_2{\cdot}2H_2O$ (18.1 mg, 82.5 µmol, 10 eq) in degassed DMF was prepared in an oven-dried, argon-purged 1.5 mL vial. With a syringe, the $Zn(OAc)_2{\cdot}2H_2O$ solution was quickly added to the ligand solution while stirring under a stream of argon. Immediate precipitation of a solid was observed. The reaction was stirred for 30 min. The suspension was transferred to a 1.5 mL Eppendorf vial and centrifuged. The solvent was decanted and replaced with fresh degassed DMF. The washing process was repeated three times.

AuPPh_2-*rt*MUF-77 Freshly synthesized PPh_2-*rt*MUF-77 was washed with DCM (5x). The sample was transferred to a 4.5 mL vial protected from light. $(Me_2S)AuCl$ (3.2 mg) was dissolved in DCM (1 mL) and protected from light. The gold precursor solution was quickly added to the MOF-suspension and the reaction mixture was allowed to stand undisturbed at room temperature overnight. The mother liquor was replaced with fresh DCM (3x) and the solid was allowed to soak overnight. The solvent was then replenished twice.

3.4.5 Phosphoramidites

3.4.5.1 Ligand Synthesis

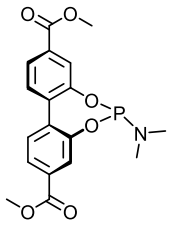

1

Under argon, tris(dimethylamino)phosphine (150 µL, 0.993 mmol, 3 eq.) was dissolved in anhydrous toluene (1 mL). While stirring, $(OH)_2$-bpdc dimethyl ester (99.6 mg, 0.330 mmol, 1 eq.) suspended in anhydrous toluene (4 mL) was added. The solid quickly dissolved after addition to the reaction mixture. The solution was set to reflux for 17 h. The brown suspension was allowed to cool to room temperature and the solvent was removed under vacuum. The brown solid was extracted with EtOAc and purified by column chromatography over silica with EtOAc:*n*-hexane 1:4 as eluent.

^{1}H NMR (500 MHz, $CDCl_3$) δ 7.89 (dd, *J* = 8.0, 1.7 Hz, 2H), 7.83 (s, 2H), 7.51 (d, *J* = 8.0 Hz, 2H), 2.64 (d, *J* = 9.1 Hz, 6H). ^{31}P NMR (202 MHz, $CDCl_3$) δ 149.90.

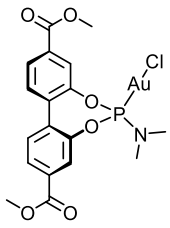

2

Under argon, an oven-dried 4 mL vial charged with Me_2SAuCl (27.2 mg, 0.0923 mmol, 1 eq.) was dissolved in anhydrous DCM (1 mL). The solution was cooled to 0 °C and a solution of the phosphoramidite bpdc ester (**1**) (35.0 mg 0.0906 mmol, 1 eq.) in DCM (1 mL) was added while stirring. The vial was rinsed with DCM (1 mL) and the solution was allowed to warm to room temperature and stirring was continued for 2 h. The solvent was removed under vacuum to give the product as a white solid.

^{1}H NMR (500 MHz, $CDCl_3$) δ 8.07 (d, *J* = 8.0 Hz, 2H), 7.93 (s, 2H), 7.64 (d, *J* = 8.0 Hz, 2H), 3.98 (s, 6H), 2.90 (d, *J* = 12.1 Hz, 6H). ^{31}P NMR (202 MHz, $CDCl_3$) δ 129.12.

3.4.5.2 MOF Synthesis

$(OH)_2$-MUF-77 A 4.5 mL vial was charged with hmtt (2.2 mg, 3.9 µmol, 1.0 eq), bdc (1.3 mg, 7.8 µmol, 2.0 eq), and $(OH)_2$-bpdc (1.4 mg, 5.1 µmol, 1.3 eq). The ligands were suspended in DEF (0.7 mL) and water (50 µL). A 0.631 M solution of $Zn(NO_3)_2{\cdot}4H_2O$ (100 µL, 63.1 µmol, 16.0 eq) in DEF and a 0.819 M solution of benzoic acid (80 µL, 66 µmol, 16.6 eq) in DEF were added. The suspension was sonicated for 10 minutes and was placed in an 85 °C isothermal oven for 24 h. The hot solvent was replaced with fresh, degassed DMF (5x).

$(Me_2N)PO_2$-MUF-77 In a 4.5 mL vial $(OH)_2$-MUF-77 crystals were washed with anhydrous toluene (5x). The solvent was decanted and replenished with fresh anhydrous toluene (1 mL). Under argon, tris(dimethylamino)phosphine (100 µL) was added, and the reaction was heated to 85 °C for 24 h. The solvent was replaced with anhydrous toluene (5x) over several hours.

3.4.6 N-Heterocyclic Carbenes

3.4.6.1 Ligand Synthesis

The NHC functionalized bpdc ligand was synthesized according to a reported procedure.[247]

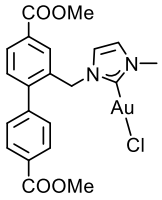

6

Under argon, im-bpdc (100 mg, 0.225 mmol, 1 eq.) and Ag_2O (31.7 mg, 0.137 mmol, 0.6 eq.) were suspended in anhydrous DCM (3 mL) and stirred for 4 h protected from light at room temperature. Solids were filtered off and $(Me_2S)AuCl$ (81.7 mg, 0.277 mmol, 1.2 eq.) was added. The reaction was stirred for 16 h at room temperature. The suspension was filtered over celite. The solvent was removed under vacuum to yield the product as an off-white solid (125.4 mg, 0.185 mmol, 82 %)

^{1}H NMR (500 MHz, $CDCl_3$) δ 8.14 (d, *J* = 8.3 Hz, 2H), 8.08 (dd, *J* = 8.0, 1.7 Hz, 1H), 7.90 (s, 1H), 7.39 (d, *J* = 8.0 Hz, 1H), 7.36 (d, *J* = 8.7 Hz, 1H), 6.86 (d, *J* = 1.9 Hz, 1H), 6.57 (d, *J* = 2.0 Hz, 1H), 5.36 (s, 2H), 3.95 (d, *J* = 12.9 Hz, 6H), 3.78 (s, 3H).

ESI (positive mode, MeOH): m/z = 619.0670 ($C_{21}H_{20}AuClN_2O_4$ + Na^+), calculated 619.0669.

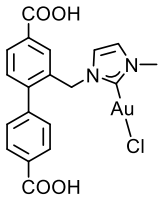

7

The AuNHC-bpdc methyl ester (**6**) (30.2 mg, 0.0506 mmol) was dissolved in a mixture of THF (1 mL). 1 M NaOH (1 mL) was added, and the reaction was stirred for 16 h. The dark suspension was filtered over celite. THF was removed under reduced pressure and the remaining aqueous phase was acidified with dil. aq. HCl to pH = 5. The solid was collected by centrifugation and washed with water (2x 0.5 mL). The dark purple solid was suspended in acetone (4 mL) and filtered through celite. The solvent was removed under vacuum to yield the product as a yellow solid.

^{1}H NMR (400 MHz, DMSO) δ 13.09 (s, 2H), 8.02 (d, *J* = 7.8 Hz, 2H), 7.97 (d, *J* = 7.8 Hz, 1H), 7.65 (s, 1H), 7.52 (d, *J* = 7.9 Hz, 2H), 7.43 (dd, *J* = 4.9, 3.0 Hz, 2H), 7.27 (d, *J* = 2.1 Hz, 1H), 5.34 (s, 2H), 3.71 (s, 3H).

ESI (negative mode, MeOH): m/z = 567.0390 ($C_{19}H_{15}AuClN_2O_4^-$), calculated 567.0380.

3.4.6.2 MOF Synthesis

im-*s*MUF-77 A 4.5 mL vial was charged with hmtt (2.2 mg, 3.9 µmol, 1.0 eq), bdc (1.3 mg, 7.8 µmol, 2.0 eq), im-bpdc (2.1 mg, 5.0 µmol, 1.3 eq), $Zn(NO_3)_2{\cdot}4H_2O$ (16.5 mg, 63.1 µmol, 16.2 eq) and benzoic acid (8.0 mg, 65.5 µmol, 16.8 eq.) as crystal growth modulator were added. The ligands were suspended in DEF (1 mL) and water (50 µL). The suspension was sonicated for 5 minutes and was placed in an 85 °C isothermal oven for 21 h. The hot solvent was replaced with fresh DMF (5x).

AuNHC-*rt*MUF-77 A 4.5 mL vial was charged with hmtt (12.0 mg, 21.5 µmol, 2.6 eq), bdc (1.4 mg, 8.4 µmol, 1.0 eq) and AuNHC-bpdc (4.9 mg, 8.6 µmol, 1.0 eq). The ligands were dissolved in DMF (1.5 mL). A solution of $Zn(OAc)_2{\cdot}2H_2O$ (18.0 mg, 82.0 µmol, 9.7 eq) in DMF was added to the ligand solution while stirring. Immediate precipitation of a solid was observed. The reaction was stirred for 45 min. The suspension was transferred to a 1.5 mL Eppendorf vial and centrifuged. The solvent was decanted and replaced with fresh degassed DMF. The washing process was repeated four times.

Au@NHC-MUF-77 A 4.5 mL vial, im-$_s$MUF-77 crystals were washed with anhydrous DCM (5x). Under argon, (Me_2S)AuCl (1.5 mg) in DCM was added. The reaction was kept undisturbed for 3 h at room temperature. The purple crystals were washed with fresh DCM (7x) over several hours and again after 24 h.

A control reaction with parent MUF-77 was conducted under similar conditions.

3.4.6.3 Catalysis

For catalysis, Au@NHC-MUF-77 crystals were washed with anhydrous toluene (5x) and transferred to a Schlenk tube. The solvent was decanted and fresh anhydrous toluene (2 mL) and benzyl alcohol (104 µL, 1 mmol, purified prior *via* column chromatography to remove possible benzaldehyde) were added. Air was passed through a column of $CaCl_2$ and continuously bubbled through the solution. The reaction was heated to 90 °C. TLC indicated product formation after 1.5 h. ^{1}H NMR spectra of the reaction were recorded after 24 h.

3.4.7 Nitrogen Acyclic Carbenes

Chloro(tetrahydrothiophene)gold(I) and *tert*-butylilisocyanogold(I) chloride were synthesized according to literature procedures.[231,248] $CDCl_3$ for NMR sample preparation was stored over activated Al_2O_3.

3.4.7.1 Ligand Synthesis

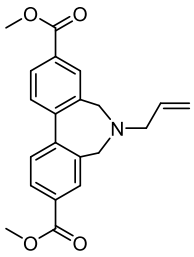

12

Crude 2,2'-di(bromomethyl)bpdc methyl ester (**11**) (661 mg) was dissolved in THF (10 mL). Allylamine (330 µL, 4.41 mmol) was added and the reaction was stirred for 24 h at 50 °C. The solvent was removed, and the crude product was further purified by column chromatography over silica, with a gradient of EtOAc:cyclohexane 1:5 to 1:2 as eluent. The crude product was dissolved in Et_2O, and the solvent was allowed to slowly evaporate overnight to yield colorless, rod-shaped crystals. The crystalline solids were isolated. The mother liquor was concentrated and placed at 5 °C to provide a second crop of crystals. The combined solids were dried under vacuum.

^{1}H NMR (500 MHz, $CDCl_3$) δ 8.12 (dd, *J* = 8.0, 1.7 Hz, 2H), 8.03 (d, *J* = 1.7 Hz, 2H), 7.59 (d, *J* = 8.0 Hz, 2H), 5.98 (ddt, *J* = 16.8, 10.1, 6.5 Hz, 1H), 5.32 (dd, *J* = 17.1, 1.8 Hz, 1H), 5.26 (dd, *J* = 10.1, 1.7 Hz, 1H), 3.96 (s, 6H), 3.44 (s, 4H), 3.21 (dd, *J* = 6.6, 1.7 Hz, 2H).

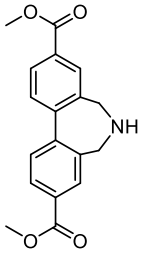

13

The deallylation protocol was adapted from a reported general procedure.[249] Under argon, **12** (691 mg, 1.97 mmol, 1 eq.) was dissolved in degassed, anhydrous dichloromethane (5 mL). 1,3-Dimethylbarbituric acid (925 mg, 5.92 mmol, 3 eq.) and tetrakis(triphenylphosphine)palladium(0) (35.0 mg, 0.0303 mmol, 1.5 mol%) were added. The reaction was stirred at 35 °C for 3 h while the reaction progress was followed by TLC. The reaction was diluted with dichloromethane and washed with aqueous Na_2CO_3 (2 x 5 mL) and water (2 x 5 mL). The organic phase was dried over magnesium sulphate and the solvent was removed under vacuum. The solid was washed with hot diethyl ether to yield the product as a brown powder (259 mg, 0.832 mmol, 42 % yield).

^{1}H NMR (500 MHz, $CDCl_3$) δ 8.12 (dd, *J* = 8.0, 1.7 Hz, 2H), 8.07 (d, *J* = 1.7 Hz, 2H), 7.57 (d, *J* = 8.0 Hz, 2H), 3.96 (d, *J* = 1.2 Hz, 6H), 3.68 (s, 4H).

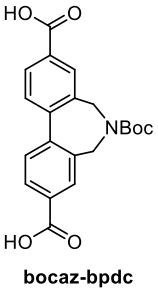

bocaz-bpdc

Under argon, **13** (94.7 mg, 0.304 mmol, 1 eq.) was suspended in anhydrous *tert*-butyl alcohol (0.5 mL). A solution of di-*tert*-butyl dicarbonate (66.1 mg, 0.302 mmol, 1 eq.) in anhydrous *tert*-butyl alcohol (0.5 mL) was added and the reaction was stirred at 35 °C. After 16 h additional di-*tert*-butyl dicarbonate (11.0 mg, 0.0504 mmol, 0.16 eq.) was added, and stirring was continued for another 24 h. Additional di-*tert*-butyl dicarbonate (14.9 mg, 0.0683 mmol, 0.23 eq.) was added, and stirring was continued for further 4 h. The solvent was removed under vacuum. The crude product was used without further purification.

The solid was dissolved in THF (0.5 mL) and 1 M aqueous NaOH (0.5 mL) was added. The reaction was stirred at 50 °C until TLC indicated consumption of all starting material. THF was removed under reduced pressure and the aqueous phase was acidified to pH=4. Solids were filtered off and washed with water. The solvent was removed under vacuum to yield the product as off white solid (30.4 mg, 0.0792 mmol, 26 %).

H NMR (500 MHz, DMSO) δ 13.18 (s, 2H), 8.08 (dt, *J* = 7.9, 1.8 Hz, 2H), 8.02 (s, 2H), 7.74 (dd, *J* = 8.0, 1.7 Hz, 2H), 4.21 (s, 4H), 1.47 (d, *J* = 1.6 Hz, 9H).

^{13}C NMR (176 MHz, DMSO) δ 166.82, 153.44, 143.31, 134.40, 131.30, 130.43, 129.58, 128.82, 79.61, 47.43*, 46.91*, 28.07.

*At 176 MHz the **C**H$_2$ signal was split into two broad peaks of low intensity. At lower frequency, the broadening was too pronounced to observe a signal. The number of carbon atoms was confirmed by HMQC and DEPT NMR experiments.

ESI (negative mode, methanol): m/z = 382.1290 ($C_{21}H_{20}NO_6^-$), calculated 382.1285.

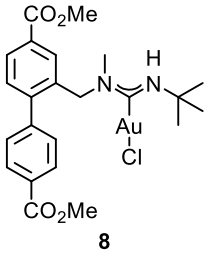

8

Under argon, im-bpdc ester (8.2 mg, 0.0262 mmol, 1 eq.) and tert-butylilisocyanogold(I) chloride (8.2 mg, 0.0260 mmol, 1 eq.) were weighed into 4.5 mL vial protected from light. The atmosphere was replaced with argon (3x) before the solids were dissolved in anhydrous DCM (1 mL). The reaction was stirred under argon at room temperature for 16 h. The solvent was removed the product was isolated by preparative thin layer chromatography over silica using a mixture of EtOAc:*n*-hexane 1:1 as eluent.

^{1}H NMR (700 MHz, $CDCl_3$) δ 8.13 (d, *J* = 8.2 Hz, 2H), 8.06 – 8.02 (m, 1H), 7.89 (d, *J* = 1.7 Hz, 1H), 7.39 (d, *J* = 8.3 Hz, 2H), 7.36 (d, *J* = 7.9 Hz, 1H), 5.76 (s, 1H), 5.31 (s, 2H), 3.95 (d, *J* = 2.6 Hz, 6H), 2.61 (s, 3H), 1.62 (s, 9H).

^{13}C NMR (176 MHz, $CDCl_3$) δ 193.07, 166.78, 166.54, 162.34, 145.33, 143.79, 133.67, 130.75, 130.42, 130.20, 130.07, 129.28, 129.05, 128.65, 63.24, 54.92, 52.57, 52.48, 33.04, 31.82.

3.4.7.2 MOF Synthesis

mam-*rt*MUF-77 In a 4.5 mL vial hmtt (6.0 mg, 11 µmol, 2.6 eq.) and mam-bpdc (1.2 mg, 4.2 µmol, 1 eq.) were suspended in DMF (550 µL). A 3.91 mM solution of bdc (105 µL, 4.1 µmol, 1 eq.) in DMF was added. The ligands were dissolved in DMF (1.5 mL). A solution of $Zn(OAc)_2{\cdot}2H_2O$ (9.2 mg, 42 µmol, 10.2 eq.) in DMF

was added to the ligand mixture while stirring. The vial was closed, and the reaction mixture was swirled. The reaction was stirred for 1 h. The suspension was transferred to a 1.5 mL Eppendorf vial and centrifuged. The solvent was decanted and replaced with fresh DMF. The washing process was repeated four times.

az-*s*MUF-77 A 4.5 mL vial was charged with hmtt (11.1 mg, 19.9 μmol, 1.1 eq.), Boc-protected az-bpdc (7.0 mg, 18 μmol, 1 eq.), bdc (6.5 mg, 39 μmol, 2.1 eq.), $Zn(NO_3)_2{\cdot}4H_2O$ (82.5 mg, 0.316 mmol, 17.6 eq.) and benzoic acid (40.0 mg). The solids were suspended in DEF (4.88 mL) and water (125 μL). The suspension was sonicated for 5 minutes and was placed in an 85 °C isothermal oven for 24 h. The hot solvent was replaced with fresh DMF (5x).

For removal of the Boc group, the crystals were washed with DCM (5x) before subsequent heating to 200 °C for 20 h with a ramp rate of 10 °C/min under vacuum using the outgasser function at the activation port of the iQ2 gas adsorption instruments.

Chapter 4 MUF-77 as a Versatile Platform for Gold(III) Catalysis

4.1 Overview

4.1.1 Homogeneous Gold(III) Catalysts

While homogeneous Au(I) catalysis is well established, efficient gold catalysts with higher oxidation states feature less prominently in the literature. This might come as a surprise as Au(III) compounds are well known.[250,251] Chloroauric acid, $H[AuCl_4]$, has been long used as an important reagent in the synthesis of Au(I) complexes. It can be obtained by dissolving elemental gold in aqua regia, a potent mixture of concentrated nitric acid and hydrochloric acid. It is often used in nanoparticle synthesis by reducing the oxidation state of gold from +3 to 0.[252] The addition of tetrahydrothiophene (tht) to a solution of H[AuCl4] in ethanol and water yields tht-AuI-Cl, a valuable precursor to Au(I) catalysts.[248] In Au(III) catalysis it is often not straightforward to determine whether the active species responsible for catalysis is the employed Au(III) complex or if an *in situ* reduction leads to an active Au(I) catalyst.[253,254] The higher redox potential of gold (Au^{III}/Au^0 = 1.52 V, Au^{III}/Au^I =1.36 V, Au^I/Au^0=1.83 V) compared to metals like platinum (Pt^{II}/Pt^0 = 1.19 V) means it is more easily reduced, mechanistic studies become convoluted.[250] The design and use of new ligands helps overcome those challenges by stabilizing the Au(III) centre. The potential ligands are manifold (Figure 4-1), yet, generally, they beneficial interactions are based on the hard Lewis acid properties of Au(III) compared to the softer Au(I) cations. While complexes of the formula $LAuX_3$ (ligands are denoted as L, X, or Z according to the covalent bond classification method[255,256]) have been employed successfully as (pre-)catalysts in 1,5-enyne cycloisomerization reactions.[253,257] Their propensity for reduction to Au(I) in other instances was reported[258]. Further N-coordinating ligands of the type $LAuX_3$ or chelating N^O complexes were found to be active catalysts, however, their catalytic activity was only slightly superior to $AuCl_3$.[259] These complexes were also found to be prone to reduction.[260] Today, chelating or pincer ligands are widely used in the stabilization of Au(III) complexes. N^C complexes have been successfully used to promote the formation of propargylic amines, chiral allenes, and isoxazole.[261] C^N^C pincer ligands are one of the most widely used scaffolds for Au(III) complexes.[262] When embedded in a MOF, they have been reported to promote the photo-reduction of methyl viologen.[263]

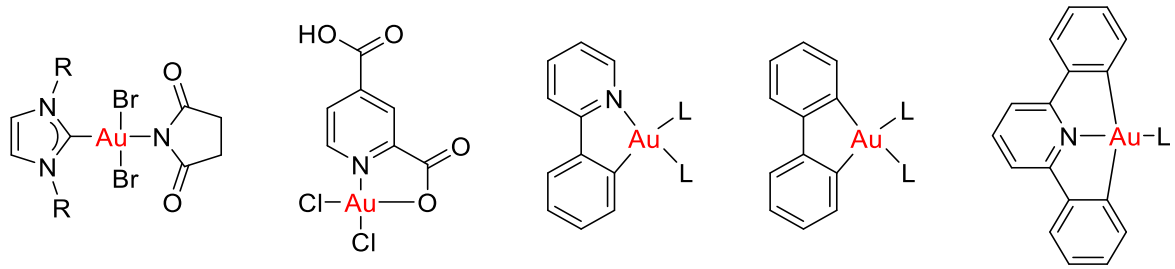

Figure 4-1 Overview of typical Au(III) catalyst scaffolds used in homogeneous transition metal catalysis.

Au(III) is a promising target for use in transition metal catalysis due to its relative carbophilicity, stability against hydrolysis, and tolerance of a wide range of functional groups.[250] Overall, research in high-valent transition metal catalysis is still lagging behind the well-established low-valent transition metal catalysis, making it a promising target for further research.[264] Such a Au(III) catalyst was reported by the Toste group in 2015 (Figure 4-2).[264] A NHC-Au(I)-Cl complex, a common catalyst in transition metal catalysis, was transformed to a stable Au(III) catalyst by oxidative addition of biphenyl. The conversion required only mild conditions compared to the strong halogen-based oxidants usually employed. That allowed the active Au(III) catalyst to form *in situ*. The hard Lewis acidic Au(III) catalyst promoted new catalytic transformations, previously not accessible through Au(I) catalysts or traditional bulky Lewis- and Brønsted-acid catalysts. The catalyst promoted Mukaiyama-Michael additions, nitronate Michael additions, a thiol addition, Hantzsch ester reductions, Diels–Alder reactions and a [2+2] cycloaddition with good selectivity. In contrast to popular Au(III) catalysts like $AuCl_3$, which show harsh and non-selective acidity,[265] the new catalyst provided intermediate reactivity. The ligand environment not only stabilized the Au(III) species but provided a unique catalytic pocket, leading to the excellent selectivity observed during the catalytic trials.

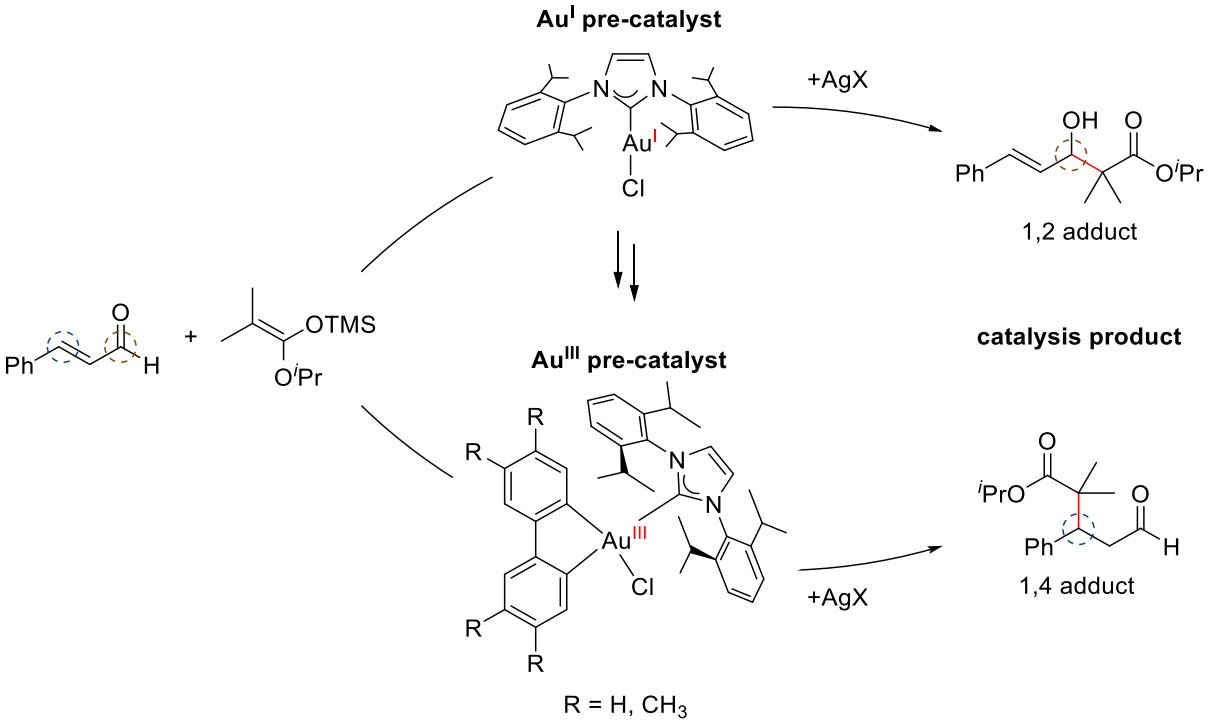

Figure 4-2 The different catalytic outcomes using a traditional Au(I) catalyst or the Au(III) catalyst reported by Toste. Upon activation with a halide abstraction reagent, the NHC-Au(I) catalyst led to the formation of the 1,2 adduct while the Au(III) catalyst promoted the formation of the 1,4 adduct. The novel biphenyl/NHC-Au(III)-Cl pre-catalyst was synthesized from NHC-Au(I)-Cl by oxidative addition of a C–C bond.

The catalytically active, cationic Au(III) complex, was obtained through chloride abstraction by a silver salt. In the case of the biphenyl-Au(III) system, the catalytic cationic complex was obtained by replacing the chloride ligand with the weakly coordinating SbF_6^- anion. A water-coordinated metal centre was proposed as the catalytic species (Figure 4-3).

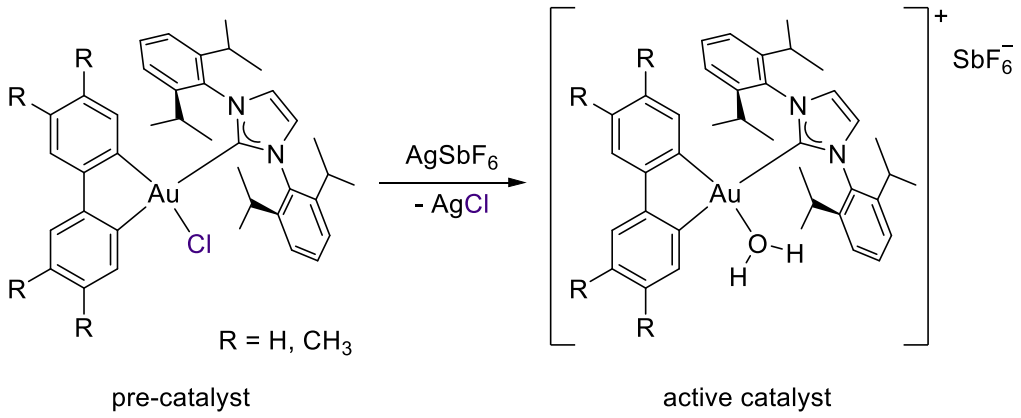

Figure 4-3 Schematic representation of the activation of the Au(III) pre-catalyst. The catalytically active cationic complex was obtained through halide abstraction with a suitable silver salt. The chlorido ligand was replaced by a weakly coordinating counterion, SbF_6^-. The catalytically active species was characterized as the respective Au(III)-aqua complex.

The square planar ligand coordination geometry of Au(III) complexes provides further advantages compared to the linear coordination environment in Au(I) species (Figure 4-4). Naturally, the ligands occupy spaces around the metal centre closer to the chlorido ligand/the active centre, allowing them to directly influence the catalytic site and create a catalytic pocket.

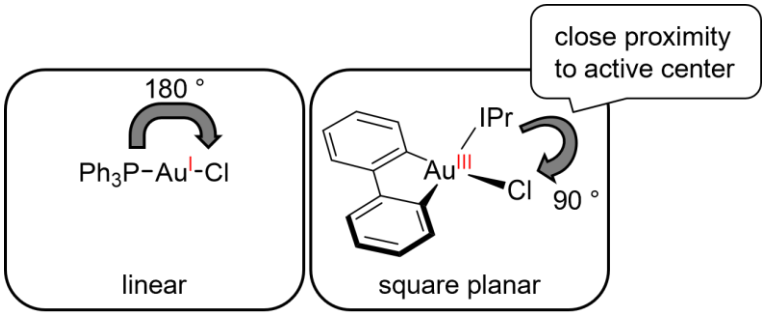

Figure 4-4 The square planar ligand arrangement of Au(III) complexes and the close proximity of (typically innocent) ligands to the active centre lead to new possibilities in shaping the catalytic pocket (IPr = [1,3-bis(2,6-diisopropylphenyl)imidazole-2-ylidene).

In 2017 the groups of Wong and Toste independently exploited the proximity of the ligands to the catalytic site to obtain enantioselective Au(III) catalysts by introducing chiral ligands (Figure 4-5).[260,266] The catalysts are stabilized through either C^N or C^C ligand complexation and a ligand bearing the chiral information. Toste utilized a chiral derivative of the NHC ligand shown earlier to obtain the biphenyl-stabilized catalyst. The catalyst was successfully employed in the direct enantioconvergent kinetic resolution of 1,5-enynes. Interestingly, when Wong introduced a BINOL ligand into an Au(III) dichloride complex, [(C^N)$AuCl_2$], C,O-chelation was observed instead of the expected O,O' chelate complex. The Au(III) complex successfully promoted the carboalkoxylation of *ortho*-alkynylbenzaldehyde with methanol and the initial selectivity trials showed 41 % ee.

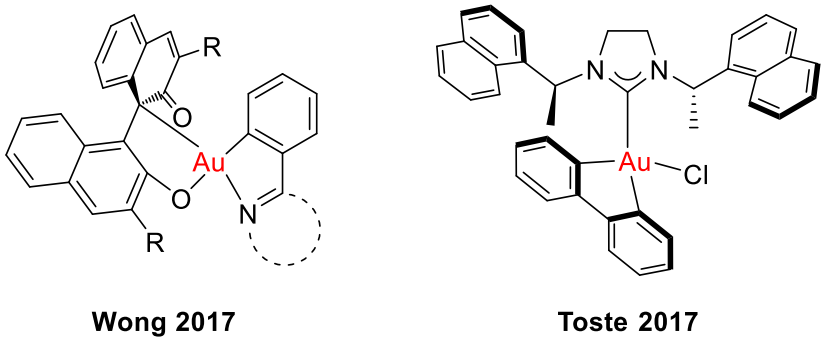

Figure 4-5 Novel selective Au(III) catalysts for asymmetric catalysis and kinetic resolution reported by Wong and Toste.

4.1.2 MOFs as Platforms for Gold(III)-catalysed Reactions

Research into Au(III)-based MOF catalysts is still in its infancy. However, the first examples provide a promising outlook into future possibilities. Levchenko *et al.* recently reported the incorporation of a stable Au(III) catalyst into UiO-67.[267] 2-Phenylpyridine-5,4′-dicarboxylic acid was transformed in two steps to the respective C^N-Au(III) coordinated ligand. However, the synthesis conditions for the UiO-67 framework led to decomposition of the Au(III) complex. Reduction of Au(III) was also reported for other attempts to incorporate Au(III) complexes into MOFs.[268,269] While the resulting hybrid materials of gold nanoparticles and/or partially formed Au(III)-salen complexes within MOFs might be exploited for catalysis, Levchenko *et al.* circumvented the decomposition by introducing Au(III)-bearing ligands through post-synthetic ligand exchange (Figure 4-6). Upon synthesis, a regular bpdc linker in UiO-67 was replaced with the catalyst and the MOF successfully promoted cyclopropanation reactions.

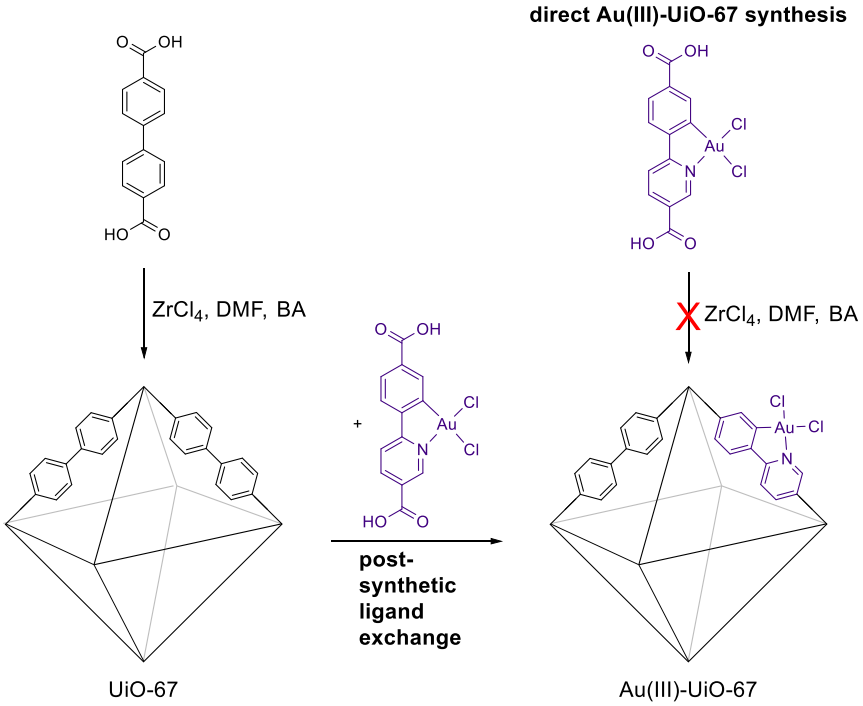

Figure 4-6 Synthesis of a novel UiO-67-Au(III) catalyst. Attempts to introduce the catalytically active ligand through a direct MOF synthesis led to the decomposition of the gold complex. Instead, the ligand was successfully incorporated into an existing traditional UiO-67 framework through post-synthetic ligand exchange.

As described previously, Lee *et al.* were successful in synthesizing a biphenyl-stabilized Au(III) catalyst, IPrAu(bpdc)Cl (IPr = [1,3-bis(2,6-diisopropylphenyl)imidazole-2-ylidene]) suitable to be incorporated into different MOF frameworks (Figure 4-7).[270] No decomposition of the Au(III) complex was observed. The frameworks, IRMOF-10 and bio-MOF-100, provided architectural stability for the catalyst. Incorporation into the framework stabilized the ligand against the unimolecular decomposition observed for the homogeneous catalyst. The catalysts successfully promoted the 1,5-enyne and the alkynyl cycloheptatriene cycloisomerization reactions. Both catalysts were recyclable and no leaching of active catalyst into solution was observed.

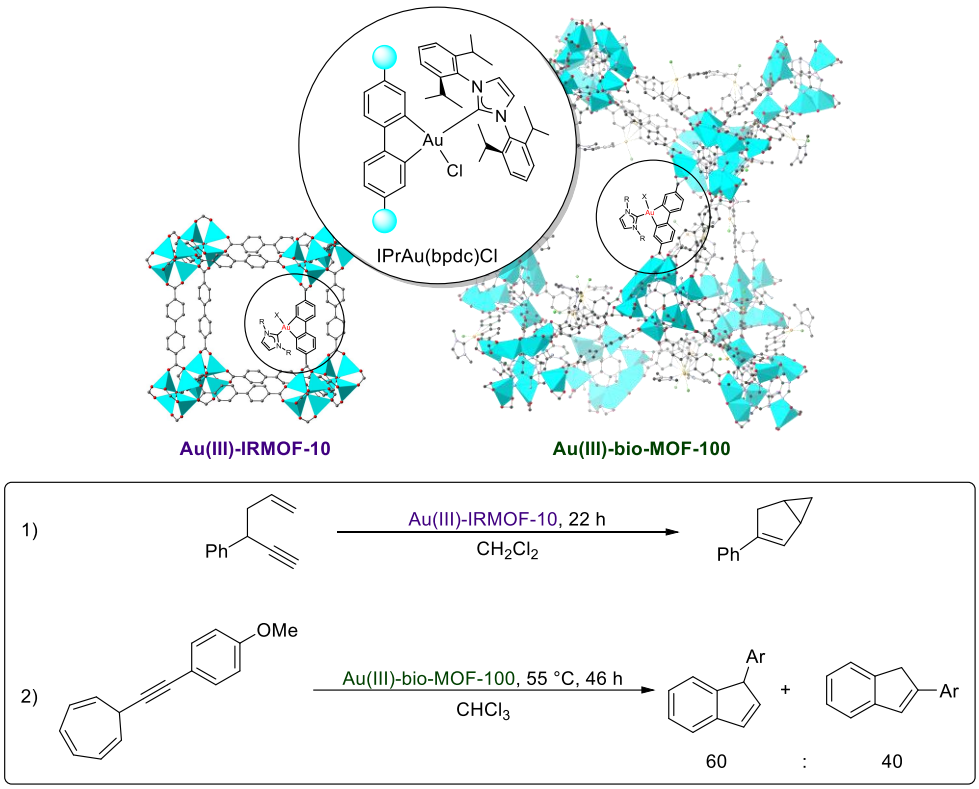

Figure 4-7 IRMOF-10 and bio-MOF-100 as platforms for a bpdc derived Au(III) catalyst. The ligand was stable during MOF synthesis. The incorporation into the framework stabilized the ligand from decomposition through reductive elimination. The functionalized MOFs were successfully promoted the 1,5-enyne and the alkynyl cycloheptatriene cycloisomerization reaction.

This proof-of-concept inspired us to target the incorporation of the IPrAu(bpdc)Cl ligand into our MUF-77 system. The common synthetic conditions for IRMOF-10 resemble those of MUF-77, indicating a promising tolerance of the employed reagents to the conditions. Lee *et al.* combined bpdc and IPrAu(bpdc)Cl with $Zn(NO_3)_2{\cdot}4H_2O$ in DEF. After heating the reaction at 90 °C for 24 h they obtained the framework as yellow crystals. The ratio of IPrAu(bpdc)Cl to bpdc was determined by NMR upon digestion to be between 5 % and 16 %. It is important to note that an increase in catalyst loading led to a decrease in crystallinity through an increase in crystal defects, which the authors attributed to the increased steric clashes of the sterically demanding IPrAu-groups. We theorized that the ligand could be introduced to MUF-77 to produce a catalyst in a similar way (Figure 4-8). Modification of the two other ligands in MUF-77 provides a way to influence the catalytic activity through pore modulation.

4.2 Results and Discussion

4.2.1 MOF Synthesis and Characterization

4.2.1.1 Synthesis of IPrAu(bpdc)Cl-$_s$MUF-77 at Different Temperatures

We synthesized IPrAu(bpdc)Cl-MUF-77 by combining the ligands hmtt, IPrAu(bpdc)Cl and bdc with zinc nitrate tetrahydrate and benzoic acid in DEF. The reactions were carried out at temperatures between 50 °C and 120 °C (Figure 4-8).

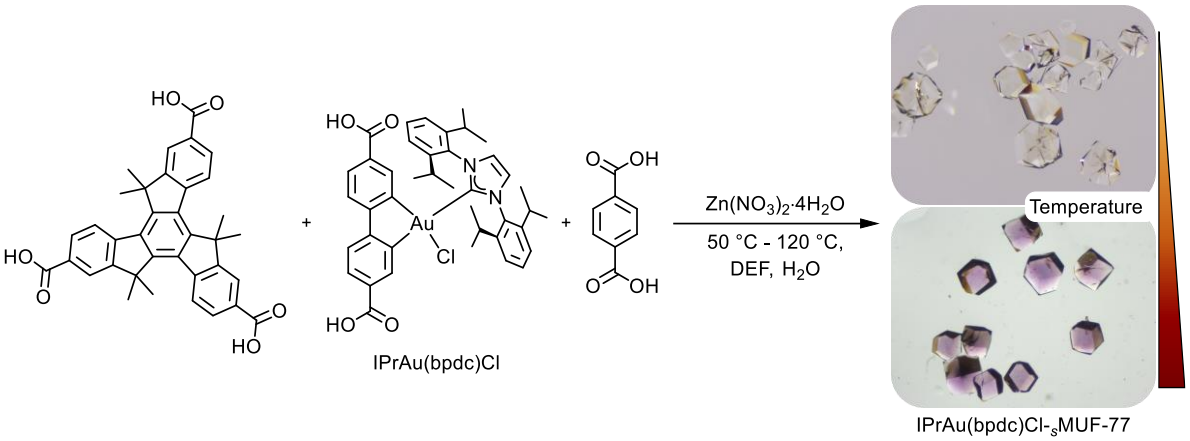

Figure 4-8 Solvothermal synthesis of IPrAu(bpdc)Cl-$_s$MUF-77 at different synthesis temperatures.

For parent MUF-77 the optimal synthesis temperatures was established earlier as 85 °C. When we adopted the common MUF-77 synthesis to incorporate IPrAu(bpdc)Cl, however, the obtained transparent crystals showed a distinct purple coloration due to gold nanoparticles (Figure 4-9). While the formation of nanoparticles is not a problem *per se*, it requires careful control of the catalytic properties of such nanoparticles. More importantly, it raises the question about the decomposition of the incorporated ligands. Alerted by these observations, we attempted the synthesis at different temperatures and reaction times.

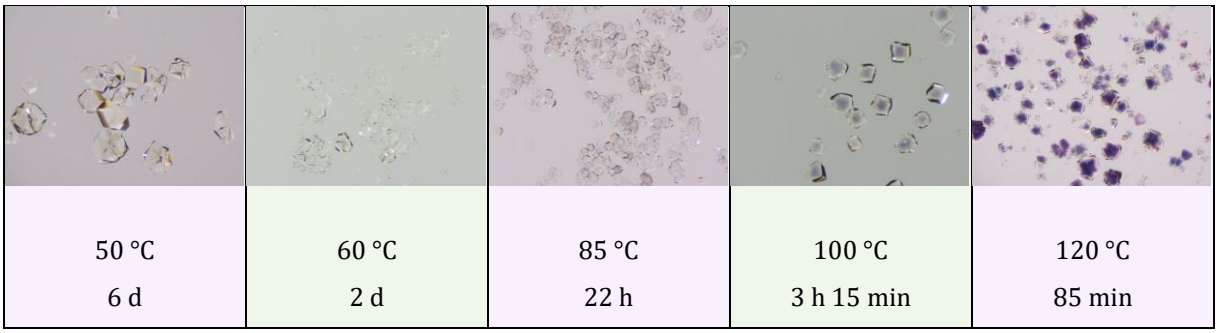

Figure 4-9 Microscopy images of $_s$MUF-77(Au^{III}) crystals obtained through solvothermal synthesis at different temperatures. At elevated temperatures, the obtained crystals show a purple coloration, an observation we correlated with complex decomposition and formation of gold nanoparticles during the MOF synthesis.

Optical inspection of the synthesized MOFs showed a clear correlation between the synthesis temperature and the occurrence of the purple coloration. At lower temperatures and longer reaction times, the crystals obtained were transparent and without any purple coloration. At 85 °C we observed purple coloration of the crystals. At 120 °C the purple colour dominant and powder diffraction patterns showed the fingerprint of gold nanoparticles (Figure 4-10).

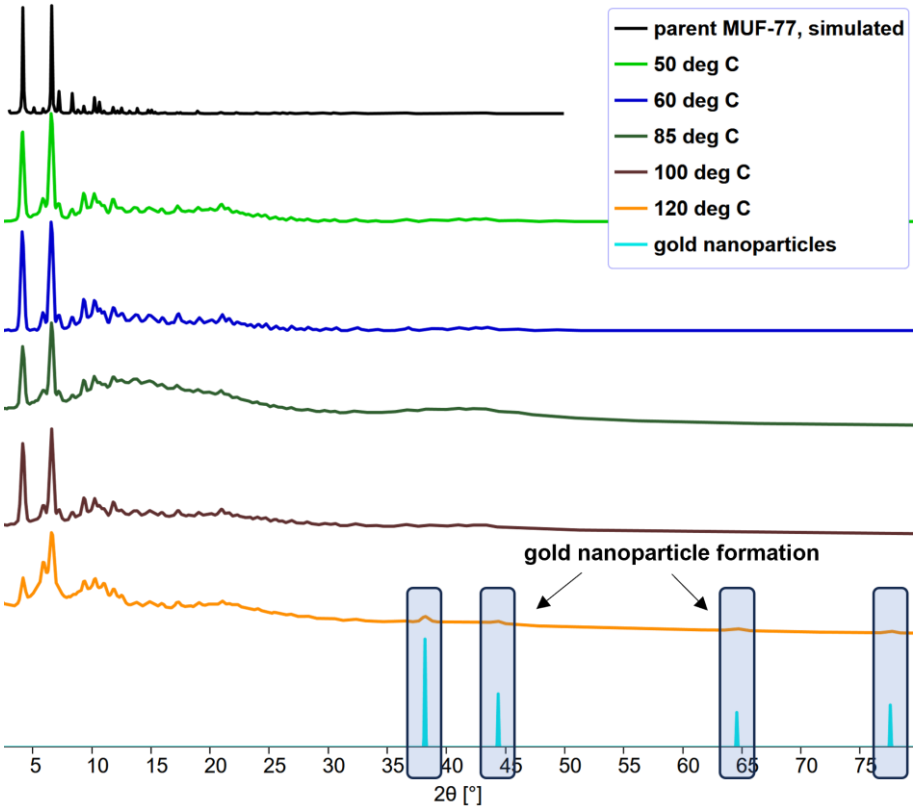

Figure 4-10 Powder X-ray diffraction pattern of IPrAu(bpdc)Cl-$_s$MUF-77 synthesized at different temperatures. The pattern showed the successful and phase-pure formation of MUF-77 crystals. Additionally, at 120 °C the characteristic peaks of gold nanoparticles were observed, supporting our conclusion about ligand decomposition during the MOF synthesis.

To determine whether the IPrAu(bpdc)Cl ligand was incorporated into IPrAu(bpdc)Cl-$_s$MUF-77 without decomposition, we digested the crystals formed at different temperatures in a mixture of DMSO-d_6 and DCl (Figure 4-11). Comparison of ^{1}H NMR spectra from digested MUF-77 synthesized at 50 °C and 60 °C with the ligand showed a shift of the characteristic isopropyl signals and the appearance of additional signals in that region. We observed similar changes for the bpdc backbone signals. While it was difficult to determine the actual complex structure, the data indicated a change in the arrangement of the side group, hinting towards a change in the coordination environment. The appearance of at least two sets of doublets correlated to the isopropyl groups of the NHC ligand pointed towards at least two different coordination complexes upon digestion. Additional signals were also observed in the aromatic region. At temperatures at or above 85 °C, we observed additional signals of bare bpdc in solution. This indicated the decomposition of the gold complex through gold nanoparticle formation. While we expected the complex to be stable under the chosen synthesis condition due to the successful synthesis of IPrAu(bpdc)Cl-IRMOF-10 by Lee *et al.*, the reduction and decomposition of Au(III) complexes by amines is well known. Reduction of Au(III) complexes was reported with DMF and other amines without the addition of further reducing agents.[271,272] Ligand decomposition to gold nanoparticles has been previously reported in different solvothermal MOF synthesis approaches.[267,268] The main difference in the synthetic procedures, despite the choice of ligands, seemed to be the addition of benzoic acid. Benzoic acid was used in MUF-77 synthesis as a growth modulator and the addition was necessary to allow for the reproducible formation of uniform crystals with a size suitable for standard SXRD measurements.

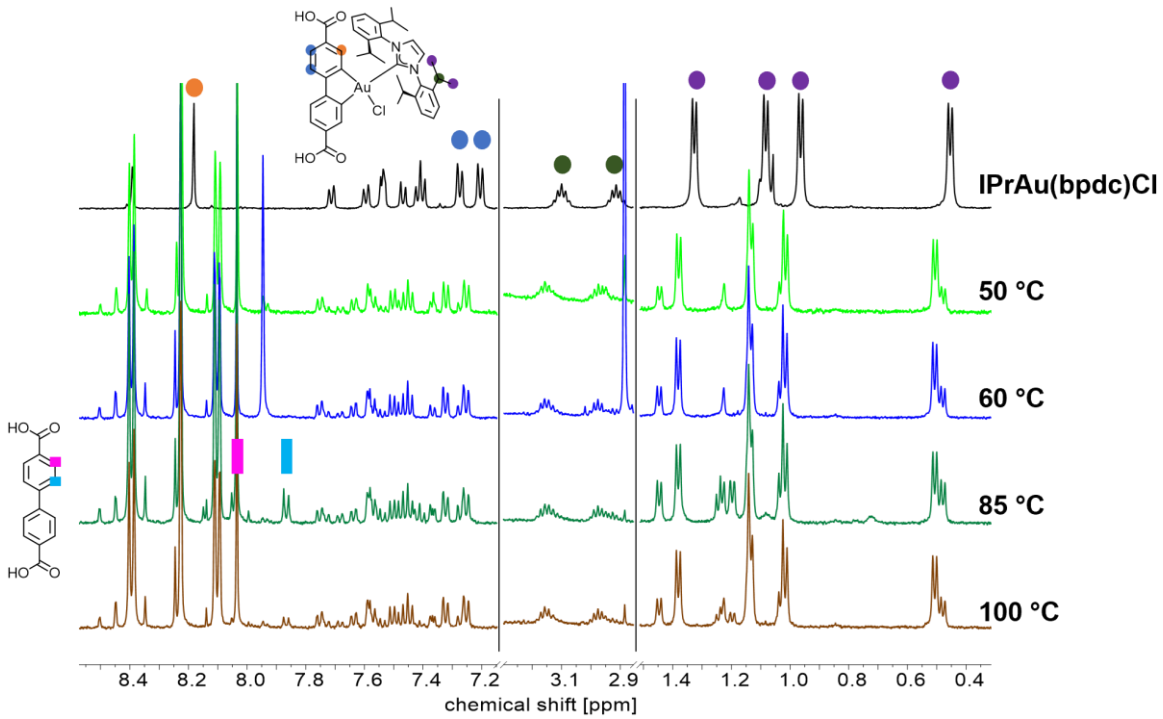

Figure 4-11 ^{1}H NMR spectra of IPrAu(bpdc)Cl-$_{s}$MUF-77 crystals synthesized at different temperatures upon digestion in a DMSO-d$_{6}$/DCl mixture.

SXRD analysis of IPrAu(bpdc)Cl-$_{s}$MUF-77 single crystals from a 85 °C solvothermal synthesis showed electron density consistent with the presence of gold chelated by the biphenyl ligand (Figure 4-12). The bpdc backbone and the coordinated gold centre were disordered, showing rotational freedom of the ligand-metal plane along the bpdc backbone axis. The most representative orientation is depicted in Figure 4-12 without any rotational adjustments. The rotation might be a result of steric pressure within the MUF-77 pore. The occupancy of the modelled gold centres was lower than expected for IPrAu(bpdc)Cl-$_{s}$MUF-77, which was in good agreement with our observation from ^{1}H NMR spectroscopy that under the employed conditions partial ligand decomposition was observed. Precise information about the coordinated co-ligands could not be obtained. No indicative electron density for any expected chlorido ligands was observed. The disorder and rotational freedom of the appended groups and the possibility of a partial reaction of the complex made it difficult to develop an accurate structural model, even at low temperatures and upon solvent removal.

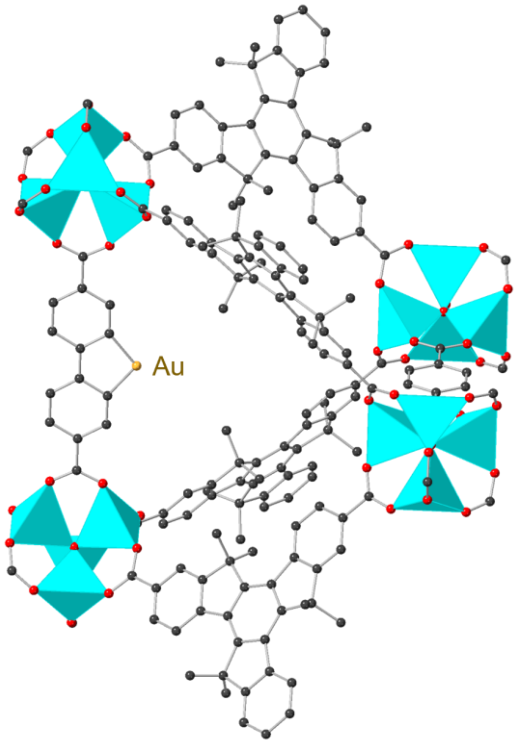

Figure 4-12 SXRD model of the small pore in IPrAu(bpdc)Cl-$_s$MUF-77 obtained from a solvothermal synthesis at 85 °C. Gold centre and bpdc backbone were disordered and are shown in representative positions. Coordinated co-ligands could not be modelled. Carbon atoms are shown in grey, gold in yellow, oxygen in red, and zinc as cyan polyhedra. Hydrogen atoms are omitted for clarity

4.2.1.2 Mixed Ligand Solvothermal Synthesis of IPrAu(bpdc)Cl-$_{ms}$MUF-77

Lee *et al.* also reported challenges for the IRMOF-10 synthesis. To obtain the desired MOF with good crystallinity IPrAu(bpdc)Cl had to be "diluted" with the parent bpdc ligand (5-16 % IPrAu(bpdc)Cl, remainder bpdc). We adopted a similar strategy to MUF-77 analogues. While maintaining the general synthetic conditions, a mixture of bpdc and IPrAu(bpdc)Cl was combined to produce IPrAu(bpdc)Cl-$_{ms}$MUF-77, where *ms* stands for **m**ixed-ligand **s**olvothermal synthesis (Figure 4-13). As IPrAu(bpdc)Cl:bpdc feed ratio we chose 25:75 and 15:85 while all other conditions were held constant. Both reaction feed ratios yielded crystals of the typical MUF-77 appearance.

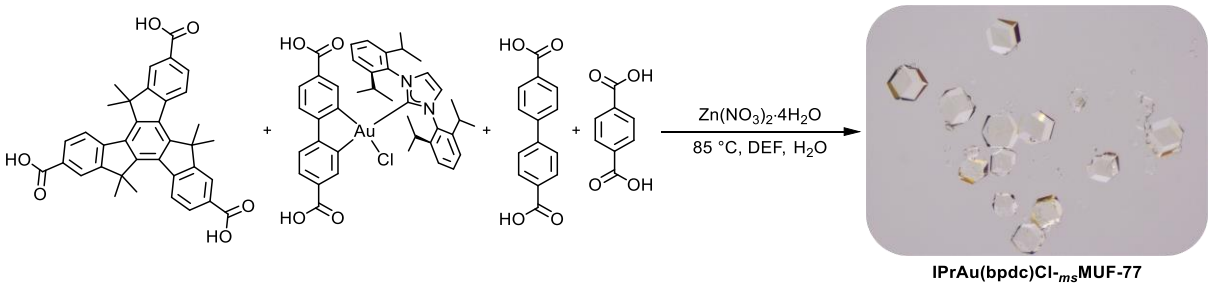

Figure 4-13 Solvothermal synthesis of IPrAu(bpdc)Cl-$_{ms}$MUF-77.

PXRD pattern of the synthesized crystals showed the phase-pure formation of MUF-77, as indicated by the good match with the simulated PXRD pattern of parent MUF-77 and of the comparable synthesis with only IPrAu(bpdc)Cl (Figure 4-14). ^{1}H NMR spectroscopy of the digested MOFs in a mixture of DMSO-d$_6$/DCl

showed both IPrAu(bpdc)Cl and bpdc were incorporated (Figure 4-15). The decreased symmetry of the bpdc backbone, indicated by the additional set of signals in the aromatic region, strongly indicated that a gold coordination complex was successfully integrated. This was further supported by the characteristic signal pattern of the IPr ligand, and the splitting of the isopropyl proton signals often seen in coordination complexes where the rotation of the benzyl-side groups is hindered. While the peak pattern was comparable to that of the homogeneous ligand, we noted a shift in the isopropyl and biphenyl signals. We attributed the shift to a change in the coordination environment of the gold complex. The diluted samples did not show any additional isopropyl or functionalized bpdc signals as observed for the samples synthesized from IPrAu(bpdc)Cl without bpdc addition.

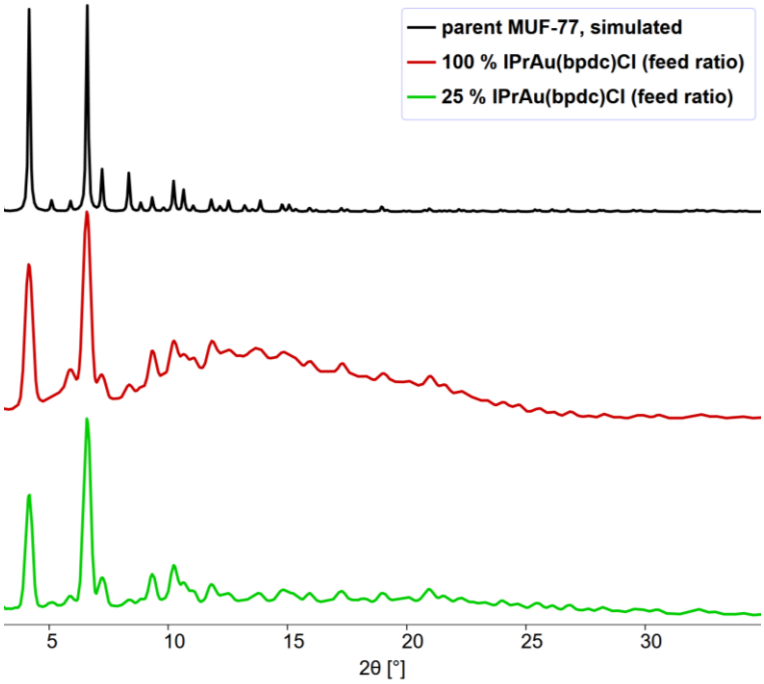

Figure 4-14 Powder X-ray diffraction pattern of IPrAu(bpdc)Cl-$_{ms}$MUF-77 crystals obtained through a mixed-linker solvothermal approach.

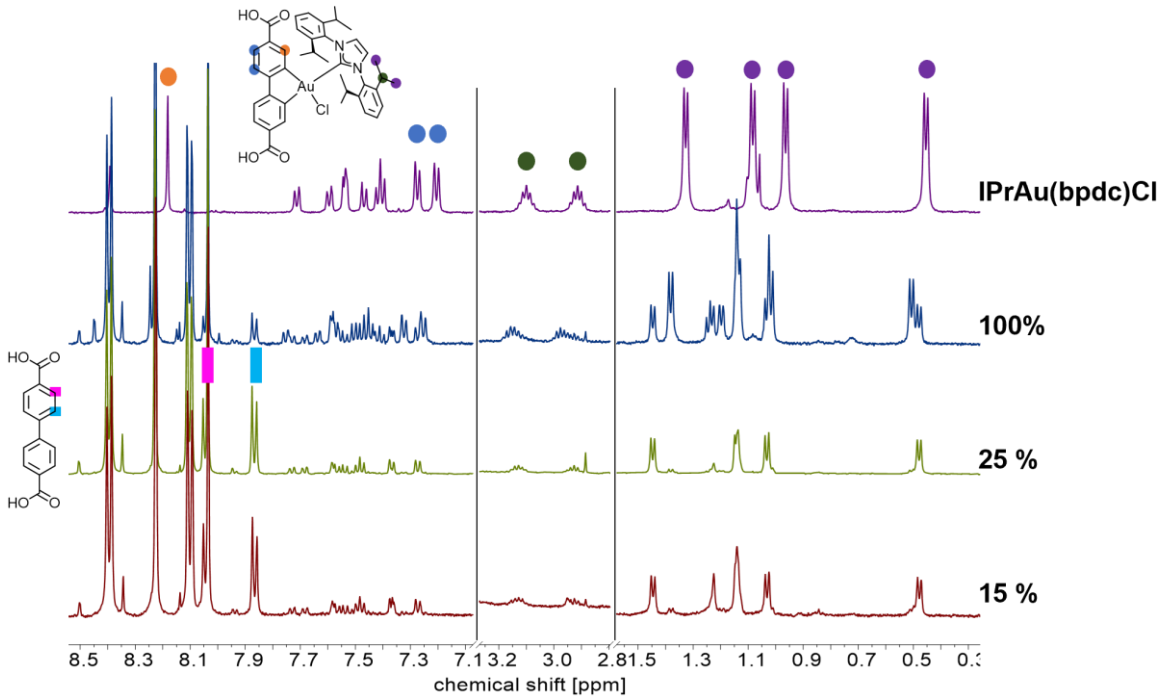

Figure 4-15 ^{1}H NMR spectra of digested IPrAu(bpdc)Cl-*ms*MUF-77. The spectra indicated a change in the coordination environment of the gold complex during the synthesis.

Initial catalytic trials with IPrAu(bpdc)Cl-*ms*MUF-77 did not show any catalytic activity (Chapter 4.2.2.2). A possible explanation was the formation of an Au(III)-hydroxo species via chloro-hydroxy exchange that occurred under the synthesis conditions at elevated temperatures.[273] This would explain the shift in ^{1}H NMR signals and the absence of catalytic activity (Figure 4-16). At this point, we halted our investigation into the ligand decomposition to examine an alternative synthetic route to IPrAu(bpdc)Cl-MUF-77.

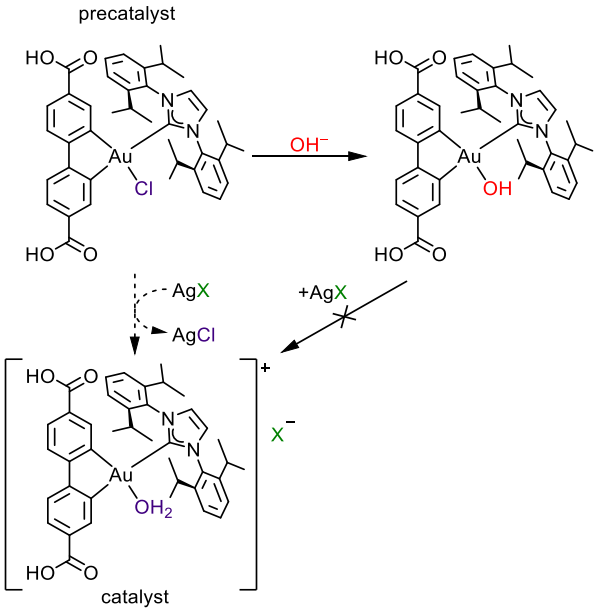

Figure 4-16 Proposed ligand replacement during the MUF-77 solvothermal synthesis in the presence of bpdc and IPrAu(bpdc)Cl leading to a catalytically inactive hydroxo complex.

4.2.1.3 Room-Temperature Synthesis of IPrAu(bpdc)Cl-*rt*MUF-77

We anticipated that a milder and quick room temperature synthesis approach would be beneficial for the stability of the IPrAu(bpdc)Cl complex during MUF-77 synthesis. A solution of hmtt, IPrAu(bpdc)Cl, and bdc in DMF was combined with dissolved zinc acetate in DMF (Figure 4-17). An off-white precipitate formed shortly after mixing ligands and metal salt. The nanocrystalline IPrAu(bpdc)Cl-*rt*MUF-77 was obtained as fine powder.

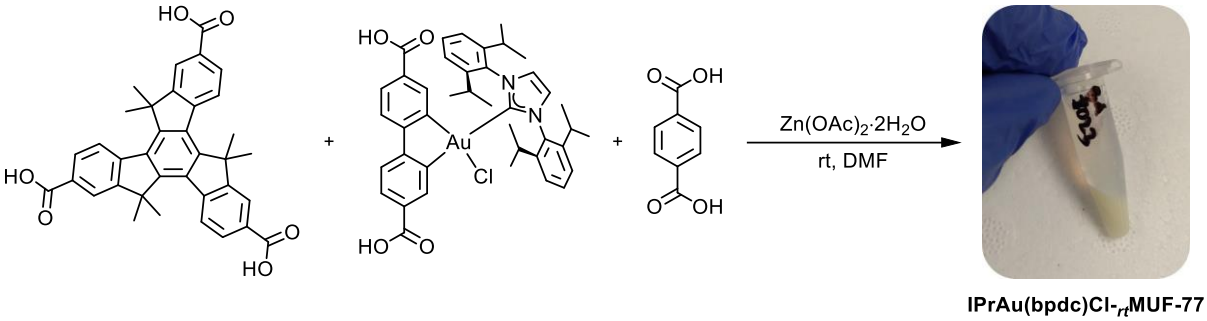

Figure 4-17 Room temperature synthesis of nanocrystalline IPrAu(bpdc)Cl-*rt*MUF-77.

PXRD pattern of the precipitate confirmed the formation of MUF-77 crystals (Figure 4-18). PXRD pattern of nano-sized materials often show broadened signals compared to samples with larger crystal-sizes. The peak width was comparable with the solvothermal-synthesis MUF-77 pattern, a good indication for the high crystallinity of the nanocrystalline sample. No additional peaks were observed, indicating phase purity of the synthesized material. No purple coloration or signals in the PXRD pattern corresponding to gold nanoparticles were observed, indicating that no nanoparticles formed during the reaction.

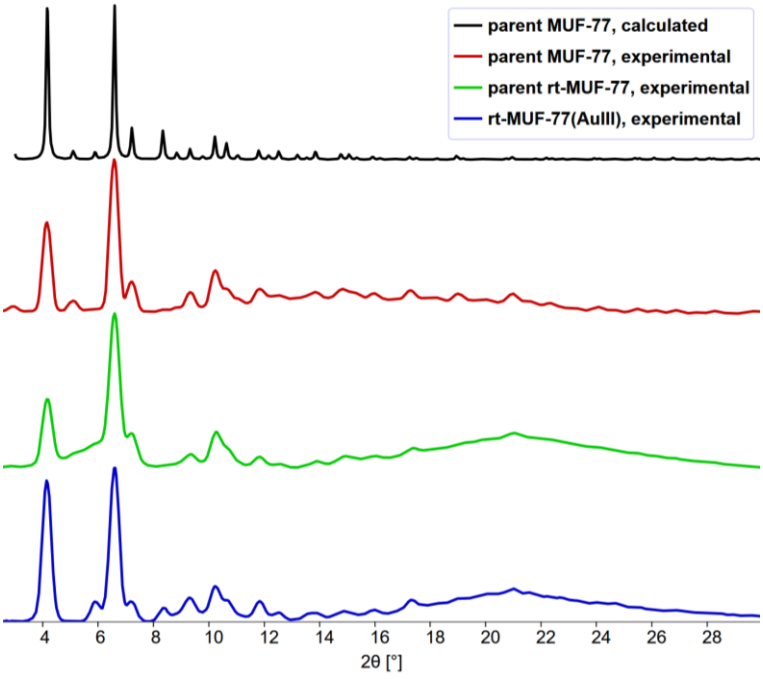

Figure 4-18 Powder X-ray diffraction pattern of IPrAu(bpdc)Cl-*rt*MUF-77 obtained through room temperature synthesis compared to parent MUF-77.

^{1}H NMR spectroscopy indicated no competing frameworks had formed. Integration of the ligand signals was in alignment with the expected molecular formula for IPrAu(bpdc)Cl-MUF-77, $[Zn_4O(hmtt)_{4/3}(IPrAu(bpdc)Cl)_{1/2}(bdc)_{1/2}]$. Moreover, the ^{1}H NMR spectrum indicated that, in contrast to our solvothermal approach, no change in coordination of the gold complex occurred during the MOF synthesis (Figure 4-19). The IPrAu(bpdc)Cl signals were in good agreement with those observed from the homogeneous ligand, only differing in a small shift to higher ppm that can be attributed to small pH differences or interactions with other dissolved ligands upon digestion.

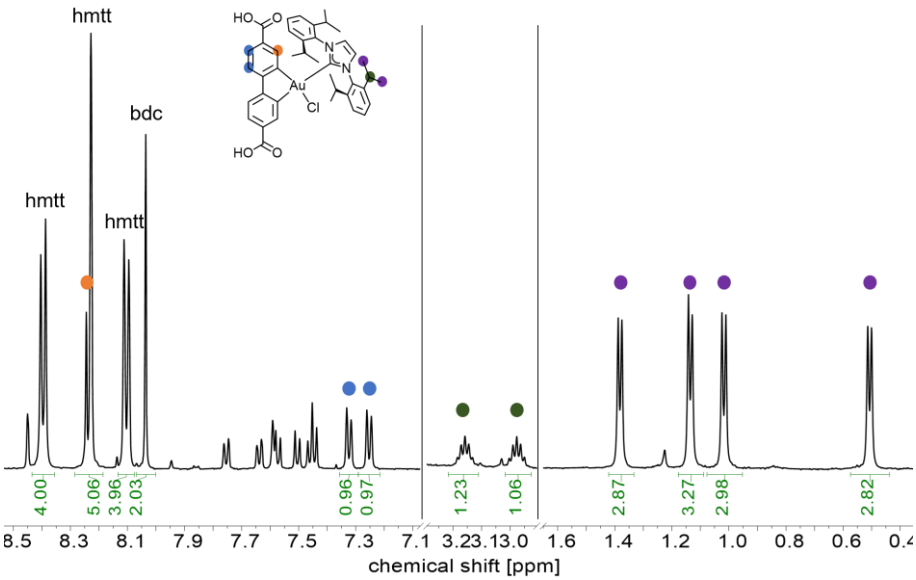

Figure 4-19 ^{1}H NMR spectrum of digested IPrAu(bpdc)Cl-*rt*MUF-77 in a DMSO-d_6/DCl mixture. The data indicated the Au(III) complex was successfully incorporated into the MUF-77 framework.

To evaluate the porosity of the nanocrystalline IPrAu(bpdc)Cl-*rt*MUF-77, the BET surface area of the material was determined. DMF was replaced with acetone and the solvent was replenished four times. The IPrAu(bpdc)Cl-*rt*MUF-77 powder was carefully pre-dried under vacuum for ten minutes before being dried at 60 °C for 24 h. The sample showed a type I isotherm, which is typically observed for the microporous MUF-77 system (Figure 4-20). In contrast to MUF-77 obtained from solvothermal synthesis, the room-temperature samples show a rapid increase in the nitrogen uptake close to $P/P_0 = 1$ due to the condensation of liquid N_2 between the nano-sized particles.[274] The BET surface area was estimated at around 2200 m^2/g. Those results demonstrated the porous nature of the material and were well in line with our expectations. Parent MUF-77 was reported with a BET surface area of 3600 m^2/g for crystals obtained from solvothermal synthesis.[275] A decrease in the N_2 uptake was in line with the expectation of a decreased available pore volume due to the introduced IPrAuCl-functionality filling the pores. The total pore volume was 1.18 cm^3/g (calculated from the N_2 adsorption isotherm at 77 K and $P/P_0 = 0.849$).

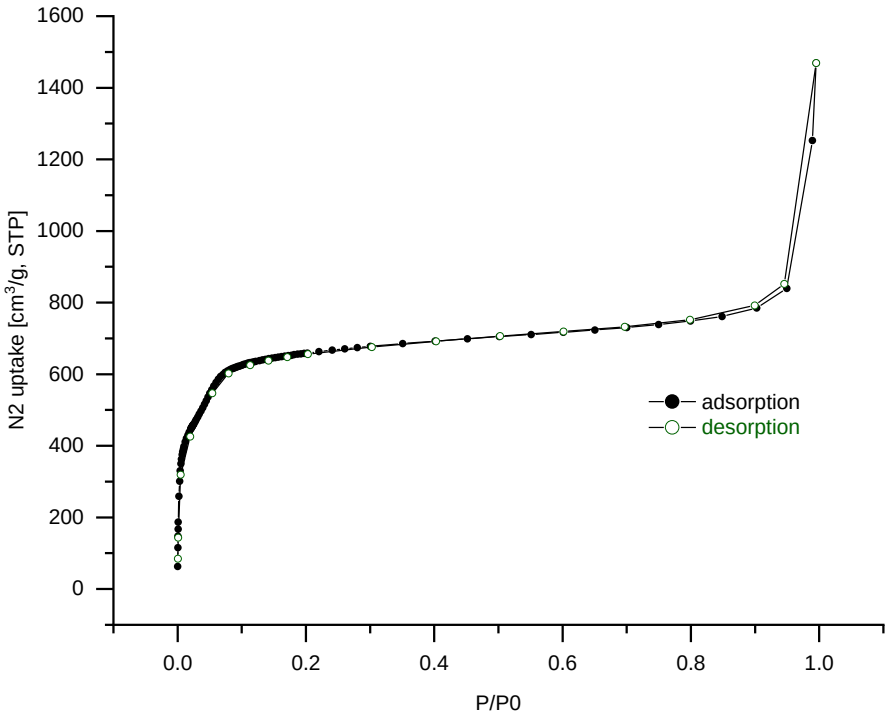

Figure 4-20 Nitrogen absorption isotherm at 77 K of IPrAu(bpdc)Cl-*rt*MUF-77 upon activation highlighting the porosity of the nanocrystalline material.

IPrAu(bpdc)Cl-*rt*MUF-77 retained crystallinity upon activation as shown by PXRD analysis (Figure 4-21).

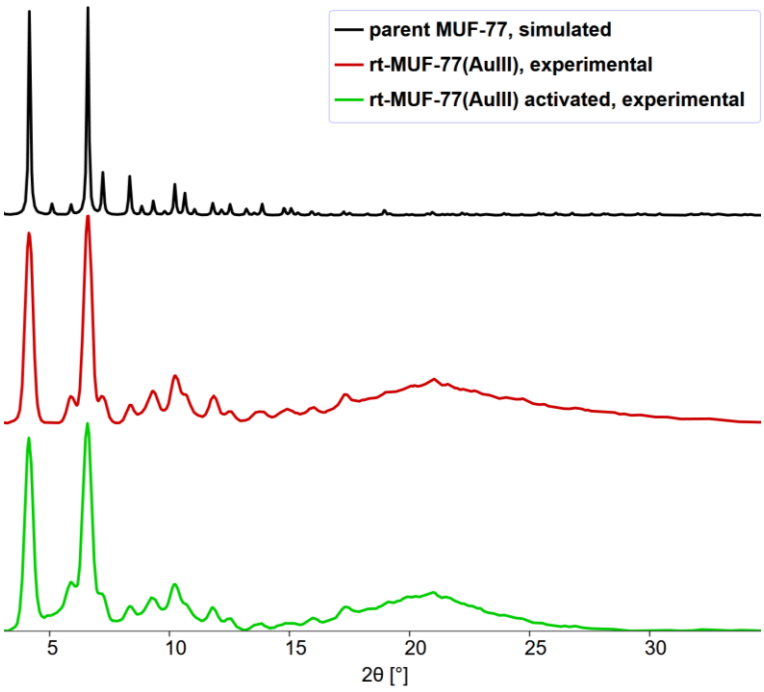

Figure 4-21 Powder X-ray diffraction pattern of IPrAu(bpdc)Cl-*rt*MUF-77 before and after solvent removal.

We were further interested in investigating the stability of IPrAu(bpdc)Cl-*rt*MUF-77. We established in previous experiments that dried nanocrystalline MUF-77 was less stable in air than the crystals obtained

from conventional solvothermal synthesis. This is not surprising as the large surface area increases the contact with water vapor, which can damage the MUF-77 structure. We investigated the stability of the nanocrystalline IPrAu(bpdc)Cl-MUF-77 in DMF and acetophenone at elevated temperatures. DMF was chosen to compare the stability of the MOF and the IPrAu(bpdc)Cl complex to the solvothermal synthesis approach, while acetophenone was reported as a suitable solvent for post-synthetic MOF modifications.[276] IPrAu(bpdc)Cl-MUF-77 was kept in the respective solvent at 85 °C for 3 d. PXRD of the powder showed that IPrAu(bpdc)Cl-MUF-77 retained crystallinity under those conditions (Figure 4-22). Additionally, no change in the ^{1}H NMR spectra of the digested MOF was observed indicating the Au(III) complex maintained stability in those solvents. The results were in line with the reported stability during IPrAu(bpdc)Cl-IRMOF-10 synthesis. The findings indicated that the observed complex decomposition during solvothermal MUF-77 synthesis was likely a cause of the reaction conditions rather than detrimental interactions between complex and MOF or solvent.

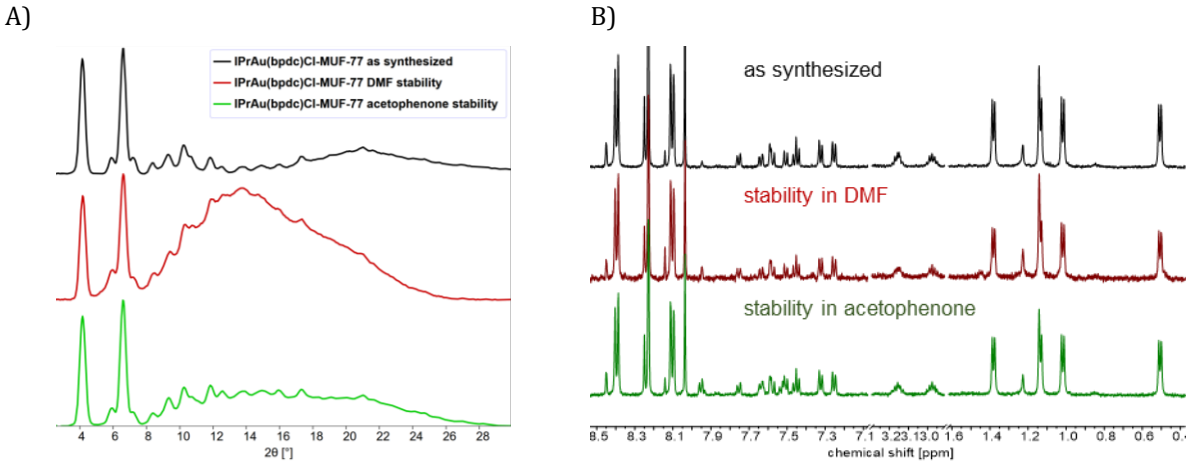

Figure 4-22 A) Powder diffraction pattern of IPrAu(bpdc)Cl-$_{rt}$MUF-77 and B) ^{1}H NMR spectra of the digested MOF following stability tests in DMF and acetophenone. The MOFs retain crystallinity under those conditions and no change in the Au(III)-ligand environment was observed.

4.2.2 Catalysis

4.2.2.1 General Considerations

To evaluate the catalytic performance of IPrAu(bpdc)Cl-$_{rt}$MUF-77 it was necessary to activate the catalyst. This is usually achieved by abstraction of the chlorido ligand, which is replaced by a non-coordinating anion.[277,278] Different salts can be employed for the catalyst activation step and a suitable silver salt/pre-catalyst pair needs to be determined experimentally. We focused on $TlPF_6$ and different silver salts that had been reported to successfully activate IPrAu(bpdc)Cl-bioMOF-100 or comparable homogeneous catalysts.[103,279–281] Our catalysis experiments were designed to provide a proof-of-concept for IPrAu(bpdc)Cl-$_{rt}$MUF-77 and no focus was placed on quantifying catalytic performance.

4.2.2.2 Hydration of Hexynes

For our first catalytic trials, we chose the hydration of 3-hexyne (Figure 4-23). The reaction is well established for many gold catalysts under a variety of conditions.[281–283] The reagents are easily accessible and not known to negatively impact MUF-77 stability, including the addition of water.[284,285]

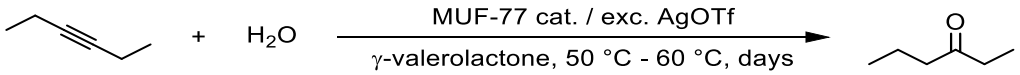

Figure 4-23 Hydration of 3-hexyne in the presence of IPrAu(bpdc)Cl-MUF-77.

We first investigated if the crystals obtained from the solvothermal synthesis approach showed catalytic activity under the chosen conditions. IPrAu(bpdc)Cl-*ms*MUF-77 (25 % feed ratio IPrAu(bpdc)Cl to bare bpdc) was combined with excess AgOTf in a solution of γ-valerolactone, 3-hexyne, and water. The reaction was conducted at 50 °C. No product signals were observed by ^{1}H NMR spectroscopy after two days. The control reaction with parent MUF-77 under similar conditions showed no catalytic activity, showing that catalytic activity cannot stem from the zinc SBUs within the framework.

We then evaluated the catalytic activity of the nanocrystalline material obtained by room temperature synthesis for this reaction. In preparation for our first catalysis trials, IPrAu(bpdc)Cl-*rt*MUF-77 was carefully washed with γ-valerolactone. We added AgOTf as halide abstraction reagent and kept the reaction at 60 °C for four days. The catalysis trial with AgOTf showed product formation by ^{1}H NMR spectroscopy. In a control experiment, the catalyst was filtered off part way through the reaction and the homogeneous reaction mixture was monitored. Additional hexan-3-one formation was observed. Moreover, the isolated MUF-77 material lost all catalytic activity in subsequent recycling experiments, despite retaining crystallinity. While it was promising to see IPrAu(bpdc)Cl-*rt*MUF-77 retained catalytic activity through MOF formation, the results indicated that the reaction conditions led to leaching of the catalyst from the MUF-77 framework and the formation of soluble, homogenous catalysts.

4.2.2.3 Cycloisomerization Reaction of Hex-5-en-1-yn-3-ylbenzene

Originally, Lee *et al.* reported the cyloisomerization of hex-5-en-1-yn-3-ylbenzene to the bicyclohexane product as a test reaction for their IPrAu(bpdc)Cl-bio-MOF-100 and IPrAu(bpdc)Cl-IRMOF-10 catalysts. We adapted the catalysis conditions with our IPrAu(bpdc)Cl-MUF-77 system to test for catalytic activity of the Au(III) complex (Figure 4-24).

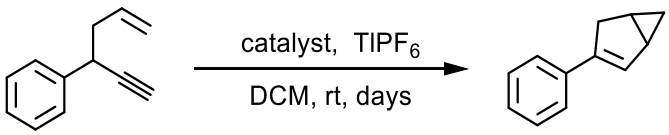

Figure 4-24 Cycloisomerization reaction of hex-5-en-1-yn-3-ylbenzene in the presence of different gold catalysts.

For the catalytic trials, desolvated IPrAu(bpdc)Cl-*rt*MUF-77 was suspended in anhydrous DCM and an excess of AgOTf, $AgBF_4$ or $TlPF_6$ was added. Control experiments were conducted under the same conditions without the MOF catalyst. The homogeneous catalytic test reaction with PPh_3AuCl and $TlPF_6$ was used for comparison, and as expected, led to product formation.[286] The reaction progress was followed by ^{1}H NMR spectroscopy and HPLC analysis (Figure 4-26). The MOF catalyst, IPrAu(bpdc)Cl-*rt*MUF-77, successfully promoted the cycloisomerization reaction in the presence of $TlPF_6$ (Figure 4-25). Other halide abstraction reagents did not lead to catalyst activation. The catalyst was tested for leaching by filtering the reaction to remove all solid IPrAu(bpdc)Cl-*rt*MUF-77 and subjecting the remaining stock solution to the synthesis conditions. Upon filtration, product formation halted, indicating that no leaching of the catalyst occurred.

Further, IPrAu(bpdc)Cl-$_{rt}$MUF-77 was recycled and subjected to fresh catalysis conditions. The catalyst maintained catalytic activity in this recycling experiment, showing no signs of decomposition.

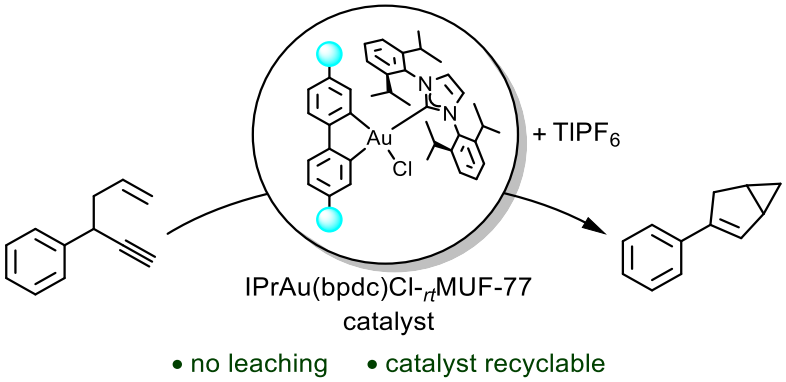

Figure 4-25 IPrAu(bpdc)Cl-$_{rt}$MUF-77 as successful catalyst for the cycloisomerization reaction in the presence of $TlPF_6$.

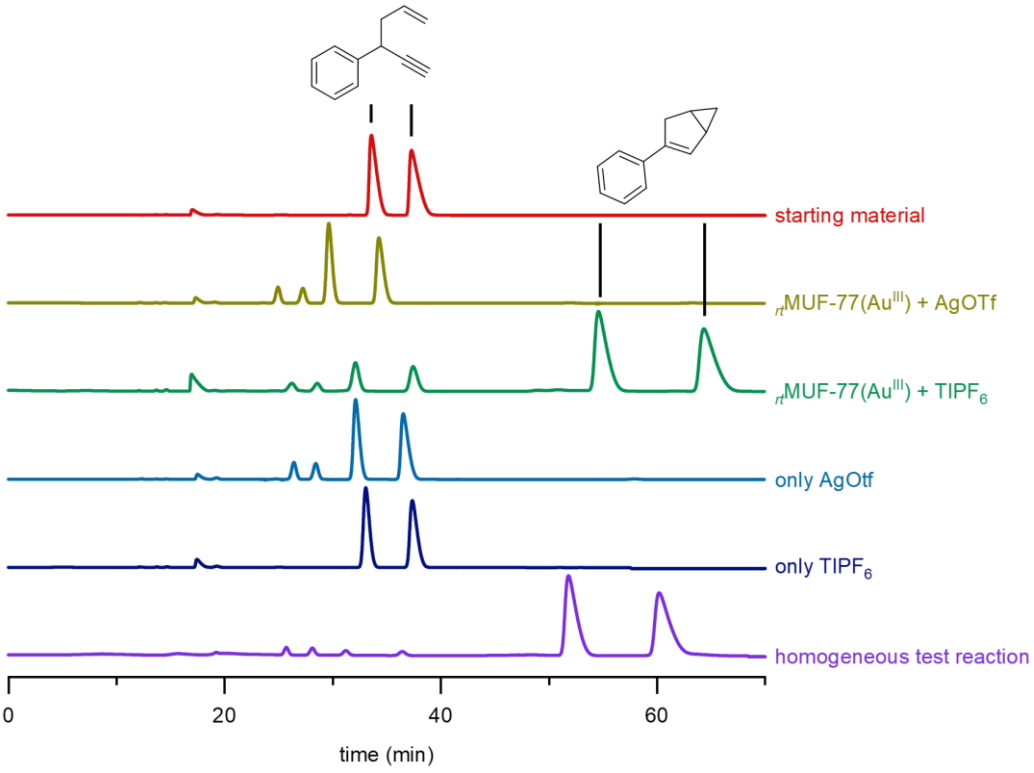

Figure 4-26 HPLC chromatograms from the Au(III)-catalyzed cycloisomerization reaction of hex-5-en-1-yn-3-ylbenzene. Chiral HPLC conditions were developed to analyse the enantiomers independently. This allows us to evaluate the catalyst selectivity in future experiments.

The MOF retained crystallinity throughout the catalysis experiment, as supported by PXRD measurements (Figure 4-27). As expected, traces of TlCl, the solid residue stemming from the halide abstraction process, were detected in the PXRD pattern, as well as excess $TlPF_6$ (Figure 4-27). The data did not show peaks for gold nanoparticles, ruling out the formation of a second, potentially, catalytically active species during the catalysis runs.

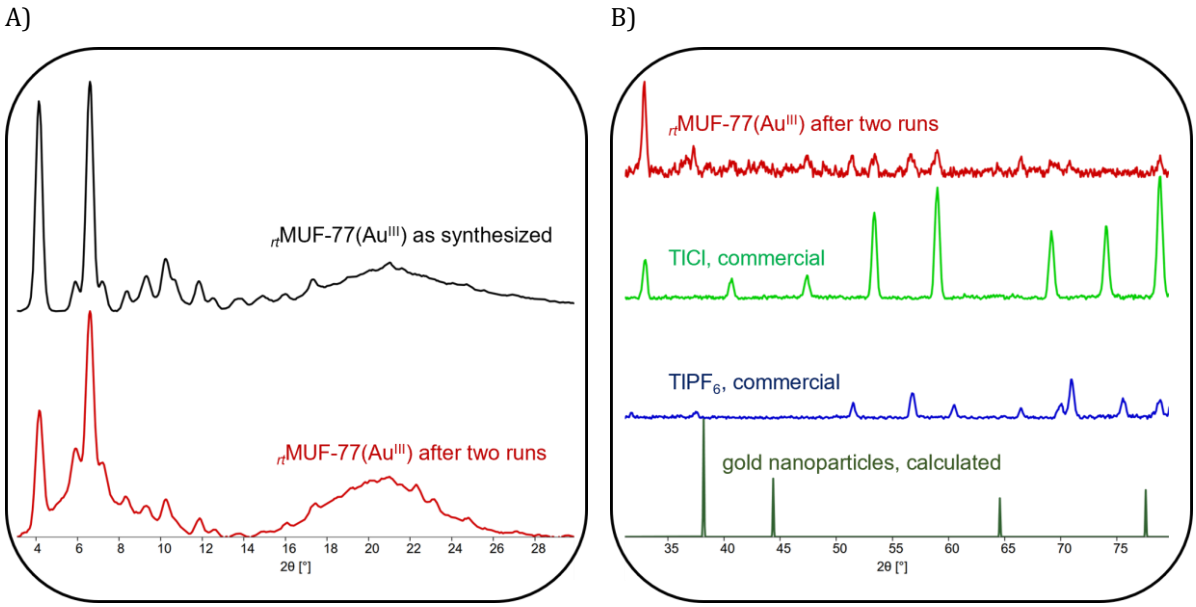

Figure 4-27 Powder X-ray diffraction pattern of the $_{rt}$MUF-77(Au^{III}) catalyst after two runs. A) A comparison with PXRD pattern from the as-synthesized MOF shows the catalyst retained crystallinity. B) The diffraction pattern at a high angle shows no sign of gold nanoparticle formation. As expected, traces of AgTlPF$_6$ and TlCl were found in the PXRD pattern.

4.3 Conclusion

Despite challenges of ligand stability during solvothermal synthesis procedures, we successfully incorporated a catalytically-active Au(III) moiety into a MUF-77 framework. The IPrAu(bpdc)Cl ligand suffered from decomposition to gold nanoparticles under standard solvothermal MUF-77 synthesis conditions. Adjusting the conditions to lower temperature or aiming for a non-functionalized bpdc/IPrAu(bpdc)Cl seemingly improved stability but was accompanied by a change in the Au(III) ligand environment. An alternative room-temperature synthesis protocol was followed to obtain MUF-77 with incorporated IPrAu(bpdc)Cl. IPrAu(bpdc)Cl-$_{rt}$MUF-77 was characterized and successfully promoted the cycloisomerization reaction of hex-5-en-1-yn-3-ylbenzene. The results were very encouraging and showcased the potential of MUF-77 as a scaffold for Au(III) catalysis. We envision exploiting the modular pore environment of MUF-77 to shape the catalyst environment in future work. We propose that decorating the catalytic pocket with functional groups on the other ligands will enable us to control the selectivity and activity of the Au(III) catalyst in a way that is not easily achievable with homogeneous Au(III) catalysts.

4.4 Experimental

4.4.1 General Procedures

All starting materials and solvents were used as received from commercial sources without further purification unless otherwise noted. Hex-5-en-1-yn-3-ylbenzene was synthesized according to the reported procedure.[260] High-performance liquid chromatography (HPLC) was carried out using a Thermo Fisher Dionex Ultimate 3000 system equipped with a UV detector. HPLC conditions were adapted from the reported procedure[260] using the following conditions: Chiralpak OD-H column; 100 % hexane as eluent; flow rate of 0.5 ml/min. Products were detected according to their absorption of 215 nm UV light. Low-pressure gas adsorption isotherms were measured by a volumetric method using a Quantachrome Autosorb iQ2 instrument. All adsorption measurements used ultra-high purity gases.

4.4.2 MOF Synthesis and Characterisation

4.4.2.1 MOF Synthesis

Solvothermal synthesis of IPrAu(bpdc)Cl-*s*MUF-77 at different temperatures

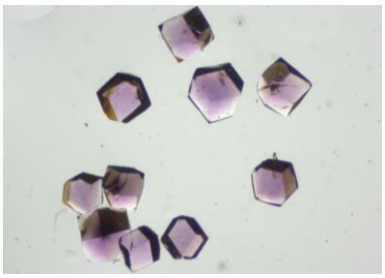

Method A, 4 mL scale: In an oven-dried 4 mL vial, hmtt (2.2 mg, 3.94 µmol), IPrAu(bpdc)Cl (4.5 mg, 5.23 µmol), bdc (1.3 mg, 7.83 µmol), benzoic acid (8.0 mg, 65.5 µmol) and $ZnNO_3 \cdot 4H_2O$ (100 µL of a 0.56 M $ZnNO_3 \cdot 4H_2O$ stock solution in anhydrous DEF, 56.0 µmol) were combined in a mixture of anhydrous DEF (850 µL) and water (50 µL). The suspension was sonicated for five minutes. The reaction mixture was placed for 20 h at 85 °C in an isothermal oven. The hot mother liquor was decanted and replaced with fresh DMF (5x). The crystals were stored in DMF.

Method B, 1.5 mL scale: In an oven-dried 1.5 mL vial, hmtt (1.1 mg, 1.97 µmol), IPrAu(bpdc)Cl (1.8 mg, 2.09 µmol), bdc (100 µL of a 0.0391 M bdc stock solution in DEF, 3.91 µmol), $ZnNO_3 \cdot 4H_2O$ (50 µL of a 0.56 M $ZnNO_3 \cdot 4H_2O$ stock solution in anhydrous DEF, 28.0 µmol) and benzoic acid (4.0 mg, 32.8 µmol) were dissolved in a mixture of anhydrous DEF (325 µL) and water (25 µL). The reaction mixture was placed for the denoted time at the respective temperature in an isothermal oven. The hot mother liquor was decanted and replaced with fresh DMF (5x). The crystals were stored in DMF.

Solvothermal synthesis of mixed ligand IPrAu(bpdc)Cl-*ms*MUF-77 at different temperatures

IPrAu(bpdc)Cl-*ms*MUF-77-(Au^{III}) was obtained through a modified **method A.** The feed ratios of bpdc and IPrAu(bpdc)Cl were adjusted to maintain the same total amount of biphenyl linker.

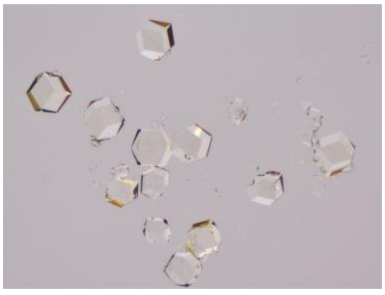

For a 25 % IPrAu(bpdc)Cl to bpdc feed ratio, in a 4 mL vial, hmtt (2.2 mg, 3.94 µmol), IPrAu(bpdc)Cl (1.1 mg, 1.28 µmol), bpdc (0.9 mg, 3.72 µmol), bdc (1.3 mg, 7.83 µmol), benzoic acid (8.0 mg, 65.5 µmol) and $ZnNO_3 \cdot 4H_2O$ (100 µL of a 0.56 M $ZnNO_3 \cdot 4H_2O$ stock solution in anhydrous DEF, 56.0 µmol) were combined in a mixture of anhydrous DEF (850 µL) and water (50 µL). The suspension was sonicated for five minutes. The reaction mixture was placed for 24 h at 85 °C in an

isothermal oven. The hot mother liquor was decanted and replaced with fresh DMF (5x). The crystals were stored in DMF.

Room-Temperature Synthesis of IPrAu(bpdc)Cl-*rt*MUF-77

Method C, large scale: In an oven-dried 4 mL vial with a magnetic stirrer, hmtt (22.4 mg, 40.1 µmol), IPrAu(bpdc)Cl (15.0 mg, 17.4 µmol) and bdc (360 µL of a 0.0391 M bdc stock solution in DEF, 14.1 µmol) were dissolved in DMF (1.12 mL). In a 1.5 mL vial, $Zn(OAc)_2 \cdot 2H_2O$ (34.5 mg, 157 µmol) was dissolved in DMF (380 µL). While stirring, the $Zn(OAc)_2 \cdot 2H_2O$ solution was quickly added to the ligand solution. The MOF formation was indicated by an immediate formation of an off-white precipitate. Upon addition, the reaction vial was closed and vigorously shaken. The reaction was stirred at room temperature for 1 h before the mother liquor was removed by centrifugation followed by decantation and replaced with fresh DMF (5x).

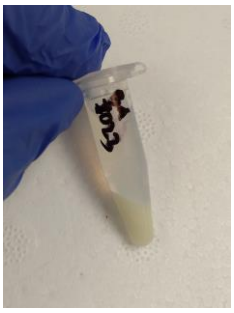

Method D, small scale: In an oven-dried 1.5 mL vial with a magnetic stirrer, hmtt (3 mg, 5.37 µmol), IPrAu(bpdc)Cl (2.0 mg, 2.32 µmol) and bdc (48 µL of a 0.0391 M bdc stock solution in DEF, 1.88 µmol) were dissolved in DMF (300 µL). In a 1.5 mL vial, $Zn(OAc)_2 \cdot 2H_2O$ (4.5 mg, 20.5 µmol) was dissolved in DMF (100 µL). While stirring, the $Zn(OAc)_2 \cdot 2H_2O$ solution was quickly added to the ligand solution. The MOF formation was indicated by an immediate formation of an off-white precipitate. Upon addition, the reaction vial was closed and vigorously shaken. The reaction was stirred at room temperature for 1 h before the mother liquor was removed by centrifugation followed by decantation and replaced with fresh DMF (5x).

4.4.2.2 ^{1}H NMR Spectroscopy of Digested MOF Samples

Solvated crystals in DMF were washed with acetone (5x) before being dried under vacuum. Desolvated nanocrystalline material was used as is.

For ^{1}H NMR spectroscopy, the desolvated crystals were digested using the following protocol: 23 µL of a 35% DCl solution in D_2O was mixed with 1 mL of DMSO-d_6 to give a DCl/DMSO-d_6 stock solution. The sample was digested in 150 µL of this stock solution together with 450 µL of DMSO-d_6. Spectra were acquired immediately following dissolution. NMR spectra were recorded at 25 °C (unless otherwise noted) on Bruker-400 and Bruker-500 Avance instruments, with the use of the solvent proton as an internal standard

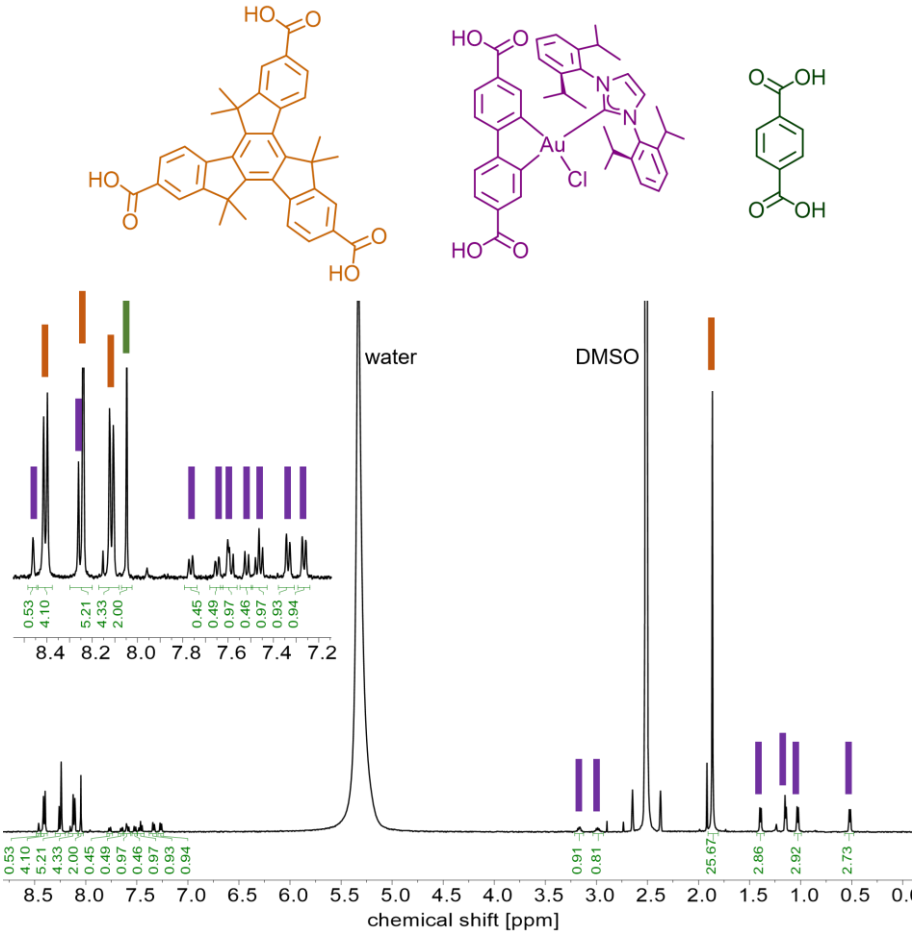

Figure 4-28 ^{1}H NMR spectrum of IPrAu(bpdc)Cl-*rt*MUF-77 upon desolvation in DMSO-d_6/DCl.

4.4.2.3 X-ray Crystallography

All powder X-ray diffraction measurements were carried out on either Rigaku Spider or Bruker D8 Venture. Rigaku Spider X-ray diffractometer is equipped with CuKα radiation (Rigaku MM007 microfocus rotating-anode generator), monochromated and focused with high-flux Osmic multilayer mirror optics and a curved image plate detector. Bruker D8 Venture diffractometer is equipped with CuKα radiation with a diamond microfocus X-ray source and a Photon III 28 detector. The two-dimensional images of the Debye rings were integrated with 2DP or Diffract Eva to give 2θ vs I diffractograms. Predicted powder patterns were generated from single-crystal structures using Mercury.

All single-crystal X-ray diffraction measurements were carried out on Bruker D8 Venture, and the measurement temperature was controlled using Oxford Cryostream if required. Bruker APEX 3 was used to collect and process data, and the structure was solved and refined using the Shelx package[168,169] under Olex2[170].

Table 4-1 Summary of X-ray crystallography data for the IPr(bpdc)Cl-*s*MUF-77.

Name	**IPr(bpdc)Cl-*s*MUF-77***
Empirical formula	$C_{59}H_{40}Au_{0.38}O_{13}Zn_4$
Formula weight	1293.89
Temperature/K	107
Crystal system	cubic
Space group	Pm-3
a/Å	29.9790(3)
b/Å	29.9790(3)
c/Å	29.9790(3)
α/°	90
β/°	90
γ/°	90
Volume/Å^3	26943.3(8)
Z	6
ρ_{calc}g/cm^3	0.478
μ/mm^{-1}	1.338
F(000)	3890
Crystal size/mm^3	0.5 × 0.5 × 0.5
Radiation	CuKα (λ = 1.54178)
2Θ range for data collection/°	2.946 to 152.19
Index ranges	-32 ≤ h ≤ 37 -32 ≤ k ≤ 37 -37 ≤ l ≤ 26
Reflections collected	220865
Independent reflections	9764 [R_{int} = 0.0335, R_{sigma} = 0.0126]
Data/restraints/ parameters	9764/18/ 207
Goodness-of-fit on F^2	2.173
Final R indexes [I>=2σ (I)]	R_1 = 0.1172 wR_2 = 0.4211
Final R indexes [all data]	R_1 = 0.1187 wR_2 = 0.4238
Largest diff. peak/hole / e Å^{-3}	3.29/-1.04

c) Gold-appended co-ligands could not be modelled. The lower-than-expected gold content was due to decomposition of the complex during synthesis

4.4.2.4 Gas Adsorption Isotherms of IPrAu(bpdc)Cl-*rt*MUF-77

Freshly prepared MOF samples were washed with acetone (5x). The samples were transferred to a pre-dried and weighed analysis tube. Excess acetone was removed under vacuum and the tube back filled with argon. The sample was then fully desolvated using the outgassing function. Temperature was increased at 1 °C per minute to 80 °C under vacuum. The sample was then held under a dynamic vacuum at 10^{-6} Torr for 24 hours. Accurate sample masses were calculated using activated samples after backfilling with nitrogen. Desolvated samples were stored in a desiccator with fresh drying agent. Air exposure was limited.

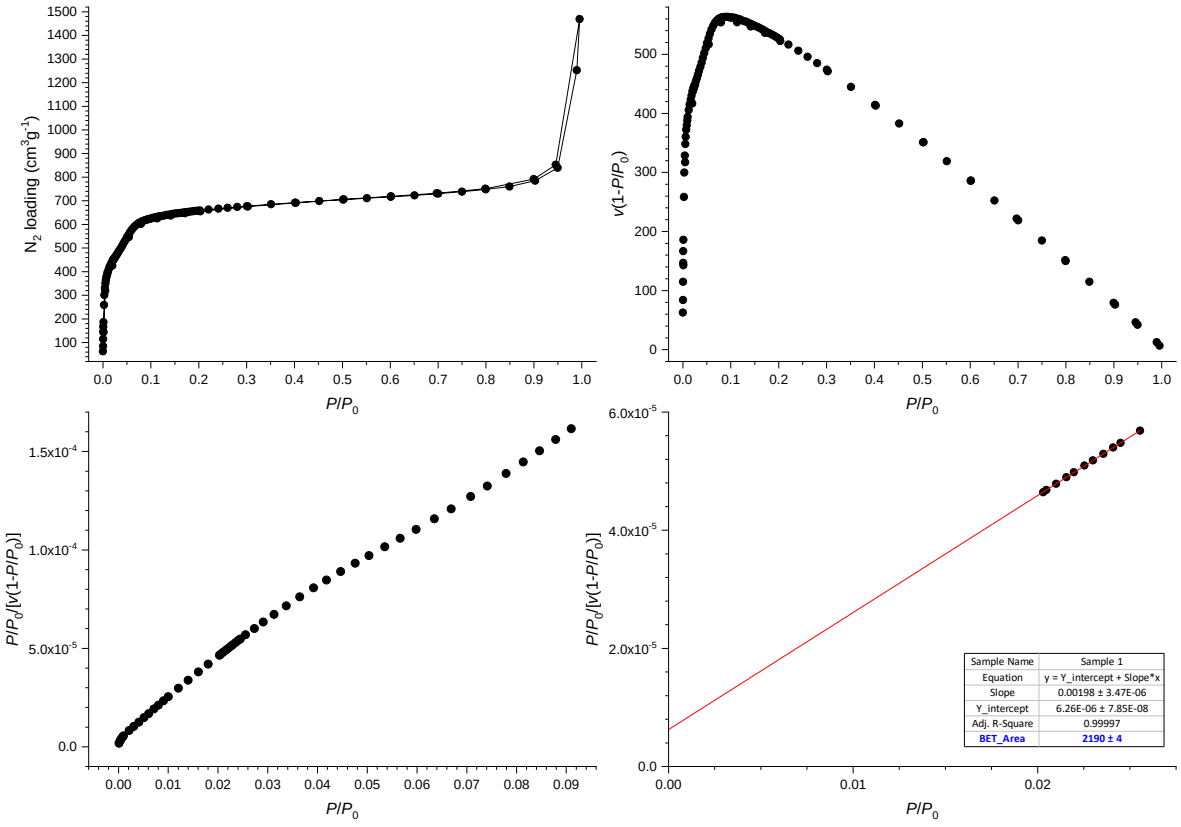

Figure 4-29 Nitrogen adsorption isotherm at 77 K and BET surface area plots for IPrAu(bpdc)Cl-*rt*MUF-77.

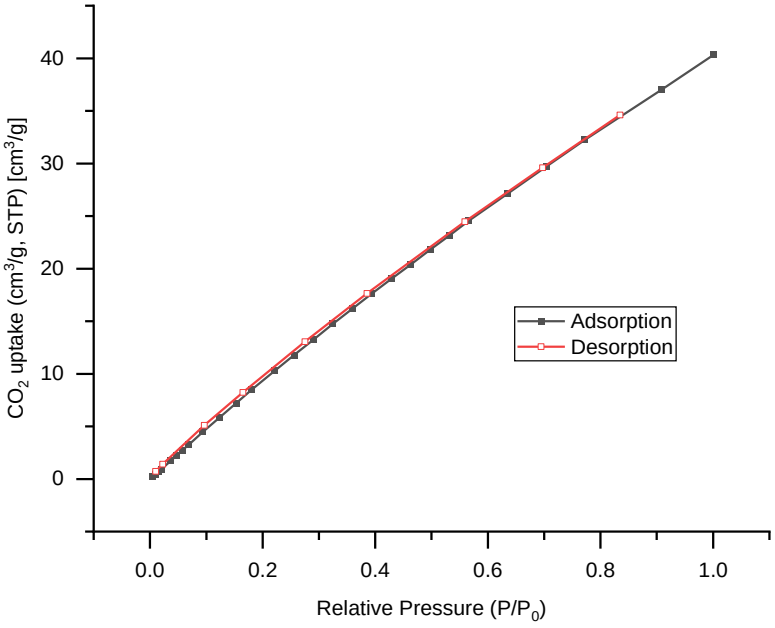

Figure 4-30 CO_2 adsorption isotherm of IPrAu(bpdc)Cl-$_{rt}$MUF-77 at 293 K.

4.4.3 Catalysis

4.4.3.1 Catalysis Trials for the Hydration of Hexynes

Hydration of 3-hexynes: IPrAu(bpdc)Cl-$_{rt}$MUF-77 was washed with γ-valerolactone (5x). IPrAu(bpdc)Cl-$_{ms}$MUF-77 and parent MUF-77 control were washed with acetone (5x) and γ-valerolactone (5x). The solvent was replaced with fresh γ-valerolactone (400 µL), 3-hexyne (100 µL), and water (18 µL). Excess AgOTF was added, and the reaction was kept at 50-60 °C.

For ^{1}H NMR spectroscopy, a small amount of sample (10 µL) was removed after the respective time interval and diluted with $CDCl_3$ (500 µL). Spectra were recorded according to the general method.

4.4.3.2 Catalysis Protocol for the Cycloisomerization Reaction

In an oven-dried 1.5 mL vial, desolvated IPrAu(bpdc)Cl-$_{rt}$MUF-77 (1-2 mg) was suspended in anhydrous DCM (0.5 mL). AgOTF or $TlPF_6$ were added in excess and hex-5-en-1-yn-3-ylbenzene (10 µL) were added. Control reactions with only halide abstraction reagents were prepared identically but without the addition of IPrAu(bpdc)Cl-$_{rt}$MUF-77. The reaction mixtures were kept undisturbed at room temperature.

A homogeneous test reaction was prepared with PPh_3AuCl and excess $TlPF_6$ under identical conditions. The crude product was isolated after 2 d by filtering the reaction mixture through a celite plug using *n*-pentane as eluent and removing the solvent under reduced pressure. The ^{1}H NMR spectra matched the reported signals for the cycloisomerization product.[260]

For ^{1}H NMR spectroscopy, 10 µL of the sample was removed from the reaction mixture after the respective time interval and diluted with 500 µL $CDCl_3$. Spectra were recorded according to the general method.

The control reactions with the respective halide abstraction reagents and the reaction with IPrAu(bpdc)Cl-$_{rt}$MUF-77 and AgOTf were kept for 12 d before being subjected to HPLC analysis. The reaction with IPrAu(bpdc)Cl-$_{rt}$MUF-77 and $TlPF_6$ was analysed after 8 d, and the homogeneous reaction after 24 h. A small

amount of sample was diluted with *n*-pentane and solids were removed by passing the solution through a 0.45 µm syringe filter.

4.4.3.3 Filtration Control Experiment

After 8 d of reaction with added IPrAu(bpdc)Cl-*rt*MUF-77 and $TlPF_6$, the suspension was centrifuged, and the reaction mixture was decanted off and passed through a 0.45 µm syringe filter to remove any solid MOF catalyst or salt. The solution was kept under catalysis conditions.

For ^1H NMR spectroscopy, a small amount of sample (10 µL) was removed after the respective time interval and diluted with $CDCl_3$ (500 µL). Spectra were recorded according to the general method.

4.4.3.4 Catalyst Recycling Experiment

After 8 d of reaction with added IPrAu(bpdc)Cl-*rt*MUF-77 and $TlPF_6$ the reaction mixture was removed. The MUF-77 catalyst was washed with DCM (3x). The solvent was removed and a solution of hex-5-en-1-yn-3-ylbenzene (10 µL) in DCM (200 µL) was added and kept at room temperature. For ^1H NMR spectroscopy, a small amount of sample (10 µL) was removed after the respective time interval and diluted with $CDCl_3$ (500 µL). Spectra were recorded according to the general method.

Chapter 5 MOF-Modified Electrodes for Bioelectrocatalysis

5.1 Overview

5.1.1 PCN-333 as Host for Enzyme Bioelectrocatalysis

Bilirubin oxidase (BOx or BOD) belongs to the class of multicopper oxidases and is a highly efficient oxygen reduction catalyst.[287,288] The enzyme contains one type 1, one type 2 and two type 3 copper centres, similar to laccases, ascorbate oxidase, and ceruloplasmin. The type 1 centre accepts electrons while the type 2 and type 3 centres are responsible for the oxygen reduction by serving as the electron-donating site.[289,290] In solution, the enzyme can be handled safely at temperatures up to 37 °C without compromising stability over short periods.[291] BOx is stable between pH 5.0 and 9.7 at 37 °C for up to 60 min. At a pH below 9, the enzyme was shown to be susceptible to degradation after five days at 5 °C. It also shows a lower sensitivity towards chloride anion inhibition in solution in contrast to laccases.[292] Chloride insensitivity is an important parameter for catalytic applications under physiological conditions. Previous studies have nevertheless shown that chloride and/or halides can inhibit direct electrochemical oxygen reduction activity e.g. thermostable bacterial BOx from *Bacillus pumilus*.[293] The most commonly employed BOx for applications in bioelectrochemistry is the fungal BOx from *Myrothecium verrucaria*, mainly due to its commercial availability.[294] BOx-modified electrodes are commonly used for bioelectrocatalytic oxygen reduction due to their high efficiency at neutral pH, because they do not produce toxic oxygen intermediates or products (e.g. H_2O_2), and due to their sustainable nature.[295] Furthermore, the modified electrodes can reduce oxygen at a high potential near physiological pH, which is especially advantageous for enzymatic biofuel cell applications to maximise output voltage.[296]

Its capability of direct electron transfer (DET) in combination with carbon nanotube (CNT) electrodes makes the system a very promising candidate for biocathodes in biofuel cell applications (Figure 5-1).[297,298] DET reactions do not require an artificial redox mediator and are therefore simpler. DET can minimize the thermodynamic overpotential required for electrochemical reactions (e.g. the O_2/H_20 reduction) to further maximise the voltage of a fuel cell set-up. Enzyme-electrode interactions can be enhanced by surface modification (e.g. grafting) on CNT-modified electrodes, leading to higher Faradaic currents.[299] An exemplary report on the immobilization of BOx on a CNT-modified glassy carbon (GC) electrode showed an enhancement of the catalytic activity by up to 26-fold compared to non-modified GC electrodes further highlighting the potential of CNT-BOx-modified electrodes.[295]

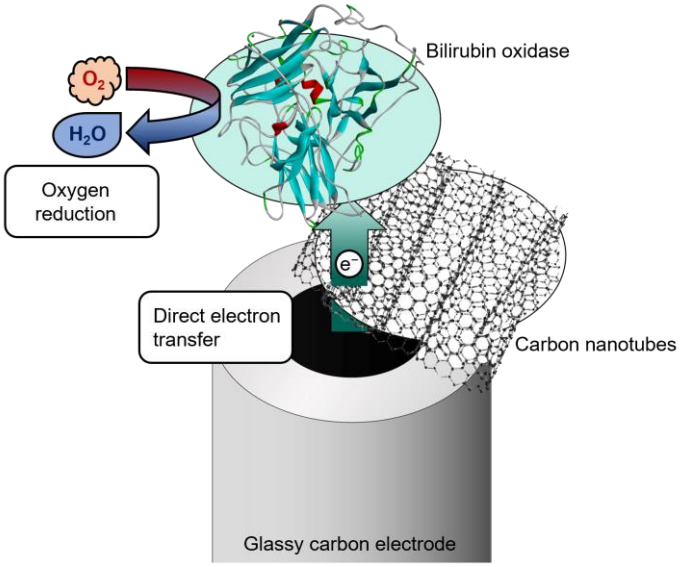

Figure 5-1 Schematic representation of direct electron transfer to the grafted BOx enzyme on a multiwalled-carbon nanotube-modified glassy carbon electrode to drive the 4-electron 4-proton bioelectrocatalytic reduction of oxygen to water.

The MOF PCN-333 is a promising host for enzyme encapsulation due to its reported good stability in aqueous media and large pore size. Following the landmark study by the Zhou group in 2015,[300] PCN-333 has been exploited as a host for different enzymes and applications.[301–303] The incorporation of enzymes like H_20_2-reducing HRP within PCN-333 motivated us to extend the scope of encapsulated enzymes and exploit the hybrid materials for the preparation of new CNT-based enzymatic electrodes to enhance bioelectrocatalysis, for example, via possible nanoconfinement and MOF 'protection' effects. A comparison of the crystal structures of HRP and BOx showed similar dimensions in the solid state, with BOx being slightly larger than HRP. We estimated the dimension of HRP around 6.6 x 4.1 x 4.8 Å (using the software Crystalmaker 9), compared to reported values[304] of 6.8 x 4.0 x 4.4 Å, and for BOx around 7.0 x 5.6 x 5.8 Å, using atom-to-atom distances found in the crystal structures. Due to the dynamic nature of enzymes in solution, those values can only serve as an indication, however, the similarities in size between HRP and BOx promised that the latter might also be suitable for the encapsulation in PCN-333. The feasibility of expanding the scope of encapsulated enzymes was demonstrated by Lian *et al.*[305] A 4,4-difluoro-4-bora-3a,4a-diaza-s-indacene (BODIPY)-functionalized, nano-sized PCN-333(Al) analogue showed good bulk stability when incubated with superoxide dismutase and catalase in water. We hypothesized that modifying BOx biocathodes with PCN-333 might lead to enhanced performance and stability of the electrodes, either through direct enzyme encapsulation or other beneficial interactions. To gain a further understanding of the behaviour of PCN-333 under enzyme catalytic conditions, we initially subjected the MOF alone to stability tests in different physiologically relevant buffers. Multiwall carbon nanotube (MWCNT)-BOx electrodes were subsequently prepared and modified with PCN-333 and BOx/PCN-333 composites to evaluate the impact of MOF modification on the oxygen reduction activity of the electrodes.

5.2 Results and Discussion

5.2.1 Synthesis of PCN-333(Fe) and PCN-333(Al)

PCN-333 synthesis procedures usually include heating tatb with a respective metal source in DMF or DEF in the presence of trifluoroacetic acid (TFA) under solvothermal conditions.[306] A variety of different metal sources can be used in the synthesis, allowing access to a series of isoreticular PCN-333 frameworks, such as PCN-333(Al), PCN-333(Fe), PCN-333(Sc), PCN-333(Cr) or PCN-333(Sc-Ti).[34,307–309] For enzyme encapsulation PCN-333(Fe) and PCN-333(Al) were primarily investigated and thus provide a promising starting point for further enzyme catalysis. We developed a strategy based on a combination of reported procedures.[307,310] Anhydrous iron(III) chloride or aluminium chloride hexahydrate and tatb ligand were suspended in DEF in a glass vial. The suspension was sonicated until all starting material was dissolved. The solution was transferred to a Teflon liner, TFA was added, and the reaction mixture was enclosed in a stainless-steel reactor. For safe practice, the reaction was carried out in a stainless-steel autoclave, due to the limitations of the standard glass vessels at higher temperatures and the use of harmful chemicals. The reaction was kept in an isothermal oven at 150 °C for PCN-333(Fe), or 135 °C for PCN-333(Al) for 12 h or 3 d to yield the MOFs as fine powders (Figure 5-2).

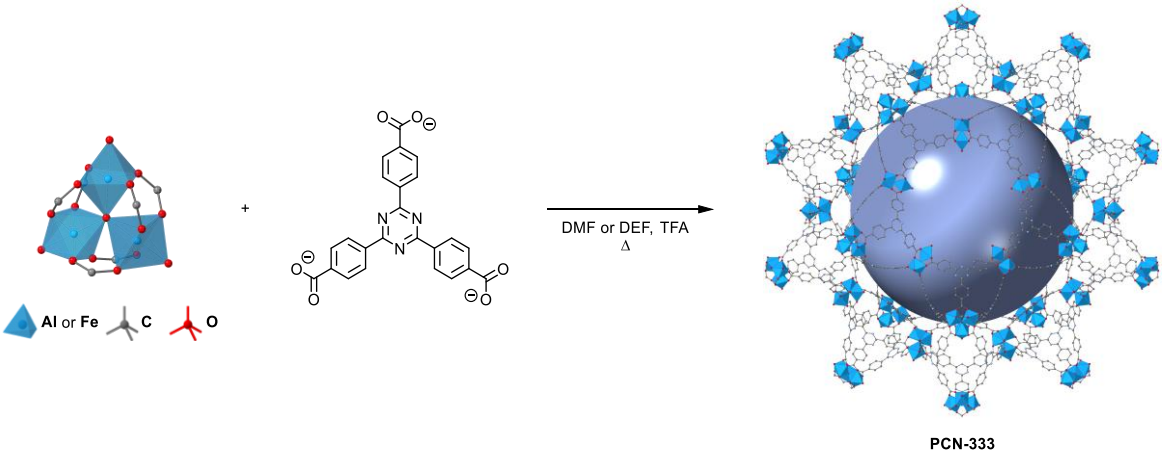

Figure 5-2 Schematic presentation of the synthesis of PCN-333 from different metal sources.

Powder X-ray diffraction showed the successful formation of PCN-333 (Figure 5-3). A comparison of the experimental data with the simulated powder pattern, obtained from the crystal structure, indicated the successful formation of PCN-333(Fe) and PCN-333(Al). The high similarity of the PXRD pattern for both variants was in good agreement with the reported crystal structures of the frameworks being almost identical.

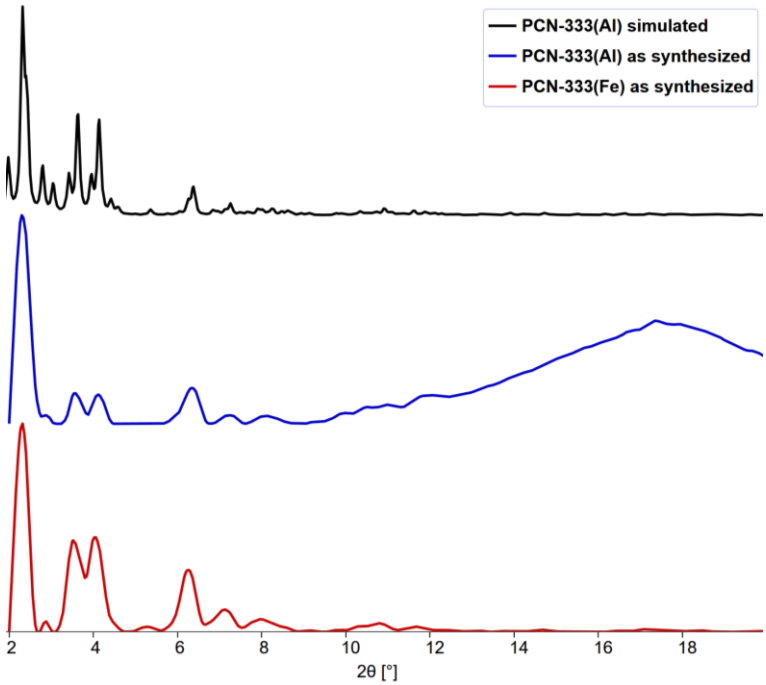

Figure 5-3 The simulated PXRD pattern of PCN-333(Al) (top, black) and the experimental PXRD pattern of synthesized PCN-333(Al) (middle, blue) and PCN-333(Fe) (bottom, red).

Broadening of characteristic PXRD peaks has been reported as an indication for nano-sized PCN-333.[305] However, in our case, it is likely a consequence of the limitations of our PXRD experimental setup as the crystals were in the same size range as reported for the original synthesis. The broad peak at 2θ = >10° was attributed to oil used in mounting the sample. The previously synthesized Fe-based material maintained its overall crystallinity after storage for six months in a desiccator (Figure 5-4). The PXRD patterns are in good agreement with the simulated powder pattern, proving that the adapted synthetic procedure was reproducibly yielding the desired PCN-333 framework.

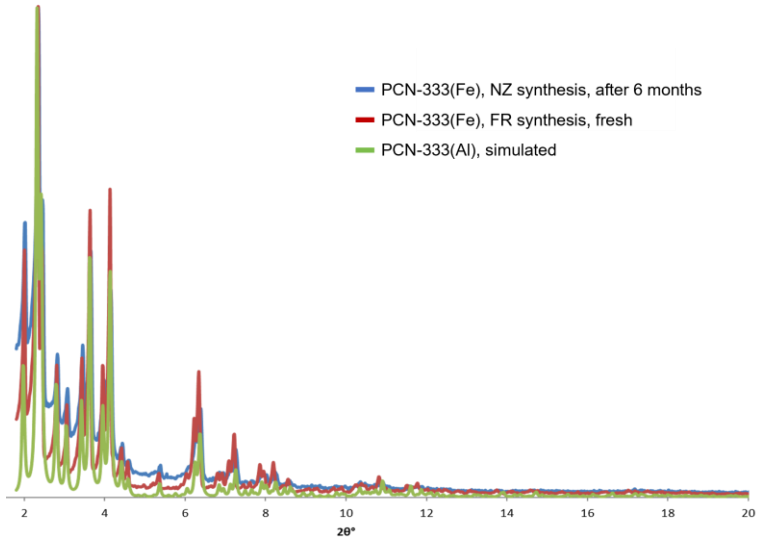

Figure 5-4 The simulated PXRD pattern of PCN-333(Al) (green) and the experimental PXRD pattern of PCN-333(Fe) after six months of storage (blue) and PCN-333(Al) synthesized at the Université Grenoble Alpes (red). PXRD patterns were collected at the Université Grenoble Alpes.

5.2.2 Stability Tests of PCN-333

Aqueous stability of a potential host framework, especially in buffers, is desirable for bioelectrochemistry applications with enzymes. While not crucial, intact crystallinity helps predict the environment of the enzyme and its behaviour under catalytic conditions. A collapse of the framework might lead to loss of protection effects, poor reproducibility, or complications relating to the porosity of the resulting hybrid material that would affect substrate diffusion to/from the enzyme catalyst. The Zhou group reported "exceptionally water-stable" performance for PCN-333 in aqueous solutions of pH 3 to pH 9.[306] Biocatalytic data was reported after 1-2 days but additional data about the MOF crystallinity was not reported. Later, Phipps *et al.* performed catalytic activity tests at pH 7 for seven days in tris(hydroxymethyl)aminomethane (Tris) buffer and showed the material retained 80-97 % of the initial activity after this period.[311] However, the authors did not include PXRD data that allowed a conclusion about the framework stability under those conditions. From the reports we expected that PCN-333(Al) and PCN-333(Fe) should show similar stability and thus decided to focus on PCN-333(Fe) for the initial aqueous stability trials. We designed our experiments to mimic the envisioned biocatalytic applications as closely as possible and followed eventual changes in bulk crystallinity by PXRD. While PXRD allowed us to efficiently and quickly display the crystallinity of a bulk sample with relatively small amounts of sample needed, it did not allow for a quantitative description of the crystallinity within the sample.

The stability upon drying from different solvents, is an important factor to consider in the preparation of the bioelectrodes; enzymatic electrodes are typically prepared via various layer-by-layer immobilisation steps with rinsing and drying. Importantly, additional PXRD experiments showed that an additional wash with acetone maintained crystallinity upon exposure of the MOF to water. We decided to focus our efforts on the stability in deionized (DI) water (pH = 7.2) and two different buffers, 0.1 M phosphate buffer (PB) at pH = 7.4 (without chloride) and 0.1 M tris(hydroxymethyl)aminomethane hydrochloride (Tris HCl) buffer at pH = 7.0. Water was used for enzyme encapsulation in many of the reported experiments on enzyme@MOF composites. While the BOx@PCN-333 has not been reported to our knowledge, we could draw comparisons to previously published observations with other enzymes. Neutral PB and Tris HCl buffer were chosen buffers due to their excellent compatibility with BOx, and simple physiological-type nature and electrolytic properties for bioelectrochemical reactions. Powder diffraction experiments showed PCN-333(Fe) retained crystallinity for at least two days in DI water. After five days, we observed a decline in crystallinity, indicated by the decreasing signal-to-noise ratio of the spectrum (Figure 5-5 A). The structural stability data was in good agreement with the reported data and underlined PCN-333's potential as a host matrix for enzyme immobilisation and biocatalytic applications (Figure 5-5 B).[300]

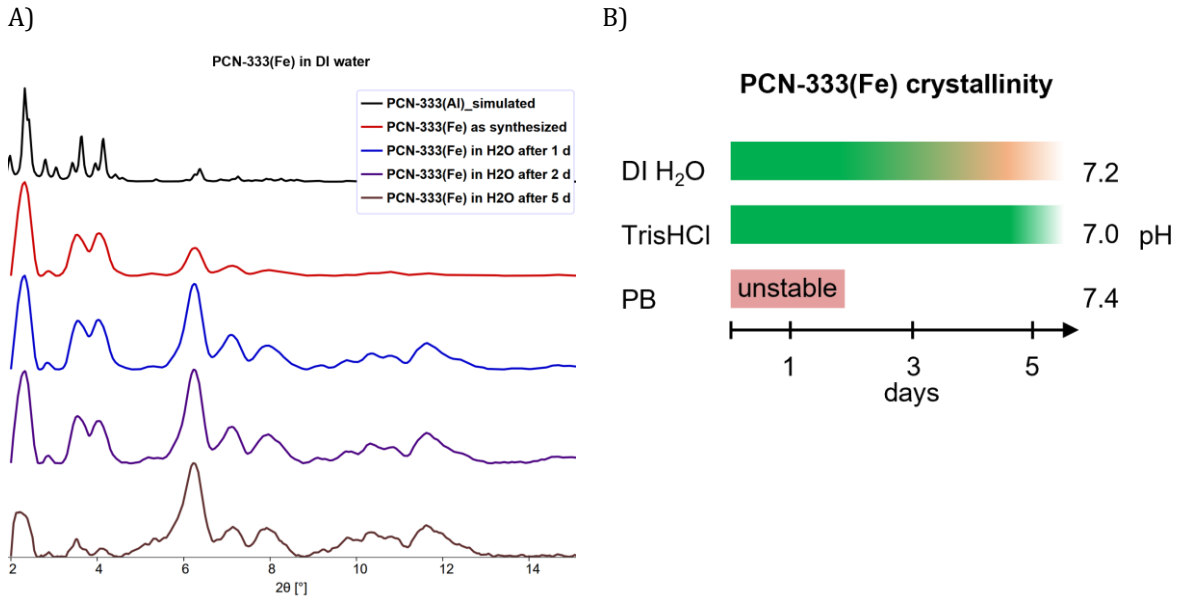

Figure 5-5 PXRD pattern of PCN-333(Fe) in deionized water over time (Figure A). The crystallinity of the framework was retained over at least two days before a decline was observed. Schematic overview of the stability data of PCN-333(Fe) in water and in different buffer solutions (Figure B).

In 0.1 M phosphate buffer (PB) at pH = 7.4, the MOF lost crystallinity within an incubation period of one hour. The susceptibility of phosphates to coordinate to Fe^{3+} and the subsequent decomposition of the framework has been previously reported for MIL-100(Fe) in phosphate-based buffers.[312,313] Nano-sized MIL-100(Fe), as an isoreticular MOF to PCN-333, degraded in 1.19 mM PBS buffer after six hours, releasing 34 ± 2.6 weight percentage of ligand. Even in diluted buffer at a concentration of 0.12 mM degradation was observed after two days. While the morphology changed, the particle sizes remained constant during the degradation. Raman microscopy allowed insight into the degradation mechanisms at the erosion fronts and using Mössbauer spectrometry the authors could determine the amorphous residues to be mainly iron phosphates. The speed of the framework collapse was also depending on the particle sizes, with smaller particles degrading faster.[313]

PCN-333(Fe) showed good stability suspended in 0.1 M Tris HCl buffer at pH 7.0 over five days with only a minimal decrease in peak intensities (Figure 5-6). The results were promising so we decided to conduct additional experiments to shed light on the stability beyond the means of bulk PXRD patterns. We measured the N_2 adsorption absorption of an as-synthesized sample and compared it to samples that were exposed to 0.1 M Tris HCl buffer at pH 7.0 for one hour before gently rinsing it with water and acetone. In this experiment, the sample was heated under vacuum at 40 °C to remove solvent under relatively mild conditions compared to traditional activation temperatures to allow comparison with enzyme@PCN-333 samples in future experiments. After exposure to buffer, PCN-333(Fe) showed a significant decrease in BET surface area from 2860 m^2/g to 1090 m^2/g. The loss of surface area could indicate incomplete solvent removal and/or partial collapse of the pores. Only minor changes in the PXRD pattern were observed. While the decline in BET surface area was more pronounced than expected from initial PXRD experiments, the maintained porosity is still high compared to most solid materials, and promising for any biocatalytic applications, proving the potential for guest incorporation and substrate and electrolyte diffusion.

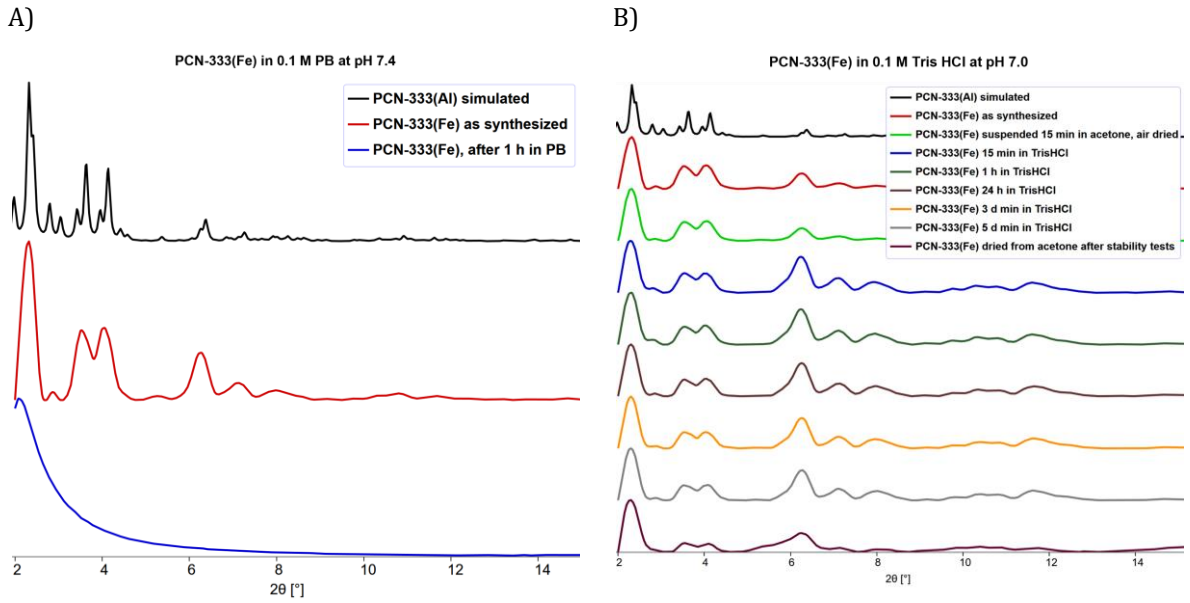

Figure 5-6 PXRD pattern of PCN-333(Fe) (A) in 0.1 M PB at pH 7.4 or 0.1 M Tris HCl at pH 7.0 and upon exposure to acetone (B).

We subsequently attempted to incorporate different enzymes into PCN-333(Fe), following the reported synthetic protocol. We focused our experiments on the incorporation of BOx due to its great potential for bioelectrocatalytic electrodes. HRP was used as a comparison, as the PCN-333/HRP hybrid material has already been reported as a working bioelectrochemical system for H_2O_2 reduction to H_2O.[314] PCN-333(Fe) was incubated with the respective enzyme for one hour, and the stability of the bulk sample then analysed by PXRD (Figure 5-7). In the presence of HRP, the MOF indicated a lower stability in water than the enzyme-free sample. After one hour in water, the PXRD pattern showed a broadening of signals, indicating an induced decline in crystallinity. The signal-to-noise ratio worsened after one day, significantly, and continued to decline over three and five days of immersing the sample in the aqueous enzyme solution. In contrast, a more rapid decline in crystallinity of the PCN-333(Fe)/HRP composite was observed in Tris HCl buffer. The characteristic peaks around 3.5 and 4.1 Å were barely visible after one hour in the solvent when in contact with HRP, indicating a partial collapse of the framework within this brief period.

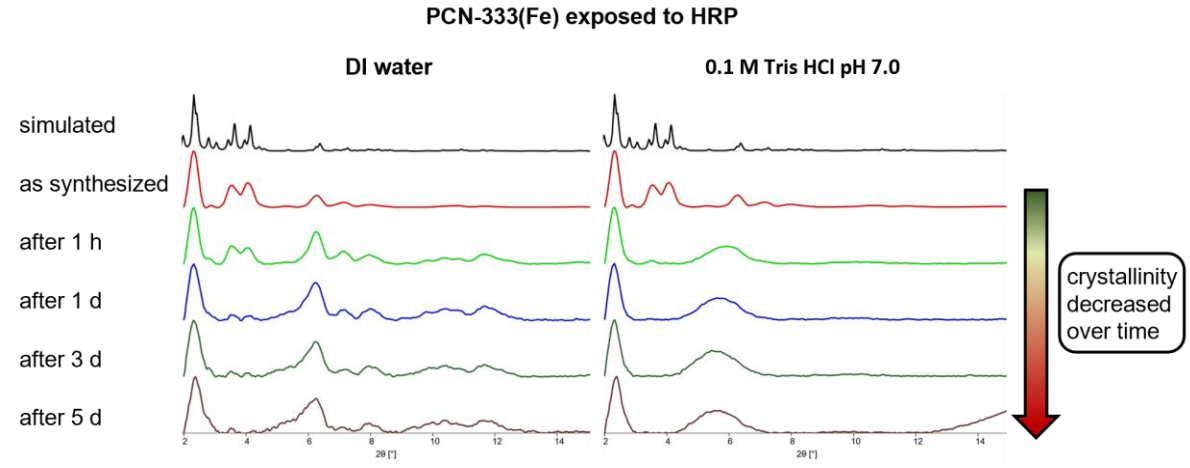

Figure 5-7 PXRD pattern of PCN-333(Fe) exposed to the enzyme HRP in water (left) and 0.1 M Tris HCl buffer at pH 7.0 (right).

We then investigated the influence of BOx in solution on the MOF stability. After one hour of incubation with enzyme in 0.1 M Tris HCl at pH 7.0, the crystallinity of the sample decreased significantly (Figure 5-8). The decrease in crystallinity was comparable to the PCN-333(Fe)/HRP samples in Tris HCl and was in contrast to stability tests without the addition of enzyme. Washing the sample upon incubation with fresh buffer after one hour did not have any impact on the crystallinity. We concluded, that the amorphization of the framework structure was permanent and that the combination of Tris HCl buffer and enzyme led to that rapid collapse. While the MOF showed only slow degradation when exposed to an aqueous solution of the enzyme, or in buffer, independently, both factors together were detrimental to the bulk crystallinity of the sample. Control experiments with PCN-333(Al)/HRP in buffer showed a similar decline in crystallinity. This was in line with our expectations that PCN-333(Fe) and PCN-333(Al) show similar stability.

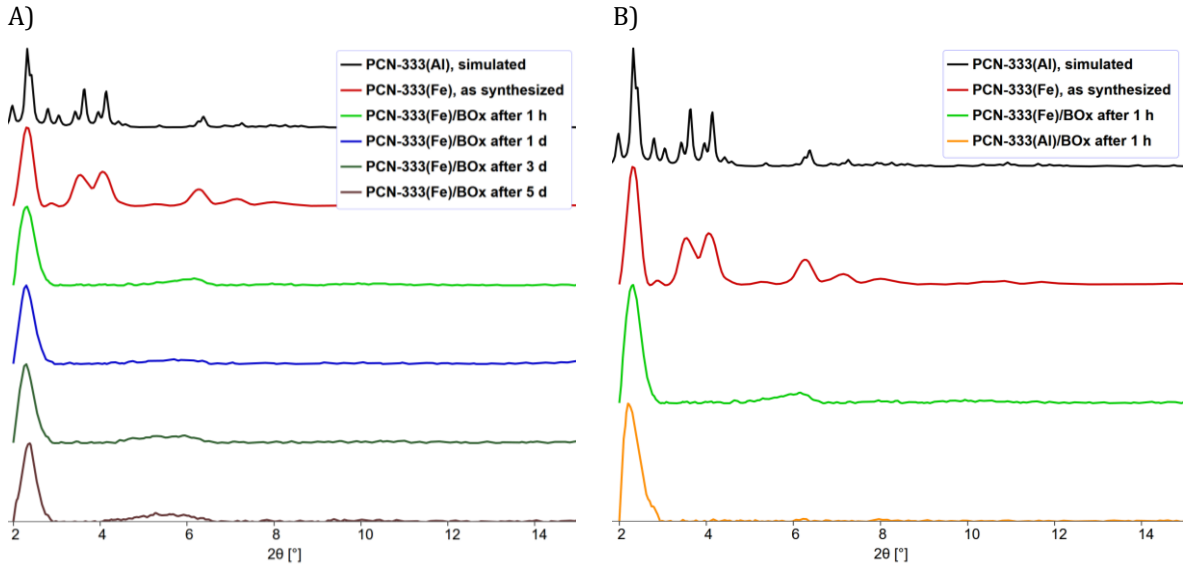

Figure 5-8 PXRD pattern of PCN-333(Fe) in the presence of BOx in 0.1 M Tris HCl pH 7.0 over time (A) and the PXRD pattern of PCN-333(Fe) and PCN-333(Al) in the presence of BOx in 0.1 M Tris HCl pH 7.0 (B) after one hour in comparison.

The loss of crystallinity contrasted with experiments conducted without the addition of HRP, which showed a slightly improved stability in comparison. Yet, the slow loss of crystallinity we observed in our tests appeared to not hinder the biocatalytic applications, for example, those reported by the Zhou group.[306] This observation is in agreement with our hypothesis that a sufficiently maintained porosity/nanostructure would still allow enzyme incorporation and could permit substrate diffusion at an electrode, even if the structure is more amorphous. Yet, as mentioned previously, it was not reported if the authors observed a similar decline in crystallinity with exposure to enzymes during their experiments. Yang *et al.* employed solid-state NMR (ssNMR) to gain a further understanding of the interactions of encapsulated enzymes within PCN-333(Al).[315] Although PCN-333(Al) was chosen in this study to facilitate ssNMR experiments, we expected that the observations could be applied to both PCN-333(Al) and PCN-333(Fe), due to the similar coordination environment of the metal ions within the MOF structure. The ssNMR studies revealed that the incorporation of the enzymes led to a decrease in overall framework flexibility due to the confinement of the enzymes within the pores, while the Al-oxo clusters showed weak interactions with the enzymes. This supports the assumption that the metal cluster-enzyme interactions were favourable for the enzyme incorporation. The observed changes in the ^{13}C NMR spectral features of the carboxylate groups indicated

a change in the metal ion coordination environment. Additionally, it was shown that the Al-atoms of the MOF showed weak interactions with the NH_2-groups of the enzyme, presumably through van der Waals forces between the metal ions and surface lysine or arginine groups. Moreover, the deprotonated form of Tris HCl, tris(hydroxymethyl)aminomethane, is known for its coordination with metal ions,[316–320] and shows a strong affinity towards coordination with Fe^{3+} ions in solution.[321,322] It is easy to imagine that the free NH_2-groups of the amino acids of the HRP and BOx enzymes could interact similarly with the metal clusters in PCN-333(Fe) or PCN-333(Al), as it was reported for the enzyme lipase. These observations were supported by reports indicating that solvents containing different amino acids and proteins had a significant impact on the stability of the MOF/enzyme composite due to additive-metal coordination, leading to framework decomposition.[323,324] We hypothesized, that PCN-333(Fe) tolerated the different additives to an extent, but that the combination of additives led to accelerated framework decomposition (Figure 5-9).

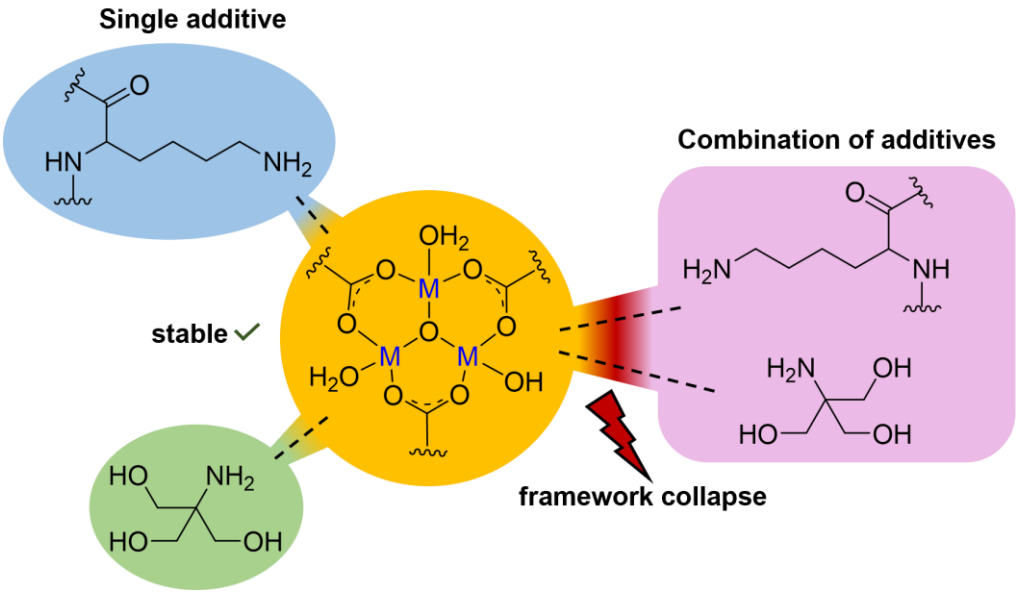

Figure 5-9 Schematic illustration of the framework decomposition induced by the simultaneous presence of both enzyme and Tris HCl buffer in solution.

5.2.3 Electrode Preparation

GC-CNT electrodes were prepared by adapting the reported procedure.[325,326] GC-CNT electrodes were either modified by drop-casting (solution adsorbs/evaporates) or incubation (solution remains during the reaction) (Figure 5-10). Multiwall carbon nanotubes in 1-methyl-2-pyrrolidinone were drop-casted onto freshly polished glassy carbon electrodes. The electrodes were carefully dried under reduced pressure to be used in subsequent modification steps. We tested different techniques and combinations to find the best compromise between practicality and MOF and enzyme stability, prioritizing the latter to ensure bioelectrocatalytic activity was retained.

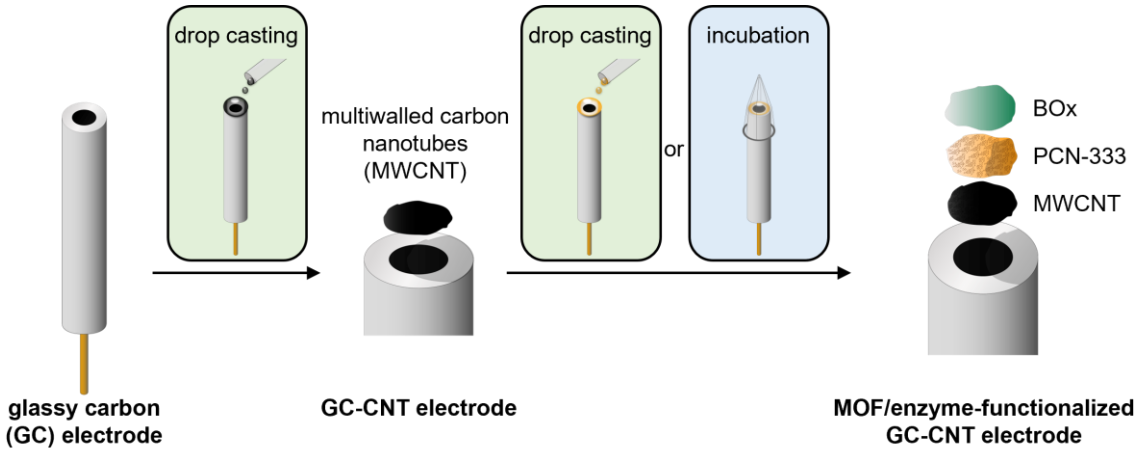

Figure 5-10 Procedure for the preparation of GC-CNT electrodes and the subsequent 'layer-by-layer' modification with MOF and enzyme for the bioelectrocatalytic application.

For drop-casting, a drop of enzyme solution or MOF suspension was carefully placed on the prepared MWCNT surface and either allowed to evaporate in air. Incubation was achieved by carefully inserting the electrode into an Eppendorf tube filled with the respective enzyme solution or MOF suspension. The enzyme immobilization process is based on simple physi-adsorption, as is widely performed in literature. The Eppendorf tube sealed the electrode, which was stored upright to ensure an even coverage with liquid. The prepared electrodes were rinsed prior to conducting bioelectrocatalytic experiments. BOx was usually handled in PB pH 7.4 and exposure to organic solvents was limited as much as possible. For example, GC-CNT electrodes were incubated with an aqueous solution of BOx overnight at 3 °C in PB. The electrodes were denoted as CNT-$_i$BOx. Handling in buffer ensured the activity of the BOx enzyme would be retained. Nevertheless, in this work, we had to develop protocols adapted to the use of MOF suspensions prepared in organic solvent. After rinsing the electrodes with ethanol, a drop of finely suspended PCN-333(Fe) in ethanol was placed on the CNT-BOx surface and allowed to dry in air to yield the new CNT-$_i$BOx-$_{dc}$PCN333(Fe) bioelectrode. Ethanol was chosen as it can be tolerated by BOx, and to limit stress on PCN-333(Fe) crystals during preparation or solvent removal.[327] In other cases, acetone was used instead, for its generally excellent compatibility with most MOFs, and volatility that limited contact time with the enzyme. In another experiment, CNT-$_i$PCN333 electrodes were prepared by incubating the GC-CNT electrodes with a fine suspension of PCN-333(Fe) in acetone for two hours, followed by rapid evaporation of the solvent in air. The obtained electrodes were further incubated with BOx overnight at 3 °C in PB to give CNT-$_i$PCN333-$_i$BOx electrodes. Based on our earlier characterization experiments, we therefore would expect loss of crystallinity (e.g. partial framework collapse) under these conditions. While crystallinity is desirable for an easier characterization and mechanistic explanation, more amorphous porous MOF structures might also provide an advantageous enzyme environment for bioelectrocatalysis, in line with previous literature concerning biocatalysis.[328] Additional experiments in Tris HCl buffer were conducted by a Master's student, Ardeshir Dadgar Yeganeh, under the supervision of Dr Andrew Gross, in collaborative work. In those experiments, short and long incubation times were explored (data not shown). As shown earlier in this chapter, the crystalline structure of PCN-333 showed better stability in Tris HCl during the incubation timeframe.

Through layer-by-layer deposition, several CNT-modified glassy carbon electrodes were functionalised with the purpose of analysing the effect of these modifiers on the bioelectrocatalysis of BOx (Figure 5-11).

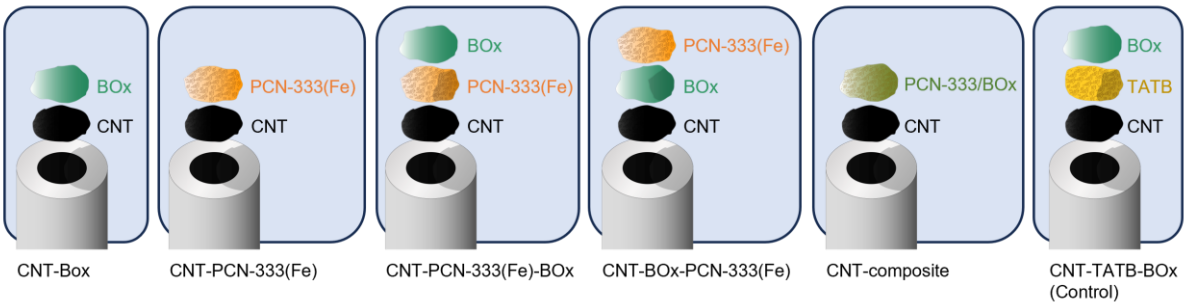

Figure 5-11 General design of the electrodes prepared by layer-by-layer assembly and used in this study.

GC-CNT electrodes were modified with either BOx, PCN-333(Fe) and the enzyme/MOF composite, BOx/PCN-333, or the tatb ligand, to study the influence of PCN-333(Fe) on the electrode performance (Figure 5-11). SEM images of PCN-333 layered on a MWCNT surface are shown in Figure 5-12 (A and B, in comparison to PCN-333(Fe) after different treatments, Figure 5-12 C and D). The electrodes were named in order of the applied layers. CNT-BOx-PCN-333(Fe), CNT-PCN-333(Fe)-BOx and electrodes CNT-TATB-BOx electrodes were designed by applying additional layers of PCN-333(Fe), BOx or free ligand as control. These electrodes contained the catalytically active BOx and PCN-333(Fe) and we were interested in analysing the influence of the different compositions on bioelectrocatalysis. Adapting the methodology of Feng *et al.*[306] we also attempted to encapsulate BOx into the PCN-333(Fe) framework and graft the CNT-BOx/PCN-333 composite on the GC-CNT electrodes. To control for the influence of MOF decomposition and the free linker on the catalytic behaviour, we grafted the free tatb linker onto a GC-CNT electrode. To our knowledge, this tripodal ligand was not previously explored in combination with bilirubin oxidase for bioelectrocatalysis. For the latter electrode, a layer of BOx was added, and the electrode was denoted as CNT-TATB-BOx.

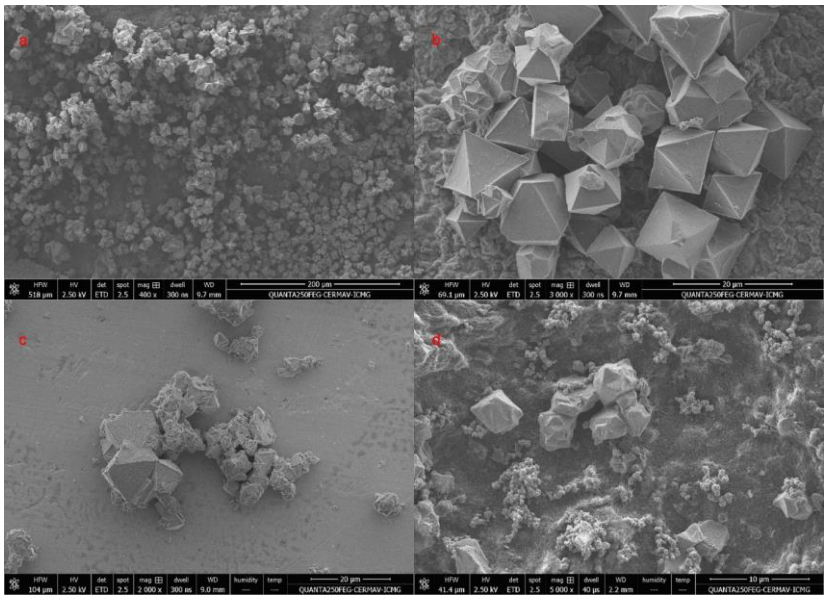

Figure 5-12 SEM image of PCN-333(Fe) layered on the surface of MWCNT (A and B), treated with Tris HCl (C) and as MOF/enzyme composite (D). SEM data was collected at the Université Grenoble Alpes.

5.2.4 Electrochemical Evaluation of Modified Electrodes

The electrochemical characterization of the CNT-modified electrodes was first performed in 0.1 M PB at pH 7.0 using cyclic voltammetry. In this technique, the potential of the working electrode (the modified electrode) is swept between different potentials (e.g. the initial/final potential and the switching potential) versus a reference electrode, and the resulting current at the working electrode is measured. First, to establish the baseline activity across the bioelectrochemically-relevant range, GC-CNT electrodes were measured across a wide potential range in the presence of ambient O_2, between an initial potential of E_i = −0.5 V and a switching potential of E_1 = 1.0 V *vs.* a saturated calomel electrode (SCE), with a scan rate υ = 20.0 mV/s. The GC-CNT electrode (Figure 5-13) showed the expected reduction peak due to the electrochemical reduction of dissolved oxygen at CNTs, and the propensity of the CNT-modified electrodes for this reaction that occurs with a low negative onset potential of ca. -0.05 V. Smaller, quasi-reversible peaks at ca. 0 to -0.25 V were attributed to redox-active oxygenated functionalities (e.g. quinones) at the CNT surface. The observed capacitive current stands in close relation to the CNT surface area while at high positive potentials of ca. 1 V we approach the solvent limit of the carbon-based electrode in aqueous media. A current spike at the beginning of the experiment was associated with a discharge current and omitted for clarity in the following voltammograms.

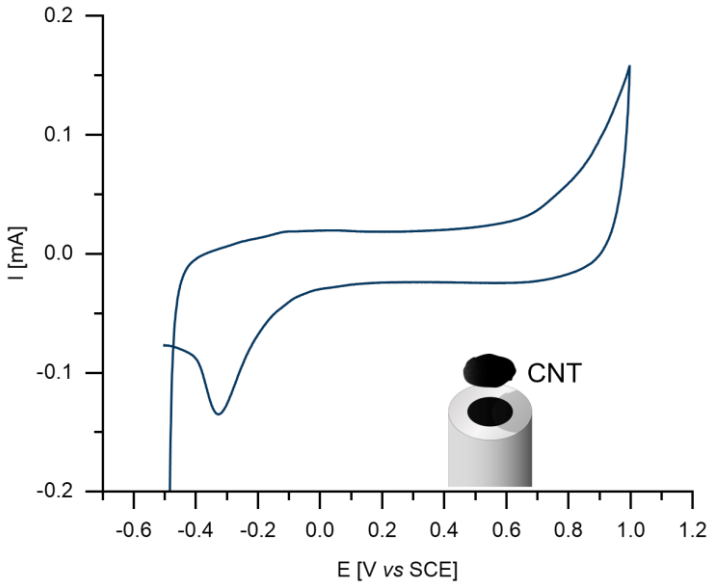

Figure 5-13 Cyclic voltammograms of a GC-CNT electrode. Cyclic voltammograms were collected in 0.1 M PB pH 7.0, with a scan rate υ = 20.0 mV/s, using a saturated calomel electrode (SCE) as reference.

Cyclic voltammograms of BOx-modified electrodes (Figure 5-14 A), CNT-BOx, showed the expected catalytic current at a high positive potential correlated to the four-electron reduction of oxygen to water,[289] indicating that the enzyme was effectively immobilised and oriented, and able to undergo the direct electron transfer reaction at the CNT electrode. Our observations were in good agreement with the reported literature. Under ambient conditions, the amount of dissolved oxygen as substrate can often be the limiting factor for electrocatalytic performance. Saturating the buffer solution with oxygen increased the substrate concentration and thus allowed us to evaluate the catalytic performance under more ideal conditions with less oxygen diffusion and concentration limitations. Oxygen was bubbled through the buffer solution for at

least 30 min prior to the experiment and a low stream of oxygen was maintained above the solution throughout the electrochemical testing. Care was taken to avoid any disturbance around the electrodes to not impact the measurements and electrode surfaces, for example to avoid random hydrodynamic effects on O_2 mass transport. Testing CNT-BOx electrodes under saturated oxygen conditions led to the expected increase in oxygen reduction current (Figure 5-14 B). This supported our expectation, that the maximum catalytic performance of the electrodes was limited by the amount of dissolved oxygen in solution and that the electrodes did not reach substrate saturation under ambient conditions.

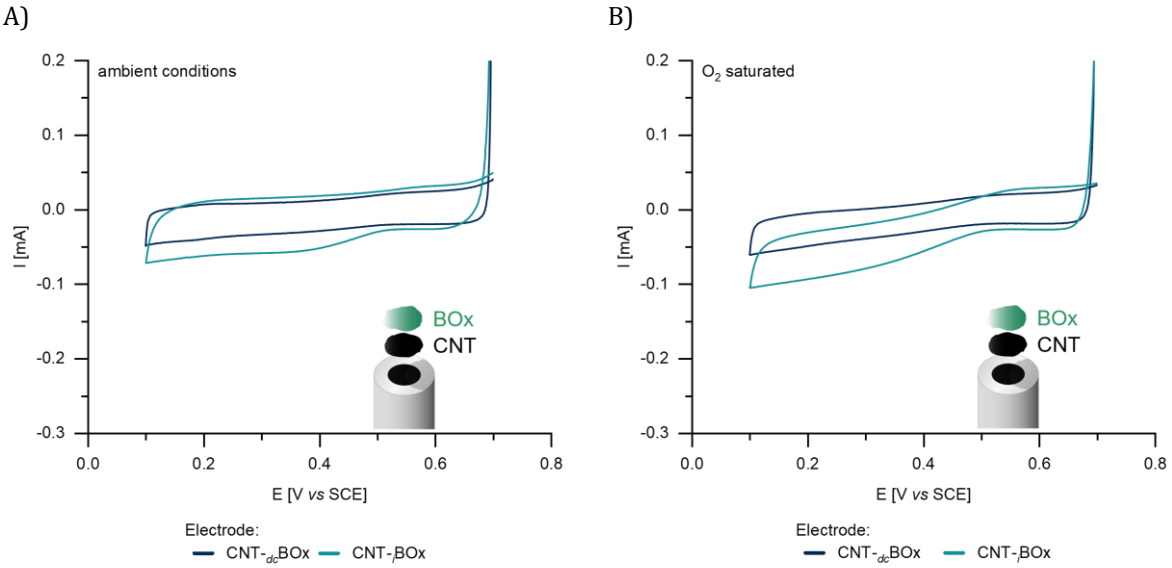

Figure 5-14 Cyclic voltammograms of CNT-BOx electrodes under ambient conditions (A) or under saturated oxygen conditions (B). Cyclic voltammograms were collected in 0.1 M PB pH 7.0, with a scan rate υ = 20.0 mV/s, using a SCE as reference.

Modifying the electrodes with an additional layer of PCN-333(Fe) led to differing results depending on the order the layers that were added to the electrode. When PCN-333(Fe) was added as an external layer onto a CNT-BOx electrode, the measured reduction current was around 26 % reduced compared to non-modified CNT-BOx electrodes (Figure 5-15). The loss in catalytic current might be explained by the solvent choice for adding the PCN-333(Fe) layer onto each electrode, that may have deactivated the immobilised enzyme, or through limited transport of oxygen caused by the MOF layer. Overall, the most promising condition when using the PCN-333 as a membrane layer was CNT-$_i$BOx-$_i$PCN-333(Fe).

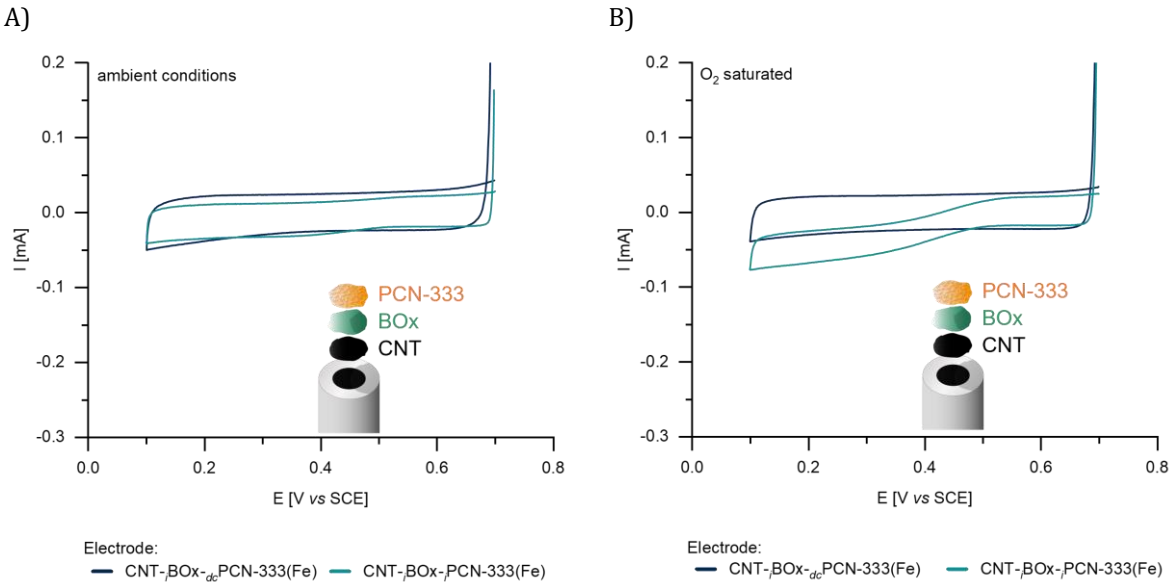

Figure 5-15 Cyclic voltammograms of CNT-BOx-PCN-333(Fe) electrodes under ambient conditions (A) or under saturated oxygen conditions (B). Cyclic voltammograms were collected in 0.1 M PB pH 7.0, with a scan rate υ = 20.0 mV/s, using a SCE as reference.

We next shifted to an alternative modification strategy whereby the MOF was used as a porous host matrix and not as an external membrane. When the layers were applied in inverted order, as seen for GC-CNT-PCN333-BOx, the electrodes showed improved performance compared to bare GC-CNT-BOx electrodes (Figure 5-16). This result appears to reflect a significant beneficial effect of the MOF structure on promoting the bioelectrocatalytic reduction of oxygen. Since our earlier data revealed the limited stability of PCN-333(Fe) in PB and PB-enyzme solution, we can expect that this enhancement may be due to the tatb linker and/or the MOF structure. We estimated the onset potentials from representative graphs under oxygen-saturated conditions from the intersection point between the tangent lines of the Faradaic and non-Faradaic currents.[329] The onset potential for CNT-BOx electrodes was estimated to be 0.52 V *vs* SCE, while we found the onset potential for CNT-PCN-333-BOx electrodes around 0.53 V *vs* SCE. The catalytic peak maxima were -0.11 mA for CNT-BOx and -0.26 mA for CNT-PCN-333-BOx, respectively. The trend towards higher onset potentials for CNT-PCN-333-BOx compared to CNT-BOx electrodes indicated the influence of additional modifications on the catalytic performance. It was reported, that by influencing the orientation of the enzyme on the electrode surface, specific redox centres within the protein can be targeted.[330] The surface charge played an important role in this process and negatively charged surface modifications, e.g. through carboxylate electrostatic interactions between the positively charged Cu T1 environment and the carboxylate functionalities, were shown to improve performance.[331] The enhancement of catalytic performance through PCN-333(Fe) modified electrodes might be explained by a similar supportive layering, increasing availability of specific redox centres, or electron transfer. A control CNT-TATB-BOx electrode showed a catalytic performance enhancement compared to the CNT-BOx electrodes and similar performance to the GC-CNT-PCN333-BOx electrode (Figure 5-17). An onset potential of 0.53 V *vs* SCE was observed. Due to the ligand enhancement affect, it is not straightforward to determine the effect of the MOF structure on the bioelectrocatalytic response. Similar observations were made in further independent experiments in Grenoble. Additional experiments are necessary to establish whether the increased performance is solely a result of MOF decomposition and ligand exposure or if the porous PCN-333(Fe)

structure provides additional benefits, and to gain mechanistic insights e.g. relating to nanoconfinement effects.

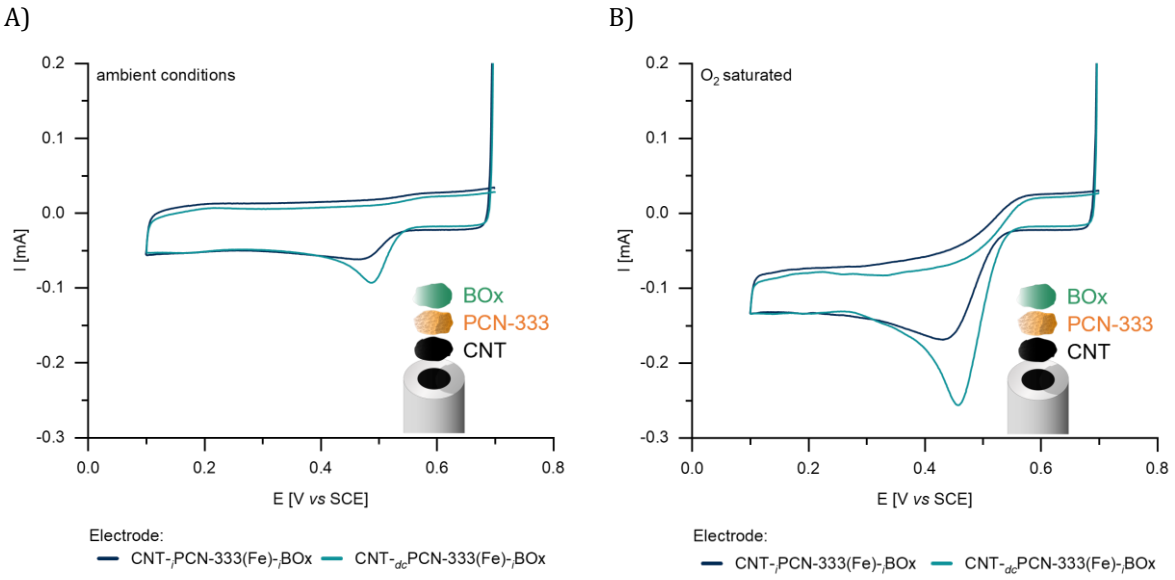

Figure 5-16 Cyclic voltammograms of CNT-PCN-333(Fe)-BOx electrodes under ambient conditions (A) or under saturated oxygen conditions (B). Cyclic voltammograms were collected in 0.1 M PB pH 7.0, with a scan rate υ = 20.0 mV/s, using a SCE as reference.

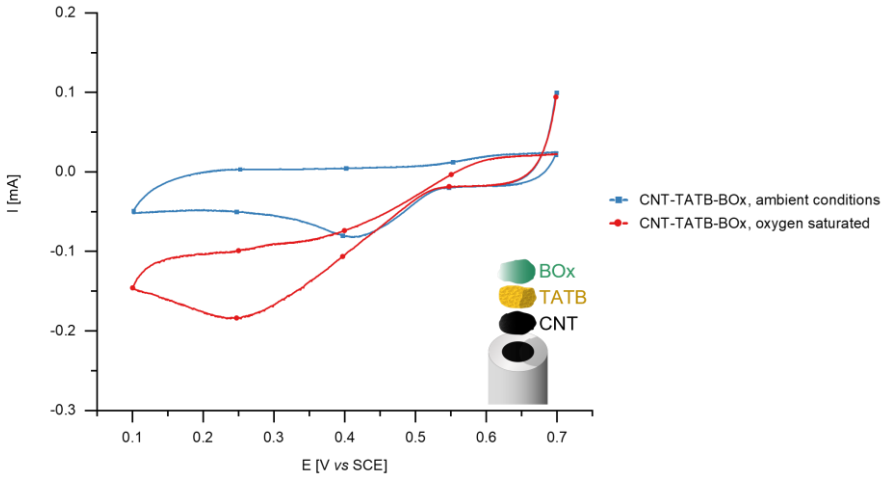

Figure 5-17 Cyclic voltammogram CNT-TATB-BOx electrodes as control. Cyclic voltammograms were collected in 0.1 M PB pH 7.0, with a scan rate υ = 20.0 mV/s, using a SCE as reference.

In the final strategy, we explored the possibility to better confine and protect the enzyme via an enzyme encapsulation process prior to electrode modification. For the preparation of the BOx/PCN-333 composite, we adapted the reported procedure used to obtain HRP@PCN-333(Fe).[306] Enzyme and MOF were combined in water for 90 min and vortexed several times to ensure thorough mixing. The suspension was then centrifuged. The solid was washed thoroughly with water before being adsorbed onto the GC-CNT electrodes. The thus prepared electrodes did not show any catalytic activity under ambient or oxygen-saturated conditions. We found it most likely that the enzyme encapsulation within the MOF matrix was not successful or that the composite-CNT interaction was not sufficient to ensure the stable attachment of the PCN-333 particles on the electrode surface. Other possibilities include the enzyme losing activity during the

encapsulation process in water, or that the enzyme was indeed encapsulated but not accessible for effects oxygen diffusion and/or electron transfer between the active site of the enzyme and the electrode. Further experiments are necessary to fully characterize any BOx/PCN-333(Fe) composite and optimize the modification procedure. For example, an adjusted composite preparation protocol led to retained catalytic activity of the prepared electrodes and even showed increased enzyme activity and stability.

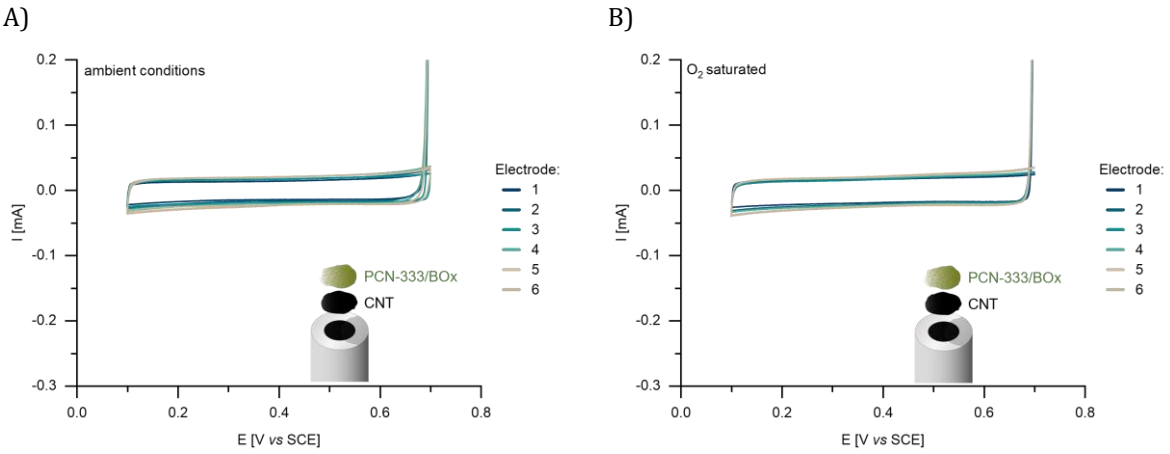

Figure 5-18 Cyclic voltammograms of CNT-composite electrodes under ambient conditions (A) or under saturated oxygen conditions (B). Cyclic voltammograms were collected in 0.1 M PB pH 7.0, with a scan rate υ = 20.0 mV/s, using a SCE as reference.

We further investigated the influence of the modifications on the retained bioelectrocatalytic activity of the grafted enzyme in the presence of an inhibitor. BOx activity is well known to be inhibited by halide anions in solution.[332] The inhibition through chloride ions was explained through an induced change of the BOx redox state and a concentration dependence was observed.[293] To establish the impact of chloride anions on modified electrodes, we repeated our cyclic voltammetry experiments with CNT-$_i$BOx and CNT-$_{dc}$PCN-333(Fe)-$_i$BOx electrodes in phosphate-buffered saline solution (PBS) at pH 7.5 (Figure 5-19). We tested two electrodes of each making and conducted our electrocatalytic tests under similar conditions. The CNT-$_i$BOx electrodes showed a decrease in bioelectrocatalytic oxygen reduction current of around 24 % of oxygen reduction activity upon exposure to chloride ion-containing PBS buffer. For CNT-$_{dc}$PCN-333(Fe)-$_i$BOx electrodes, the difference was between 15 % and 24 %. While CNT-$_{dc}$PCN-333(Fe)-$_i$BOx electrodes seemed to provide some advantages, further experiments are necessary to draw a more robust conclusion.

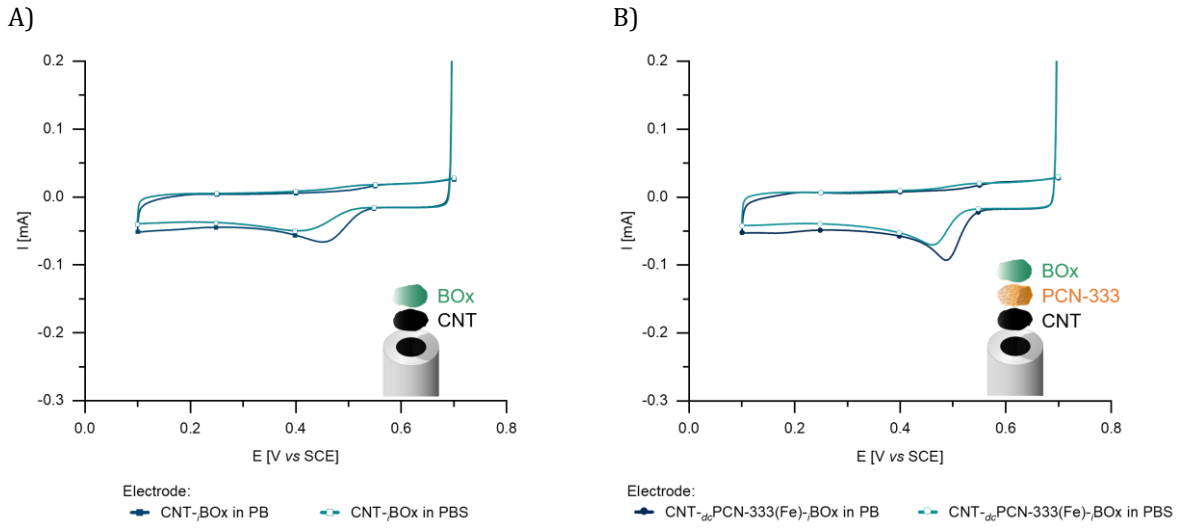

Figure 5-19 Cyclic voltammograms of CNT-$_i$BOx electrodes (A) and CNT-$_{dc}$PCN-333(Fe)-$_i$BOx electrodes (B) under ambient conditions in PB at pH 7.0 or in PBS at pH 7.5. Cyclic voltammograms were collected with a scan rate υ = 20.0 mV/s, using a SCE as reference.

To explore the longer-term stability and activity of selected electrodes we conducted chronoamperometry experiments over several days under ambient conditions in PB and subsequently in PBS. The tests were conducted at a fixed applied potential of E_i = 0.25 V. At this potential, as can be deduced from the CV data, the oxygen reduction reaction is strongly driven. Between experiments, the electrodes were stored in the respective buffer at 3 °C. Both, CNT-$_i$BOx and a CNT-CNT-$_i$PCN-333(Fe)-$_i$BOx electrodes retained their electrocatalytic activity in PB over at least six days (Figure 5-20). After exposure to chloride-containing PBS, the current observed for the CNT-$_i$BOx electrode was diminished and did not recover. In contrast, the activity for CNT-CNT-$_i$PCN-333(Fe)-$_i$BOx electrodes was only slightly impacted, even after several days. While additional tests are necessary to confirm those findings, the data indicated the potential of the supportive PCN-333(Fe) layering, which not only improved catalytic activity but decreased the impact of chloride inhibition in our tests.

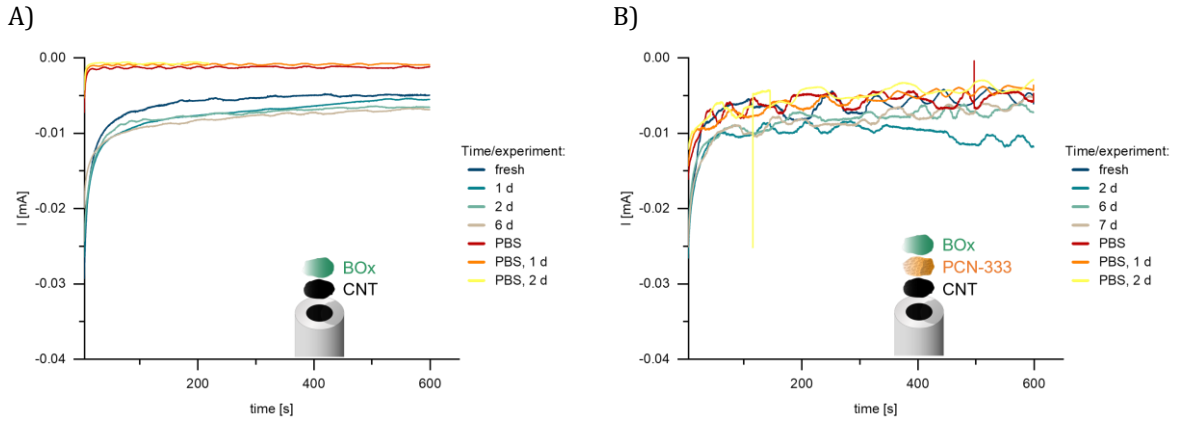

Figure 5-20 Chronoamperometry data of a CNT-$_i$BOx electrode (A) and a CNT-CNT-$_i$PCN-333(Fe)-$_i$BOx electrode (B) over time under ambient conditions in PB at pH 7.0 or in PBS at pH 7.5.

Additional experiments by Ardeshir Dadgar Yeganeh at the Département de Chimie Moléculaire, Université Grenoble Alpes under the supervision of Dr Andrew Gross were conducted following up on these studies. Additional modified electrodes were prepared, and the different electrode modifications were tested in Tris

HCl. Stability tests were also conducted with fluoride as an inhibitor. Ascorbic and uric acid, compounds often present in biological fluids, are known to interfere with bioelectrode applications. The impact of those compounds on the newly developed electrodes was also tested. From our initial tests, a new preparation method of an enzyme/MOF combination layer was developed. Further, additional hemin-functionalized electrodes were investigated as an external standard to establish the relative performance of our electrodes to this system. These electrodes profit from improved enzyme orientation, leading to high catalytic currents and low overpotentials.[333] The results further supported our observations that PCN-333 and tatb-modified electrodes showed increased activity compared to bare CNT-Box electrodes. They also exceeded the CNT-hemin-BOx electrodes and decreased the inhibitory effects of fluorides or ascorbic and uric acid[334] on electrode performance with better recovery. Combined enzyme/MOF layer modification led to slightly improved results compared to subsequent MOF/BOx or TATB/BOx layering.

5.3 Conclusion

We showed that PCN-333(Fe), while widely regarded as a very stable MOF in aqueous solution, suffered from stability issues in PB and in Tris HCl buffer when combined with HRP or BOx. This knowledge is important for the design and preparation of enzyme and MOF-modified electrodes and their evaluation. We successfully showed that modifying glassy carbon CNT-BOx electrodes with PCN-333(Fe) increased the oxygen reduction activity of the electrodes. However, the catalytic response was sensitive to the modification conditions and electrode design. Adding enzyme onto the MOF layer enhanced activity, in contrast, an inverted order led to decreased bioelectrocatalysis. The latter system, with PCN-333 used as a membrane, opens up new perspectives e.g. as a flux-limiting or protecting membrane layer to improve stability and/or increase the linear dynamic range of electrochemical biosensors. The PCN-333(Fe)-Box-modified electrodes were also more efficient in protecting the enzyme from inhibition in chloride-containing buffer. Our preliminary results with a ligand-modified electrode also showed enhanced activity. In additional experiments, functionalization with the free tatb ligand and BOx showed similar performance to MOF-BOx-functionalized electrodes, indicating, that much of the bioelectrocatalytic enhancements stemmed from improved enzyme orientation on the electrode surface. To the best of our knowledge, this class of tritopic ligands for direct electron application with BOx is not reported, nor are the PCN-333/BOx materials. Future experiments should be conducted to evaluate the impact of MOF decomposition on the electrode performance, and both the nature and extent of enzyme encapsulation. Further, it was reported that PCN-333 can be modified to increase MOF stability. Post-synthetic metal exchange allowed the synthesis of PCN-333(Cr) and PCN-333(Sc-Ti). PCN-333(Cr) showed increased stability compared to the parent PCN-333(Fe) framework while the introduction of titanium nodes extended the limited scope of titanium-based MOFs.[307–309] Those modifications might extend the stability in buffers suitable for enzyme catalysis, enabling electrode preparation without sacrificing MOF crystallinity, and should be investigated in further experiments.

5.4 Experimental

5.4.1 General

All chemicals were used as purchased. Commercial grade multiwalled carbon nanotubes (NC7000, Ø=9.5 nm, 1.5 μm length, ≥95% purity, batch A2206) were obtained from Nanocyl and used as received without purification. Bilirubin Oxidase from *Myrothecium Verrucaria* (M=68000 g/mol) was purchased from Amano, stored at -20 °C, and used as received. Purified water was obtained by water purification to a resistivity of 18.2 MΩ cm using a Millipore Ultrapure system. High purity oxygen was obtained from Messer. Powder X-ray diffraction data at the Université Grenoble Alpes was collected with a X'Pert PRO MPD PANalytical diffractometer with Cu Kα radiation (α = 1.5412 Å). All powder X-ray diffraction measurements at Massey University were carried out on either a Rigaku Spider or Bruker D8 Venture instrument. Rigaku Spider X-ray diffractometer is equipped with CuKα radiation (Rigaku MM007 microfocus rotating-anode generator), monochromated and focused with high-flux Osmic multilayer mirror optics and a curved image plate detector. Bruker D8 Venture diffractometer is equipped with CuKα radiation with a diamond microfocus X-ray source and a Photon III 28 detector. The two-dimensional images of the Debye rings were integrated with 2DP or Diffract Eva to give 2θ vs I diffractograms. Predicted powder patterns were generated from single-crystal structures using Mercury 4.0[335].

5.4.2 MOF Synthesis

PCN-333(Fe) In a sealed glass vial, tatb (59.5 mg) and anhydrous $FeCl_3$ (60.7 mg) were suspended in DMF (10 mL). The mixture was sonicated for 10 min until all solids were dissolved. The yellow solution was transferred to a Teflon liner and placed in a stainless-steel reactor. TFA (0.6 mL) was added with a syringe and the reaction vessel was closed and placed in an isothermal oven for 16 h at 150 °C. The dark brown suspension was centrifuged (4000 rpm, rt, 5 min) and the mother liquor was decanted. DMF (10 mL) was added. The centrifugation tube was vortexed for a few seconds to ensure a homogeneous dispersion of the solid. The washing process was repeated three times in DMF and subsequently three times with acetone. The solid was dried in an oven at 65 °C overnight to yield the product as an orange-brown powder.

PCN-333(Al) In a sealed glass vial, tatb (50.2 mg) and anhydrous $AlCl_3{\cdot}6H_2O$ (203 mg) were suspended in DMF (10 mL). The mixture was sonicated for 10 min until all solids were dissolved. The yellow solution was transferred to a Teflon liner and placed in a stainless-steel reactor. TFA (0.6 mL) was added with a syringe and the reaction vessel was closed and placed in an isothermal oven for 2 d at 135 °C. The colourless suspension was centrifuged (4000 rpm, rt, 5 min) and the mother liquor was decanted. DMF (10 mL) was added. The centrifugation tube was vortexed for a few seconds to ensure a homogeneous dispersion of the solid. The washing process was repeated three times in DMF and subsequently three times with acetone. The solid was dried in an oven at 65 °C overnight to yield the product as a colourless powder.

5.4.3 Stability Experiments

In an Eppendorf tube, PCN-333 (5 mg) was suspended in water or the denoted buffer solution (1 mL). After the respective time interval, the suspension was centrifuged but kept immersed. A small amount of aggregated wet sample was quickly extracted with a spatula, placed on a glass slide and carefully coated with oil. The sample was quickly mounted on an 18 mm Mounted CryoLoop and immediately measured on

either a Rigaku Spider or Bruker D8 Venture instrument. The MOF was stored in the respective solvent at room temperature and powder X-ray diffraction patterns were collected over the described time periods.

To evaluate the impact of added enzyme, PCN-333(Fe) (5 mg) was suspended in a solution of HRP (5 mg of MOF) in the respective buffer or water (1 mL) at room temperature. Continuous dispersion of the MOF was achieved either through the usage of a shaking plate or the attachment to 'ferris-wheel'-type setup, slowly rotating the Eppendorf tube perpendicular to the surface. After 1 h, the mother liquor was removed by centrifugation and replenished, where mentioned, with fresh solvent.

5.4.4 Porosity Measurements

N_2 adsorption isotherms were measured by a volumetric method using a Quantachrome Autosorb iQ2 instrument. Before the initial measurements, as-synthesized samples were activated under dynamic vacuum at 40 °C for 24 h. Upon measurement, the sample was incubated according to the conditions described in the previous paragraph. The MOF was washed with Milli-Q water (1 x 1.3 mL) and acetone (3 x 1.3 mL). The MOF was dried at 65 °C. Upon activation under a dynamic vacuum at 40 °C for 24 h the nitrogen isotherm at 77 K was measured again and the BET surface area was calculated.

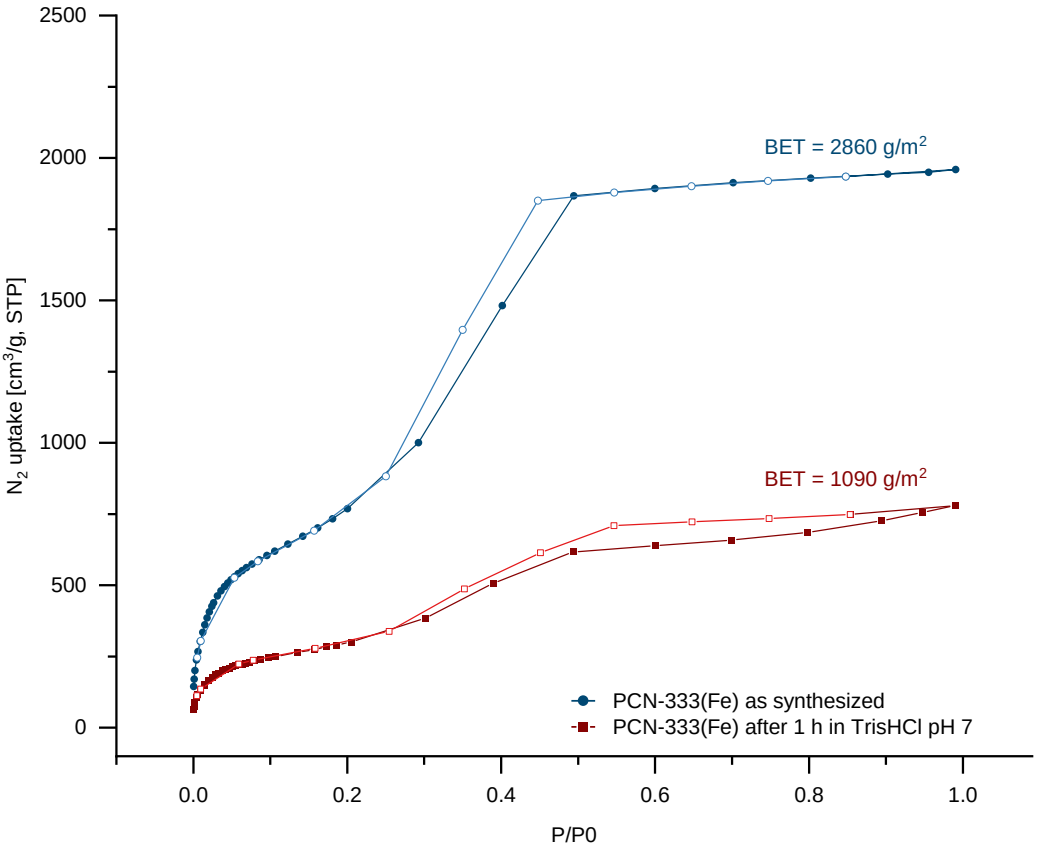

Figure 5-21 N2 adsorption isotherms of PCN-333(Fe) as synthesized and after treatment in Tris HCl pH 7 for one hour.

5.4.5 Electrode Preparation

GC electrodes GC electrodes were polished using a Presi polishing cloth with 1 µm diamond slurry. The electrodes were rinsed with water and sonicated in distilled water for 5 min. The washing process was repeated in ethanol before the electrodes were allowed to dry at air.

GC-CNT electrodes In a sealed glass vial, CNTs (5 mg) were suspended in 1-methyl-2-pyrrolidinione (1 mL). The suspension was sonicated for 2 h to achieve a homogeneous dispersion. The CNT (20 µL) dispersion was then drop-casted onto the GC electrode. The modified electrode was subsequently dried under vacuum.

GC-CNT-*i*BOx electrodes BOx (0.6 mg) was dissolved in PB pH 7.4 buffer (300 µL). For incubation GC-CNT electrodes were covered with enzyme suspension (20 µL or 40 µL) and sealed with an Eppendorf tube. The electrodes were incubated for 22 h at 3 °C.

GC-CNT-*dc*BOx electrodes BOx (0.6 mg) was dissolved in PB pH 7.4 buffer (300 µL). The enzyme solution (20 µL) was drop-casted onto the GC-CNT-BOx electrodes. The solvent was slowly evaporated at 3 °C.

GC-CNT-*i*BOx-*dc*PCN333(Fe) electrodes PCN-333(Fe) (0.6 mg) was suspended in ethanol (300 µL). The MOF suspension (20 µL) was drop-casted onto the GC-CNT-*i*BOx electrodes. The electrodes were carefully dried under reduced pressure.

GC-CNT-*i*BOx-*i*PCN333(Fe) electrodes PCN-333(Fe) (0.5 mg) was suspended in water (250 µL). GC-CNT-PCN333(Fe) electrodes were prepared by incubation at rt for 20 h. For incubation the electrodes were rinsed with water, covered with MOF suspension (40 µL) and sealed with an Eppendorf tube.

GC-CNT-*i*PCN333(Fe) electrodes PCN-333(Fe) (0.5 mg) was suspended in acetone (250 µL). GC-CNT-PCN333(Fe) electrodes were prepared by incubation at rt for 2 h. For incubation, the electrodes were covered with MOF suspension (20 µL) and sealed with an Eppendorf tube. The electrodes were allowed to dry at air.

GC-CNT-*dc*PCN333(Fe) electrodes PCN-333(Fe) (0.5 mg) was suspended in acetone (250 µL). The MOF suspension (20 µL) was drop-casted onto the GC-CNT electrodes. The electrodes were allowed to dry at air.

GC-CNT-*dc*PCN333(Fe)-*i*Box electrodes BOx (0.5 mg) was dissolved in PB pH 7.4 buffer (250 µL). For incubation, GC-CNT-DCPCN333(Fe) electrodes were covered with enzyme suspension (40 µL) and sealed with an Eppendorf tube. The electrodes were incubated for 22 h at 3 °C and rinsed with ethanol.

GC-CNT-TATB-BOx electrodes tatb (0.5 mg) was suspended in acetone (250 µL). The ligand suspension (20 µL) was drop-casted onto the GC-CNT-BOx electrodes. The electrodes were allowed to dry at air.

GC-CNT-*i*PCN333(Fe)-*i*BOx electrodes BOx (0.6 mg) was dissolved in PB pH 7.4 (300 µL). For incubation, GC-CNT-PCN333(Fe) electrodes were covered with enzyme suspension (20 µL) and sealed with an Eppendorf tube. The electrodes were incubated with BOx for 20 h at 3 °C.

GC-CNT-Composite electrodes PCN-333(Fe) (4.0 mg) and BOx (4.0 mg) were suspended in water (0.5 mL). The suspension was kept at room temperature for 90 min. During that period, the suspension was

vortexed several times to ensure dispersion. The solids were isolated by centrifugation and the mother liquor was replaced with fresh water three times. After the last washing step, the suspension was separated by centrifugation one more time and the isolated solid was suspended in water (1 mL). This suspension was then used for grafting onto the prepared GC-CNT electrodes by drop casting (20 µL) or incubation (40 µL).

5.4.6 Electrochemistry

Electrochemical measurements were performed using a Biologic VMP3 Multi Potentiostat with EC-lab software. Experiments were performed at room temperature. A conventional three-electrode cell setup was used comprising a modified GC working electrode (Ø= 3 mm), a saturated calomel reference electrode (SCE), and a Pt wire counter electrode. Electrochemical experiments were performed in 0.1 M phosphate buffer (PB) pH = 7 or phosphate-buffered saline (PBS) pH7.5 under ambient or oxygen-saturated conditions. Oxygen saturation was achieved by bubbling purified oxygen through the buffer solution for at least 30 min prior to the experiment. A low oxygen flow was maintained throughout the experiments and care was taken that the bubbles did not cause disturbance near the electrodes. The bioelectrodes were rinsed with water prior to electrochemical testing and were stored in fresh buffer solution at 3 °C between experiments. Cyclic voltammograms were collected between an initial potential E_i = −0.5 V and a switching potential E_1 = 0.7 V *vs.* a saturated calomel electrode (SCE) unless otherwise noted, with a scan rate υ = 20.0 mV/s in 0.1 M PB. Chronoamperometry experiments were performed in fresh buffer with E_i = 0.25 V and data was recorded every 0.1 s.

Chapter 6 Summary and Perspective

6.1 Current Work

MUF-77 is a versatile platform for the incorporation of catalytic moieties. Its multicomponent structure provides a pore environment that can be exploited to impact the performance of the embedded catalyst. In this work, we deepened our understanding of the MUF-77 synthesis and discovered several new promising MOFs. We synthesized different transition metal-functionalized ligands to expand the scope of catalytic motifs that can be embedded in MUF-77. These represent the first examples of transition metal catalytic systems in MUF-77, moving beyond the organocatalysts employed in earlier studies. We also developed post-synthetic strategies for ligand exchange in MUF-77 and applied alternative synthesis protocols to improve complex stability throughout the synthesis. While we encountered challenges with the decomposition of some embedded transition metal complexes, we achieved promising results with certain Au(I) and Au(III) systems. We further expanded our scope to investigate the interplay of MOFs with enzymes in electrocatalysis.

In Chapter 2 we investigated typical crystalline side products from the MUF-77 synthesis. Experiments with only tritopic linker, hmtt, yielded four different new frameworks, which were characterized. We were able to establish reproducible synthesis protocols for two of the MOFs, but we were not successful in tuning the parameters to produce the other frameworks reliably. With the addition of a second, ditopic organic linker the product formation was shifted towards two new multicomponent MOFs, M[$Zn_4O(hmtt)_2(bpdc)_{0.5}$] and M[$Zn_4O(hmtt)_2(bdc)_{0.5}$]. The new MOFs were characterized. The findings supported our empirical observations that the formation of MUF-77 from hmtt, bpdc, and bdc is preferred under ideal conditions. If a ditopic linker is removed from the synthesis, either directly or resulting from poor solubility, steric hindrance, or unfavorable interactions in solution, the newly discovered multicomponent MOFs seemed to be favored. When the reaction conditions are altered sufficiently, several MOFs are accessible from each linker, as shown in the example of hmtt. These insights are valuable to improve the outcome of MUF-77 syntheses with novel linkers, and the new MOFs expand the scope of potential multicomponent MOFs. While the limited stability after solvent removal is a disadvantage, multicomponent MOFs are promising candidates for the incorporation of different catalysts to exploit the frameworks' unique pore environments. The high porosity of M[$Zn_4O(hmtt)_2(bdc)_{0.5}$] makes it also a potential target for gas separation applications, where isoreticular ligand exchange could alter selectivity for different gasses.

In Chapter 3 we broadened our scope of catalysts by moving from traditional organocatalytic systems to embedding transition metal complexes. Inspired by literature examples, we attempted to incorporate bipyridyl units in MUF-77 but attempts to form the MOF were unsuccessful. We successfully introduced diphenyl- and diethyl phosphine ligands into MUF-77. Ligand oxidation was minimized by synthesizing the MOF under inert conditions. Metalation of nanocrystalline samples to form a Au(I) complex was promising, however, we could not confirm the complex formation by SXRD in larger crystals. Phosphoramidite ligand precursors were successfully synthesized and metalated, but the complex was not stable during the final hydrolysis step. Instead, we incorporated the phosphoramidite by post-synthetic modification of 2,2'-dihydroxy-bpdc-functionalized MUF-77. Metalation of the ligand was attempted but limited ligand

stability during MOF digestion for NMR interfered with the analysis. Functionalization of bpdc with a Au(I)-NHC complex was completed. While the complex decomposed under solvothermal MOF synthesis conditions, the Au(I)-NHC-linker was successfully embedded within MUF-77 following an alternative and milder room-temperature approach. However, the complex suffered from decomposition over time. We also attempted to install the complex through post-synthetic modification of MUF-77. Unexpectedly, the reaction led to gold nanoparticle formation within the MOF pores. This reaction was unique to the imidazole functionalized linkers and was not observed with parent MUF-77. The nanoparticles were catalytically active in the oxidation of benzyl alcohol. The pore-directed nanoparticle formation might allow for precise size control, a property critical for the catalytic performance,[227,336] and should be evaluated in future work. Further, we synthesized an acyclic Au(I)-carbene functionalized linker precursor. The complex suffered from decomposition during the final hydrolysis step towards the MOF linker. Attempts to introduce the complex by post-synthetic modification of secondary amine-bearing linkers were unsuccessful. We propose that future adjustments of the ligand design, for example increasing the steric bulk around the NHC coordination site, would stabilize the potential complexes. However, size limitations by the MUF-77 pore need to be considered. Shifting the focus back to organocatalysis shows potential for our novel linker and MUF-77 systems beyond transition metal catalysis. NHCs and phosphines are known as efficient organocatalysts.[337–340] For example, phosphine catalysts have successfully been employed in Michael additions,[341] nitroaldol reactions,[342] enantioselective acylations,[343] and asymmetric Morita-Baylis-Hillman reactions.[208] With the functionalized MUF-77 systems in hand, the potential for organocatalytic applications should be investigated in future work.

In Chapter 4, we evaluated a Au(III) functionalized ditopic linker, IPrAu(bpdc)Cl, for incorporation into MUF-77. While solvothermal synthesis attempts, with or without ligand dilution with bare bpdc, led to the decomposition of the ligand, our milder room-temperature synthesis protocol allowed to form IPrAu(bpdc)Cl-$_{rt}$MUF-77 without impacting the complex stability (Figure 6-1). The MOF successfully promoted the Au(III)-catalyzed cycloisomerization reaction of hex-5-en-1-yn-3-ylbenzene. Catalyst leaching was not detected, and the MOF retained crystallinity and catalytic activity upon recycling. In future work, the potential of MUF-77 as a catalytic scaffold should be fully exploited by modulating the pore environment to influence catalyst performance.

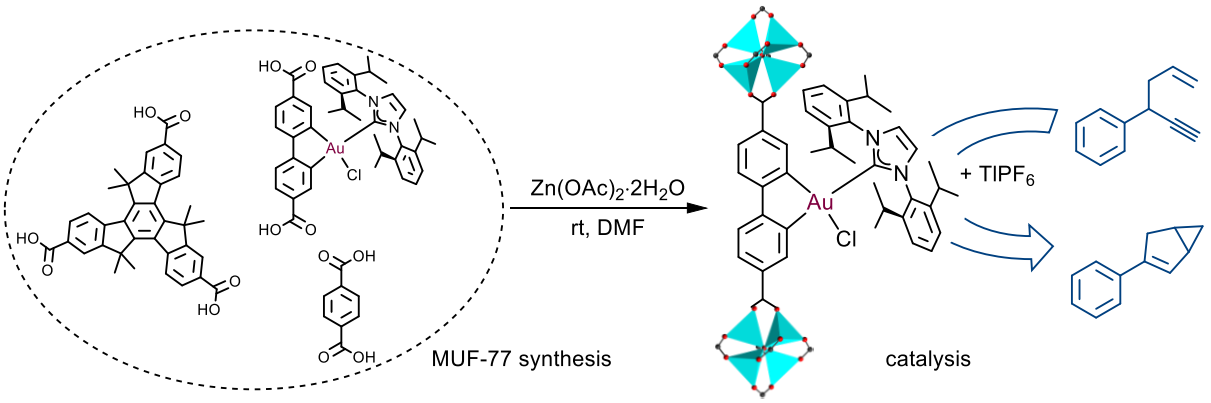

Figure 6-1 Synthesis of IPrAu(bpdc)Cl-$_{rt}$MUF-77, a Au(III)-catalyst embedded in MUF-77.

In Chapter 5 our interest in MOF catalysis led us to explore MOF-enzyme interactions. We investigated the enzyme bilirubin oxidase in combination with the MOF PCN-333 for the catalytic reduction of oxygen. We evaluated the stability of PCN-333 in different buffers and with different additives for later use in electrocatalysis with bilirubin oxidase-functionalized electrodes. For the bioelectrocatalytic application, glassy carbon electrodes were modified with multi-walled carbon nanotubes. Through layer-by-layer deposition, MOF, enzyme, or MOF/enzyme composite materials were grafted onto the electrodes by drop-casting or incubation. The new electrodes were subjected to electrocatalytic testing under ambient conditions or oxygen saturation. Layering the enzyme on top of the MOF improved the catalytic activity and stability toward inhibiting chloride ions in solution. In additional collaborative work by our colleagues at the Université Grenoble Alpes a similar impact was observed by layering the free ligand instead of the MOF, indicating MOF decomposition was a major factor in the shift in performance. Overall, the bioelectrodes showed improved catalytic performance and stability, but additional testing is needed to understand the underlying mechanisms. Further experiments under conditions supportive of PCN-333 stability should be conducted to understand the enzyme/MOF interactions and to guide further electrode design.

Overall, we successfully characterized several new MOFs and deepened our understanding of the MUF-77 formation. Several promising transition metal complexes were evaluated for their incorporation into MUF-77. Integration of a Au(III) complex into MUF-77 yielded IPrAu(bpdc)Cl-*rt*MUF-77, which is a very promising candidate for tuning the catalytic performance by altering the pore environment of MUF-77. We also evaluated potential of modifying bioelectrodes with MOFs like PCN-333 and found promising improvements in performance and stability.

6.2 Future Organocatalysts for MUF-77

We propose a post-synthetic modification protocol for installing a sulfonic acid functionality within the MUF-77 pore (Figure 6-2). In preliminary tests, we observed the full conversation of an amino-functionalized bpdc linker with 2-sulfobenzoic acid cyclic anhydride. Under optimized conditions, MUF-77 demonstrated good stability during the procedure. In preliminary catalytic trials, the system showed promising activity as Brønsted acid catalyst for the ring-opening reaction of styrene oxide.[344–346] The post-synthetically modified MOF displayed superior catalytic performance compared to MOFs obtained through a direct synthesis approach, highlighting the advantage of the post-synthetic protocol. We suggest that similar post-synthetic catalyst incorporations should be evaluated for other organocatalysts in MUF-77, as they overcome potential catalyst poisoning during the MOF synthesis and improve catalytic performance. Brønsted acid catalysts are promising candidates for several reactions, including Mannich-type reactions and other asymmetric transformations.[347–351] In future work, the sulfonic acid-MUF-77 catalyst should be evaluated for its broad catalytic performance. We see much potential for our catalyst to be used in remote asymmetric induction through MUF-77, as currently developed by our group. Brønsted acid-MUF-77 catalysts allow us to expand the scope of reactions, and the performance upon pore modulation should be examined. Further, the catalysts might be exploited for cooperative catalysis through additional functionalization of the other MUF-77 linkers.[352]

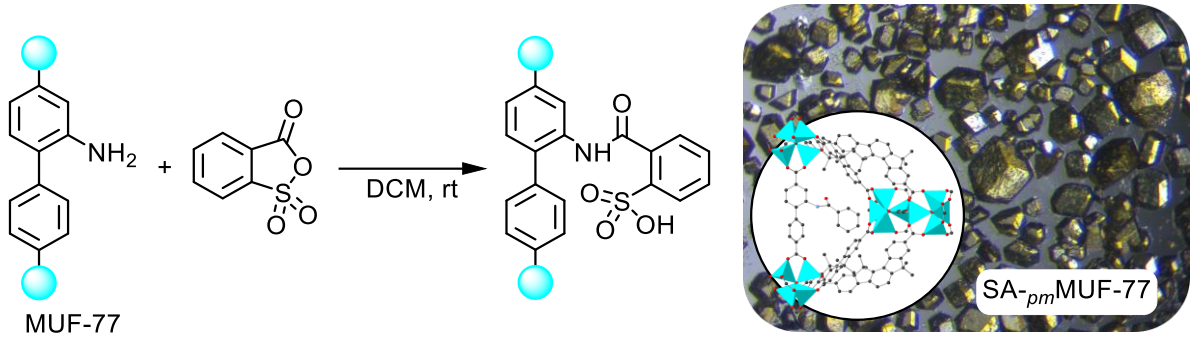

Figure 6-2 Post-synthetic synthesis of a novel sulfonic-acid MUF-77 catalyst.

In preliminary experiments, we identified the secondary amine functionalized MUF-77, az-$_s$MUF-77 (Chapter 5) as a potential organocatalyst. Secondary amines provide powerful tools for organocatalytic applications.[353,354] Preliminary experiments showed that the MOF catalyst successfully promoted the aldol reaction of different *para*- or *meta*-nitrobenzaldehydes with acetone (Figure 6-3). The MOF was also active in the Friedel-Crafts alkylation of 2-chloro-5-nitrobenzaldehyde with acetone and *trans*-β-nitrostyrene with indole.[355] Proline is well-known for promoting the Hajos-Parrish-Eder-Sauer-Wiechert reaction.[153,154,356,357] In contrast, our catalyst did not yield the desired Hajos-Wiechert-ketone when added to 2-methyl-2-(3-oxobutyl)cyclohexane-1,3-dione but led to the formation of a reported triketone.[358] In DMF and other solvents, the control reaction with parent MUF-77 showed significant background reactivity, however, in acetonitrile, background reactions were minimized and the az-$_s$MUF-77 led to three times higher consumption of starting material. Similarly, while az-$_s$MUF-77 was an active catalyst for the methanolysis of carbic anhydride, background reactions were observed. While the protocols for the catalyst testing needed further improvement, the initial results show the potential of az-$_s$MUF-77 as a versatile organocatalyst that should be exploited further in future work.

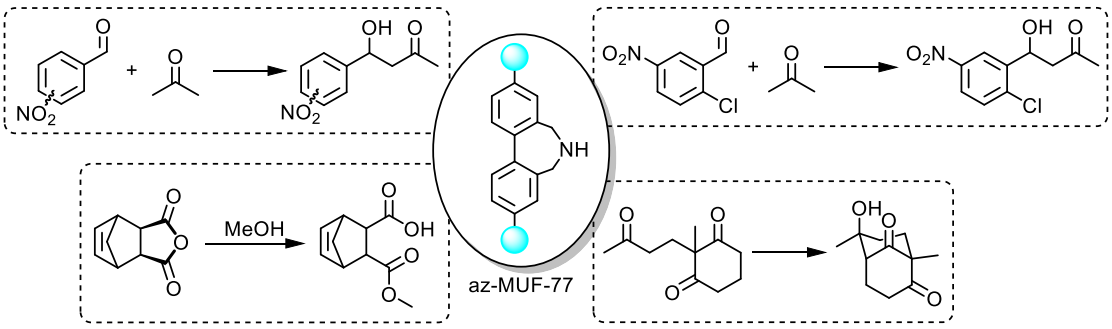

Figure 6-3 Reactions catalysed by az-MUF-77.

Further provisional results indicate that different chiral guanidine-functionalized MUF-77 materials are good catalysts for the Michael Reaction of β-nitrostyrene and dibenzoylmethane (Figure 6-4).[359–361] With increasing volume of the modulator group, the conversion slowed down significantly, and we observed differences in enantioselectivity depending on the chosen pore modulator. For example, pore modulation with (*S*)-Boc-protected-proline-bdc led to an improvement in ee from 9.0 to 28.7. The MOF also catalysed the reaction of cyclohex-2-en-1-one with malonitrile,[362,363] but the formation of three different products complicated the analysis and indicated a lack of product selectivity. While those results were promising,

further experiments are necessary to understand the interplay between pore modulator and catalyst and to evaluate more catalysts and reactions.

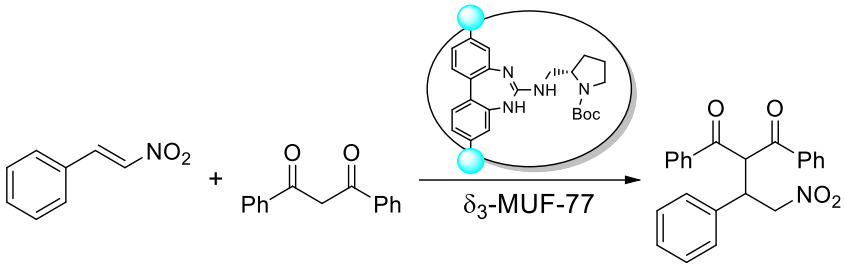

Figure 6-4 Exemplary Michael reaction in toluene at 25 °C catalysed by δ_3-MUF-77.

6.3 Future Chiral Truxene Linkers for Pore Modulation

While our library of MUF-77 ligands today includes numerous chiral ditopic bpdc and bdc linkers, the functionalization of the truxene-derived ligands has proven more challenging. However, access to such linkers would be valuable as it would offer us an additional handle for pore modulation in MUF-77 and would free the ditopic linkers for functionalization with other modulators or catalysts. For that purpose, *syn*-tribenzyl- and *syn*-triphenyl-substituted truxenes were synthesized according to the literature.[364] Carboxylation with aluminium chloride and oxalyl chloride led us to the respective truxene ligands (Figure 6-5). We attempted to resolve the ligands by crystallization with chiral anions, however, the same poor solubility that impeded the synthesis of many truxene-derived compounds before also hindered this approach. Instead, we shifted to the covalent synthesis of diastereomers, either through amine or through ester formation. We obtained the diastereomeric esters by direct Steglich esterification. We also found the respective acyl chloride to be readily synthesized and converted to the diastereomeric ester in the presence of a base and the respective chiral alcohol. We successfully synthesized the (*S*)-(−)-sec phenylethyl and (1*R*)-(−)-Myrtenol-esters of the tribenzyl-substituted truxene. However, attempts to resolve the products through column chromatography or crystallization were not successful. Alternatively, the respective amine was synthesized from acyl chloride with (*S*)-(−)-1-phenylethylamine and successfully resolved by column chromatography. Unfortunately, the amide proved harder to cleave than anticipated and attempts to obtain the final tricarboxylate ligands were unsuccessful. However, this work provides a good foundation for future attempts to synthesize a chiral truxene ligand.

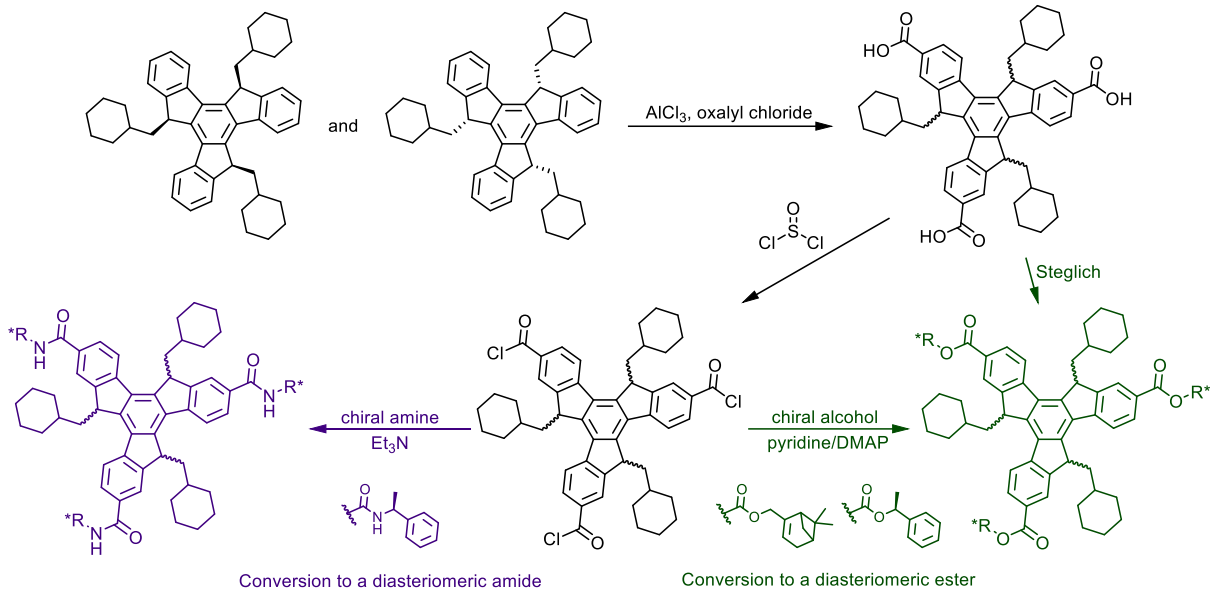

Figure 6-5 Synthesis of different diastereomers for the resolution of the tribenzyl-truxene ligand.

References

1. Wheatley, P. S.; Chlubná-Eliášová, P.; Greer, H.; Zhou, W.; Seymour, V. R.; Dawson, D. M.; Ashbrook, S. E.; Pinar, A. B.; McCusker, L. B.; Opanasenko, M.; Čejka, J.; Morris, R. E. Zeolites with Continuously Tuneable Porosity. *Angew. Chem., Int. Ed.* **2014**, *53* (48), 13210–13214.
2. Giraldo, L. F.; López, B. L.; Pérez, L.; Urrego, S.; Sierra, L.; Mesa, M. Mesoporous Silica Applications. *Macromol. Symp.* **2007**, *258*, 129–141.
3. Li, P.; Ryder, M. R.; Stoddart, J. F. Hydrogen-Bonded Organic Frameworks: A Rising Class of Porous Molecular Materials. *Acc. Mater. Res.* **2020**, *1* (1), 77–87.
4. Altaf, A.; Baig, N.; Sohail, M.; Sher, M.; Ul-Hamid, A.; Altaf, M. Covalent Organic Frameworks: Advances in Synthesis and Applications. *Mater. Today Commun.* **2021**, *28*, 102612.
5. Zhang, X.; Chen, Z.; Liu, X.; Hanna, S. L.; Wang, X.; Taheri-Ledari, R.; Maleki, A.; Li, P.; Farha, O. K. A Historical Overview of the Activation and Porosity of Metal-Organic Frameworks. *Chem. Soc. Rev.* **2020**, *49* (20), 7406–7427.
6. Zhang, W.; Taheri-Ledari, R.; Saeidirad, M.; Qazi, F. S.; Kashtiaray, A.; Ganjali, F.; Tian, Y.; Maleki, A. Regulation of Porosity in MOFs: A Review on Tunable Scaffolds and Related Effects and Advances in Different Applications. *J. Environ. Chem. Eng.* **2022**, *10* (6), 108836.
7. Lin, R. B.; Xiang, S.; Zhou, W.; Chen, B. Microporous Metal-Organic Framework Materials for Gas Separation. *Chem* **2020**, *6* (2), 337–363.
8. Fan, W.; Zhang, X.; Kang, Z.; Liu, X.; Sun, D. Isoreticular Chemistry within Metal–Organic Frameworks for Gas Storage and Separation. *Coord. Chem. Rev.* **2021**, *443*, 213968.
9. Alezi, D.; Belmabkhout, Y.; Suyetin, M.; Bhatt, P. M.; Weseliński, L. J.; Solovyeva, V.; Adil, K.; Spanopoulos, I.; Trikalitis, P. N.; Emwas, A. H.; Eddaoudi, M. MOF Crystal Chemistry Paving the Way to Gas Storage Needs: Aluminum-Based Soc -MOF for CH_4, O_2, and CO_2 Storage. *J. Am. Chem. Soc.* **2015**, *137* (41), 13308–13318.
10. Jiang, C.; Wang, X.; Ouyang, Y.; Lu, K.; Jiang, W.; Xu, H.; Wei, X.; Wang, Z.; Dai, F.; Sun, D. Recent Advances in Metal-Organic Frameworks for Gas Adsorption/Separation. *Nanoscale Adv.* **2022**, *4* (9), 2077–2089.
11. Kato, S.; Otake, K. I.; Chen, H.; Akpinar, I.; Buru, C. T.; Islamoglu, T.; Snurr, R. Q.; Farha, O. K. Zirconium-Based Metal-Organic Frameworks for the Removal of Protein-Bound Uremic Toxin from Human Serum Albumin. *J. Am. Chem. Soc.* **2019**, *141* (6), 2568–2576.
12. Jeong, C.; Ansari, M. Z.; Hakeem Anwer, A.; Kim, S. H.; Nasar, A.; Shoeb, M.; Mashkoor, F. A Review on Metal-Organic Frameworks for the Removal of Hazardous Environmental Contaminants. *Sep. Purif. Technol.* **2023**, *305*, 122416.
13. Rojas, S.; Baati, T.; Njim, L.; Manchego, L.; Neffati, F.; Abdeljelil, N.; Saguem, S.; Serre, C.; Najjar, M. F.; Zakhama, A.; Horcajada, P. Metal-Organic Frameworks as Efficient Oral Detoxifying Agents. *J. Am. Chem. Soc.* **2018**, *140* (30), 9581–9586.
14. Dolgopolova, E. A.; Rice, A. M.; Martin, C. R.; Shustova, N. B. Photochemistry and Photophysics of MOFs: Steps towards MOF-Based Sensing Enhancements. *Chem. Soc. Rev.* **2018**, *47* (13), 4710–4728.
15. Cheng, W.; Tang, X.; Zhang, Y.; Wu, D.; Yang, W. Applications of Metal-Organic Framework (MOF)-Based Sensors for Food Safety: Enhancing Mechanisms and Recent Advances. *Trends Food Sci. Technol.* **2021**, *112*, 268–282.
16. Lawson, H. D.; Walton, S. P.; Chan, C. Metal-Organic Frameworks for Drug Delivery: A Design Perspective. *ACS Appl. Mater. Interfaces* **2021**, *13* (6), 7004–7020.
17. Mallakpour, S.; Nikkhoo, E.; Hussain, C. M. Application of MOF Materials as Drug Delivery Systems for Cancer Therapy and Dermal Treatment. *Coord. Chem. Rev.* **2022**, *451*, 214262.
18. Xu, C.; Fang, R.; Luque, R.; Chen, L.; Li, Y. Functional Metal–Organic Frameworks for Catalytic Applications. *Coord. Chem. Rev.* **2019**, *388*, 268–292.
19. Rogge, S. M. J.; Bavykina, A.; Hajek, J.; Garcia, H.; Olivos-Suarez, A. I.; Sepúlveda-Escribano, A.; Vimont, A.; Clet, G.; Bazin, P.; Kapteijn, F.; Daturi, M.; Ramos-Fernandez, E. V.; Llabrés i Xamena, F. X.; Van Speybroeck, V.; Gascon, J. Metal–Organic and Covalent Organic Frameworks as Single-Site Catalysts. *Chem. Soc. Rev.* **2017**, *46* (11), 3134–3184.

20. Jiao, L.; Wang, Y.; Jiang, H.-L.; Xu, Q. Metal-Organic Frameworks as Platforms for Catalytic Applications. *Adv. Mater.* **2018**, *30* (37), 1703663.

21. Pascanu, V.; González Miera, G.; Inge, A. K.; Martín-Matute, B. Metal–Organic Frameworks as Catalysts for Organic Synthesis: A Critical Perspective. *J. Am. Chem. Soc.* **2019**, *141* (18), 7223–7234.

22. Liu, J.; Chen, L.; Cui, H.; Zhang, J.; Zhang, L.; Su, C.-Y. Applications of Metal–Organic Frameworks in Heterogeneous SupraMol. Catal.. *Chem. Soc. Rev.* **2014**, *43* (16), 6011–6061.

23. Liang, J.; Liang, Z.; Zou, R.; Zhao, Y. Heterogeneous Catalysis in Zeolites, Mesoporous Silica, and Metal-Organic Frameworks. *Adv. Mater.* **2017**, *29* (30), 1701139.

24. Batten, S. R.; Champness, N. R.; Chen, X.-M.; Garcia-Martinez, J.; Kitagawa, S.; Öhrström, L.; O'Keeffe, M.; Paik Suh, M.; Reedijk, J. Terminology of Metal–Organic Frameworks and Coordination Polymers (IUPAC Recommendations 2013). *Pure Appl. Chem.* **2013**, *85* (8), 1715–1724.

25. Hoskins, B. F.; Robson, R. Design and Construction of a New Class of Scaffolding-like Materials Comprising Infinite Polymeric Frameworks of 3D-Linked Molecular Rods. A Reappraisal of the Zinc Cyanide and Cadmium Cyanide Structures and the Synthesis and Structure of the Diamond-Related Frameworks $[N(CH_3)_4][Cu^{I}Zn^{II}(CN)_4]$ and Cu^{I}[4,4',4'',4'''-Tetracyanotetraphenylmethane]$BF_4 \cdot x C_6H_5NO_2$. *J. Am. Chem. Soc.* **1990**, *112* (4), 1546–1554.

26. Li, H.; Eddaoudi, M.; O'Keeffe, M.; Yaghi, O. M. Design and Synthesis of an Exceptionally Stable and Highly Porous Metal-Organic Framework. *Nature* **1999**, *402* (6759), 276–279.

27. Rosi, N. L.; Eckert, J.; Eddaoudi, M.; Vodak, T. D.; Kim, J.; Keeffe, M. O.; Yaghi, O. M. Hydrogen Storage in Microporous Metal-Organic Frameworks. *Science* **2003**, *300* (5622), 1127–1129.

28. Suh, M. P.; Park, H. J.; Prasad, T. K.; Lim, D.-W. Hydrogen Storage in Metal–Organic Frameworks. *Chem. Rev.* **2012**, *112* (2), 782–835.

29. Van de Voorde, B.; Bueken, B.; Denayer, J.; De Vos, D. Adsorptive Separation on Metal–Organic Frameworks in the Liquid Phase. *Chem. Soc. Rev.* **2014**, *43* (16), 5766–5788.

30. Eddaoudi, M.; Kim, J.; Rosi, N.; Vodak, D.; Wachter, J.; O'Keeffe, M.; Yaghi, O. M. Systematic Design of Pore Size and Functionality in Isoreticular MOFs and Their Application in Methane Storage. *Science* **2002**, *295* (5554), 469–472.

31. Rowsell, J. L. C.; Yaghi, O. M. Metal–Organic Frameworks: A New Class of Porous Materials. *Microporous and Mesoporous Mater.* **2004**, *73* (1–2), 3–14.

32. Hausdorf, S.; Baitalow, F.; Seidel, J.; Mertens, F. O. R. L. Gaseous Species as Reaction Tracers in the Solvothermal Synthesis of the Zinc Oxide Terephthalate MOF-5. *J. Phys. Chem. A* **2007**, *111* (20), 4259–4266.

33. Chui, S. S.-Y.; Lo, S. M.-F.; Charmant, J. P. H.; Orpen, A. G.; Williams, I. D. A Chemically Functionalizable Nanoporous Material. *Science* **1999**, *283* (5405), 1148–1150.

34. Feng, D.; Liu, T.-F.; Su, J.; Bosch, M.; Wei, Z.; Wan, W.; Yuan, D.; Chen, Y.-P.; Wang, X.; Wang, K.; Lian, X.; Gu, Z.-Y.; Park, J.; Zou, X.; Zhou, H.-C. Stable Metal-Organic Frameworks Containing Single-Molecule Traps for Enzyme Encapsulation. *Nat. Commun.* **2015**, *6* (1), 5979.

35. Férey, G.; Mellot-Draznieks, C.; Serre, C.; Millange, F.; Dutour, J.; Surblé, S.; Margiolaki, I.; Berry, N. G.; Khimyak, Y. Z.; Ganin, A. Y.; Wiper, P.; Claridge, J. B.; Rosseinsky, M. J.; Stoddart, J. F.; Yaghi, O. M. A Chromium Terephthalate-Based Solid with Unusually Large Pore Volumes and Surface Area. *Science* **2005**, *309* (5743), 2040–2042.

36. Howarth, A. J.; Peters, A. W.; Vermeulen, N. A.; Wang, T. C.; Hupp, J. T.; Farha, O. K. Best Practices for the Synthesis, Activation, and Characterization of Metal–Organic Frameworks. *Chem. Mater.* **2017**, *29* (1), 26–39.

37. Ma, J.; Kalenak, A. P.; Wong-Foy, A. G.; Matzger, A. J. Rapid Guest Exchange and Ultra-Low Surface Tension Solvents Optimize Metal–Organic Framework Activation. *Angew. Chem., Int. Ed.* **2017**, *56* (46), 14618–14621.

38. Woo, H.; Devlin, A. M.; Matzger, A. J. In Situ Observation of Solvent Exchange Kinetics in a MOF with Coordinatively Unsaturated Sites. *J. Am. Chem. Soc.* **2023**, *145* (33), 18634–18641.

39. O. M. Yaghi; Guangming Li; Hailian Li. Selective Binding and Removal of Guests in a Microporous Metal-Organic Framework. *Nature* **1995**, *378*, 703–706.

40. Murdock, C. R.; Hughes, B. C.; Lu, Z.; Jenkins, D. M. Approaches for Synthesizing Breathing MOFs by Exploiting Dimensional Rigidity. *Coord. Chem. Rev.* **2014**, *258–259* (1), 119–136.

41. Hamon, L.; Llewellyn, P. L.; Devic, T.; Ghoufi, A.; Clet, G.; Guillerm, V.; Pirngruber, G. D.; Maurin, G.; Serre, C.; Driver, G.; Van Beek, W.; Jolimaître, E.; Vimont, A.; Daturi, M.; Férey, G. Co-Adsorption and Separation of CO_2-CH_4 Mixtures in the Highly Flexible MIL-53(Cr) MOF. *J. Am. Chem. Soc.* **2009**, *131* (47), 17490–17499.

42. Li, J. R.; Kuppler, R. J.; Zhou, H. C. Selective Gas Adsorption and Separation in Metal-Organic Frameworks. *Chem. Soc. Rev.* **2009**, *38* (5), 1477–1504.

43. Takashima, Y.; Martínez, V. M.; Furukawa, S.; Kondo, M.; Shimomura, S.; Uehara, H.; Nakahama, M.; Sugimoto, K.; Kitagawa, S. Molecular Decoding Using Luminescence from an Entangled Porous Framework. *Nat. Commun.* **2011**, *2*, 168.

44. Serre, C.; Mellot-Draznieks, C.; Surblé, S.; Audebrand, N.; Filinchuk, Y.; Férey, G. Role of Solvent-Host Interactions That Lead to Very Large Swelling of Hybrid Frameworks. *Science* **2007**, *315* (5820), 1828–1831.

45. Koutsianos, A.; Pallach, R.; Frentzel-Beyme, L.; Das, C.; Paulus, M.; Sternemann, C.; Henke, S. Breathing Porous Liquids Based on Responsive Metal-Organic Framework Particles. *Nat. Commun.* **2023**, *14*, 4200.

46. Mukoyoshi, M.; Kitagawa, H. Nanoparticle/Metal-Organic Framework Hybrid Catalysts: Elucidating the Role of the MOF. *Chem. Commun.* **2022**, *58* (77), 10757–10767.

47. Yu, J.; Mu, C.; Yan, B.; Qin, X.; Shen, C.; Xue, H.; Pang, H. Nanoparticle/MOF Composites: Preparations and Applications. *Mater. Horiz.* **2017**, *4* (4), 557–569.

48. Liu, Y.; Liu, C. H.; Debnath, T.; Wang, Y.; Pohl, D.; Besteiro, L. V.; Meira, D. M.; Huang, S.; Yang, F.; Rellinghaus, B.; Chaker, M.; Perepichka, D. F.; Ma, D. Silver Nanoparticle Enhanced Metal-Organic Matrix with Interface-Engineering for Efficient Photocatalytic Hydrogen Evolution. *Nat. Commun.* **2023**, *14* (1), 1–12.

49. Liu, Y.; Liu, Z.; Huang, D.; Cheng, M.; Zeng, G.; Lai, C.; Zhang, C.; Zhou, C.; Wang, W.; Jiang, D.; Wang, H.; Shao, B. Metal or Metal-Containing Nanoparticle@MOF Nanocomposites as a Promising Type of Photocatalyst. *Coord. Chem. Rev.* **2019**, *388*, 63–78.

50. Hao, C.; Wu, X.; Sun, M.; Zhang, H.; Yuan, A.; Xu, L.; Xu, C.; Kuang, H. Chiral Core-Shell Upconversion Nanoparticle@MOF Nanoassemblies for Quantification and Bioimaging of Reactive Oxygen Species in Vivo. *J. Am. Chem. Soc.* **2019**, *141* (49), 19373–19378.

51. Ma, Y.; Li, X.; Li, A.; Yang, P.; Zhang, C.; Tang, B. H_2S-Activable MOF Nanoparticle Photosensitizer for Effective Photodynamic Therapy against Cancer with Controllable Singlet-Oxygen Release. *Angew. Chem., Int. Ed.* **2017**, *56* (44), 13752–13756.

52. Lee, H. K.; Koh, C. S.; Lo, W. S.; Liu, Y.; Phang, I. Y.; Sim, H. Y.; Lee, Y. H.; Phan-Quang, G. C.; Han, X.; Tsung, C. K.; Ling, X. Y. Applying a Nanoparticle@MOF Interface to Activate an Unconventional Regioselectivity of an Inert Reaction at Ambient Conditions. *J. Am. Chem. Soc.* **2020**, *142* (26), 11521–11527.

53. Wang, Z.; Cohen, S. M. Postsynthetic Modification of Metal–Organic Frameworks. *Chem. Soc. Rev.* **2009**, *38* (5), 1315–1329.

54. Yin, Z.; Wan, S.; Yang, J.; Kurmoo, M.; Zeng, M. H. Recent Advances in Post-Synthetic Modification of Metal–Organic Frameworks: New Types and Tandem Reactions. *Coord. Chem. Rev.* **2019**, *378*, 500–512.

55. Mandal, S.; Natarajan, S.; Mani, P.; Pankajakshan, A. Post-Synthetic Modification of Metal–Organic Frameworks Toward Applications. *Adv. Funct. Mater.* **2021**, *31* (4).

56. Kalaj, M.; Cohen, S. M. Postsynthetic Modification: An Enabling Technology for the Advancement of Metal-Organic Frameworks. *ACS Cent. Sci.* **2020**, *6* (7), 1046–1057.

57. Wang, Z.; Cohen, S. M. Postsynthetic Covalent Modification of a Neutral Metal-Organic Framework. *J. Am. Chem. Soc.* **2007**, *129* (41), 12368–12369.

58. Tanabe, K. K.; Wang, Z.; Cohen, S. M. Systematic Functionalization of a Metal-Organic Framework via a Postsynthetic Modification Approach. *J. Am. Chem. Soc.* **2008**, *130* (26), 8508–8517.

59. Dugan, E.; Wang, Z.; Okamura, M.; Medina, A.; Cohen, S. M. Covalent Modification of a Metal-Organic Framework with Isocyanates: Probing Substrate Scope and Reactivity. *Chem. Commun.* **2008**, *7345* (29), 3366–3368.

60. Wang, Z.; Tanabe, K. K.; Cohen, S. M. Accessing Postsynthetic Modification in a Series of Metal-Organic Frameworks and the Influence of Framework Topology on Reactivity. *Inorg. Chem.* **2009**, *48* (1), 296–306.

61. Lun, D. J.; Waterhouse, G. I. N.; Telfer, S. G. A General Thermolabile Protecting Group Strategy for Organocatalytic Metal-Organic Frameworks. *J. Am. Chem. Soc*, **2011**. *133* (15), 5806–5809.

62. Chuan-De Wu; Aiguo Hu; Lin Zhang, A.; Lin*, W.; Wu, C. De; Hu, A.; Zhang, L.; Lin, W. A Homochiral Porous Metal-Organic Framework for Highly Enantioselective Heterogeneous Asymmetric Catalysis. *J. Am. Chem. Soc.* **2005**, *127* (25), 8940–8941.

63. Park, K. S.; Ni, Z.; Côté, A. P.; Choi, J. Y.; Huang, R.; Uribe-Romo, F. J.; Chae, H. K.; O'Keeffe, M.; Yaghi, O. M. Exceptional Chemical and Thermal Stability of Zeolitic Imidazolate Frameworks. *Proc. Natl. Acad. Sci. U.S.A* **2006**, *103* (27), 10186–10191.

64. Chen, P.; He, M.; Chen, B.; Hu, B. Size- and Dose-Dependent Cytotoxicity of ZIF-8 Based on Single Cell Analysis. *Ecotoxicol. Environ. Saf.* **2020**, *205*, 111110.

65. Lee, Y. R.; Jang, M. S.; Cho, H. Y.; Kwon, H. J.; Kim, S.; Ahn, W. S. ZIF-8: A Comparison of Synthesis Methods. *Chem. Eng. J.* **2015**, *271*, 276–280.

66. Wang, Q.; Sun, Y.; Li, S.; Zhang, P.; Yao, Q. Synthesis and Modification of ZIF-8 and Its Application in Drug Delivery and Tumor Therapy. *RSC Adv.* **2020**, *10* (62), 37600–37620.

67. Hobday, C. L.; Woodall, C. H.; Lennox, M. J.; Frost, M.; Kamenev, K.; Düren, T.; Morrison, C. A.; Moggach, S. A. Understanding the Adsorption Process in ZIF-8 Using High Pressure Crystallography and Computational Modelling. *Nat. Commun.* **2018**, *9*, 1429.

68. Liang, K.; Coghlan, C. J.; Bell, S. G.; Doonan, C.; Falcaro, P. Enzyme Encapsulation in Zeolitic Imidazolate Frameworks: A Comparison between Controlled Co-Precipitation and Biomimetic Mineralisation. *Chem. Commun.* **2016**, *52* (3), 473–476.

69. Bavykina, A.; Kolobov, N.; Khan, I. S.; Bau, J. A.; Ramirez, A.; Gascon, J. Metal-Organic Frameworks in Heterogeneous Catalysis: Recent Progress, New Trends, and Future Perspectives. *Chem. Rev.* **2020**, *120* (16), 8468–8535.

70. Wu, Z.; Li, Y.; Zhang, C.; Huang, X.; Peng, B.; Wang, G. Recent Advances in Metal-Organic-Framework-Based Catalysts for Thermocatalytic Selective Oxidation of Organic Substances. *Chem Catal.* **2022**, *2* (5), 1009–1045.

71. Wang, Y.; Chen, L.; Hou, C. C.; Wei, Y. S.; Xu, Q. Multiple Catalytic Sites in MOF-Based Hybrid Catalysts for Organic Reactions. *Org. Biomol. Chem.* **2020**, *18* (42), 8508–8525.

72. Zhao, S. Y.; Chen, Z. Y.; Wei, N.; Liu, L.; Han, Z. B. Highly Efficient Cooperative Catalysis of Single-Site Lewis Acid and Brønsted Acid in a Metal-Organic Framework for the Biginelli Reaction. *Inorg. Chem.* **2019**, *58* (12), 7657–7661.

73. Etter, M. C.; Zia-Ebrahimi, M.; Urbañczyk-Lipkowska, Z.; Panunto, T. W. Hydrogen Bond Directed Cocrystallization and Molecular Recognition Properties of Diarylureas. *J. Am. Chem. Soc.* **1990**, *112* (23), 8415–8426.

74. George, S.; Nangia, A. *N,N'*-Bis(4-Biphenylyl) Urea. *Acta Crystallogr. Sect. E* **2003**, *59* (6), o901–o902.

75. Custelcean, R. Crystal Engineering with Urea and Thiourea Hydrogen-Bonding Groups. *Chem. Commun.* **2008**, 295–307.

76. Mohammadian, R.; Amini, M. M.; Shaabani, A. Thiourea-Functionalized MIL-101(Cr) Metal-Organic Framework as a Hydrogen-Bond-Donating Heterogeneous Organocatalyst for the Friedel-Crafts Alkylation and Biginelli Reactions. *Catal. Commun.* **2020**, *136*.

77. Yi, X. C.; Xi, F. G.; Qi, Y.; Gao, E. Q. Synthesis and Click Modification of an Azido-Functionalized Zr(Iv) Metal-Organic Framework and a Catalytic Study. *RSC Adv.* **2015**, *5* (2), 893–900.

78. Das, A.; Nagaraj, A.; SK, M.; Dhakshinamoorthy, A.; Biswas, S. A Functionalized UiO-66 MOF for Turn-On Fluorescent Sensing of Superoxide in Water and Efficient Catalysis of Knoevenagel Condensation. *Dalton Trans.* **2019**, *4,* 17371–17380.

79. Moreno, J. M.; Gil-San-Millan, R.; Mas-Ballesté, R.; Alemán, J.; Platero-Prats, A. E. Enhanced Organocatalytic Processes through an Engineered Acid-Base Site Bifunctional Pore in a Zirconium Metal-Organic Framework. *ChemCatChem* **2024**, *16*, 202400676.

80. Das, A.; Anbu, N.; Reinsch, H.; Dhakshinamoorthy, A.; Biswas, S. A Thiophene-2-Carboxamide-Functionalized Zr(IV) Organic Framework as a Prolific and Recyclable Heterogeneous Catalyst for Regioselective Ring Opening of Epoxides. *Inorg. Chem.* **2019**, *58* (24), 16581–16591.

81. Canivet, J.; Vandichel, M.; Farrusseng, D. Origin of Highly Active Metal–Organic Framework Catalysts: Defects? Defects! *Dalton Trans.* **2016**, *45* (10), 4090–4099.

82. Xamena, F. X. L. I.; Cirujano, F. G.; Corma, A. An Unexpected Bifunctional Acid Base Catalysis in IRMOF-3 for Knoevenagel Condensation Reactions. *Microporous and Mesoporous Mater.* **2012**, *157*, 112–117.

83. Guo, J.; Lian, Y.; Li, F.; Duan, Y.; Xue, X.; Long, C.; Zhang, Y.; Tang, Z. Metal-Organic Frameworks' Tricks in Asymmetric Catalysis. *Chem Catal.* **2022**, *2* (11), 2986–3018.

84. Deria, P.; Mondloch, J. E.; Karagiaridi, O.; Bury, W.; Hupp, J. T.; Farha, O. K. Beyond Post-Synthesis Modification: Evolution of Metal–Organic Frameworks via Building Block Replacement. *Chem. Soc. Rev.* **2014**, *43* (16), 5896–5912.

85. Li, C.; Tang, H.; Fang, Y.; Xiao, Z.; Wang, K.; Wu, X.; Niu, H.; Zhu, C.; Zhou, H. C. Bottom-Up Assembly of a Highly Efficient Metal-Organic Framework for Cooperative Catalysis. *Inorg. Chem.* **2018**, *57* (21), 13912–13919.

86. Zhu, C.; Xia, Q.; Chen, X.; Liu, Y.; Du, X.; Cui, Y. Chiral Metal–Organic Framework as a Platform for Cooperative Catalysis in Asymmetric Cyanosilylation of Aldehydes. *ACS Catal.* **2016**, *6* (11), 7590–7596.

87. Garibay, S. J.; Wang, Z.; Tanabe, K. K.; Cohen, S. M. Postsynthetic Modification: A Versatile Approach Toward Multifunctional Metal-Organic Frameworks. *Inorg. Chem.* **2009**, *48* (15), 7341–7349.

88. Cozzi, P. G. Metal-Salen Schiff Base Complexes in Catalysis: Practical Aspects. *Chem. Soc. Rev.* **2004**, *33* (7), 410–421.

89. Shaw, S.; White, J. D. Asymmetric Catalysis Using Chiral Salen-Metal Complexes: Recent Advances. *Chem. Rev.* **2019**, *119* (16), 9381–9426.

90. Zhang, W.; Loebach, J. L.; Wilson, S. R.; Jacobsen, E. N. Enantioselective Epoxidation of Unfunctionalized Olefins Catalyzed by Salen Manganese Complexes. *J. Am. Chem. Soc.* **1990**, *112* (8), 2801–2803.

91. Zhang, W.; Jacobsen, N. Asymmetric Olefin Epoxidation with Sodium Hypochlorite Catalyzed by Easily Prepared Chiral Manganese(III) Salen Complexes. *J. Org. Chem.* **1991**, *56* (7), 2296–2298.

92. Ingleson, M. J.; Perez Barrio, J.; Guilbaud, J.-B. B.; Khimyak, Y. Z.; Rosseinsky, M. J. Framework Functionalisation Triggers Metal Complex Binding. *Chem. Commun.* **2008**, No. 23, 2680–2682.

93. Doonan, C. J.; Morris, W.; Furukawa, H.; Yaghi, O. M. Isoreticular Metalation of Metal–Organic Frameworks. *J. Am. Chem. Soc.* **2009**, *131* (27), 9492–9493.

94. Sun, R.; Liu, B.; Li, B. G.; Jie, S. Palladium(II)@Zirconium-Based Mixed-Linker Metal–Organic Frameworks as Highly Efficient and Recyclable Catalysts for Suzuki and Heck Cross-Coupling Reactions. *ChemCatChem* **2016**, *8* (20), 3261–3271.

95. Thacker, N. C.; Lin, Z.; Zhang, T.; Gilhula, J. C.; Abney, C. W.; Lin, W. Robust and Porous β-Diketiminate-Functionalized Metal–Organic Frameworks for Earth-Abundant-Metal-Catalyzed C–H Amination and Hydrogenation. *J. Am. Chem. Soc.* **2016**, *138* (10), 3501–3509.

96. Tan, C.; Han, X.; Li, Z.; Liu, Y.; Cui, Y. Controlled Exchange of Achiral Linkers with Chiral Linkers in Zr-Based UiO-68 Metal-Organic Framework. *J. Am. Chem. Soc.* **2018**, *140* (47), 16229–16236.

97. Manna, K.; Zhang, T.; Carboni, M.; Abney, C. W.; Lin, W. Salicylaldimine-Based Metal - Organic Framework Enabling Highly Active Olefin Hydrogenation with Iron and Cobalt Catalysts. *J. Am. Chem. Soc.* **2014**, *136* (38), 13182–13185.

98. An, B.; Zeng, L.; Jia, M.; Li, Z.; Lin, Z.; Song, Y.; Zhou, Y.; Cheng, J.; Wang, C.; Lin, W. Molecular Iridium Complexes in Metal-Organic Frameworks Catalyze CO_2 Hydrogenation via Concerted Proton and Hydride Transfer. *J. Am. Chem. Soc.* **2017**, *139* (49), 17747–17750.

99. Václavík, J.; Servalli, M.; Lothschütz, C.; Szlachetko, J.; Ranocchiari, M.; van Bokhoven, J. A. Au^{I} Catalysis on a Coordination Polymer: A Solid Porous Ligand with Free Phosphine Sites. *ChemCatChem* **2013**, *5* (3), 692–696.

100. Ranieri, B.; Escofet, I.; Echavarren, A. M. Anatomy of Gold Catalysts: Facts and Myths. *Org. Biomol. Chem.* **2015**, *13* (26), 7103–7118.

101. Wang, D.; Cai, R.; Sharma, S.; Jirak, J.; Thummanapelli, S. K.; Akhmedov, N. G.; Zhang, H.; Liu, X.; Petersen, J. L.; Shi, X. "Silver Effect" in Gold(I) Catalysis: An Overlooked Important Factor. *J. Am. Chem. Soc.* **2012**, *134* (21), 9012–9019.

102. Ma, L.; Falkowski, J. M.; Abney, C.; Lin, W. A Series of Isoreticular Chiral Metal-Organic Frameworks as a Tunable Platform for Asymmetric Catalysis. *Nat. Chem.* **2010**, *2* (10), 838–846.

103. Lee, J. S.; Kapustin, E. A.; Pei, X.; Llopis, S.; Yaghi, O. M.; Toste, F. D. Architectural Stabilization of a Gold(III) Catalyst in Metal-Organic Frameworks. *Chem* **2020**, *6* (1), 142–152.

104. Sawano, T.; Lin, Z.; Boures, D.; An, B.; Wang, C.; Lin, W. Metal–Organic Frameworks Stabilize Mono(Phosphine)–Metal Complexes for Broad-Scope Catalytic Reactions. *J. Am. Chem. Soc.* **2016**, *138* (31), 9783–9786.

105. Feng, L.; Wang, K. Y.; Day, G. S.; Zhou, H. C. The Chemistry of Multi-Component and Hierarchical Framework Compounds. *Chem. Soc. Rev*. **2019**, *48* (18), 4823–4853.

106. Chen, C.-X.; Wei, Z.-W.; Jiang, J.-J.; Zheng, S.-P.; Wang, H.-P.; Qiu, Q.-F.; Cao, C.-C.; Fenske, D.; Su, C.-Y. Dynamic Spacer Installation for Multirole Metal–Organic Frameworks: A New Direction toward Multifunctional MOFs Achieving Ultrahigh Methane Storage Working Capacity. *J. Am. Chem. Soc.* **2017**, *139* (17), 6034–6037.

107. Cao, C.-C.; Chen, C.-X.; Wei, Z.-W.; Qiu, Q.-F.; Zhu, N.-X.; Xiong, Y.-Y.; Jiang, J.-J.; Wang, D.; Su, C.-Y. Catalysis through Dynamic Spacer Installation of Multivariate Functionalities in Metal–Organic Frameworks. *J. Am. Chem. Soc.* **2019**, *141* (6), 2589–2593.

108. Drake, T.; Ji, P.; Lin, W. Site Isolation in Metal–Organic Frameworks Enables Novel Transition Metal Catalysis. *Acc. Chem. Res.* **2018**, *51* (9), 2129–2138.

109. Ma, L.; Abney, C.; Lin, W. Enantioselective Catalysis with Homochiral Metal–Organic Frameworks. *Chem. Soc. Rev.* **2009**, *38* (5), 1248.

110. Le, C.; Liang, Y.; Evans, R. W.; Li, X.; MacMillan, D. W. C. Selective Sp3 C–H Alkylation via Polarity-Match-Based Cross-Coupling. *Nature* **2017**, *547* (7661), 79–83.

111. Liu, X.; Wang, F. Transition Metal Complexes That Catalyze Oxygen Formation from Water: 1979-2010. *Coord. Chem. Rev.* **2012**, *256* (11–12), 1115–1136.

112. Kärkäs, M. D.; Åkermark, B. Water Oxidation Using Earth-Abundant Transition Metal Catalysts: Opportunities and Challenges. *Dalton Trans.* **2016**, *45* (37), 14421–14461.

113. Gualandi, A.; Marchini, M.; Mengozzi, L.; Natali, M.; Lucarini, M.; Ceroni, P.; Cozzi, P. G. Organocatalytic Enantioselective Alkylation of Aldehydes with $[Fe(Bpy)_3]Br_2$ Catalyst and Visible Light. *ACS Catal.*. **2015**, *5* (10), 5927–5931.

114. Manna, K.; Zhang, T.; Lin, W. Postsynthetic Metalation of Bipyridyl-Containing Metal–Organic Frameworks for Highly Efficient Catalytic Organic Transformations. *J. Am. Chem. Soc.* **2014**, *136* (18), 6566–6569.

115. Izawa, Y.; Pun, D.; Stahl, S. S. Palladium-Catalyzed Aerobic Dehydrogenation of Substituted Cyclohexanones to Phenols. *Science* **2011**, *333* (6039), 209–213.

116. Manna, K.; Zhang, T.; Greene, F. X.; Lin, W. Bipyridine- and Phenanthroline-Based Metal-Organic Frameworks for Highly Efficient and Tandem Catalytic Organic Transformations via Directed C-H Activation. *J. Am. Chem. Soc.* **2015**, *137* (7), 2665–2673.

117. Wolfe, J. P.; Buchwald, S. L. A Highly Active Catalyst for the Room-Temperature Amination and Suzuki Coupling of Aryl Chlorides. *Angew. Chem., Int. Ed.* **1999**, *38* (16), 2413–2416.

118. Walker, S. D.; Barder, T. E.; Martinelli, J. R.; Buchwald, S. L. A Rationally Designed Universal Catalyst for Suzuki-Miyaura Coupling Processes. *Angew. Chem., Int. Ed.* **2004**, *43* (14), 1871–1876.

119. Barder, T. E.; Walker, S. D.; Martinelli, J. R.; Buchwald, S. L. Catalysts for Suzuki-Miyaura Coupling Processes: Scope and Studies of the Effect of Ligand Structure. *J. Am. Chem. Soc.* **2005**, *127* (13), 4685–4696.

120. Surry, D. S.; Buchwald, S. L. Biaryl Phosphane Ligands in Palladium-Catalyzed Amination. *Angew. Chem., Int. Ed.* **2008**, *47* (34), 6338–6361.

121. Miyashita, A.; Yasuda, A.; Takaya, H.; Toriumi, K.; Ito, T.; Souchi, T.; Noyori, R. Synthesis of 2,2'-Bis(Diphenylphosphino)-1,1'-Binaphthyl (BINAP), an Atropisomeric Chiral Bis(Triaryl)Phosphine, and Its Use in the Rhodium(I)-Catalyzed Asymmetric Hydrogenation of α-(Acylamino)Acrylic Acids. *J. Am. Chem. Soc.* **1980**, *102* (27), 7932–7934.

122. Framery, E.; Andrioletti, B.; Lemaire, M. Recent Progress in Homogeneous Supported Asymmetric Catalysis: Example of the BINAP and the BOX Ligands. *Tetrahedron: Asymmetry* **2010**, *21* (9–10), 1110–1124.

123. Wöste, T. H.; Oestreich, M. BINAP versus BINAP(O) in Asymmetric Intermolecular Mizoroki-Heck Reactions: Substantial Effects on Selectivities. *Chem. - Eur. J.* **2011**, *17* (42), 11914–11918.

124. Noyori, R.; Takaya, H. BINAP: An Efficient Chiral Element for Asymmetric Catalysis. *Acc. Chem. Res.* **1990**, *23* (10), 345–350.

125. Sawano, T.; Lin, Z.; Boures, D.; An, B.; Wang, C.; Lin, W. Metal–Organic Frameworks Stabilize Mono(Phosphine)–Metal Complexes for Broad-Scope Catalytic Reactions. *J. Am. Chem. Soc.* **2016**, *138* (31), 9783–9786.

126. Falkowski, J. M.; Sawano, T.; Zhang, T.; Tsun, G.; Chen, Y.; Lockard, J. V.; Lin, W. Privileged Phosphine-Based Metal–Organic Frameworks for Broad-Scope Asymmetric Catalysis. *J. Am. Chem. Soc.* **2014**, *136* (14), 5213–5216.

127. Teichert, J. F.; Feringa, B. L. Phosphoramidites: Privileged Ligands in Asymmetric Catalysis. *Angew. Chem., Int. Ed.* **2010**, *49* (14), 2486–2528.

128. Boogers, J. A. F.; Felfer, U.; Kotthaus, M.; Lefort, L.; Steinbauer, G.; De Vries, A. H. M.; De Vries, J. G. A Mixed-Ligand Approach Enables the Asymmetric Hydrogenation of an α-Isopropylcinnamic Acid En Route to the Renin Inhibitor Aliskiren. *Org. Process Res. Dev.* **2007**, *11* (3), 585–591.

129. Gonz, A. Z.; Benitez, D.; Tkatchouk, E.; Goddard, W. A.; Toste, F. D. Phosphoramidite Gold(I)-Catalyzed Diastereo- and Enantioselective Synthesis of 3,4-Substituted Pyrrolidines. **2011**, *133* (14), 5500–5507.

130. Faller, J. W.; Fontaine, P. P. Resolution and Diels-Alder Catalysis with Planar Chiral Arene-Tethered Ruthenium Complexes. *Organometallics* **2005**, *24* (17), 4132–4138.

131. Graening, T.; Hartwig, J. F. Iridium-Catalyzed Regio- and Enantioselective Allylation of Ketone Enolates. *J. Am. Chem. Soc.* **2005**, *127* (49), 17192–17193.

132. Hayashi, T. Chiral Monodentate Phosphine Ligand MOP for Transition-Metal-Catalyzed Asymmetric Reactions. *Acc. Chem. Res.* **2000**, *33* (6), 354–362.

133. Jiang, H.; Zhang, W.; Kang, X.; Cao, Z.; Chen, X.; Liu, Y.; Cui, Y. Topology-Based Functionalization of Robust Chiral Zr-Based Metal-Organic Frameworks for Catalytic Enantioselective Hydrogenation. *J. Am. Chem. Soc.* **2020**, *142* (21), 9642–9652.

134. Arduengo, A. J.; Harlow, R. L.; Kline, M. A Stable Crystalline Carbene. *J. Am. Chem. Soc.* **1991**, *113* (1), 361–363.

135. Lin, J. C. Y.; Huang, R. T. W.; Lee, C. S.; Bhattacharyya, A.; Hwang, W. S.; Lin, I. J. B. Coinage Metal-N-Heterocyclic Carbene Complexes. *Chem. Rev.* **2009**, *109* (8), 3561–3598.

136. Singh, R.; Nolan, S. P. N-Heterocyclic Carbenes: Advances in Transition Metal and Organic Catalysis. *Annu. Rep. Prog. Chem., Sect. B: Org. Chem.* **2006**, *102*, 168–196.

137. Díez-González, S.; Marion, N.; Nolan, S. P. N-Heterocyclic Carbenes in Late Transition Metal Catalysis. *Chem. Rev.* **2009**, *109* (8), 3612–3676.

138. Díez-González, S.; Nolan, S. P. Stereoelectronic Parameters Associated with N-Heterocyclic Carbene (NHC) Ligands: A Quest for Understanding. *Coord. Chem. Rev.* **2007**, *251* (5–6), 874–883.

139. Kong, G.-Q.; Ou, S.; Zou, C.; Wu, C.-D. Assembly and Post-Modification of a Metal–Organic Nanotube for Highly Efficient Catalysis. *J. Am. Chem. Soc.* **2012**, *134* (48), 19851–19857.

140. Dong, Y.; Li, W. H.; Dong, Y. Bin. Dual-Metal N-Heterocyclic Carbene Complex (M = Au and Pd)-Functionalized UiO-67 MOF for Alkyne Hydration-Suzuki Coupling Tandem Reaction. *J. Org. Chem.* **2021**, *86* (2), 1818–1826.

141. Carson, F.; Martínez-Castro, E.; Marcos, R.; Miera, G. G.; Jansson, K.; Zou, X.; Martín-Matute, B. Effect of the Functionalisation Route on a Zr-MOF with an Ir-NHC Complex for Catalysis. *Chem. Commun.* **2015**, *51* (54), 10864–10867.

142. Liu, L.; Telfer, S. G. Systematic Ligand Modulation Enhances the Moisture Stability and Gas Sorption Characteristics of Quaternary Metal–Organic Frameworks. *J. Am. Chem. Soc.* **2015**, *137* (11), 3901–3909.

143. Liu, L.; Zhou, T.-Y. Y.; Telfer, S. G. Modulating the Performance of an Asymmetric Organocatalyst by Tuning Its Spatial Environment in a Metal–Organic Framework. *J. Am. Chem. Soc.* **2017**, *139* (39), 13936–13943.

144. Wong-Foy, A. G.; Matzger, A. J.; Yaghi, O. M. Exceptional H_2 Saturation Uptake in Microporous Metal-Organic Frameworks. *J. Am. Chem. Soc.* **2006**, *128* (11), 3494–3495.

145. Chae, H. K.; Siberio-Pérez, D. Y.; Kim, J.; Go, Y. B.; Eddaoudi, M.; Matzger, A. J.; O'Keeffe, M.; Yaghi, O. M. A Route to High Surface Area, Porosity and Inclusion of Large Molecules in Crystals. *Nature* **2004**, *427* (6974), 523–527.

146. Eddaoudi, M.; Kim, J.; Rosi, N.; Vodak, D.; Wachter, J.; O'Keeffe, M.; Yaghi, O. M. Systematic Design of Pore Size and Functionality in Isoreticular MOFs and Their Application in Methane Storage. *Science* **2002**, *295* (5554), 469–472.

147. Koh, K.; Wong-Foy, A. G.; Matzger, A. J. A Crystalline Mesoporous Coordination Copolymer with High Microporosity. *Angew. Chem., Int. Ed.* **2008**, *47* (4), 677–680.

148. Cornelio, J.; Zhou, T.-Y.; Alkaş, A.; Telfer, S. G. Systematic Tuning of the Luminescence Output of Multicomponent Metal–Organic Frameworks. *J. Am. Chem. Soc.* **2018**, *140* (45), 15470–15476.

149. Benjamin, L.; Lerner, R. A.; Barbas III, C. F. Proline-Catalyzed Direct Asymmetric Aldol Reactions. *J. Am. Chem. Soc.* **2000**, *122* (10), 2395–2396.

150. List, B.; Hoang, L.; Martin, H. J. New Mechanistic Studies on the Proline-Catalyzed Aldol Reaction. *Proc. Natl. Acad. Sci. U.S.A.* **2004**, *101* (16), 5839–5842.

151. Sakthivel, K.; Notz, W.; Bui, T.; Barbas, C. F. Amino Acid Catalyzed Direct Asymmetric Aldol Reactions: A Bioorganic Approach to Catalytic Asymmetric Carbon-Carbon Bond-Forming Reactions. *J. Am. Chem. Soc.* **2001**, *123* (22), 5260–5267.

152. List, B. Proline-Catalyzed Asymmetric Reactions. *Tetrahedron* **2002**, *58* (28), 5573–5590.

153. Hajos, Z. G.; Parrish, D. R. Asymmetric Synthesis of Bicyclic Intermediates of Natural Product Chemistry. *J. Org. Chem* **1974**, *39* (12), 1615–1621.

154. Eder, U.; Sauer, G.; Wiechert, R. New Type of Asymmetric Cyclization to Optically Active Steroid CD Partial Structures. *Angew. Chem., Int. Ed.* **1971**, *10* (7), 496–497.

155. List, B.; Pojarliev, P.; Biller, W. T.; Martin, H. J. The Proline-Catalyzed Direct Asymmetric Three-Component Mannich Reaction: Scope, Optimization, and Application to the Highly Enantioselective Synthesis of 1,2-Amino Alcohols. *J. Am. Chem. Soc.* **2002**, *124* (5), 827–833.

156. List, B. Direct Catalytic Asymmetric α-Amination of Aldehydes. *J. Am. Chem. Soc.* **2002**, *124* (20), 5656–5657.

157. List, B.; Pojarliev, P.; Martin, H. J. Efficient Proline-Catalyzed Michael Additions of Unmodified Ketones to Nitro Olefins. *Org. Lett.* **2001**, *3* (16), 2423–2425.

158. List, B.; Lerner, R. A.; Barbas III, C. F. Proline-Catalyzed Direct Asymmetric Aldol Reactions. *J. Am. Chem. Soc.* **2000**, *122* (10), 2395–2396.

159. Koh, K.; Wong-Foy, A. G.; Matzger, A. J. A Crystalline Mesoporous Coordination Copolymer with High Microporosity. *Angew. Chem., Int. Ed.* **2008**, *47* (4), 677–680.

160. Chae, H. K.; Siberio-Pérez, D. Y.; Kim, J.; Go, Y.; Eddaoudi, M.; Matzger, A. J.; O'Keeffe, M.; Yaghi, O. M. A Route to High Surface Area, Porosity and Inclusion of Large Molecules in Crystals. *Nature* **2004**, *427* (6974), 523–527.

161. Lee, S. J.; Telfer, S. G. Multicomponent Metal-Organic Frameworks. *Angew. Chem., Int. Ed.* **2023**, *62*, e*202306341*.

162. Furukawa, H.; Ko, N.; Go, Y. B.; Aratani, N.; Choi, S. B.; Choi, E.; Yazaydin, A. Ö.; Snurr, R. Q.; O'Keeffe, M.; Kim, J.; Yaghi, O. M. Ultrahigh Porosity in Metal-Organic Frameworks. *Science* **2010**, *329* (5990), 424–428.

163. Duan, J.; Higuchi, M.; Kitagawa, S. Predesign and Systematic Synthesis of 11 Highly Porous Coordination Polymers with Unprecedented Topology. *Inorg. Chem.* **2015**, *54* (4), 1645–1649.

164. Hanwell, M. D.; Curtis, D. E.; Lonie, D. C.; Vandermeersch, T.; Zurek, E.; Hutchison, G. R. Avogadro: An Advanced Semantic Chemical Editor, Visualization, and Analysis Platform. *J. Cheminform.* **2012**, *4* (1), 17.

165. Zoubritzky, L.; Coudert, F.-X. CrystalNets.Jl: Identification of Crystal Topologies. *SciPost Chem.* **2022**, *1* (2), 1–30.

166. Shevchenko, A. P.; Shabalin, A. A.; Karpukhin, I. Yu.; Blatov, V. A. Topological Representations of Crystal Structures: Generation, Analysis and Implementation in the TopCryst System. *Sci. Technol. Adv. Mater. Meth.* **2022**, *2* (1), 250–265.

167. Alkaş, A.; Telfer, S. G. Synthesis and Characterization of Zn-Carboxylate Metal-Organic Frameworks Containing Triazatruxene Ligands. *Aust. J. Chem.* **2019**, *72* (10), 786-796.

168. Sheldrick, G. M. SHELXT - Integrated Space-Group and Crystal-Structure Determination. *Acta. Crystallogr. A* **2015**, *71* (1), 3–8.

169. Sheldrick, G. M. A Short History of SHELX. *Acta. Crystallogr. A* **2008**, *64* (1), 112–122.

170. Dolomanov, O. V.; Bourhis, L. J.; Gildea, R. J.; Howard, J. A. K.; Puschmann, H. OLEX2: A Complete Structure Solution, Refinement and Analysis Program. *J. Appl. Crystallogr.* **2009**, *42* (2), 339–341.

171. Walton, K. S.; Snurr, R. Q. Applicability of the BET Method for Determining Surface Areas of Microporous Metal-Organic Frameworks. *J. Am. Chem. Soc.* **2007**, *129* (27), 8552–8556.

172. Sonogashira, K.; Tohda, Y.; Hagihara, N. A Convenient Synthesis of Acetylenes: Catalytic Substitutions of Acetylenic Hydrogen with Bromoalkenes, Iodoarenes and Bromopyridines. *Tetrahedron Lett.* **1975**, *16* (50), 4467–4470.

173. Miyaura, N.; Suzuki, A. Stereoselective Synthesis of Arylated (*E*)-Alkenes by the Reaction of Alk-1-Enylboranes with Aryl Halides in the Presence of Palladium Catalyst. *J. Chem. Soc., Chem. Commun.* **1979**, (19), 866–867.

174. Miyaura, N.; Yamada, K.; Suzuki, A. A New Stereospecific Cross-Coupling by the Palladium-Catalyzed Reaction of 1-Alkenylboranes with 1-Alkenyl or 1-Alkynyl Halides. *Tetrahedron Lett.* **1979**, *20* (36), 3437–3440.

175. Miyaura, N.; Suzuki, A. Palladium-Catalyzed Cross-Coupling Reactions of Organoboron Compounds. *Chem. Rev.* **1995**, *95* (7), 2457–2483.

176. Heck, R. F. Palladium-Catalyzed Vinylation of Organic Halides. *In Organic Reactions,* John Wiley & Sons, Inc., 2005.

177. Obligacion, J. V.; Chirik, P. J. Earth-Abundant Transition Metal Catalysts for Alkene Hydrosilylation and Hydroboration. *Nat. Rev. Chem*. **2018**, *2*, 15–34.

178. Tasker, S. Z.; Standley, E. A.; Jamison, T. F. Recent Advances in Homogeneous Nickel Catalysis. *Nature* **2014**, *509*, 299–309.

179. Gao, W.; Lv, H.; Zhang, T.; Yang, Y.; Chung, L. W.; Wu, Y.-D.; Zhang, X. Nickel-Catalyzed Asymmetric Hydrogenation of β-Acylamino Nitroolefins: An Efficient Approach to Chiral Amines. *Chem. Sci.* **2017**, *8* (9), 6419–6422.

180. Pflästerer, D.; Hashmi, A. S. K. Gold Catalysis in Total Synthesis - Recent Achievements. *Chem. Soc. Rev.* **2016**, *45* (5), 1331–1367.

181. Zi, W.; Dean Toste, F. Recent Advances in Enantioselective Gold Catalysis. *Chem. Soc. Rev.*, **2016**, *45* (16), 4567–4589.

182. Sengupta, S.; Shi, X. Recent Advances in Asymmetric Gold Catalysis. *ChemCatChem* **2010**, *2* (6), 609–619.

183. Surry, D. S.; Buchwald, S. L. Dialkylbiaryl Phosphines in Pd-Catalyzed Amination: A User's Guide. *Chem. Sci.* **2011**, *2* (1), 27–50.

184. Clavier, H.; Nolan, S. P. Percent Buried Volume for Phosphine and N-Heterocyclic Carbene Ligands: Steric Properties in Organometallic Chemistry. *Chem. Commun.* **2010**, *46* (6), 841.

185. Birkholz (née Gensow), M.-N.; Freixa, Z.; van Leeuwen, P. W. N. M. Bite Angle Effects of Diphosphines in C–C and C–X Bond Forming Cross Coupling Reactions. *Chem. Soc. Rev.* **2009**, *38* (4), 1099-1118.

186. Barder, T. E.; Walker, S. D.; Martinelli, J. R.; Buchwald, S. L. Catalysts for Suzuki-Miyaura Coupling Processes: Scope and Studies of the Effect of Ligand Structure. *J. Am. Chem. Soc.* **2005**, *127* (13), 4685–4696.

187. Manna, K.; Zhang, T.; Lin, W. Postsynthetic Metalation of Bipyridyl-Containing Metal-Organic Frameworks for Highly Efficient Catalytic Organic Transformations. *J. Am. Chem. Soc.* **2014**, *136* (18), 6566–6569.

188. Pearson, R. G. Hard and Soft Acids and Bases. *J. Am. Chem. Soc.* **1963**, *85* (22), 3533–3539.

189. Wang, D.; Zhang, Y.; Gao, J.; Ge, G.; Li, C. A Polyhedron-Based Heterometallic MOF Constructed by HSAB Theory and SBB Strategy: Synthesis, Structure, and Adsorption Properties. *Cryst. Growth. Des*. **2019**, *19* (8), 4571–4578.

190. Manna, K.; Zhang, T.; Lin, W. Postsynthetic Metalation of Bipyridyl-Containing Metal-Organic Frameworks for Highly Efficient Catalytic Organic Transformations. *J. Am. Chem. Soc.* **2014**, *136* (18), 6566–6569.

191. Drake, T.; Ji, P.; Lin, W. Site Isolation in Metal–Organic Frameworks Enables Novel Transition Metal Catalysis. *Acc. Chem. Res.* **2018**, *51* (9), 2129–2138.

192. Brozek, C. K.; Dincă, M. Cation Exchange at the Secondary Building Units of Metal-Organic Frameworks. *Chem. Soc. Rev.* **2014**, *43* (16), 5456–5467.

193. Lalonde, M.; Bury, W.; Karagiaridi, O.; Brown, Z.; Hupp, J. T.; Farha, O. K. Transmetalation: Routes to Metal Exchange within Metal-Organic Frameworks. *J. Mater. Chem. A* **2013**, *1* (18), 5453–5468.

194. Dincă, M.; Long, J. R. High-Enthalpy Hydrogen Adsorption in Cation-Exchanged Variants of the Microporous Metal-Organic Framework $Mn_3[(Mn_4Cl)_3(BTT)_8(CH_3OH)_{10}]_2$. *J. Am. Chem. Soc.* **2007**, *129* (36), 11172–11176.

195. Liu, J.; Goetjen, T. A.; Wang, Q.; Knapp, J. G.; Wasson, M. C.; Yang, Y.; Syed, Z. H.; Delferro, M.; Notestein, J. M.; Farha, O. K.; Hupp, J. T. MOF-Enabled Confinement and Related Effects for Chemical Catalyst Presentation and Utilization. *Chem. Soc. Rev.* **2022**, *51* (3), 1045–1097.

196. Zhang, C.-J.; Chen, Z.-W.; Lin, R.-G.; Zhang, M.-J.; Li, P.-X.; Wang, M.-S.; Guo, G.-C. Design and Syntheses of Electron-Transfer Photochromic Metal–Organic Complexes Using Nonphotochromic Ligands: A Model Compound and the Roles of Its Ligands. *Inorg. Chem.* **2014**, *53* (2), 847–851.

197. Miao, X.-H.; Xiao, H.-P.; Zhu, L.-G.; Poly[Zinc(II)-μ_2-4,4′-Bipyridine-Di-μ_2-Formato]: A Chiral Three-Dimensional Coordination Polymer. *Acta Crystallogr. Sect. E* **2006**, *62* (8), m1756–m1757.

198. Yadav, Y. J.; Mastropietro, T. F.; Szerb, E. I.; Talarico, A. M.; Pirillo, S.; Pucci, D.; Crispini, A.; Ghedini, M. 2,2′-Bipyridine Zn(II) Complexes: Effect of the 4,4′ Substituents on the Crystalline Solid State Properties. *New J. Chem.* **2013**, *37* (5), 1486–1493.

199. Leadbeater, N. E.; Resouly, S. M. Suzuki Aryl Couplings Mediated by Phosphine-Free Nickel Complexes. *Tetrahedron* **1999**, *55* (40), 11889–11894.

200. Kim, M. J.; Ahn, S.; Yi, J.; Hupp, J. T.; Notestein, J. M.; Farha, O. K.; Lee, S. J. Ni(II) Complex on a Bispyridine-Based Porous Organic Polymer as a Heterogeneous Catalyst for Ethylene Oligomerization. *Catal. Sci. Technol.* **2017**, *7* (19), 4351–4354.

201. Sun, Z.; Kumagai, N.; Shibasaki, M. Photocatalytic α-Acylation of Ethers. *Org. Lett.* **2017**, *19* (14), 3727–3730.

202. Xiao, Y.-L.; Min, Q.-Q.; Xu, C.; Wang, R.-W.; Zhang, X. Nickel-Catalyzed Difluoroalkylation of (Hetero)Arylborons with Unactivated 1-Bromo-1,1-Difluoroalkanes. *Angew. Chem., Int. Ed.* **2016**, *55* (19), 5837–5841.

203. Zhang, Y. Q.; Wei, X. W.; Yu, R. Fe3O4 Nanoparticles-Supported Palladium-Bipyridine Complex: Effective Catalyst for Suzuki Coupling Reaction. *Catal. Lett.* **2010**, *135* (3–4), 256–262.

204. Jagtap, S. V.; Deshpande, R. M. $PdCl_2$(Bipy) Complex-An Efficient Catalyst for Heck Reaction in Glycol-Organic Biphasic Medium. *Catal. Today* **2008**, *131* (1–4), 353–359.

205. Li, X.; Van Zeeland, R.; Maligal-Ganesh, R. V.; Pei, Y.; Power, G.; Stanley, L.; Huang, W. Impact of Linker Engineering on the Catalytic Activity of Metal-Organic Frameworks Containing Pd(II)-Bipyridine Complexes. *ACS Catal.* **2016**, *6* (9), 6324–6328.

206. Kurpik, G.; Walczak, A.; Gołdyn, M.; Harrowfield, J.; Stefankiewicz, A. R. Pd(II) Complexes with Pyridine Ligands: Substituent Effects on the NMR Data, Crystal Structures, and Catalytic Activity. *Inorg. Chem.* **2022**, *61* (35), 14019–14029.

207. Wu, K.; Doyle, A. G. Parameterization of Phosphine Ligands Demonstrates Enhancement of Nickel Catalysis via Remote Steric Effects. *Nat. Chem.* **2017**, *9* (8), 779–784.

208. Wei, Y.; Shi, M. Multifunctional Chiral Phosphine Organocatalysts in Catalytic Asymmetric Morita−Baylis−Hillman and Related Reactions. *Acc. Chem. Res.* **2010**, *43* (7), 1005–1018.

209. Surry, D. S.; Buchwald, S. L. Dialkylbiaryl Phosphines in Pd-Catalyzed Amination: A User's Guide. *Chem. Sci.* **2011**, *2* (1), 27–50.

210. Morel, F. L.; Ranocchiari, M.; van Bokhoven, J. A. Synthesis and Characterization of Phosphine-Functionalized Metal–Organic Frameworks Based on MOF-5 and MIL-101 Topologies. *Ind. Eng. Chem. Res.* **2014**, *53* (22), 9120–9127.

211. Beloqui Redondo, A.; Morel, F. L.; Ranocchiari, M.; van Bokhoven, J. A. Functionalized Ruthenium–Phosphine Metal–Organic Framework for Continuous Vapor-Phase Dehydrogenation of Formic Acid. *ACS Catal.* **2015**, *5* (12), 7099–7103.

212. Morel, F. L.; Ranocchiari, M.; van Bokhoven, J. A. Synthesis and Characterization of Phosphine-Functionalized Metal–Organic Frameworks Based on MOF-5 and MIL-101 Topologies. *Ind. Eng. Chem. Res.* **2014**, *53* (22), 9120–9127.

213. Paz Muñoz, M.; Adrio, J.; Carretero, J. C.; Echavarren, A. M. Ligand Effects in Gold- and Platinum-Catalyzed Cyclization of Enynes: Chiral Gold Complexes for Enantioselective Alkoxycyclization. *Organometallics* **2005**, *24* (6), 1293–1300.

214. González, A. Z.; Toste, F. D. Gold(I)-Catalyzed Enantioselective [4+2]-Cycloaddition of Allene-Dienes. Org. Lett. **2009**, *12* (1), 200–203.

215. Alonso, I.; Trillo, B.; López, F.; Montserrat, S.; Ujaque, G.; Castedo, L.; Lledós, A.; Mascareñas, J. L. Gold-Catalyzed [4C+2C] Cycloadditions of Allenedienes, Including an Enantioselective Version with New Phosphoramidite-Based Catalysts: Mechanistic Aspects of the Divergence between [4C+3C] and [4C+2C] Pathways. *J. Am. Chem. Soc.* **2009**, *131* (36), 13020–13030.

216. Václavík, J.; Servalli, M.; Lothschütz, C.; Szlachetko, J.; Ranocchiari, M.; van Bokhoven, J. A. Au^{I} Catalysis on a Coordination Polymer: A Solid Porous Ligand with Free Phosphine Sites. *ChemCatChem* **2013**, *5* (3), 692–696.

217. Galassi, R.; Oumarou, C. S.; Burini, A.; Dolmella, A.; Micozzi, D.; Vincenzetti, S.; Pucciarelli, S. A Study on the Inhibition of Dihydrofolate Reductase (DHFR) from Escherichia Coli by Gold(I) Phosphane Compounds. X-Ray Crystal Structures of (4,5-Dichloro-1H-Imidazolate-1-Yl)-Triphenylphosphane-Gold(I) and (4,5-Dicyano-1H-Imidazolate-1-Yl)-Triphenylphosphane-Gold(I). *Dalton Trans.* **2015**, *44* (7), 3043–3056.

218. de Haro, T.; Nevado, C. Gold-Catalyzed Ethynylation of Arenes. *J. Am. Chem. Soc.* **2010**, *132* (5), 1512–1513.

219. Hu, A. G.; Fu, Y.; Xie, J. H.; Zhou, H.; Wang, L. X.; Zhou, Q. L. Monodentate Chiral Spiro Phosphoramidites: Efficient Ligands for Rhodium-Catalyzed Enantioselective Hydrogenation of Enamides. *Angew. Chem., Int. Ed.* **2002**, *41* (13), 2348–2350.

220. Bartels, B.; García-Yebra, C.; Rominger, F.; Helmchen, G. Iridium-Catalysed Allylic Substitution: Stereochemical Aspects and Isolation of Ir^{III} Complexes Related to the Catalytic Cycle. *Eur J Inorg. Chem.* **2002**, 2569–2586.

221. Lefort, L.; de Vries, J. G. Phosphoramidite Ligands. In *Phosphorus(III) Ligands in Homogeneous Catalysis: Design and Synthesis*; 2012; pp 133–157.

222. Feringa, B. L. Phosphoramidites: Marvellous Ligands in Catalytic Asymmetric Conjugate Addition. *Acc. Chem. Res.* **2000**, *33* (6), 346–353.

223. Liu, Y.; Ding, K. Modular Monodentate Phosphoramidite Ligands for Rhodium-Catalyzed Enantioselective Hydrogenation. *J. Am. Chem. Soc.* **2005**, *127* (30), 10488–10489.

224. Boiteau, J. G.; Imbos, R.; Minnaard, A. J.; Feringa, B. L. Rhodium-Catalyzed Asymmetric Conjugate Additions of Boronic Acids Using Monodentate Phosphoramidite Ligands. *Org. Lett.* **2003**, *5* (5), 681–684.

225. Bartels, B.; García-Yebra, C.; Rominger, F.; Helmchen, G. Iridium-Catalysed Allylic Substitution: Stereochemical Aspects and Isolation of Ir^{III} Complexes Related to the Catalytic Cycle. *Eur. J. Inorg. Chem.* **2002**, No. 10, 2569–2586.

226. Hölscher, M.; Franciò, G.; Leitner, W. Origin of Enantioselectivity in Asymmetric Hydrovinylations Catalyzed by Phosphoramidite Nickel Catalysts: An Experimentally Supported Density Functional Study. *Organometallics* **2004**, *23* (23), 5606–5617.

227. Jin, R.; Zeng, C.; Zhou, M.; Chen, Y. Atomically Precise Colloidal Metal Nanoclusters and Nanoparticles: Fundamentals and Opportunities. *Chem. Rev.* **2016**, *116* (18), 10346–10413.

228. Simoens, A.; Scattolin, T.; Cauwenbergh, T.; Pisanò, G.; Cazin, C. S. J.; Stevens, C. V.; Nolan, S. P. Continuous Flow Synthesis of Metal–NHC Complexes. *Chem. - Eur. J.* **2021**, *27* (18), 5653–5657.

229. Johnson, A.; Gimeno, M. C. An Efficient and Sustainable Synthesis of NHC Gold Complexes. *Chem. Commun.* **2016**, *52* (62), 9664–9667.

230. de Frémont, P.; Scott, N. M.; Stevens, E. D.; Nolan, S. P. Synthesis and Structural Characterization of N - Heterocyclic Carbene Gold (I) Complexes. *Organometallics* **2005**, *24* (10), 2411–2418.

231. Hashmi, A. S. K.; Hengst, T.; Lothschütz, C.; Rominger, F. New and Easily Accessible Nitrogen Acyclic Gold(I) Carbenes: Structure and Application in the Gold-Catalyzed Phenol Synthesis as Well as the Hydration of Alkynes. *Adv. Synth. Catal.* **2010**, *352* (8), 1315–1337.

232. Göker, V.; Kohl, S. R.; Rominger, F.; Meyer-Eppler, G.; Volbach, L.; Schnakenburg, G.; Lützen, A.; Hashmi, A. S. K. Chiral [2.2]Paracyclophane-Based NAC- and NHC-Gold(I) Complexes. *J. Organomet. Chem.* **2015**, *795*, 45–52.

233. Fèvre, M.; Pinaud, J.; Leteneur, A.; Gnanou, Y.; Vignolle, J.; Taton, D.; Miqueu, K.; Sotiropoulos, J. M. Imidazol(in)Ium Hydrogen Carbonates as a Genuine Source of N-Heterocyclic Carbenes (NHCs): Applications to the Facile Preparation of NHC Metal Complexes and to NHC-Organocatalyzed Molecular and Macromolecular Syntheses. *J. Am. Chem. Soc.* **2012**, *134* (15), 6776–6784.

234. Visbal, R.; Laguna, A.; Gimeno, M. C. Simple and Efficient Synthesis of [MCI(NHC)] (M = Au, Ag) Complexes. *Chem. Commun.* **2013**, *49* (50), 5642–5644.

235. Powell, A. B.; Bielawski, C. W.; Cowley, A. H. Electropolymerization of an N-Heterocyclic Carbene–Gold(I) Complex. *J. Am. Chem. Soc.* **2009**, *131* (51), 18232–18233.

236. Krishnamurthy, S.; Esterle, A.; Sharma, N. C.; Sahi, S. V. Yucca-Derived Synthesis of Gold Nanomaterial and Their Catalytic Potential. *Nanoscale Res. Lett.* **2014**, *9* (1), 1–9.

237. Hu, Y.; Liao, J.; Wang, D.; Li, G. Fabrication of Gold Nanoparticle-Embedded Metal-Organic Framework for Highly Sensitive Surface-Enhanced Raman Scattering Detection. *Anal Chem* **2014**, *86* (8), 3955–3963.

238. Clauberg, M. H.; Schmidt, D.; Rust, J.; Lehmann, C. W.; Arefyeva, N.; Wickleder, M.; Mohr, F. Nickel(II) NHC-Complexes with Tridentate, Dianionic Ligands. *J. Organomet. Chem.* **2019**, *881*, 45–50.

239. Oisaki, K.; Li, Q.; Furukawa, H.; Czaja, A. U.; Yaghi, O. M. A Metal–Organic Framework with Covalently Bound Organometallic Complexes. *J. Am. Chem. Soc.* **2010**, *132* (27), 9262–9264.

240. Luo, S.; Zeng, Z.; Zeng, G.; Liu, Z.; Xiao, R.; Chen, M.; Tang, L.; Tang, W.; Lai, C.; Cheng, M.; Shao, B.; Liang, Q.; Wang, H.; Jiang, D. Metal Organic Frameworks as Robust Host of Palladium Nanoparticles in Heterogeneous Catalysis: Synthesis, Application, and Prospect. *ACS Appl. Mater. Interfaces.* **2019**, *11* (36), 32579–32598.

241. Hu, Y. H.; Liu, C. X.; Wang, J. C.; Ren, X. H.; Kan, X.; Dong, Y. Bin. TiO_2@UiO-68-CIL: A Metal-Organic-Framework-Based Bifunctional Composite Catalyst for a One-Pot Sequential Asymmetric Morita-Baylis-Hillman Reaction. *Inorg. Chem.* **2019**, *58* (8), 4722–4730.

242. Liu, H.; Liu, Y.; Li, Y.; Tang, Z.; Jiang, H. Metal-Organic Framework Supported Gold Nanoparticles as a Highly Active Heterogeneous Catalyst for Aerobic Oxidation of Alcohols. *J. Phys. Chem. C* **2010**, *114* (31), 13362–13369.

243. Luan, Y.; Qi, Y.; Gao, H.; Zheng, N.; Wang, G. Synthesis of an Amino-Functionalized Metal-Organic Framework at a Nanoscale Level for Gold Nanoparticle Deposition and Catalysis. *J Mater Chem A Mater* **2014**, *2* (48), 20588–20596.

244. Cure, J.; Mattson, E.; Cocq, K.; Assi, H.; Jensen, S.; Tan, K.; Catalano, M.; Yuan, S.; Wang, H.; Feng, L.; Zhang, P.; Kwon, S.; Veyan, J. F.; Cabrera, Y.; Zhang, G.; Li, J.; Kim, M.; Zhou, H. C.; Chabal, Y. J.; Thonhauser, T. High Stability of Ultra-Small and Isolated Gold Nanoparticles in Metal-Organic Framework Materials. *J. Mater. Chem. A* **2019**, *7* (29), 17536–17546.

245. Bartolomé, C.; García-Cuadrado, D.; Ramiro, Z.; Espinet, P. Synthesis and Catalytic Activity of Gold Chiral Nitrogen Acyclic Carbenes and Gold Hydrogen Bonded Heterocyclic Carbenes in Cyclopropanation of Vinyl Arenes and in Intramolecular Hydroalkoxylation of Allenes. *Inorg. Chem.* **2010**, *49* (21), 9758–9764.

246. Heravi, M. M.; Ghavidel, M.; Mohammadkhani, L. Beyond a Solvent: Triple Roles of Dimethylformamide in Organic Chemistry. *RSC Adv.* **2018**, *8* (49), 27832–27862.

247. Roberts, J. M.; Farha, O. K.; Sarjeant, A. A.; Hupp, J. T.; Scheidt, K. A. Two Azolium Rings Are Better Than One: A Strategy for Controlling Catenation and Morphology in Zn and Cu Metal–Organic Frameworks. *Cryst. Growth Des.* **2011**, *11* (11), 4747–4750.

248. Uson, R.; Laguna, A.; Laguna, M.; Briggs, D. A.; Murray, H. H.; Fackler Jr., J. P. (Tetrahydrothiophene)Gold(I) or Gold(III) Complexes. In *Inorganic Syntheses*; Kaesz, H. D., Ed.; John Wiley & Sons, Ltd, 1989; Vol. 26, pp 85–91.

249. Garro-Helion, F.; Merzouk, A.; Guibé, F. Mild and Selective Palladium(0)-Catalyzed Deallylation of Allylic Amines. Allylamine and Diallylamine as Very Convenient Ammonia Equivalents for the Synthesis of Primary Amines. *J. Org. Chem* **1993**, *58* (22), 6109–6113.

250. Rocchigiani, L.; Bochmann, M. Recent Advances in Gold(III) Chemistry: Structure, Bonding, Reactivity, and Role in Homogeneous Catalysis. *Chem. Rev.* **2021**, *121* (14), 8364–8451.

251. Schmidbaur, H.; Schier, A. Gold(III) Compounds for Homogeneous Catalysis: Preparation, Reaction Conditions, and Scope of Application. *Arab. J. Sci. Eng.* **2012**, *37* (5), 1187–1225.

252. Daniel, M.-C.; Astruc, D. Gold Nanoparticles: Assembly, Supramolecular Chemistry, Quantum-Size-Related Properties, and Applications toward Biology, Catalysis, and Nanotechnology. *Chem. Rev.* **2004**, *104* (1), 293–346.

253. Reeds, J. P.; Healy, M. P.; Fairlamb, I. J. S. Mechanistic Examination of Au^{III}-Mediated 1,5-Enyne Cycloisomerization by $AuBr_2$(N-Imidate)(NHC)/AgX Precatalysts-Is the Active Catalyst Au^{III} or Au^{I}? *Catal. Sci. Technol.* **2014**, *4* (10), 3524–3533.

254. Hashmi, A. S. K.; Blanco, M. C.; Fischer, D.; Bats, J. W. Gold Catalysis: Evidence for the in-Situ Reduction of Gold(III) during the Cyclization of Allenyl Carbinols. *European J. Org. Chem.* **2006**, No. 6, 1387–1389.

255. Green, M. L. H. A New Approach to the Formal Classification of Covalent Compounds of the Elements. *J. Organomet. Chem.* **1995**, *500* (1–2), 127–148.

256. Green, M. L. H.; Parkin, G. Application of the Covalent Bond Classification Method for the Teaching of Inorganic Chemistry. *J. Chem. Educ.* **2014**, *91* (6), 807–816.

257. Reeds, J. P.; Whitwood, A. C.; Healy, M. P.; Fairlamb, I. J. S. Synthesis and Reactivity of N-Heterocyclic Carbene Gold(I) and Gold(III) Imidate Complexes and Their Catalytic Activity in 1,5-Enyne Cycloisomerization. *Organometallics* **2013**, *32* (10), 3108–3120.

258. Nolan, S. P. The Development and Catalytic Uses of N-Heterocyclic Carbene Gold Complexes. *Acc. Chem. Res.* **2011**, *44* (2), 91–100.

259. Hashmi, A. S. K.; Weyrauch, J. P.; Rudolph, M.; Kurpejović, E. Gold Catalysis: The Benefits of N and N,O Ligands. *Angew. Chem., Int. Ed.* **2004**, *43* (47), 6545–6547.

260. Bohan, P. T.; Dean Toste, F. Well-Defined Chiral Gold(III) Complex Catalyzed Direct Enantioconvergent Kinetic Resolution of 1,5-Enynes. *J. Am. Chem. Soc.* **2017**, *139* (32), 11016–11019.

261. Kung, K. K. Y.; Lo, V. K. Y.; Ko, H. M.; Li, G. L.; Chan, P. Y.; Leung, K. C.; Zhou, Z.; Wang, M. Z.; Che, C. M.; Wong, M. K. Cyclometallated Gold(III) Complexes as Effective Catalysts for Synthesis of Propargylic Amines, Chiral Allenes and Isoxazoles. *Adv. Synth. Catal.* **2013**, *355* (10), 2055–2070.

262. Kumar, R.; Nevado, C. Cyclometalated Gold(III) Complexes: Synthesis, Reactivity, and Physicochemical Properties. *Angew. Chem., Int. Ed.* **2017**, *56* (8), 1994–2015.

263. Sun, C. Y.; To, W. P.; Wang, X. L.; Chan, K. T.; Su, Z. M.; Che, C. M. Metal-Organic Framework Composites with Luminescent Gold(III) Complexes. Strongly Emissive and Long-Lived Excited States in Open Air and Photo-Catalysis. *Chem. Sci.* **2015**, *6* (12), 7105–7111.

264. Wu, C.-Y. Y.; Horibe, T.; Jacobsen, C. B.; Toste, F. D. Stable Gold(III) Catalysts by Oxidative Addition of a Carbon-Carbon Bond. *Nature* **2015**, *517* (7535), 449–454.

265. Hashmi, A. S. K.; Frost, T. M.; Bats, J. W. Highly Selective Gold-Catalyzed Arene Synthesis. *J. Am. Chem. Soc.* **2000**, *122* (46), 11553–11554.

266. Cui, J. F.; Ko, H. M.; Shing, K. P.; Deng, J. R.; Lai, N. C. H.; Wong, M. K. C,O-Chelated BINOL/Gold(III) Complexes: Synthesis and Catalysis with Tunable Product Profiles. *Angew. Chem., Int. Ed.* **2017**, *56* (11), 3074–3079.

267. Levchenko, V. A.; Siah, H. S. M.; Øien-Ødegaard, S.; Kaur, G.; Fiksdahl, A.; Tilset, M. Catalytic Studies of Cyclometalated Gold(III) Complexes and Their Related UiO-67 MOF. *Mol. Catal.* **2020**, *492*, 111009.

268. Liu, L.; Xin, Z.; Gao, J.; Xu, C. Engineering Metal-Organic Frameworks Immobilize Gold Catalysts for Highly Efficient One-Pot Synthesis of Propargylamines. *Green Chem.* **2012**, *14* (6), 1710–1720.

269. Lili, L.; Xin, Z.; Shumin, R.; Ying, Y.; Xiaoping, D.; Jinsen, G.; Chunming, X.; Jing, H. Catalysis by Metal-Organic Frameworks: Proline and Gold Functionalized MOFs for the Aldol and Three-Component Coupling Reactions. *RSC Adv.* **2014**, *4* (25), 13093–13107.

270. Lee, J. S.; Kapustin, E. A.; Pei, X.; Llopis, S.; Yaghi, O. M.; Toste, F. D. Architectural Stabilization of a Gold(III) Catalyst in Metal-Organic Frameworks. *Chem* **2020**, *6* (1), 142–152.

271. Han, M. Y.; Quek, C. H.; Huang, W.; Chew, C. H.; Gan, L. M. A Simple and Effective Chemical Route for the Preparation of Uniform Nonaqueous Gold Colloids. *Chem. Mater.* **1999**, *11* (4), 1144–1147.

272. Newman, J. D. S.; Blanchard, G. J. Formation of Gold Nanoparticles Using Amine Reducing Agents. *Langmuir* **2006**, *22* (13), 5882–5887.

273. Gaillard, S.; Slawin, A. M. Z.; Nolan, S. P. A N-Heterocyclic Carbene Gold Hydroxide Complex: A Golden Synthon. *Chem. Commun.* **2010**, *46* (16), 2742–2744.

274. Gemici, Z.; Schwachulla, P. I.; Williamson, E. H.; Rubner, M. F.; Cohen, R. E. Targeted Functionalization of Nanoparticle Thin Films via Capillary Condensation. *Nano Lett.* **2009**, *9* (3), 1064–1070.

275. Liu, L. Multicomponent Metal-Organic Frameworks. *Doctoral Thesis Massey University* **2015**.

276. Dodson, R. A.; Kalenak, A. P.; Matzger, A. J. Solvent Choice in Metal-Organic Framework Linker Exchange Permits Microstructural Control. *J. Am. Chem. Soc.* **2020**, *142* (49), 20806–20813.

277. Nolan, S. P. The Development and Catalytic Uses of N-Heterocyclic Carbene Gold Complexes. *Acc. Chem. Res.* **2011**, *44* (2), 91–100.

278. Ranieri, B.; Escofet, I.; Echavarren, A. M. Anatomy of Gold Catalysts: Facts and Myths. *Org. Biomol. Chem.* **2015**, *13* (26), 7103–7118.

279. Zhukhovitskiy, A. V.; Kobylianskii, I. J.; Wu, C. Y.; Toste, F. D. Migratory Insertion of Carbenes into Au(III)-C Bonds. *J. Am. Chem. Soc.* **2018**, *140* (1), 466–474.

280. Wu, C.-Y. Y.; Horibe, T.; Jacobsen, C. B.; Toste, F. D. Stable Gold(III) Catalysts by Oxidative Addition of a Carbon-Carbon Bond. *Nature* **2015**, *517* (7535), 449–454.

281. Segato, J.; Del Zotto, A.; Belpassi, L.; Belanzoni, P.; Zuccaccia, D. Hydration of Alkynes Catalyzed by [Au(X)(L)(Ppy)]X in the Green Solvent γ-Valerolactone under Acid-Free Conditions: The Importance of the Pre-Equilibrium Step. *Catal. Sci. Technol.* **2020**, *10* (22), 7757–7767.

282. Gatto, M.; Del Zotto, A.; Segato, J.; Zuccaccia, D. Hydration of Alkynes Catalyzed by L-Au-X under Solvent- and Acid-Free Conditions: New Insights into an Efficient, General, and Green Methodology. *Organometallics* **2018**, *37* (24), 4685–4691.

283. Gatto, M.; Belanzoni, P.; Belpassi, L.; Biasiolo, L.; Del Zotto, A.; Tarantelli, F.; Zuccaccia, D. Solvent-, Silver-, and Acid-Free NHC-Au-X Catalyzed Hydration of Alkynes. The Pivotal Role of the Counterion. *ACS Catal.* **2016**, *6* (11), 7363–7376.

284. Liu, L.; Zhou, T.-Y. Y.; Telfer, S. G. Modulating the Performance of an Asymmetric Organocatalyst by Tuning Its Spatial Environment in a Metal–Organic Framework. *J. Am. Chem. Soc.* **2017**, *139* (39), 13936–13943.

285. Zhou, T.-Y.; Auer, B.; Lee, S. J.; Telfer, S. G. Catalysts Confined in Programmed Framework Pores Enable New Transformations and Tune Reaction Efficiency and Selectivity. *J. Am. Chem. Soc.* **2019**, *141*, 1577–1582.

286. Luzung, M. R.; Markham, J. P.; Toste, F. D. Catalaytic Isomerization of 1,5-Enynes to Bicyclo[3.1.0]Hexenes. *J. Am. Chem. Soc.* **2004**, *126* (35), 10858–10859.

287. Mano, N.; Edembe, L. Bilirubin Oxidases in Bioelectrochemistry: Features and Recent Findings. *Biosens. Bioelectron.* **2013**, *50*, 478–485.

288. Shimizu, A.; Kwon, J. H.; Sasaki, T.; Satoh, T.; Sakurai, N.; Sakurai, T.; Yamaguchi, S.; Samejima, T. Myrothecium Verrucaria Bilirubin Oxidase and Its Mutants for Potential Copper Ligands. *Biochemistry* **1999**, *38* (10), 3034–3042.

289. Tsujimura, S.; Kano, K.; Ikeda, T. Bilirubin Oxidase in Multiple Layers Catalyzes Four-Electron Reduction of Dioxygen to Water without Redox Mediators. *J. Electroanal. Chem.* **2005**, *576* (1), 113–120.

290. Tsujimura, S.; Nakagawa, T.; Kano, K.; Ikeda, T. Kinetic Study of Direct Bioelectrocatalysis of Dioxygen Reduction with Bilirubin Oxidase at Carbon Electrodes. *Electrochemistry* **2004**, *72* (6), 437–439.

291. Tanaka, N.; Murao, S. Purification and Some Properties of Bilirubin Oxidase of Myrothecium Verrucaria Mt-1. *Agric. Biol. Chem.* **1982**, *46* (10), 2499–2503.

292. Mano, N. Features and Applications of Bilirubin Oxidases. *Appl. Microbiol. Biotechnol.* **2012**, *96* (2), 301–307.

293. De Poulpiquet, A.; Kjaergaard, C. H.; Rouhana, J.; Mazurenko, I.; Infossi, P.; Gounel, S.; Gadiou, R.; Giudici-Orticoni, M. T.; Solomon, E. I.; Mano, N.; Lojou, E. Mechanism of Chloride Inhibition of Bilirubin Oxidases and Its Dependence on Potential and PH. *ACS Catal.* **2017**, *7* (6), 3916–3923.

294. Tasca, F.; Farias, D.; Castro, C.; Acuna-Rougier, C.; Antiochia, R. Bilirubin Oxidase from Myrothecium Verrucaria Physically Absorbed on Graphite Electrodes. Insights into the Alternative Resting Form and the Sources of Activity Loss. *PLoS One* **2015**, *10* (7), 1–9.

295. Weigel, M. C.; Tritscher, E.; Lisdat, F. Direct Electrochemical Conversion of Bilirubin Oxidase at Carbon Nanotube-Modified Glassy Carbon Electrodes. *Electrochem. Commun.* **2007**, *9* (4), 689–693.

296. Tsujimura, S.; Kawaharada, M.; Nakagawa, T.; Kano, K.; Ikeda, T. Mediated Bioelectrocatalytic O_2 Reduction to Water at Highly Positive Electrode Potentials near Neutral PH. *Electrochem. Commun.* **2003**, *5* (2), 138–141.

297. Gentil, S.; Carrière, M.; Cosnier, S.; Gounel, S.; Mano, N.; Le Goff, A. Direct Electrochemistry of Bilirubin Oxidase from Magnaporthe Orizae on Covalently-Functionalized MWCNT for the Design of High-Performance Oxygen-Reducing Biocathodes. *Chem. - Eur. J.* **2018**, *24* (33), 8404–8408.

298. Mano, N.; Mao, F.; Heller, A. Characteristics of a Miniature Compartment-Less Glucose-O2 Biofuel Cell and Its Operation in a Living Plant. *J. Am. Chem. Soc.* **2003**, *125* (21), 6588–6594.

299. Salimi, A.; Compton, R. G.; Hallaj, R. Glucose Biosensor Prepared by Glucose Oxidase Encapsulated Sol-Gel and Carbon-Nanotube-Modified Basal Plane Pyrolytic Graphite Electrode. *Anal. Biochem.* **2004**, *333* (1), 49–56.

300. Feng, D.; Liu, T. F.; Su, J.; Bosch, M.; Wei, Z.; Wan, W.; Yuan, D.; Chen, Y. P.; Wang, X.; Wang, K.; Lian, X.; Gu, Z. Y.; Park, J.; Zou, X.; Zhou, H. C. Stable Metal-Organic Frameworks Containing Single-Molecule Traps for Enzyme Encapsulation. *Nat. Commun.* **2015**, *6*, 1–8.

301. Chen, W.; Yang, W.; Lu, Y.; Zhu, W.; Chen, X. Encapsulation of Enzyme into Mesoporous Cages of Metal-Organic Frameworks for the Development of Highly Stable Electrochemical Biosensors. *Anal. Methods* **2017**, *9* (21), 3213–3220.

302. Phipps, J.; Haseli, M.; Pinzon-Herrera, L.; Wilson, B.; Corbitt, J.; Servoss, S.; Almodovar, J. Delivery of Immobilized IFN-γ With PCN-333 and Its Effect on Human Mesenchymal Stem Cells. *ACS Biomater. Sci. Eng.* **2023**, *9* (2), 671–679.

303. Chen, W.; Yang, W.; Lu, Y.; Zhu, W.; Chen, X. Encapsulation of Enzyme into Mesoporous Cages of Metal-Organic Frameworks for the Development of Highly Stable Electrochemical Biosensors. *Anal. Methods* **2017**, *9* (21), 3213–3220.

304. Chen, W.; Yang, W.; Lu, Y.; Zhu, W.; Chen, X. Encapsulation of Enzyme into Mesoporous Cages of Metal-Organic Frameworks for the Development of Highly Stable Electrochemical Biosensors. *Anal. Methods* **2017**, *9* (21), 3213–3220.

305. Lian, X.; Erazo-Oliveras, A.; Pellois, J.-P.; Zhou, H.-C. High Efficiency and Long-Term Intracellular Activity of an Enzymatic Nanofactory Based on Metal-Organic Frameworks. *Nat. Commun.* **2017**, *8* (1), 2075.

306. Feng, D.; Liu, T.-F. F.; Su, J.; Bosch, M.; Wei, Z.; Wan, W.; Yuan, D.; Chen, Y.-P. P.; Wang, X.; Wang, K.; Lian, X.; Gu, Z.-Y. Y.; Park, J.; Zou, X.; Zhou, H.-C. C. Stable Metal-Organic Frameworks Containing Single-Molecule Traps for Enzyme Encapsulation. *Nat. Commun.* **2015**, *6* (1), 5979.

307. Lian, X.; Feng, D.; Chen, Y.-P.; Liu, T.-F.; Wang, X.; Zhou, H.-C. The Preparation of an Ultrastable Mesoporous Cr(Iii)-MOF via Reductive Labilization. *Chem. Sci.* **2015**, *6* (12), 7044–7048.

308. Park, J.; Feng, D.; Zhou, H.-C. C. Dual Exchange in PCN-333: A Facile Strategy to Chemically Robust Mesoporous Chromium Metal-Organic Framework with Functional Groups. *J. Am. Chem. Soc.* **2015**, *137* (36), 11801–11809.

309. Zou, L.; Feng, D.; Liu, T.-F.; Chen, Y.-P.; Yuan, S.; Wang, K.; Wang, X.; Fordham, S.; Zhou, H.-C. A Versatile Synthetic Route for the Preparation of Titanium Metal–Organic Frameworks. *Chem. Sci.* **2016**, *7* (2), 1063–1069.

310. Park, J.; Feng, D.; Zhou, H.-C. Structure-Assisted Functional Anchor Implantation in Robust Metal–Organic Frameworks with Ultralarge Pores. *J. Am. Chem. Soc.* **2015**, *137* (4), 1663–1672.

311. Phipps, J.; Chen, H.; Donovan, C.; Dominguez, D.; Morgan, S.; Weidman, B.; Fan, C.; Fan, C.; Beyzavi, M. H.; Beyzavi, M. H. Catalytic Activity, Stability, and Loading Trends of Alcohol Dehydrogenase Enzyme Encapsulated in a Metal-Organic Framework. *ACS Appl. Mater. Interfaces* **2020**, *12* (23), 26084–26094.

312. Bellido, E.; Guillevic, M.; Hidalgo, T.; Santander-Ortega, M. J.; Serre, C.; Horcajada, P. Understanding the Colloidal Stability of the Mesoporous MIL-100(Fe) Nanoparticles in Physiological Media. *Langmuir* **2014**, *30* (20), 5911–5920.

313. Li, X.; Lachmanski, L.; Safi, S.; Sene, S.; Serre, C.; Grenèche, J. M.; Zhang, J.; Gref, R. New Insights into the Degradation Mechanism of Metal-Organic Frameworks Drug Carriers. *Sci. Rep.* **2017**, *7* (1), 1–11.

314. Bocanegra-Rodríguez, S.; Molins-Legua, C.; Campíns-Falcó, P.; Giroud, F.; Gross, A. J.; Cosnier, S. Monofunctional Pyrenes at Carbon Nanotube Electrodes for Direct Electron Transfer H_2O_2 Reduction with HRP and HRP-Bacterial Nanocellulose. *Biosens. Bioelectron.* **2021**, *187*, 113304.

315. Yang, W.; Liang, W.; O'Dell, L. A.; Toop, H. D.; Maddigan, N.; Zhang, X.; Kochubei, A.; Doonan, C. J.; Jiang, Y.; Huang, J. Insights into the Interaction between Immobilized Biocatalysts and Metal–Organic Frameworks: A Case Study of PCN-333. *JACS Au* **2021**, *1* (12), 2172–2181.

316. Fischer, B. E.; Haering, U. K.; Tribolet, R.; Sigel, H. Metal Ion/Buffer Interactions. *Eur. J. Biochem.* **1979**, *94* (2), 523–530.

317. Allen, D. E.; Baker, D. J.; Gillard, R. D. Metal Complexing by Tris Buffer. *Nature* **1967**, *214* (5091), 906–907.

318. Nagaj, J.; Stokowa-Sołtys, K.; Kurowska, E.; Frączyk, T.; Ježowska-Bojczuk, M.; Bal, W. Revised Coordination Model and Stability Constants of Cu(II) Complexes of Tris Buffer. *Inorg. Chem.* **2013**, *52* (24), 13927–13933.

319. Xiao, C. Q.; Huang, Q.; Zhang, Y.; Zhang, H. Q.; Lai, L. Binding Thermodynamics of Divalent Metal Ions to Several Biological Buffers. *Thermochim. Acta* **2020**, *691*, 178721.

320. Ferreira, C. M. H.; Pinto, I. S. S.; Soares, E. V.; Soares, H. M. V. M. (Un)Suitability of the Use of PH Buffers in Biological, Biochemical and Environmental Studies and Their Interaction with Metal Ions-a Review. *RSC Adv.* **2015**, *5* (39), 30989–31003.

321. Ferreira, C. M. H.; Pinto, I. S. S.; Soares, E. V.; Soares, H. M. V. M. (Un)Suitability of the Use of PH Buffers in Biological, Biochemical and Environmental Studies and Their Interaction with Metal Ions-a Review. *RSC Adv.* **2015**, *5* (39), 30989–31003.

322. Gupta, B. S.; Taha, M.; Lee, M. J. Stability Constants for the Equilibrium Models of Iron(III) with Several Biological Buffers in Aqueous Solutions. *J. Solution Chem.* **2013**, *42* (12), 2296–2309.

323. Taheri, M.; Ashok, D.; Sen, T.; Enge, T. G.; Verma, N. K.; Tricoli, A.; Lowe, A.; R. Nisbet, D.; Tsuzuki, T. Stability of ZIF-8 Nanopowders in Bacterial Culture Media and Its Implication for Antibacterial Properties. *Chem. Eng. J.* **2021**, *413* (August 2020), 127511.

324. Luzuriaga, M. A.; Benjamin, C. E.; Gaertner, M. W.; Lee, H.; Herbert, F. C.; Mallick, S.; Gassensmith, J. J. ZIF-8 Degrades in Cell Media, Serum, and Some—but Not All—Common Laboratory Buffers. *Supramol. Chem.* **2019**, *31* (8), 485–490.

325. Blanchard, P. Y.; Buzzetti, P. H. M.; Davies, B.; Nedellec, Y.; Girotto, E. M.; Gross, A. J.; Le Goff, A.; Nishina, Y.; Cosnier, S.; Holzinger, M. Electrosynthesis of Pyrenediones on Carbon Nanotube Electrodes for Efficient Electron Transfer with FAD-Dependent Glucose Dehydrogenase in Biofuel Cell Anodes. *ChemElectroChem* **2019**, *6* (20), 5242–5247.

326. Gross, A. J.; Tanaka, S.; Colomies, C.; Giroud, F.; Nishina, Y.; Cosnier, S.; Tsujimura, S.; Holzinger, M. Diazonium Electrografting vs. Physical Adsorption of Azure A at Carbon Nanotubes for Mediated Glucose Oxidation with FAD-GDH. *ChemElectroChem* **2020**, *7* (22), 4543–4549.

327. Artner, C.; Bohrer, B.; Pasquini, L.; Mazurenko, I.; Lahrach, N.; Byrne, D.; de Poulpiquet, A.; Lojou, E. Effects of Interactions between SPEEK or Nafion Ionomers and Bilirubin Oxidase on O_2 Enzymatic Reduction. *Electrochim. Acta* **2022**, *426* (May), 140787.

328. Wu, X.; Yue, H.; Zhang, Y.; Gao, X.; Li, X.; Wang, L.; Cao, Y.; Hou, M.; An, H.; Zhang, L.; Li, S.; Ma, J.; Lin, H.; Fu, Y.; Gu, H.; Lou, W.; Wei, W.; Zare, R. N.; Ge, J. Packaging and Delivering Enzymes by Amorphous Metal-Organic Frameworks. *Nat. Commun.* **2019**, *10* (1), 1–8.

329. Blasco-Ahicart, M.; Soriano-Lopez, J.; Carbo, J. J.; Poblet, J. M.; Galan-Mascaros, J. R. Polyoxometalate Electrocatalysts Based on Earthabundant Metals for Efficient Water Oxidation in Acidic Media. *Nat. Chem.* **2018**, *10* (1), 24–30.

330. Lalaoui, N.; Holzinger, M.; Le Goff, A.; Cosnier, S. Diazonium Functionalisation of Carbon Nanotubes for Specific Orientation of Multicopper Oxidases: Controlling Electron Entry Points and Oxygen Diffusion to the Enzyme. *Chem. - Eur. J.* **2016**, *22* (30), 10494–10500.

331. Tominaga, M.; Ohtani, M.; Taniguchi, I. Gold Single-Crystal Electrode Surface Modified with Self-Assembled Monolayers for Electron Tunneling with Bilirubin Oxidase. *Phys. Chem. Chem. Phys* **2008**, *10* (46), 6928–6934.

332. Hirose, J.; Inoue, K.; Sakuragi, H.; Kikkawa, M.; Minakami, M.; Morikawa, T.; Iwamoto, H.; Hiromi, K. Anions Binding to Bilirubin Oxidase from Trachyderma Tsunodae K-2593. *Inorg. Chim. Acta* **1998**, *273* (1–2), 204–212.

333. Lalaoui, N.; Le Goff, A.; Holzinger, M.; Cosnier, S. Fully Oriented Bilirubin Oxidase on Porphyrin-Functionalized Carbon Nanotube Electrodes for Electrocatalytic Oxygen Reduction. *Chem. - Eur. J.* **2015**, *21* (47), 16868–16873.

334. Göbel, G.; Dietz, T.; Lisdat, F. Biosensor Based on an Oxygen Reducing Bilirubin Oxidase Electrode. *Procedia Chem.* **2009**, *1* (1), 273–276.

335. MacRae, C. F.; Sovago, I.; Cottrell, S. J.; Galek, P. T. A.; McCabe, P.; Pidcock, E.; Platings, M.; Shields, G. P.; Stevens, J. S.; Towler, M.; Wood, P. A. Mercury 4.0: From Visualization to Analysis, Design and Prediction. *J. Appl. Crystallogr.* **2020**, *53*, 226–235.

336. Ishida, T.; Murayama, T.; Taketoshi, A.; Haruta, M. Importance of Size and Contact Structure of Gold Nanoparticles for the Genesis of Unique Catalytic Processes. *Chem. Rev.* **2020**, *120* (2), 464–525.

337. Ohmiya, H. N-Heterocyclic Carbene-Based Catalysis Enabling Cross-Coupling Reactions. *ACS Catal.* **2020**, 6862–6869.

338. Enders, D.; Niemeier, O.; Henseler, A. Organocatalysis by N-Heterocyclic Carbenes. *Chem. Rev.* **2007**, *107* (12), 5606–5655.

339. Hollóczki, O. The Mechanism of N-Heterocyclic Carbene Organocatalysis through a Magnifying Glass. *Chem. - Eur. J.* **2020**, *26* (22), 4885–4894.

340. Flanigan, D. M.; Romanov-Michailidis, F.; White, N. A.; Rovis, T. Organocatalytic Reactions Enabled by N-Heterocyclic Carbenes. *Chem. Rev.* **2015**, *115* (17), 9307–9387.

341. Gimbert, C.; Lumbierres, M.; Marchi, C.; Moreno-Mañas, M.; Sebastián, R. M.; Vallribera, A. Michael Additions Catalyzed by Phosphines. An Overlooked Synthetic Method. *Tetrahedron* **2005**, *61* (36), 8598–8605.

342. Weeden, J. A.; Chisholm, J. D. Phosphine-Catalyzed Nitroaldol Reactions. *Tetrahedron Lett.* **2006**, *47* (52), 9313–9316.

343. Vedejs, E.; Daugulis, O.; Diver, S. T. Enantioselective Acylations Catalyzed by Chiral Phosphines. *J. Org. Chem* **1996**, *61* (2), 430–431

344. Garibay, S. J.; Wang, Z.; Cohen, S. M. Evaluation of Heterogeneous Metal-Organic Framework Organocatalysts Prepared by Postsynthetic Modification. *Inorg. Chem.* **2010**, *49* (17), 8086–8091.

345. Rho, H. S.; Oh, S. H.; Lee, J. W.; Lee, J. Y.; Chin, J.; Song, C. E. Bifunctional Organocatalyst for Methanolytic Desymmetrization of Cyclic Anhydrides: Increasing Enantioselectivity by Catalyst Dilution. *Chem. Commun.* **2008**, No. 10, 1208–1210.

346. Das, S.; Asefa, T. Epoxide Ring-Opening Reactions with Mesoporous Silica-Supported Fe(III) Catalysts. *ACS Catal.* **2011**, *1* (5), 502–510.

347. Merad, J.; Lalli, C.; Bernadat, G.; Maury, J.; Masson, G. Enantioselective Brønsted Acid Catalysis as a Tool for the Synthesis of Natural Products and Pharmaceuticals. *Chem. - Eur. J.* **2018**, *24* (16), 3925–3943.

348. Min, C.; Seidel, D. Asymmetric Brønsted Acid Catalysis with Chiral Carboxylic Acids. *Chem. Soc. Rev.* **2017**, *46* (19), 5889–5902.

349. Rueping, M.; Antonchick, A. P.; Sugiono, E.; Grenader, K. Asymmetric Brønsted Acid Catalysis: Catalytic Enantioselective Synthesis of Highly Biologically Active Dihydroquinazolinones. *Angew. Chem., Int. Ed.* **2009**, *48* (5), 908–910.

350. Testa, M. L.; La Parola, V. Sulfonic Acid-Functionalized Inorganic Materials as Efficient Catalysts in Various Applications: A Minireview. *Catalysts* **2021**, *11* (10).

351. Iimura, S.; Nobutou, D.; Manabe, K.; Kobayashi, S. Mannich-Type Reactions in Water Using a Hydrophobic Polymer-Supported Sulfonic Acid Catalyst. *Chem. Commun.* **2003**, *3* (14), 1644–1645.

352. Margelefsky, E. L.; Zeidan, R. K.; Dufaud, V.; Davis, M. E. Organized Surface Functional Groups: Cooperative Catalysis via Thiol/Sulfonic Acid Pairing. *J. Am. Chem. Soc.* **2007**, *129* (44), 13691–13697.

353. Ramachary, D. B.; Ramakumar, K.; Narayana, V. V. Organocatalytic Cascade Reactions Based on Push-Pull Dienamine Platform: Synthesis of Highly Substituted Anilines. *J. Org. Chem.* **2007**, *72* (4), 1458–1463.

354. Kano, T.; Sugimoto, H.; Maruoka, K. Efficient Organocatalytic Cross-Aldol Reaction between Aliphatic Aldehydes through Their Functional Differentiation. *J. Am. Chem. Soc.* **2011**, *133* (45), 18130–18133.

355. Trost, B. M.; Müller, C. Asymmetric Friedel-Crafts Alkylation of Pyrroles with Nitroalkenes Using a Dinuclear Zinc Catalyst. *J. Am. Chem. Soc.* **2008**, *130* (8), 2438–2439.

356. Bui, T.; Barbas, C. F. A Proline-Catalyzed Asymmetric Robinson Annulation Reaction. *Tetrahedron Lett.* **2000**, *41* (36), 6951–6954.

357. Hajos, Z. G.; Parrish, D. R. Synthesis and Conversion of 2-Methyl-2-(3-Oxobutyl)-l,3-Cyclopentanedione to the Isomeric Racemic Ketols of the [3.2.1] Bicyclooctane and of the Perhydroindan. *J. Org. Chem.* **1974**, *39* (12), 1612–1615.

358. Chen, B.; Berger, G.; Hanessian, S. Metal Coordination Controlled and Bifunctional H-Bonded Catalysis in Stereoselective Intramolecular Aldol Cyclizations toward Carbocyclic Tertiary β-Ketols. *European J. Org. Chem.* **2017**, (18), 2631–2636.

359. Malerich, J. P.; Hagihara, K.; Rawal, V. H. Chiral Squaramide Derivatives Are Excellent Hydrogen Bond Donor Catalysts. *J. Am. Chem. Soc.* **2008**, *130* (44), 14416–14417.

360. Wei, S.; Yalalov, D. A.; Tsogoeva, S. B.; Schmatz, S. New Highly Enantioselective Thiourea-Based Bifunctional Organocatalysts for Nitro-Michael Addition Reactions. *Catal. Today* **2007**, *121* (1–2), 151–157.

361. Tan, B.; Zhang, X.; Chua, P. J.; Zhong, G. Recyclable Organocatalysis: Highly Enantioselective Michael Addition of 1,3-Diaryl-1,3-Propanedione to Nitroolefins. *Chem. Commun.* **2009**, No. 7, 779–781.

362. Wang, Z.-X.; Zhou, Z.; Xiao, W.; Ouyang, Q.; Du, W.; Chen, Y.-C. Double Activation Catalysis for A′-Alkylidene Cyclic Enones with Chiral Amines and Thiols. *Chem. - Eur. J.* **2017**, *23* (44), 10678–10682.

363. Tong, B. M. K.; Chiba, S. Diamine-Catalyzed Conjugate Addition to Acrylate Derivatives. *Org. Lett.* **2011**, *13* (11), 2948–2951.

364. de Frutos, Ó.; Granier, T.; Gómez-Lor, B.; Jiménez-Barbero, J.; Monge, Á.; Gutiérrez-Puebla, E.; Echavarren, A. M. Synthesis and Self-Association of Syn-5,10,15-Trialkylated Truxenes. *Chem. - Eur. J.* **2002**, *8* (13), 2879–2890.

Appendix A | For Chapter 2

A 1. M[$Zn_4O(hmtt)_2(bpdc)_{0.5}$], BMUF-2

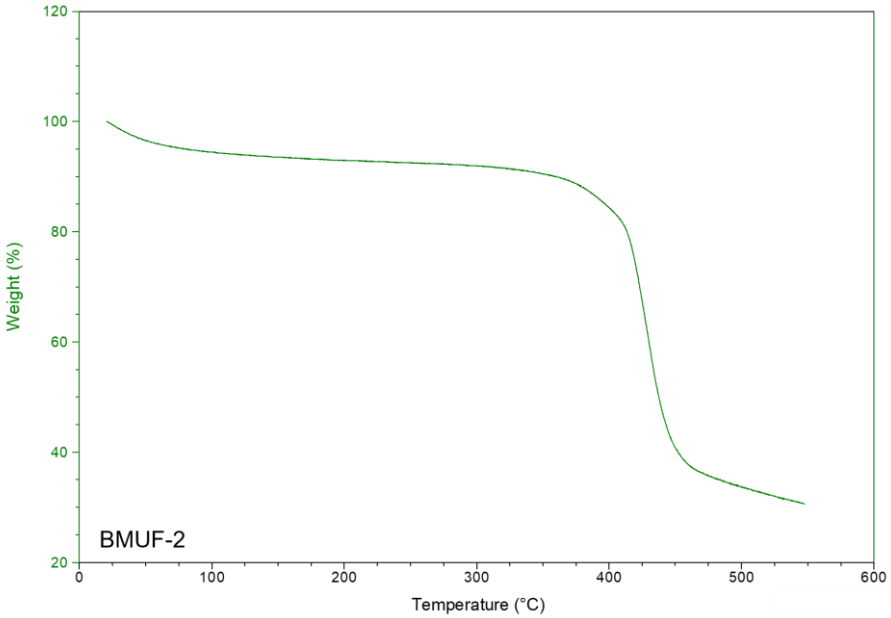

Figure A-1 TGA of BMUF-2 after activation at 150 °C for 12 h under vacuum.

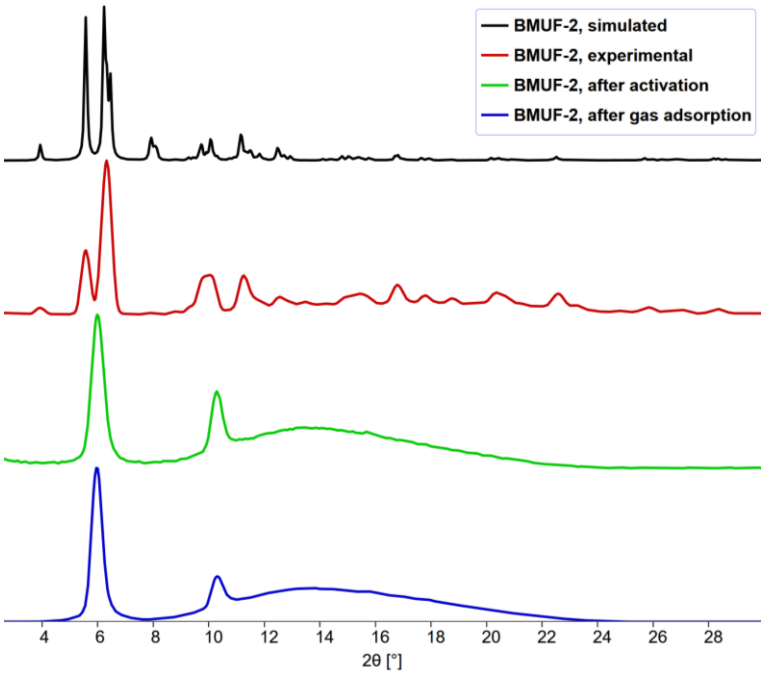

Figure A-2 PXRD patterns of BMUF-2.

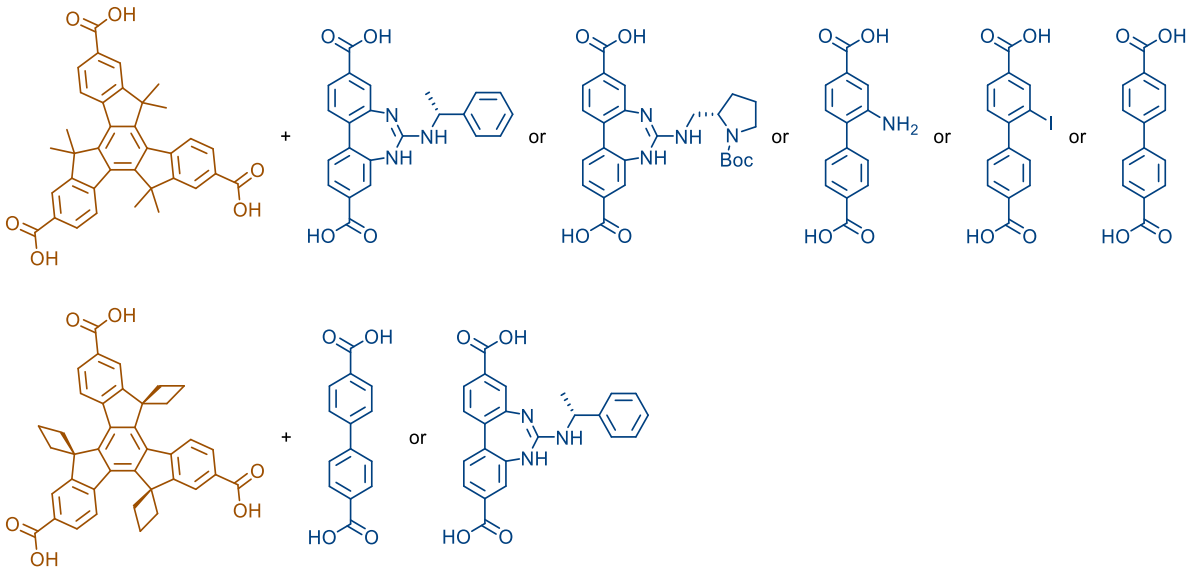

Figure A-3 Exemplary ligand combinations yielding BMUF-2.

A 2. M[$Zn_4O(hmtt)_2(bdc)_{0.5}$], BMUF-4

A 2.1 Room Temperature Synthesis

Preliminary room temperature synthesis protocol for BMUF-4, $hmtt_2|bdc_{0.5}|Zn_4O$

Hmtt (17.8 mg, 0.0319 mmol, 2.4 eq.) was suspended in DMF (0.67 mL). A 0.04 M solution of bdc in DMF (330 µL, 0.0132 mmol, 1 eq.) was added. While stirring, a solution of $Zn(OAc)_2 \cdot 2H_2O$ (29.2 mg, 0.133 mmol, 10 eq.) in DMF (0.5 mL) and water (25 µL) was added. Immediate formation of a precipitate was observed. The reaction was stirred for 60 min before the solid was collected by centrifugation and washed with DMF (5x).

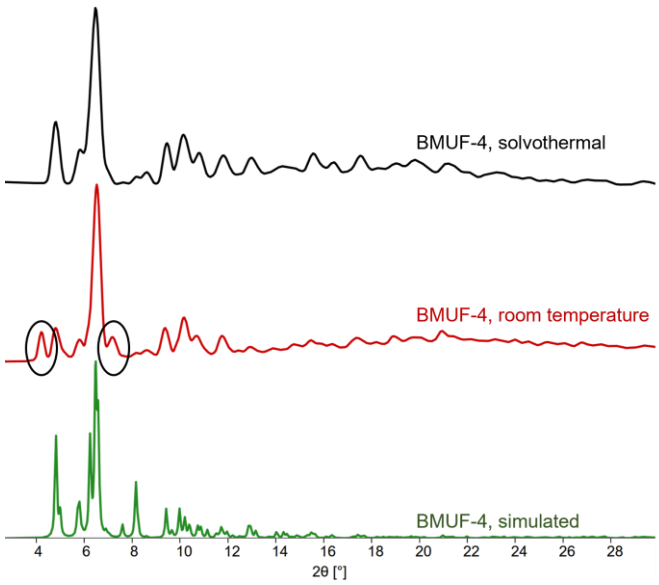

Figure A-4 PXRD pattern of the sample obtained through room temperature synthesis (red, middle) in comparison to a solvothermal synthesis (top, black) and the simulated PXRD pattern (bottom, green). While BMUF-2 was obtained, the sample was not phase pure.

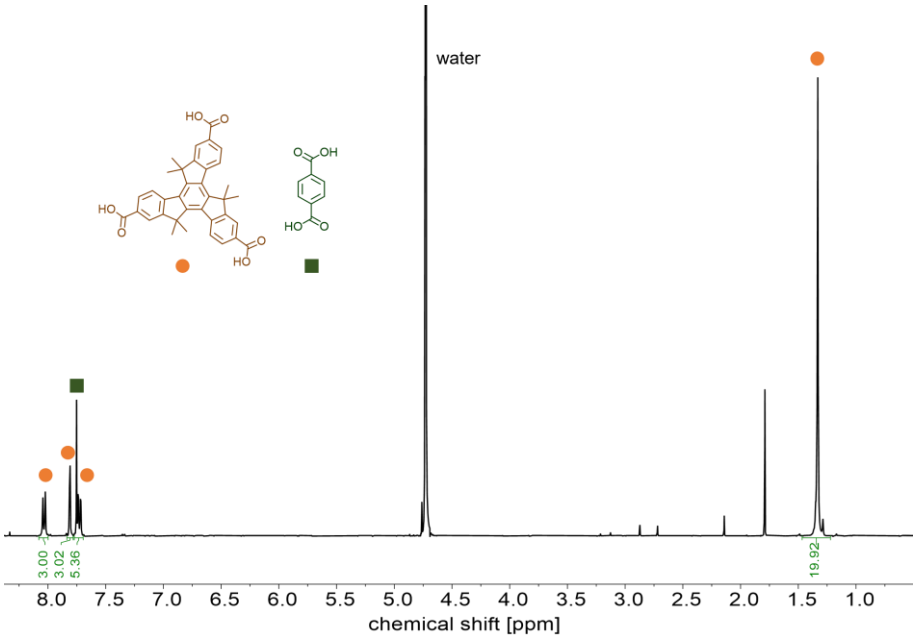

Figure A-5 ^{1}H NMR spectrum of BMUF-4 obtained through a room temperature synthesis protocol in 0.1 M NaOD in D_2O. The increased amount of bdc compared to hmtt indicated the co-precipitation of a second phase during the room temperature synthesis.

A 2.2 Solvothermal Synthesis

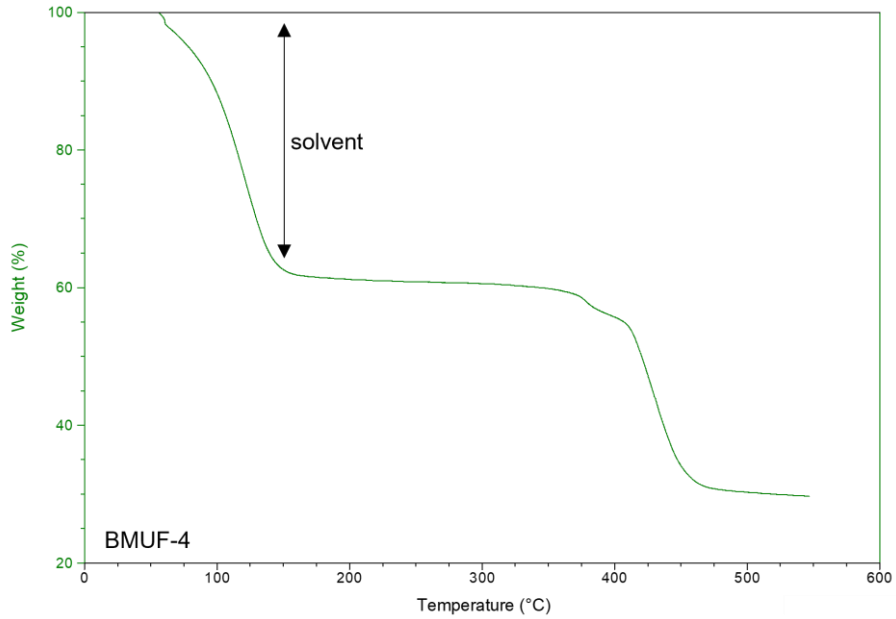

Figure A-6 TGA of BMUF-4 after drying the sample briefly under vacuum at room temperature. Trapped solvent was evaporated at elevated temperature. The MOF was stable until around 350 °C.

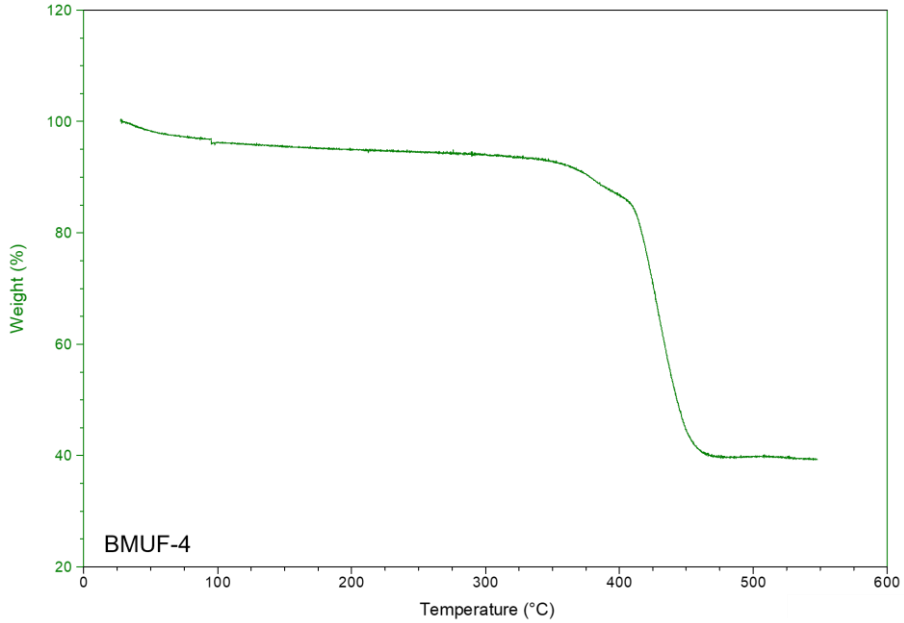

Figure A-7 TGA of BMUF-4 after activation at 150 °C for 3 h under vacuum.

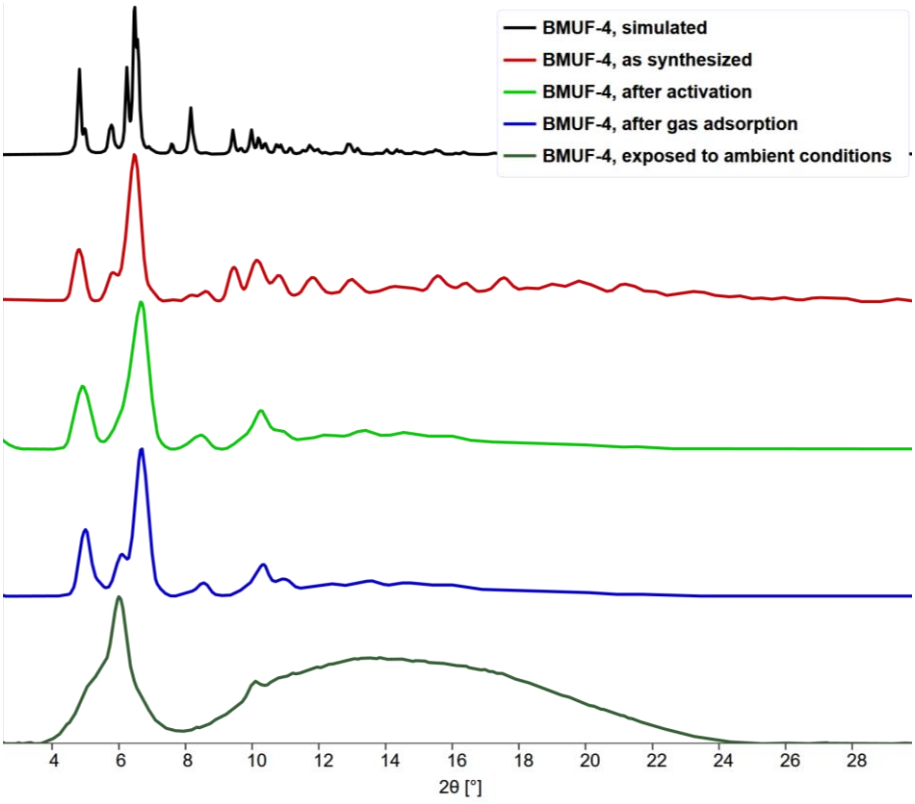

Figure A-8 PXRD patterns of BMUF-4.

A 2.3 Hmtt-Single-Linker BMUFs

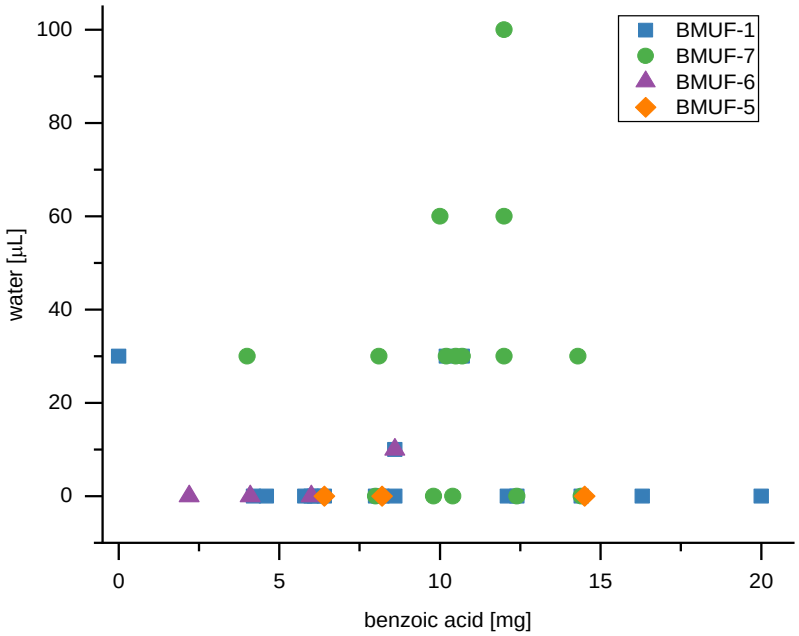

Figure A-9 BMUF-phases observed during standard syntheses from hmtt (2.0 mg), $Zn(NO_3)_2 \cdot 4H_2O$, benzoic acid, and water (where applicable) in DMF.

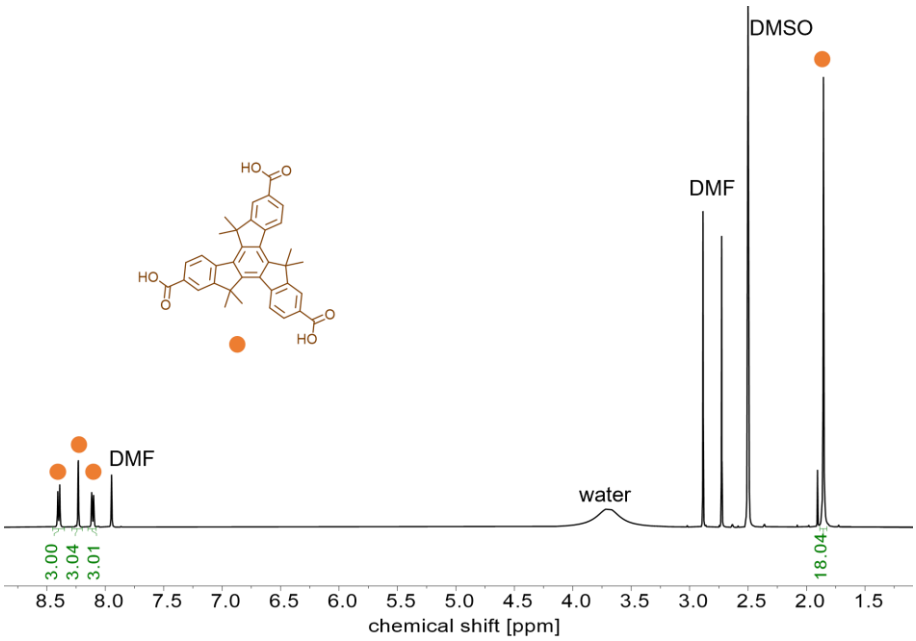

Figure A-10 ^1H NMR of BMUF-1 derived from room temperature synthesis upon digestion in DMSO-d_6/DCl.

Appendix B | For Chapter 3

B 1. Phosphine-Functionalized MUF-77

B 1.1 MOF NMR Spectra

Table B-1 Crystalline phases observed during the synthesis of PEt_{2}-$_{s}$MUF-77 with different amounts of added triethyl amine.

Triethyl amine added	Product
-	BMUF-1/2 + second phase
1.3 µL, 2.8 eq.	BMUF-1/2+ second phase
13 µL, 28 eq.	MUF-77 + second phase

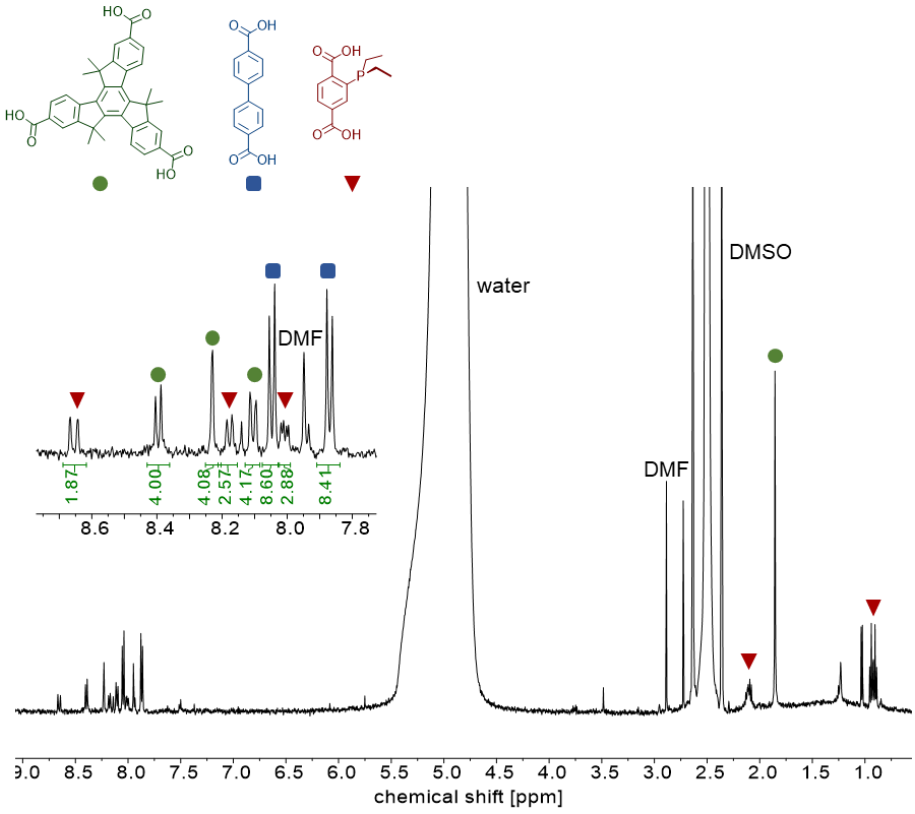

Figure B-1 ^{1}H NMR spectrum of a mixture of PEt_{2}-$_{s}$MUF-77 and second phase. The crystalline solid was dissolved in a mixture of DMSO and DCl.

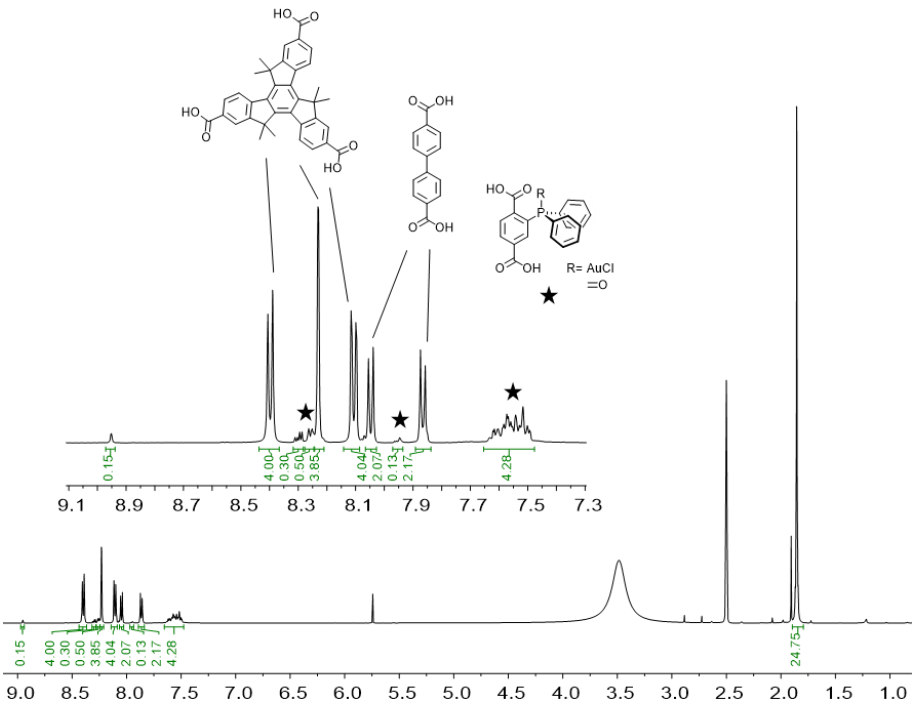

Figure B-2 ^{1}H NMR of AuPPh$_2$-*rt*MUF-77 upon digestion in a mixture of DMSO-d$_6$ and DCl.

B 2. Phosphoramidite-Functionalized MUF-77

B 2.1 Experimental Procedures

Attempted direct synthesis of $(Me_2N)PO_2$-bpdc from $(OH)_2$-bpdc Under argon, $(OH)_2$-bpdc (34.8 mg, 0.127 mmol, 1 eq.) was suspended in anhydrous toluene (1 mL). $P(NMe_2)_3$ (29 µL, 0.19 mmol, 1.5 eq.) was added while stirring. The reaction vessel was rinsed with anhydrous toluene (1 mL) and the reaction was refluxed for 16 h. The precipitate was filtered off and dried under vacuum to yield the dicarboxamide byproduct.

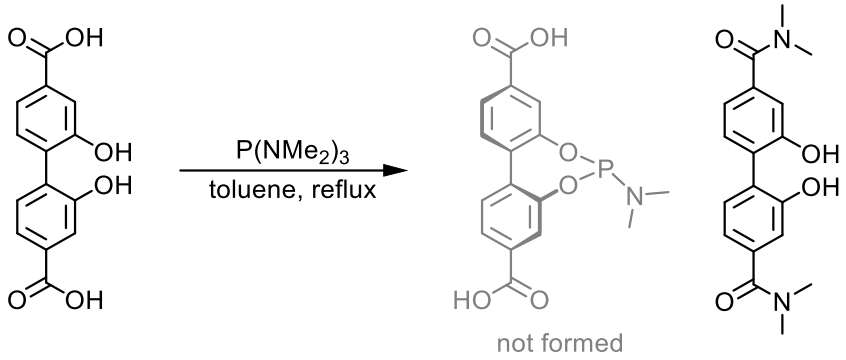

Figure B-3 Direct synthesis attempt of $(Me_2N)PO_2$-bpdc from $(OH)_2$-bpdc leading to the formation of a dicarboxamide byproduct.

B 2.2 Ligand NMR Spectra

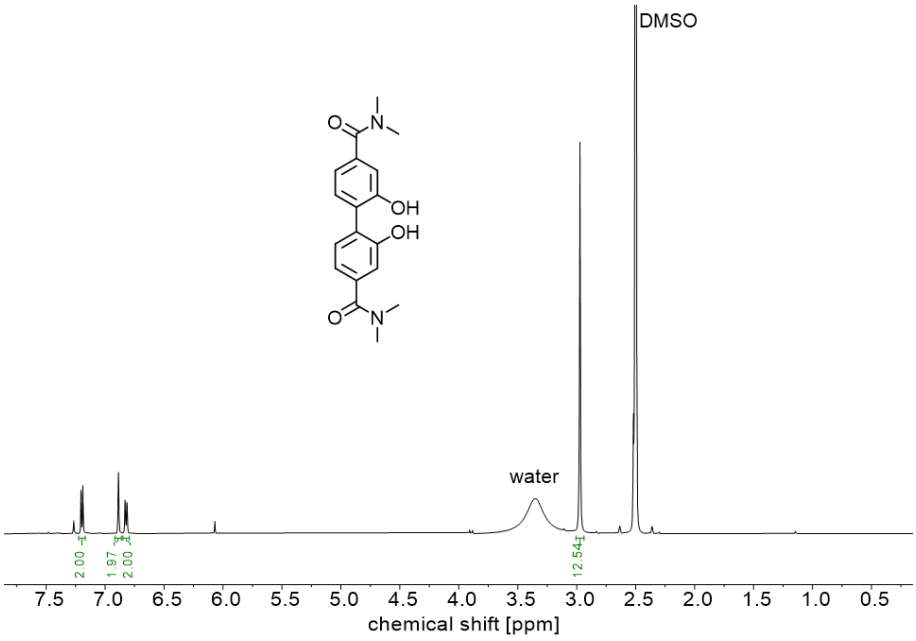

Figure B-4 ^1H NMR spectrum of 2,2'-dihydroxy-N4,N4,N4',N4'-tetramethyl-[1,1'-biphenyl]-4,4'-dicarboxamide in DMSO-d_6. The compound was isolated as a byproduct from the attempted direct synthesis of $(Me_2N)PO_2$-bpdc.

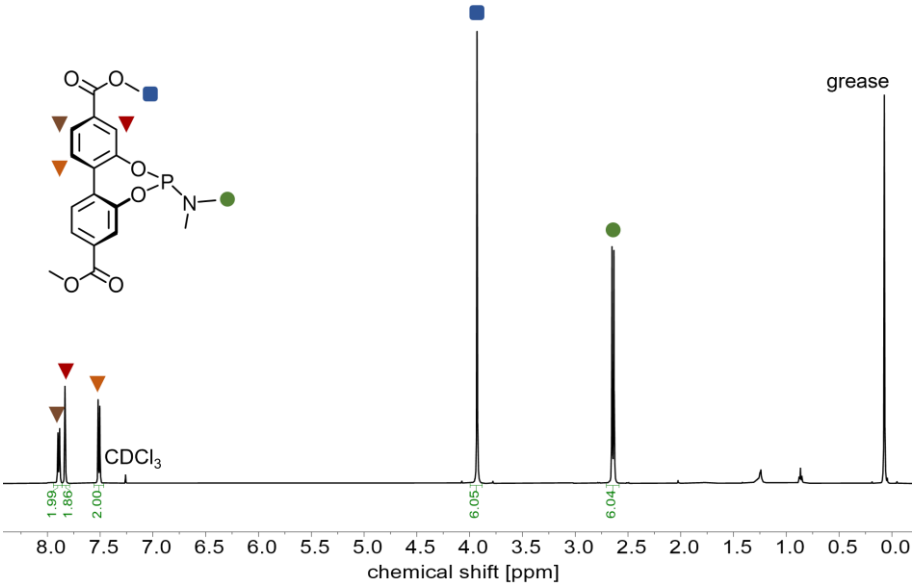

Figure B-5 ^{1}H NMR spectrum of $(Me_2N)PO_2$-bpdc dimethyl ester (**1**) in $CDCl_3$.

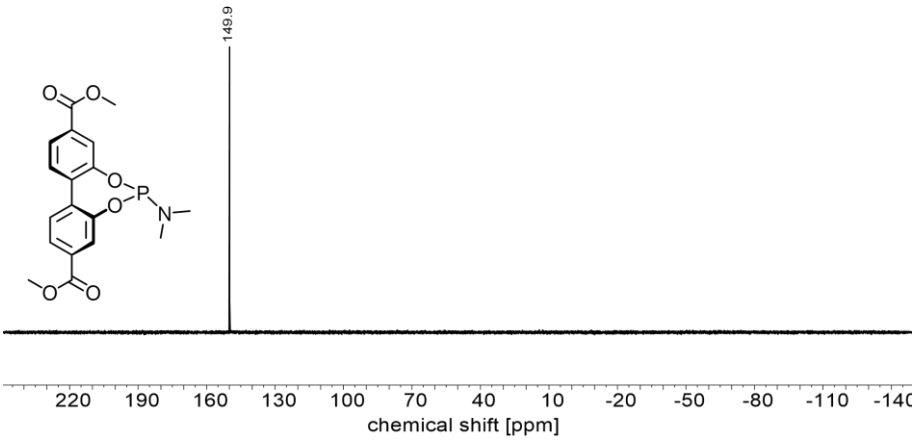

Figure B-6 ^{31}P NMR spectrum of $(Me_2N)PO_2$-bpdc dimethyl ester (**1**) in $CDCl_3$.

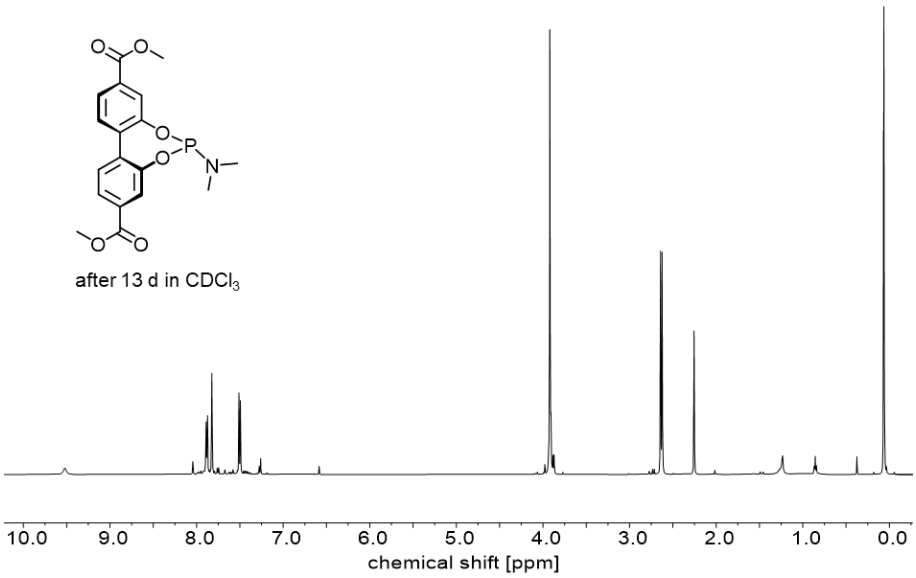

Figure B-7 ^{1}H NMR spectrum of $(Me_2N)PO_2$-bpdc dimethyl ester (**1**) after 13 d in $CDCl_3$.

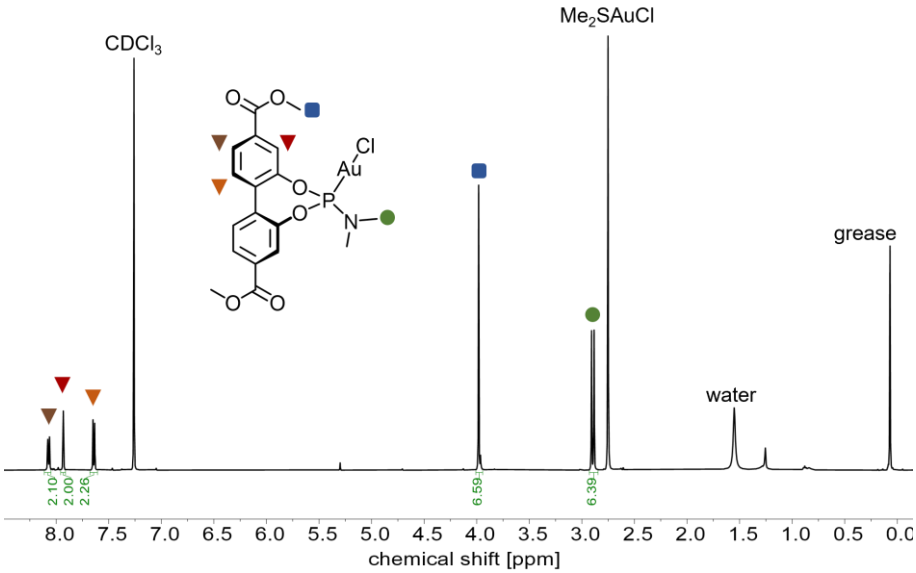

Figure B-8 ^{1}H NMR spectrum of $AuPO_2$-bpdc dimethyl ester (**2**) in $CDCl_3$.

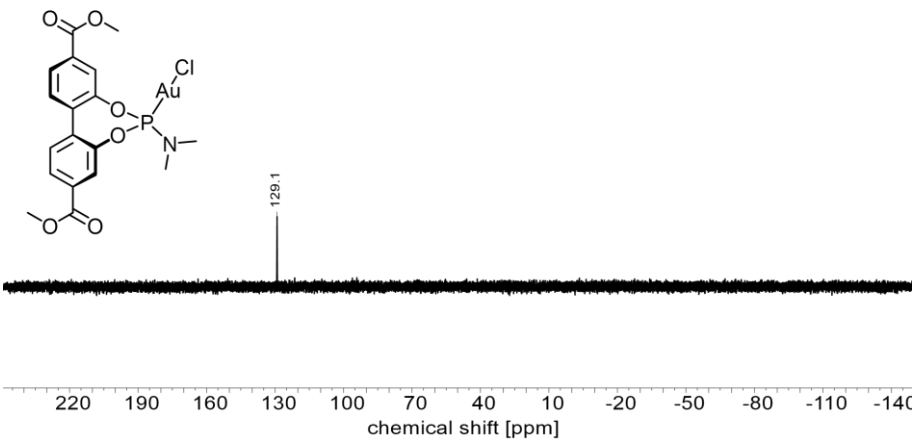

Figure B-9 ^{31}P NMR spectrum of $AuPO_2$-bpdc dimethyl ester (**2**) in $CDCl_3$.

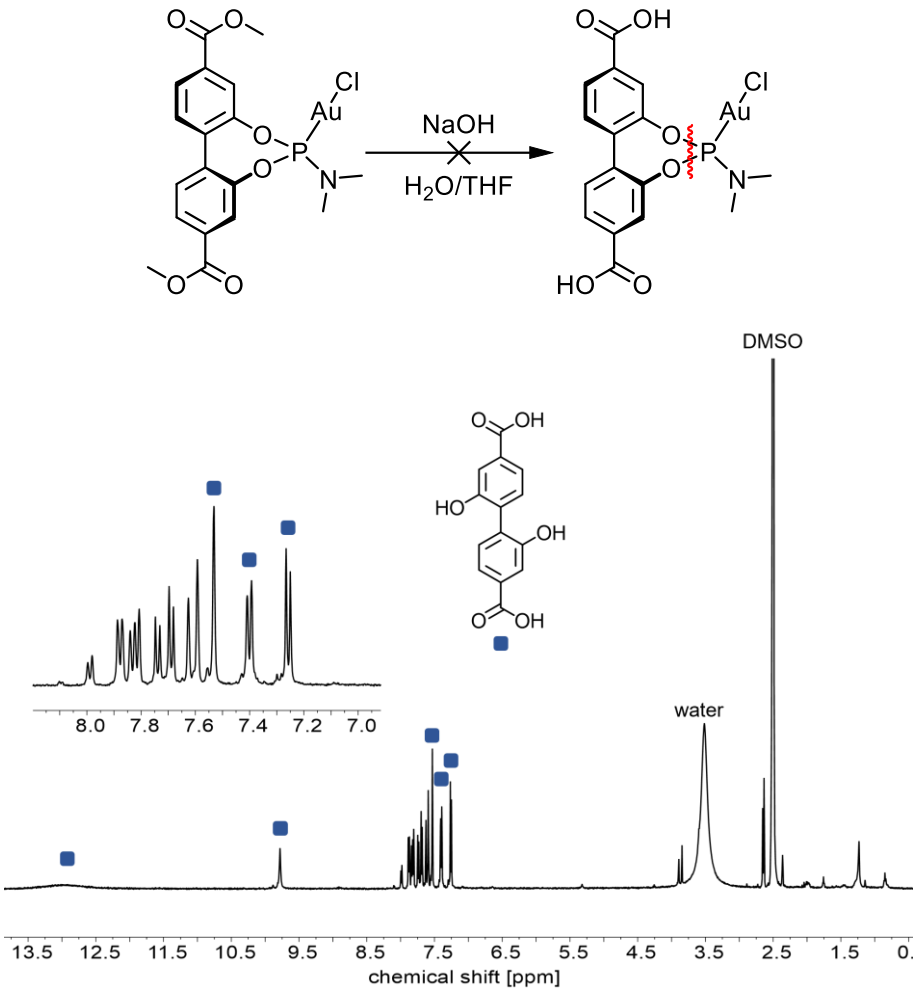

Figure B-10 ^{1}H NMR spectrum of the attempted hydrolysis of $AuPO_2$-bpdc dimethyl ester (**2**) to obtain the desired MUF-77 linker $AuPO_2$-bpdc (**3**) in DMSO-d_6. The characteristic signals for $(OH)_2$-bpdc indicate the decomposition of the gold(I) complex under the hydrolysis conditions.

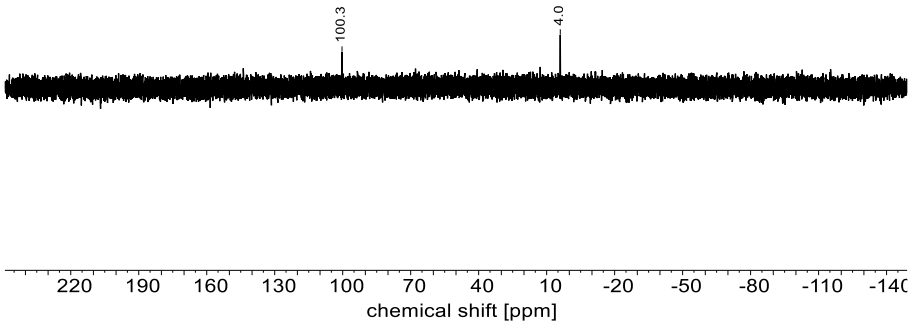

Figure B-11 ^{31}P NMR spectrum of the attempted hydrolysis in DMSO-d_6.

B 2.3 MOF NMR Spectra

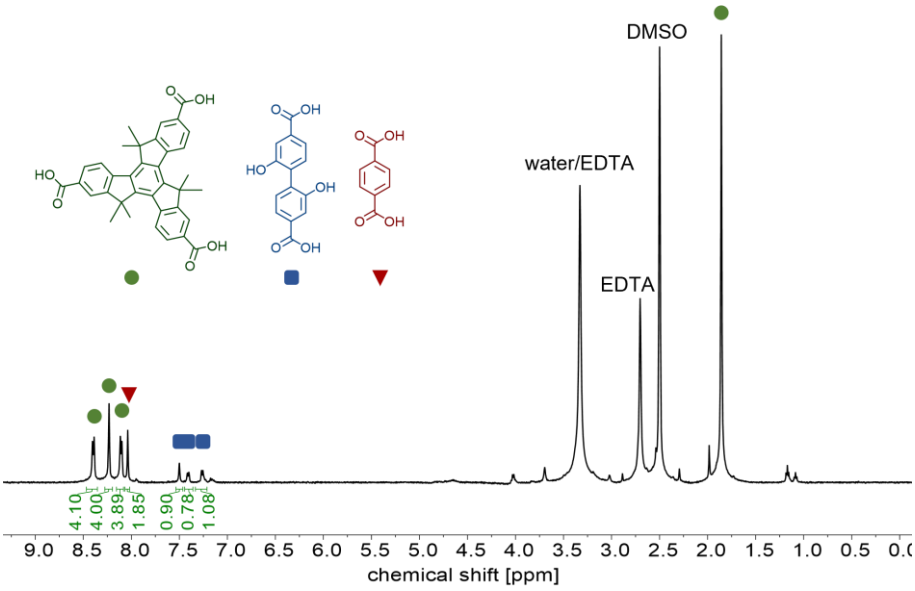

Figure B-12 ^{1}H NMR spectrum of $(OH)_2$-$_s$MUF-77 upon digestion in a solution of EDTA (1 mg) in DMSO-d_6 (0.6 mL).

B 2.4 Digestion Experiments

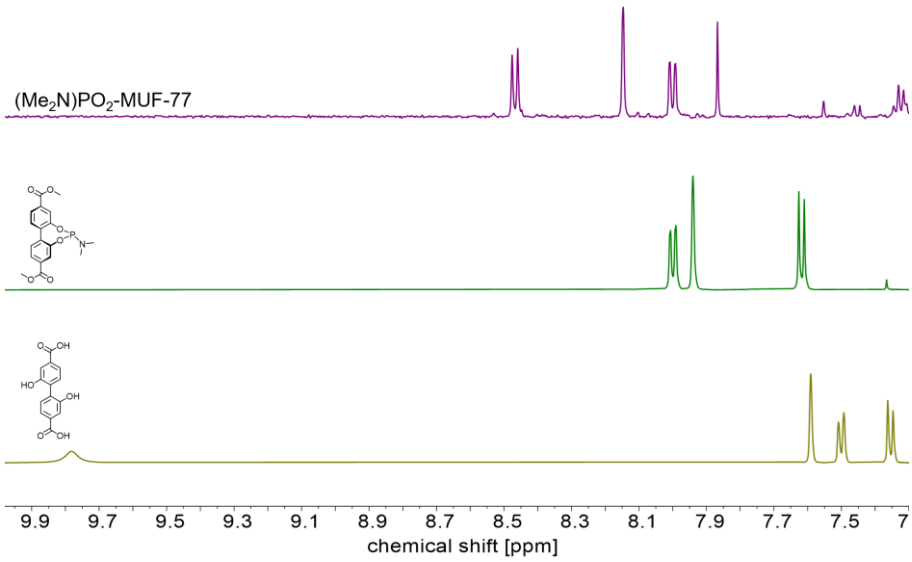

Figure B-13 ^{1}H NMR spectra of $(Me_2N)PO_2$-MUF-77 (top, purple) upon digestion in 0.1 M NaOD/D_2O in comparison with $(Me_2N)PO_2$-bpdc dimethyl ester (middle, green) and $(OH)_2$-bpdc (bottom, yellow). Only the aromatic region is shown for simplicity.

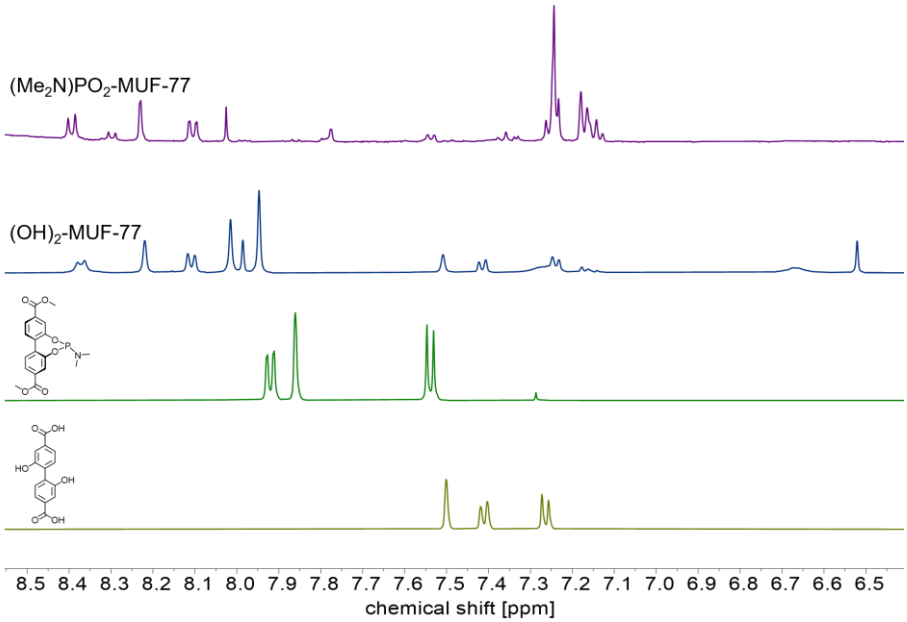

Figure B-14 ^{1}H NMR spectra of $(Me_2N)PO_2$-MUF-77 (purple) and $(OH)_2$-MUF-77 (blue) upon digestion in a solution of thioacetamide (1 mg) in DMSO-d_6 (0.6 mL) in comparison with $(Me_2N)PO_2$-bpdc dimethyl ester (green) and $(OH)_2$-bpdc (yellow). Only the aromatic region is shown for simplicity.

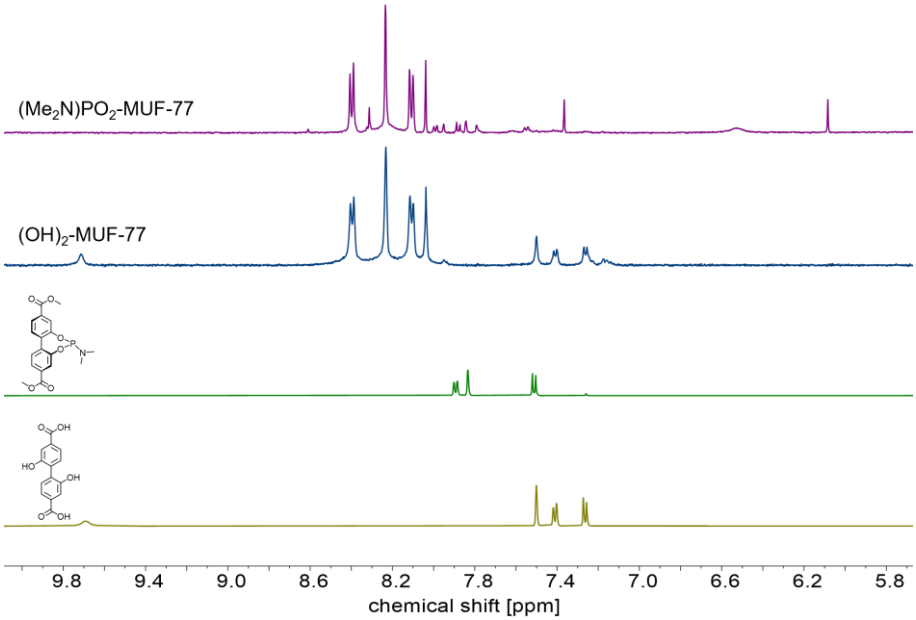

Figure B-15 ^{1}H NMR spectra of $(Me_2N)PO_2$-MUF-77 (purple) and $(OH)_2$-MUF-77 (blue) upon digestion in a solution of EDTA (1 mg) in DMSO-d_6 (0.6 mL) in comparison with $(Me_2N)PO_2$-bpdc dimethyl ester (green) and $(OH)_2$-bpdc (yellow). Only the aromatic region is shown for simplicity.

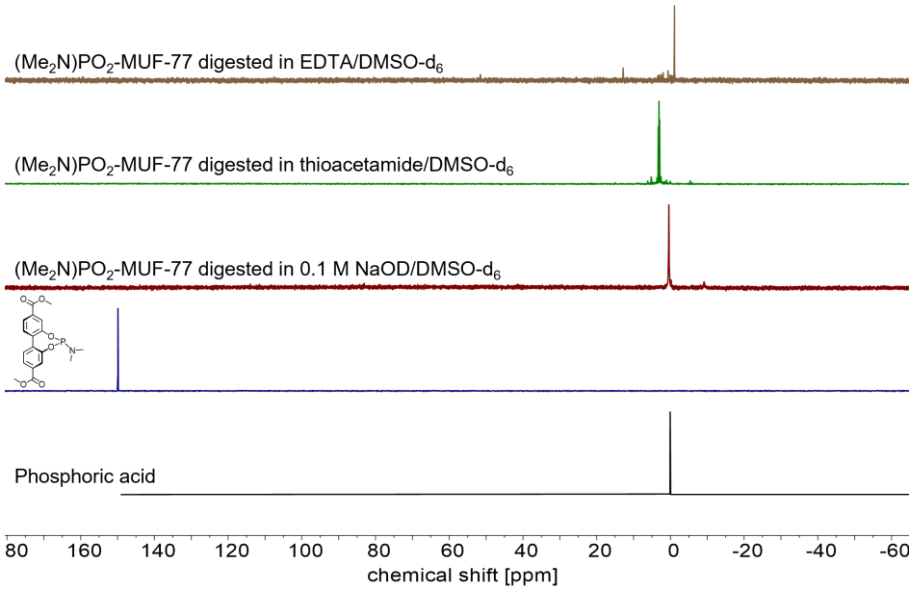

Figure B-16 ^{31}P NMR spectra of the different digestion attempts. The shift of the signal from around 149.9 ppm to a chemical shift of around 0 ppm is indicative of the decomposition of the phosphoramidite.

B 3. N-Heterocyclic Carbene–Transition Metal Complexes in MUF-77

B 3.1 Ligand NMR Spectra

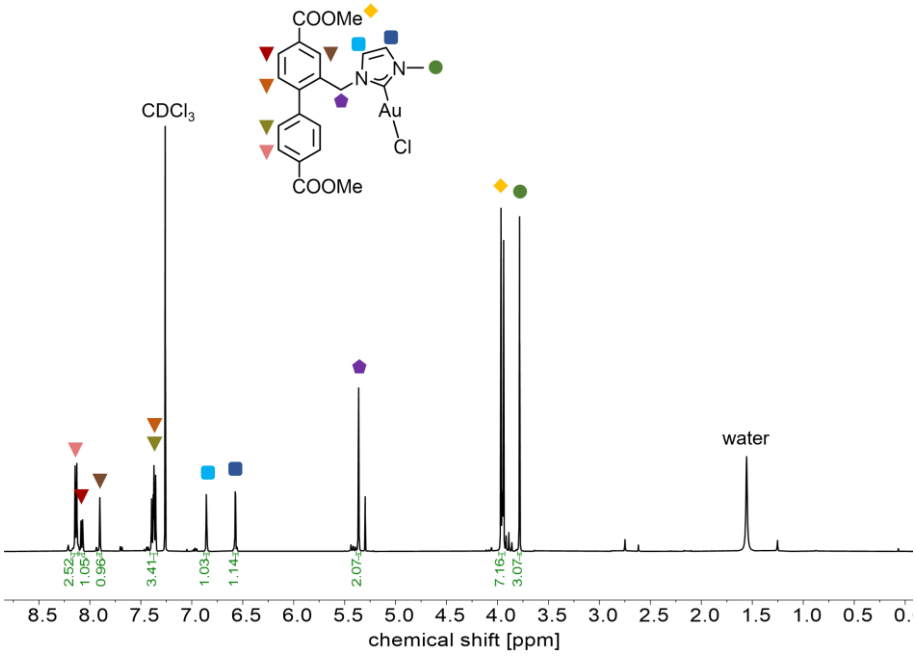

Figure B-17 ^{1}H NMR spectrum of Au(I)NHC-bpdc dimethyl ester in $CDCl_3$.

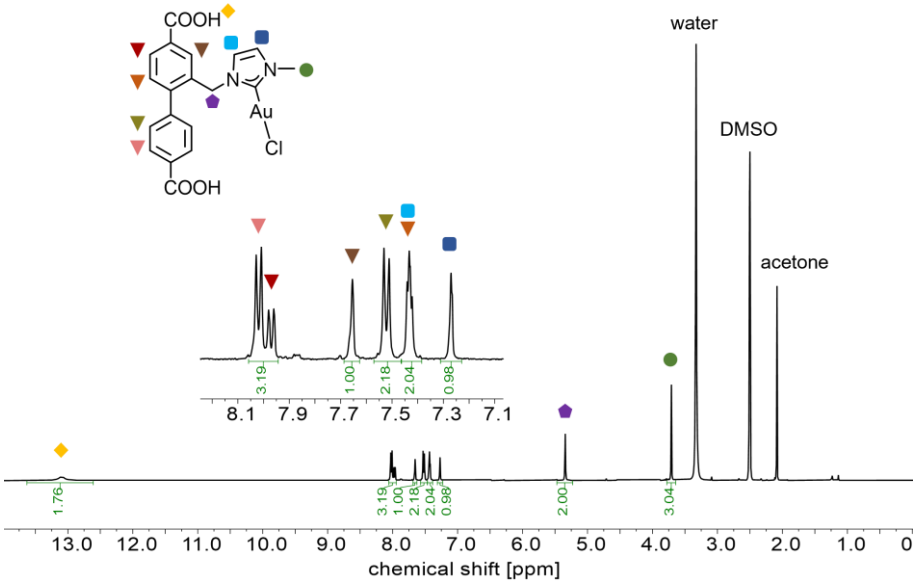

Figure B-18 ^{1}H NMR spectrum of Au(I)NHC-bpdc in DMSO-d_6.

B 3.2 MOF NMR Spectra

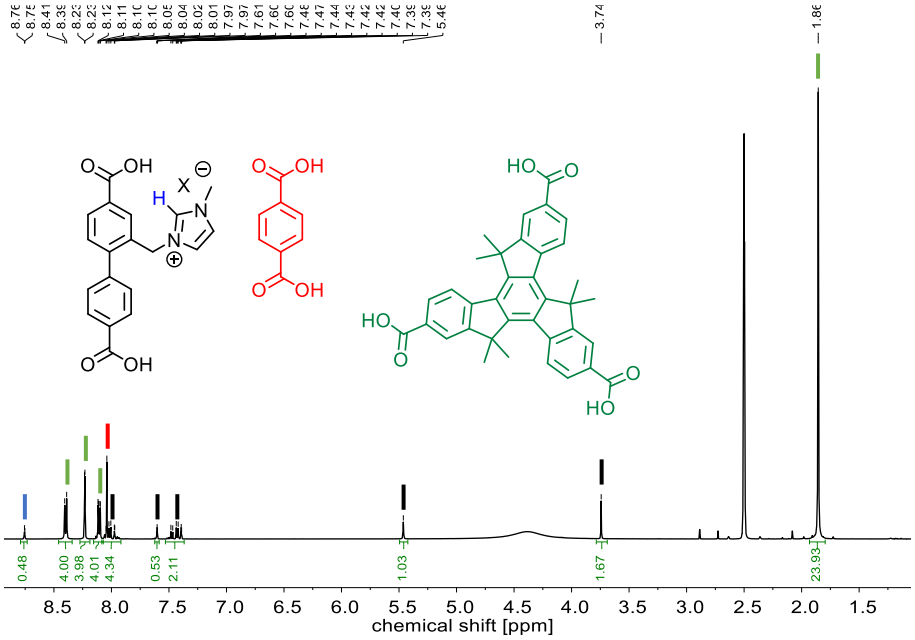

Figure B-19 ^{1}H NMR spectrum of im-$_{s}$MUF-77 upon digestion in a mixture of DMSO-d_6 and DCl.

B 3.3 MOF Pictures

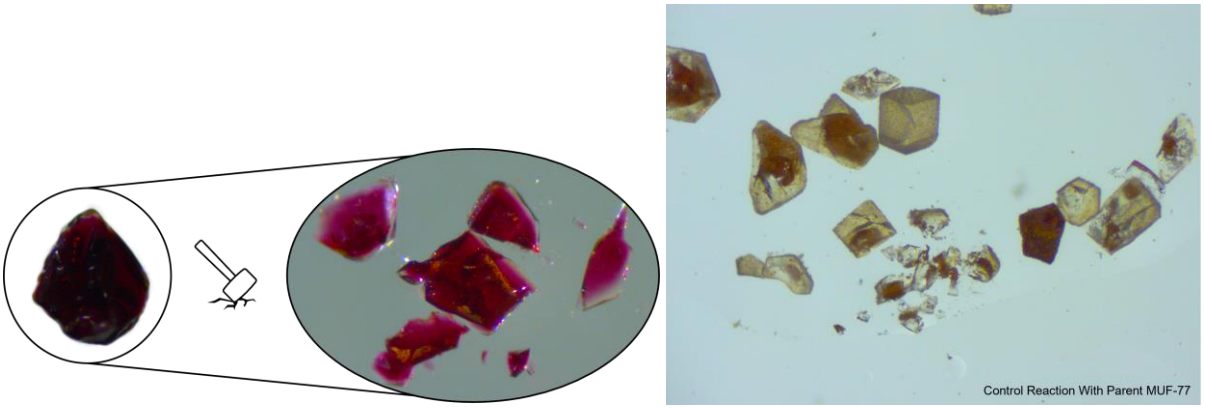

Figure B-20 Microscopic picture of a single crystal of Au@im-MUF-77 (left) as-synthesized and after carefully breaking it in comparison with the control reaction (right) using parent MUF-77.

B 3.4 Catalysis NMR

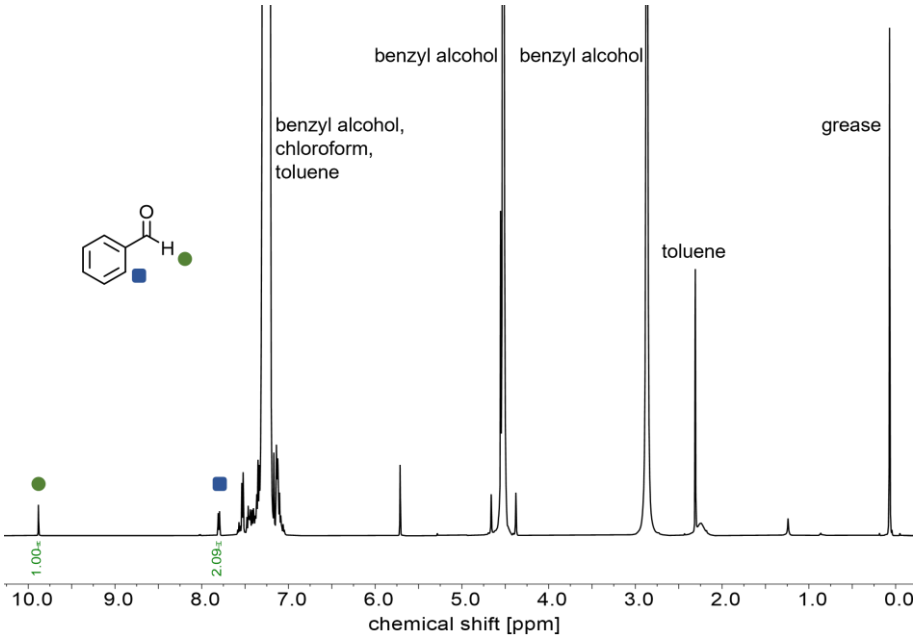

Figure B-21 ^{1}H NMR spectrum of the catalytic oxidation of benzyl alcohol by Au@im-MUF-77.

B 3.5 Ligand X-ray Crystallography

Table B-2 Summary of X-ray crystallography data for (im-bpdc-ester)[AuX_2]. Crystallization from DCM and Et_2O yielded colourless rod-like crystals.

Name	**(im-bpdc-ester)[AuX_2]**
Empirical formula	$C_{21}H_{21}AuBrClN_2O_4$
Formula weight	677.734
Temperature/K	297
Crystal system	monoclinic
Space group	$P2_1$
a/Å	7.2337(2)
b/Å	30.3193(11)
c/Å	10.4850(4)
α/°	90
β/°	92.772(2)
γ/°	90
Volume/Å³	2296.89(14)
Z	4
ρ_{calc}g/cm³	1.96
μ/mm⁻¹	15.393
F(000)	1282.9
Crystal size/mm³	0.4 × 0.1 × 0.1
Radiation	Cu Kα (λ = 1.54178)
2Θ range for data collection/°	11.68 to 144.66
Index ranges	-8 ≤ h ≤ 8, -34 ≤ k ≤ 36, -11 ≤ l ≤ 11
Reflections collected	48447
Independent reflections	7956 [R_{int} = 0.0401, R_{sigma} = 0.0301]
Data/restraints/ parameters	7956/79/ 546
Goodness-of-fit on F²	1.056
Final R indexes [I>=2σ (I)]	R_1 = 0.0697, wR_2 = 0.1956
Final R indexes [all data]	R_1 = 0.0771, wR_2 = 0.2070
Largest diff. peak/hole / e Å⁻³	3.58/-1.54
Flack parameter	0.328(3)

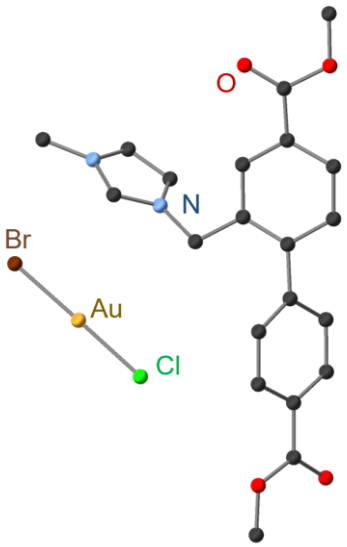

B 4. Acyclic Carbene-Functionalized MUF-77

B 4.1 Experimental

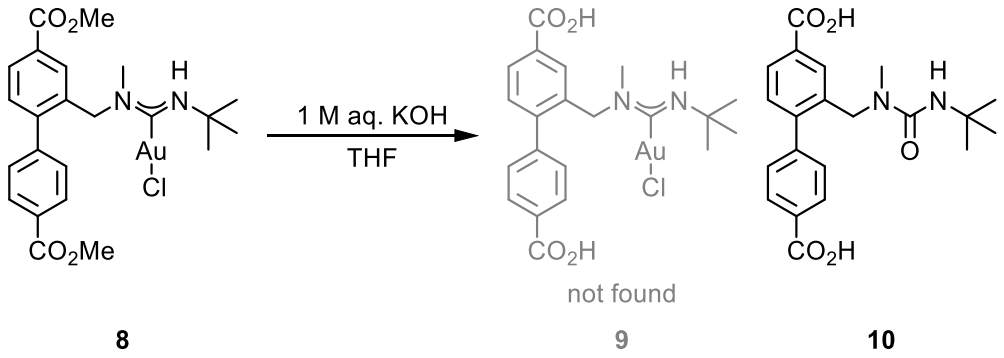

Figure B-22 Attempted hydrolysis of **8** to yield the final linker **9**.

AuNAC-bpdc ester (**8**) (24.0 mg) was dissolved in THF (1 mL). 1 M aq. KOH (1 mL) was added, and the formation of a dark precipitate was observed. The reaction was stirred for 3 d at room temperature protected from light. The suspension was filtered over celite. The organic solvent was removed under reduced pressure and the aqueous phase was acidified to pH 1 with 1 M aq. HCl. The solid was filtered off and dried under vacuum to yield the urea-type compound **10** as an off-white solid.

^{1}H NMR (500 MHz, DMSO) δ 13.01 (s, 2H), 8.02 (d, *J* = 8.0 Hz, 2H), 7.89 (dd, *J* = 7.8, 1.8 Hz, 1H), 7.83 (s, 1H), 7.49 (d, *J* = 8.1 Hz, 2H), 7.37 (d, *J* = 7.9 Hz, 1H), 5.55 (s, 1H), 4.39 (s, 2H), 2.61 (s, 3H), 1.24 (s, 9H).

^{13}C NMR (176 MHz, DMSO) δ 167.10, 167.07, 157.29, 144.25, 143.88, 136.67, 130.38, 130.11, 129.98, 129.35, 129.11, 127.91, 127.64, 50.04, 49.07, 34.23, 29.18.

m/s: theoretical: 383.1601 m/z, found: 383.1612 m/z

B 4.2 Ligand NMR Spectra

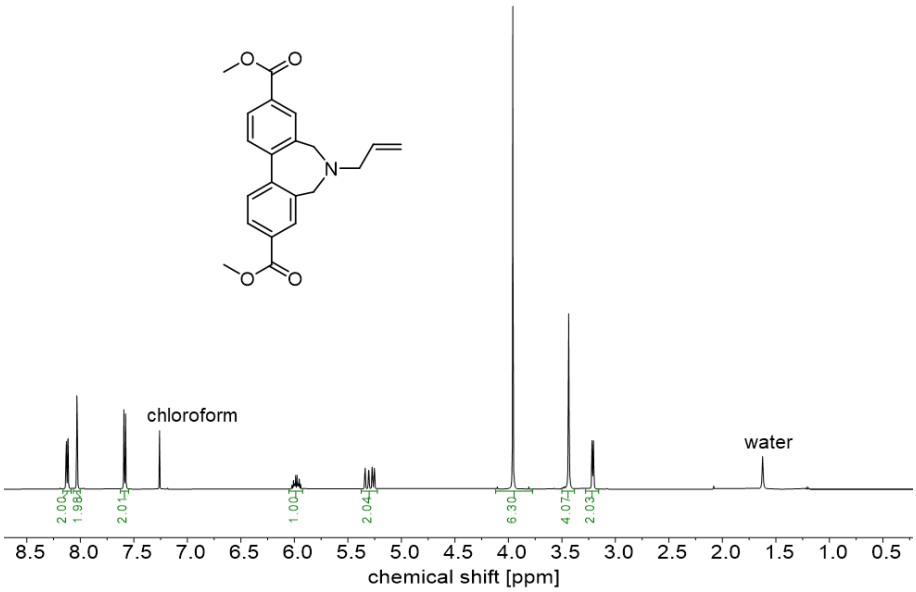

Figure B-23 ^{1}H NMR spectrum of **12** in $CDCl_3$.

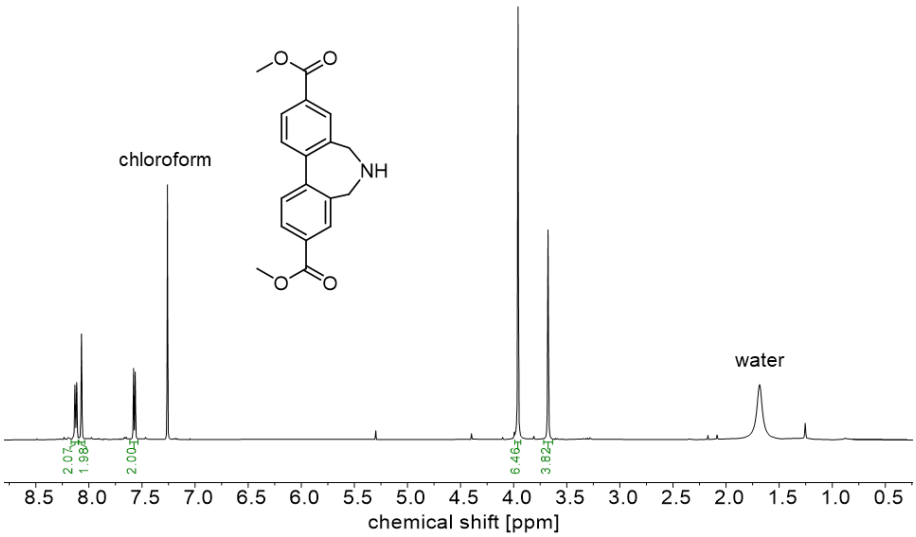

Figure B-24 ^{1}H NMR spectrum of **13** in $CDCl_3$.

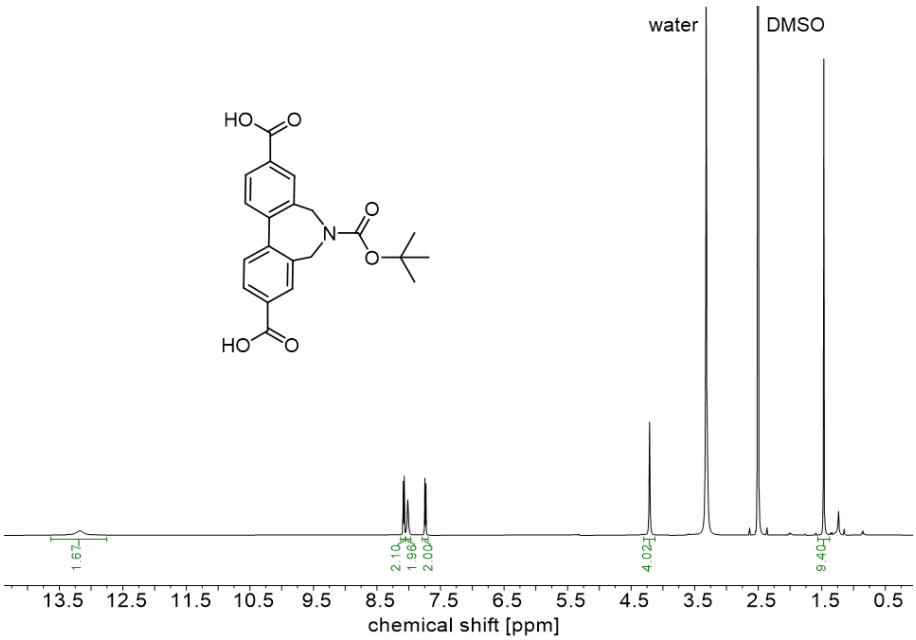

Figure B-25 ^{1}H NMR spectrum of bocaz-bpdc in DMSO-d_6.

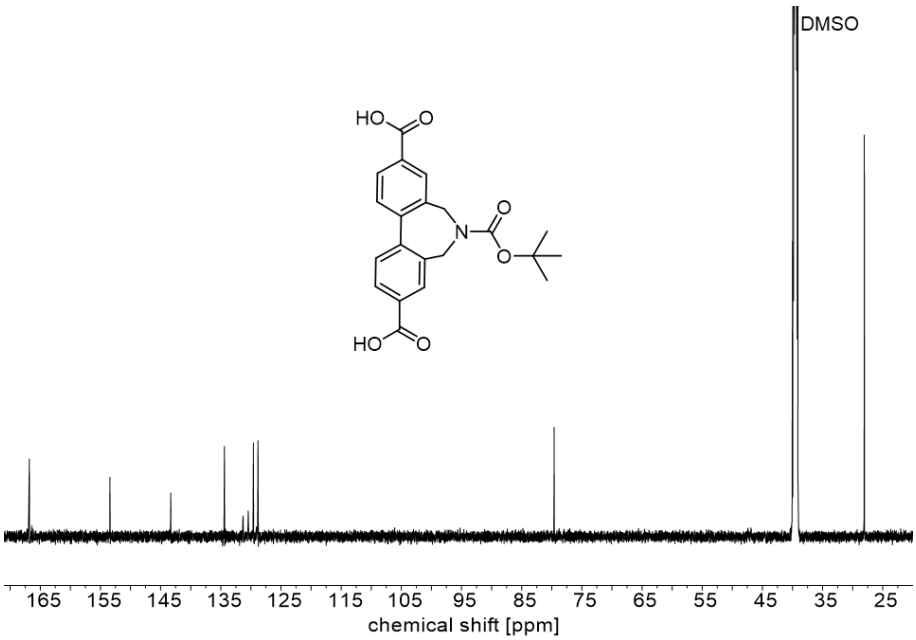

Figure B-26 ^{13}C NMR spectrum of bocaz-bpdc in DMSO-d_6.

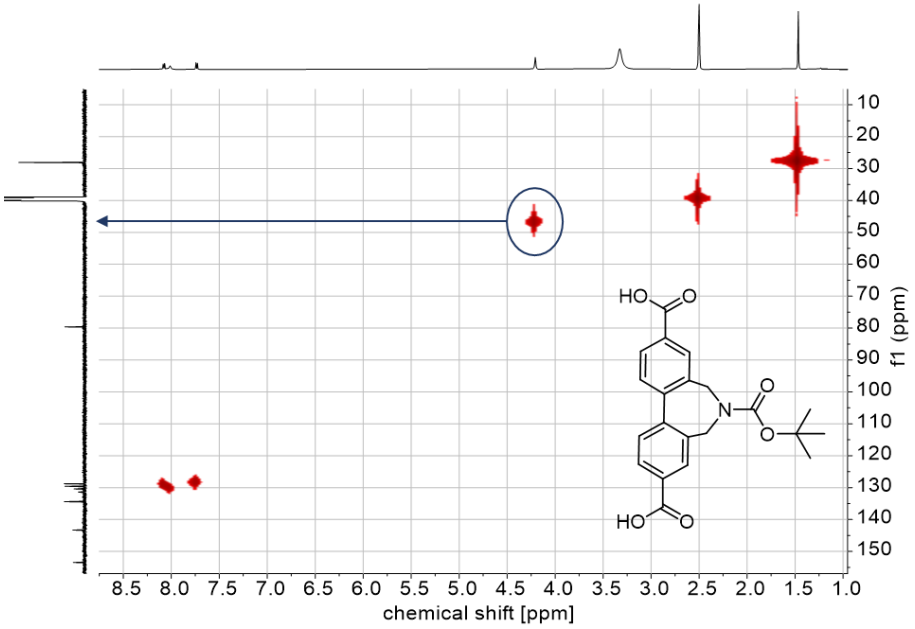

Figure B-27 HMQC NMR spectrum of bocaz-bpdc in DMSO-d_6.

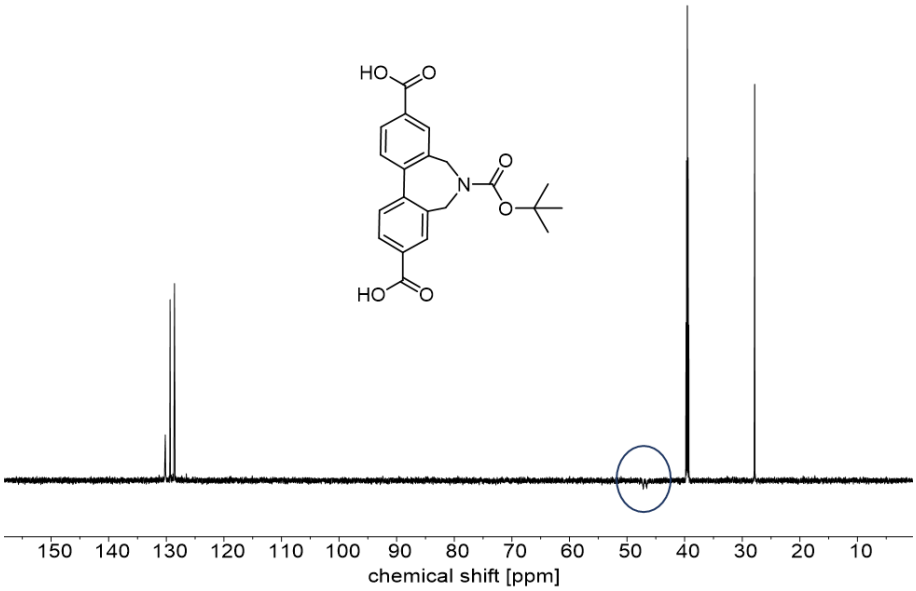

Figure B-28 DEBT NMR spectrum of bocaz-bpdc in DMSO-d_6.

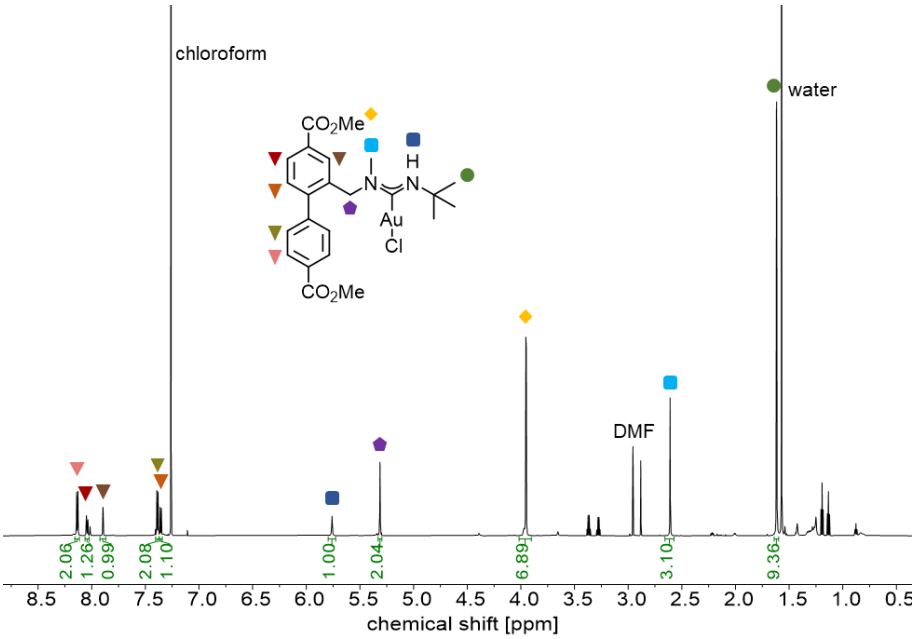

Figure B-29 ^{1}H NMR spectrum of **8** in $CDCl_3$.

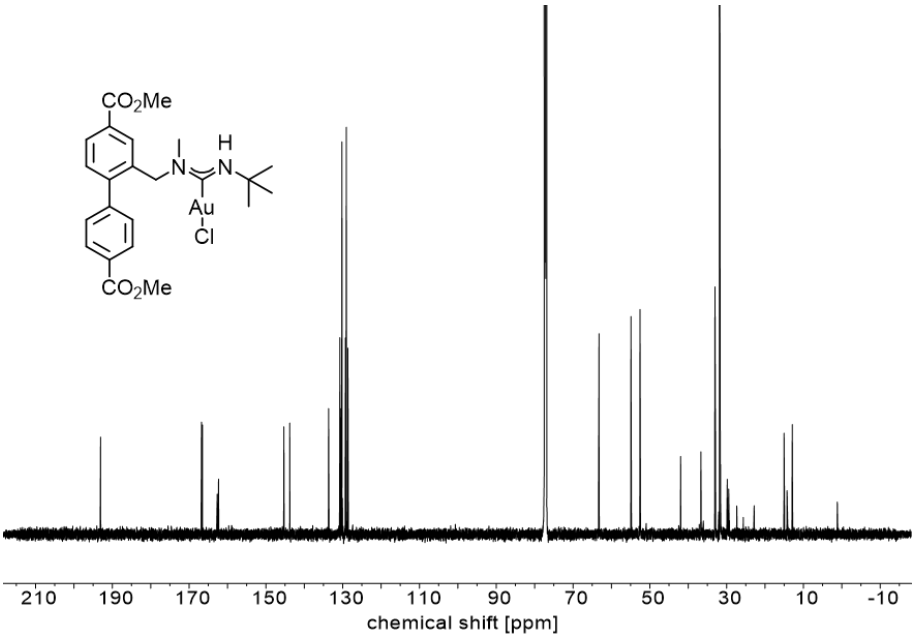

Figure B-30 ^{31}C NMR spectrum of **8** in $CDCl_3$.

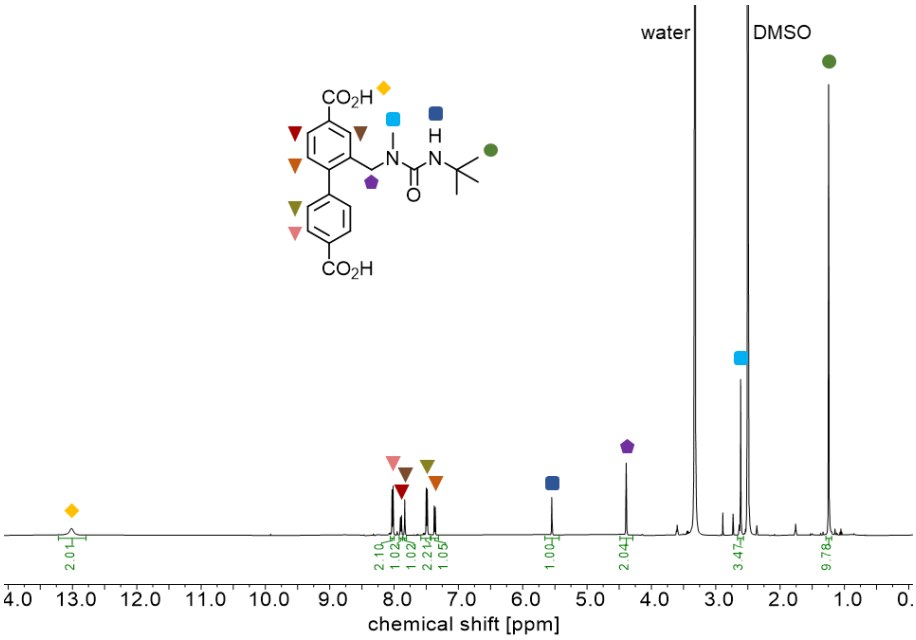

Figure B-31 ^{1}H NMR spectrum of the decomposition product from the attempted hydrolysis of **8** in DMSO-d_6.

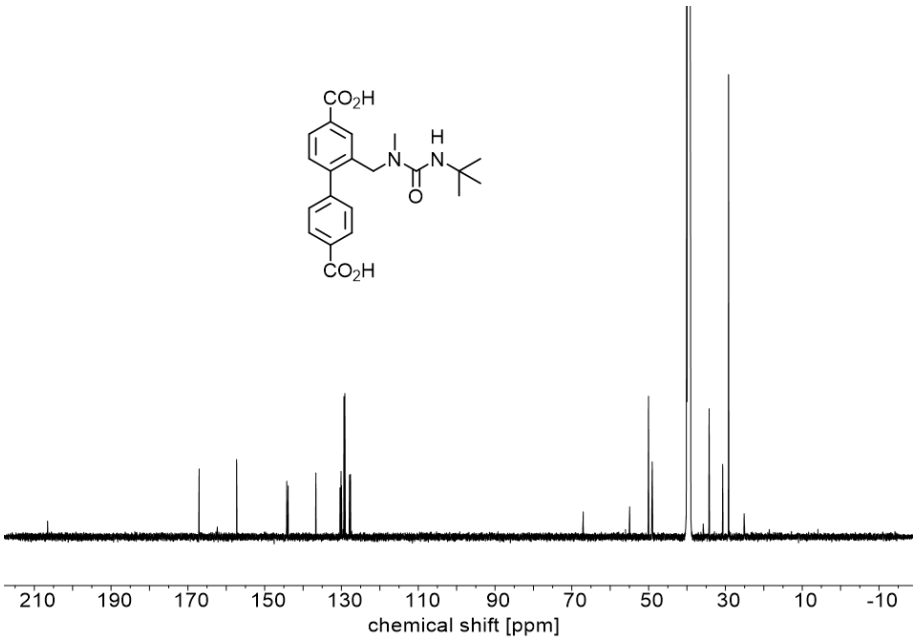

Figure B-32 ^{13}C NMR spectrum of the decomposition product from the attempted hydrolysis of **8** in DMSO-d_6.

B 4.3 Ligand X-ray Crystallography

Table B-3 Summary of X-ray crystallography data for **12**. Recrystallization in Et_2O yielded colourless, rod-like crystals.

Name	**allylamine-bpdc-ester, 12**
Empirical formula	$C_{21}H_{21}NO_4$
Formula weight	351.39
Temperature/K	100
Crystal system	monoclinic
Space group	$P2_1/c$
a/Å	18.5774(10)
b/Å	5.0393(3)
c/Å	18.5546(10)
α/°	90
β/°	92.076(2)
γ/°	90
Volume/Å³	1735.89(17)
Z	4
ρ_{calc}g/cm³	1.345
μ/mm⁻¹	0.758
F(000)	744
Crystal size/mm³	0.3 × 0.1 × 0.1
Radiation	CuKα (λ = 1.54178)
2Θ range for data collection/°	4.76 to 152.248
Index ranges	-23 ≤ h ≤ 23, -6 ≤ k ≤ 5, -22 ≤ l ≤ 22
Reflections collected	29017
Independent reflections	3579 [R_{int} = 0.0267, R_{sigma} = 0.0174]
Data/restraints/ parameters	3579/0/ 237
Goodness-of-fit on F²	1.052
Final R indexes [I>=2σ (I)]	R_1 = 0.0398, wR_2 = 0.0979
Final R indexes [all data]	R_1 = 0.0434, wR_2 = 0.1008
Largest diff. peak/hole / e Å⁻³	0.19/-0.26

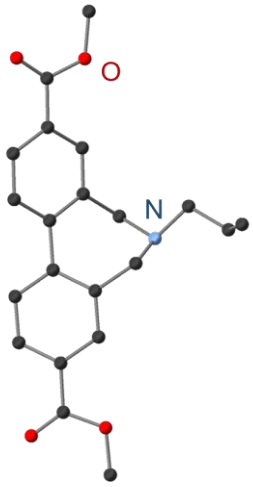

B 4.4 MOF NMR

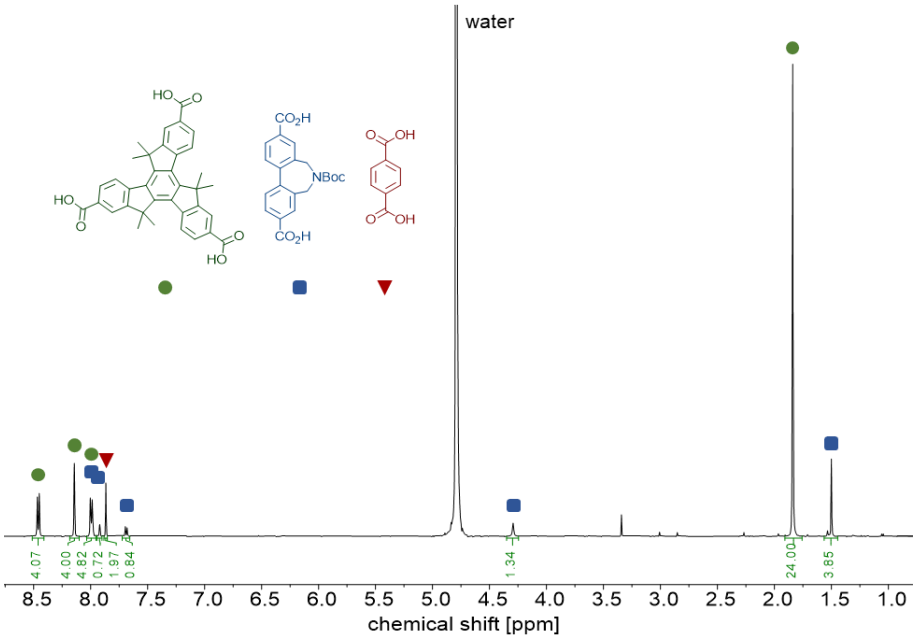

Figure B-33 ^{1}H NMR of bocaz-MUF-77 upon digestion in 0.1 M NaOD.

B 4.5 MOF TGA

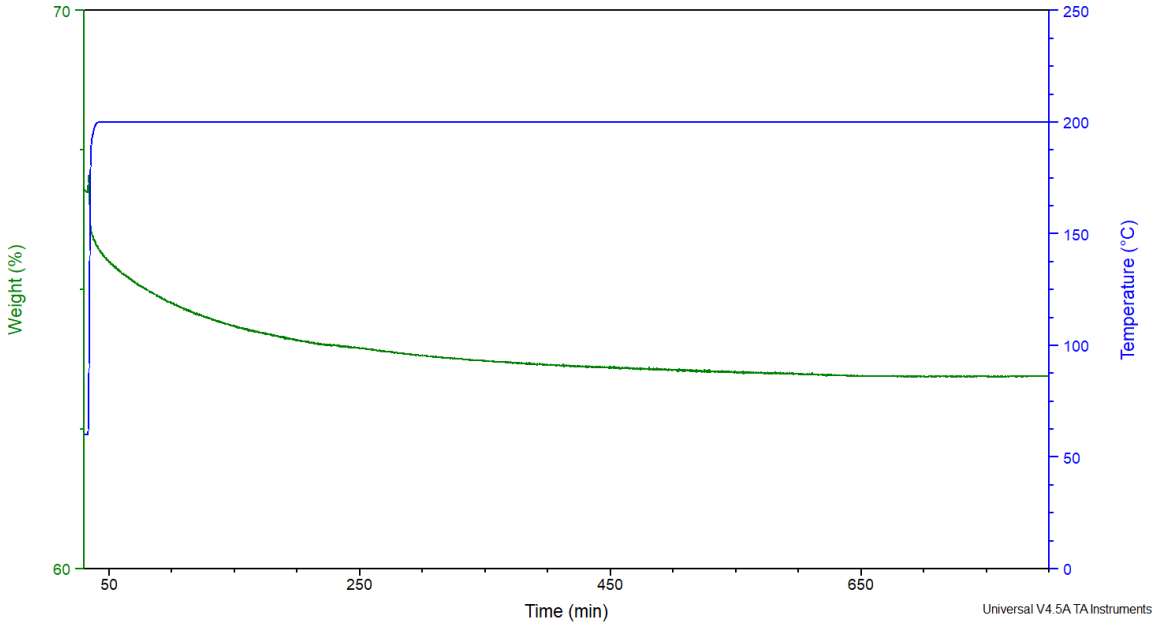

Figure B-34 TGA of the deprotection of bocaz-MUF-77 at 200 °C. To ensure stability of the sample, solvated crystals in dichloromethane were used and the solvent was removed under a flow of nitrogen at elevated temperature prior to the experiment.

Method: Ramp 10.00 °C/min to 60.00 °C; isothermal for 30.00 min; equilibrate at 200.00 °C; isothermal for 20 h.

Appendix C | For Chapter 4

C 1. Catalysis Data

C 1.1 ^{1}H NMR Spectra of the Cycloisomerization Reaction

After 8 d of reaction time, 10 µL were removed from the reaction mixture and diluted with 500 µL $CDCl_3$. Samples of the homogeneous reaction were prepared after 24 h of reaction time. ^{1}H NMR spectra were recorded immediately after sample preparation.

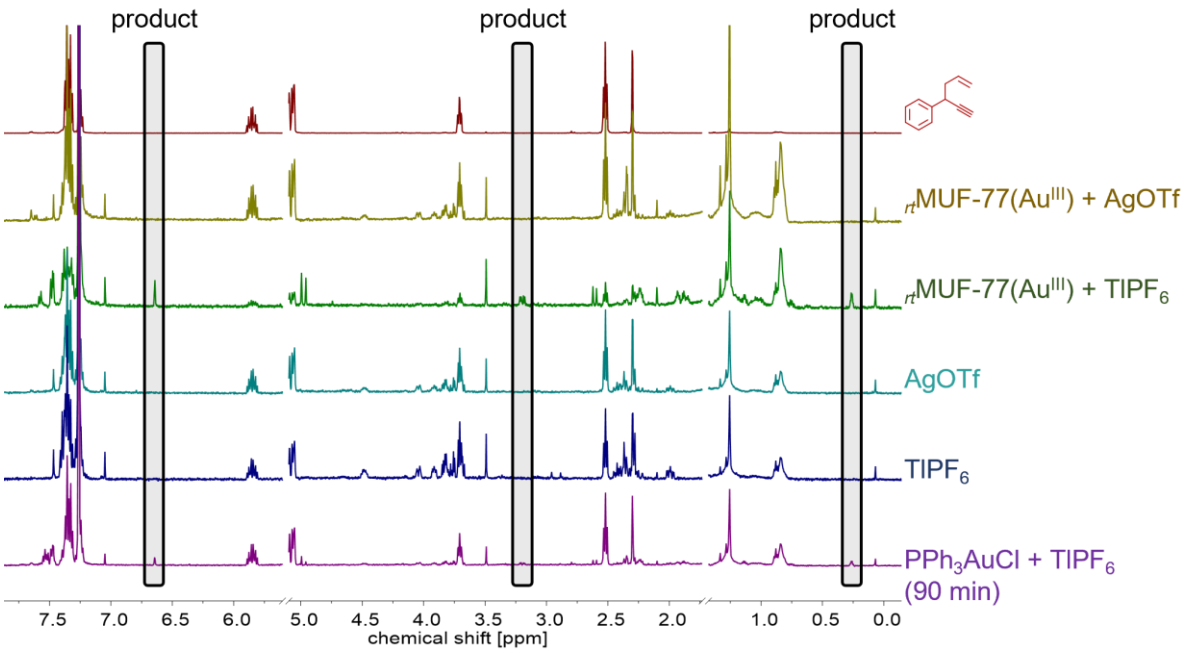

Figure C-1 ^{1}H NMR spectra from the cycloisomerization reaction of hex-5-en-1-yn-3-ylbenzene in the presence of different gold catalysts and from control reactions without catalyst addition.

C 1.2 Filtration Control Experiment

After 8 d of reaction with added IPrAu(bpdc)Cl-$_{rt}$MUF-77 and $TlPF_6$, the suspension was centrifuged, and the reaction mixture was decanted off and passed through a syringe filter to remove any solid MOF catalyst or salt. The solution was kept under catalysis conditions. ^{1}H NMR spectra were recorded from 10 µL solution diluted with 500 µL $CDCl_3$.

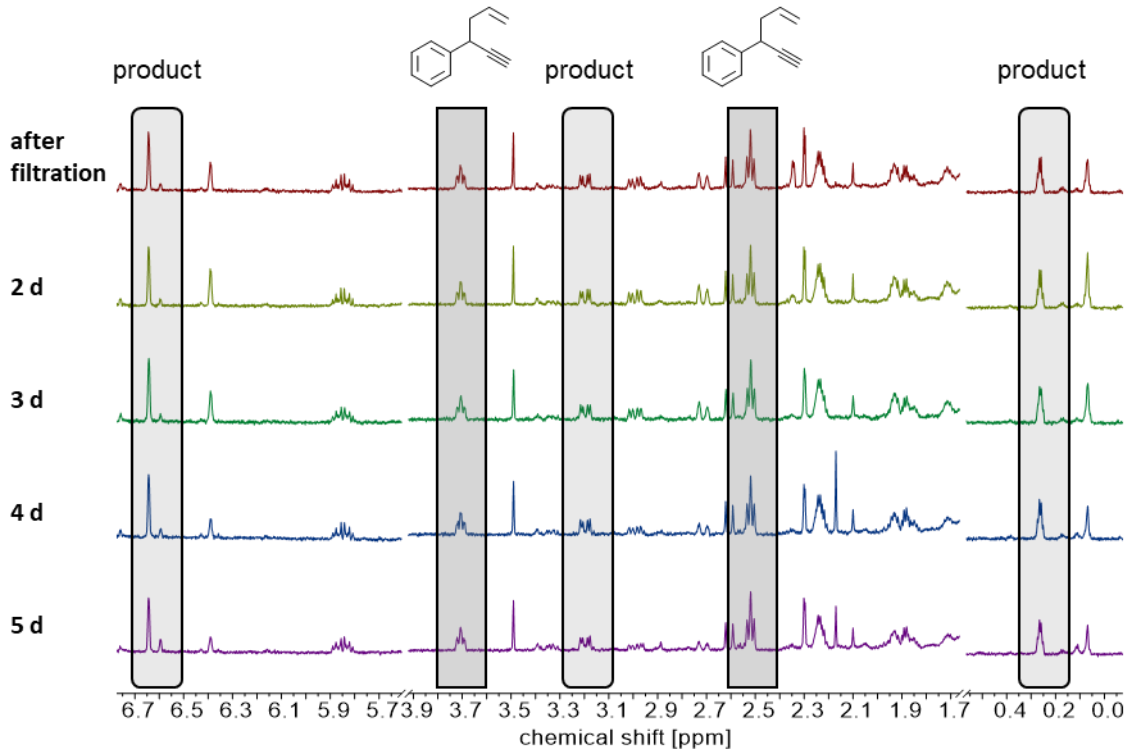

Figure C-2 ^{1}H NMR spectra of the cycloisomerization control reaction after catalyst filtration.

C 1.3 Catalyst Recyclability Experiment

After 8 d of reaction with added IPrAu(bpdc)Cl-$_{rt}$MUF-77 and $TlPF_6$ the reaction mixture was removed. The MUF-77 catalyst was washed with DCM (3x). The solvent was removed and a solution of hex-5-en-1-yn-3-ylbenzene (10 µL) in DCM (200 µL) was added and kept at room temperature. For ^{1}H NMR spectroscopy, a small amount of sample (10 µL) was removed after the respective time interval and diluted with $CDCl_3$ (500 µL). Spectra were recorded according to the general method.

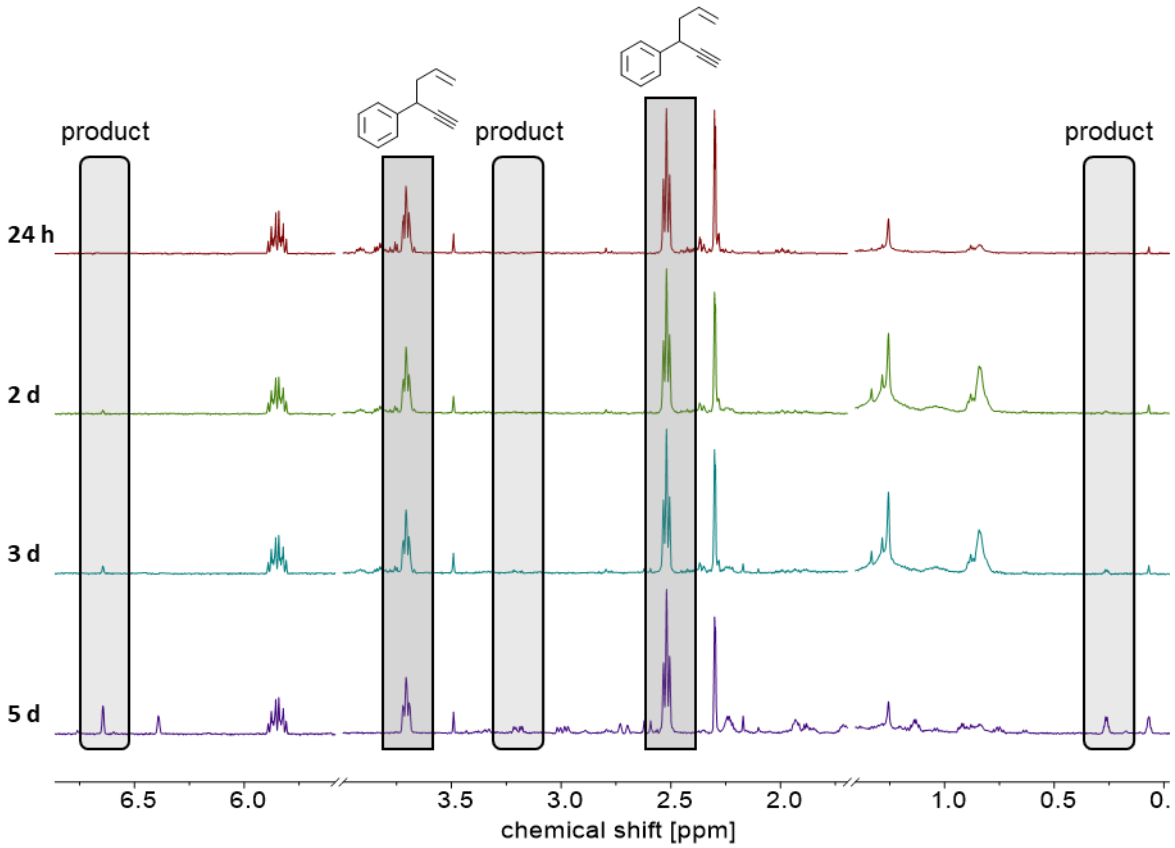

Figure C-3 ^{1}H NMR spectra of the second catalytic run upon recycling the $_{rt}$MUF-77(Au^{III}) catalyst.

C 2. MOF Characterization After Catalysis

C 2.1 MOF SEM Images

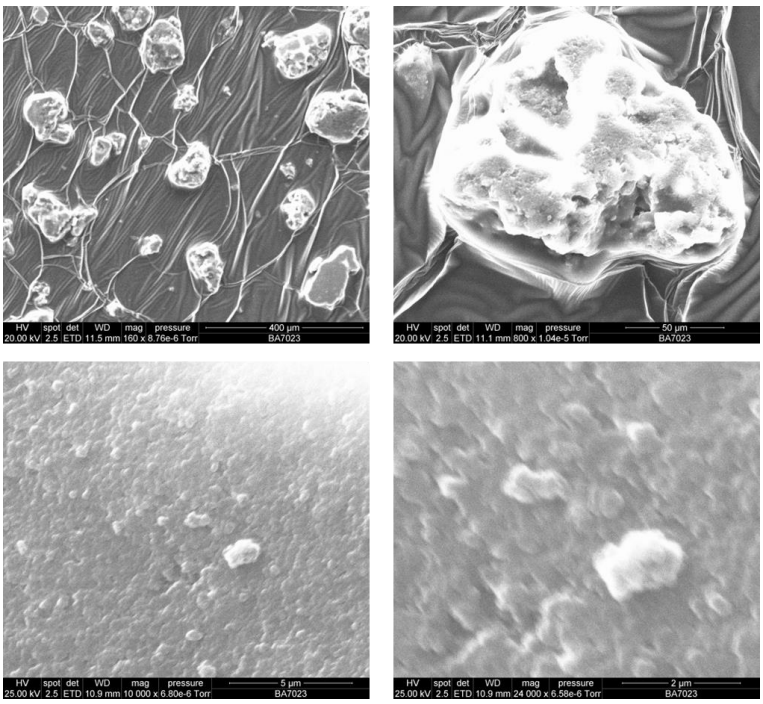

Figure C-4 SEM images of IPrAu(bpdc)Cl-$_{rt}$MUF-77 as synthesized.

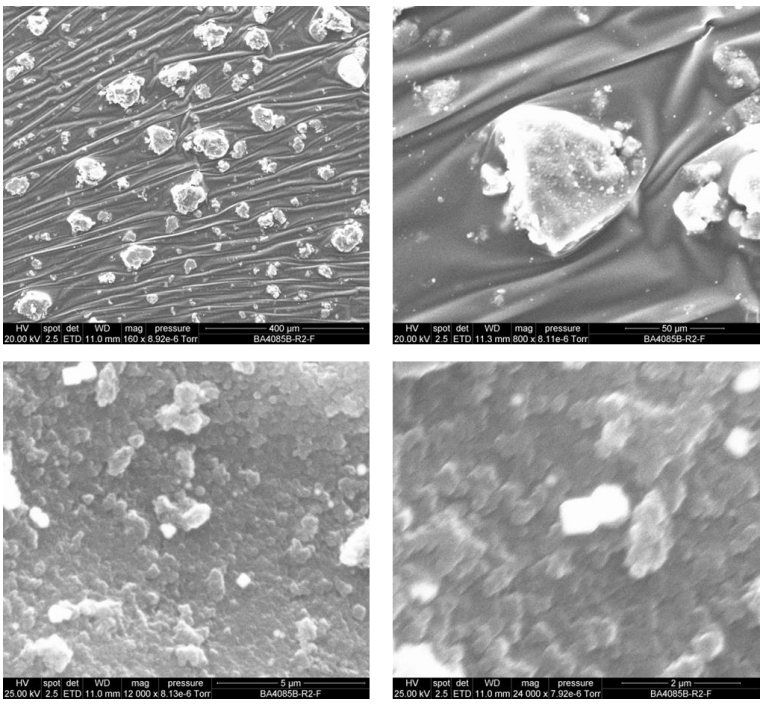

Figure C- 5 SEM images of IPrAu(bpdc)Cl-$_{rt}$MUF-77 after two runs of catalysis.

C 2.2 MOF EDX

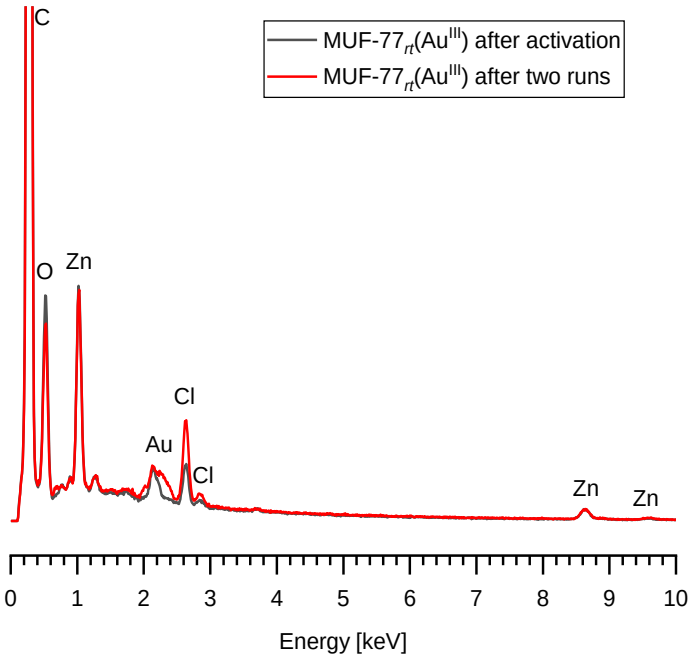

Figure C-6 EDX of IPrAu(bpdc)Cl-$_{rt}$MUF-77 after two runs of catalysis.

Appendix D | For Chapter 5

D 1. MOF Characterisation

Figure D-1 Picture of a mounted PCN-333 (Fe) sample during a typical PXRD experiment.

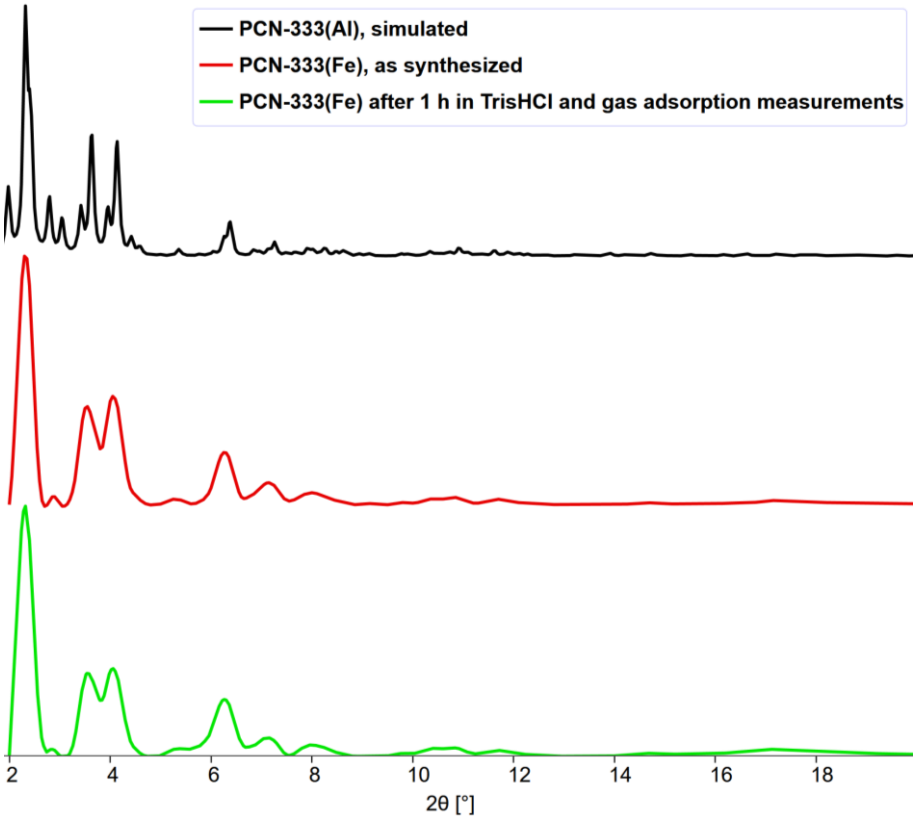

Figure D-2 PXRD pattern of PCN-333(Fe) after exposure to Tris HCl at pH 7 for 1 h, sample preparation and gas adsorption measurements (green, bottom) in comparison to an as-synthesized sample (middle, red) and the simulated PXRD pattern (top, black).

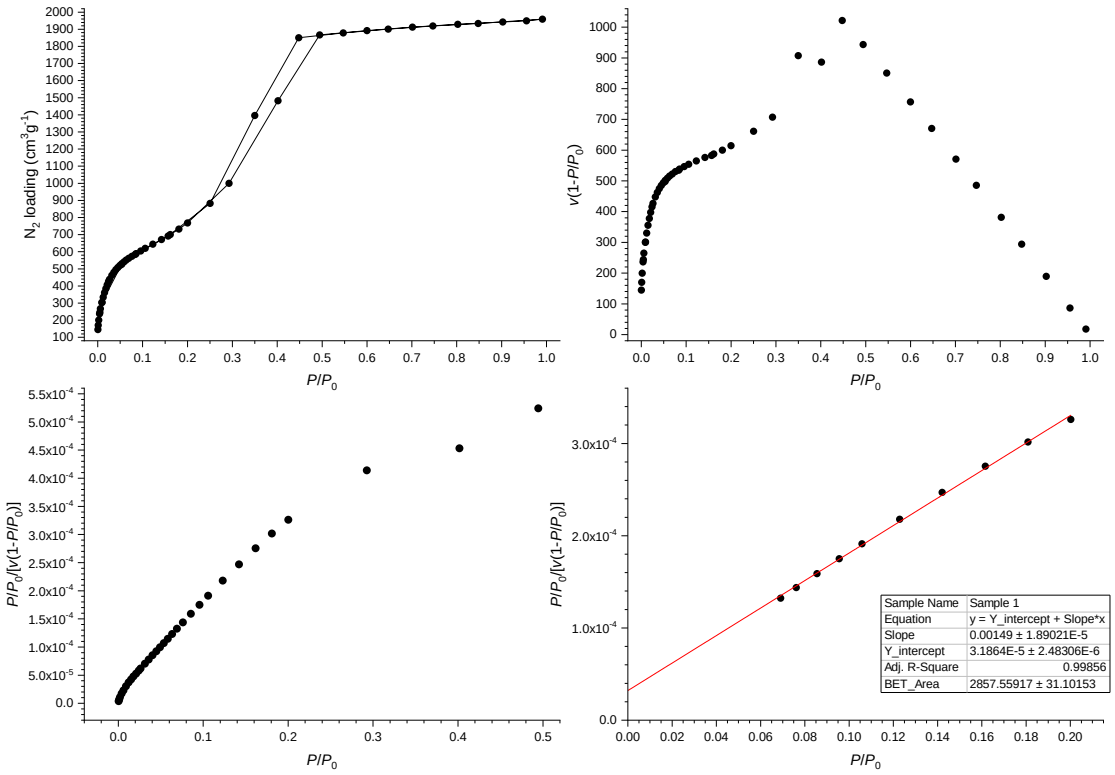

Figure D-3 Nitrogen adsorption isotherm at 77 K and BET surface area plots for PCN-333(Fe) as-synthesized.

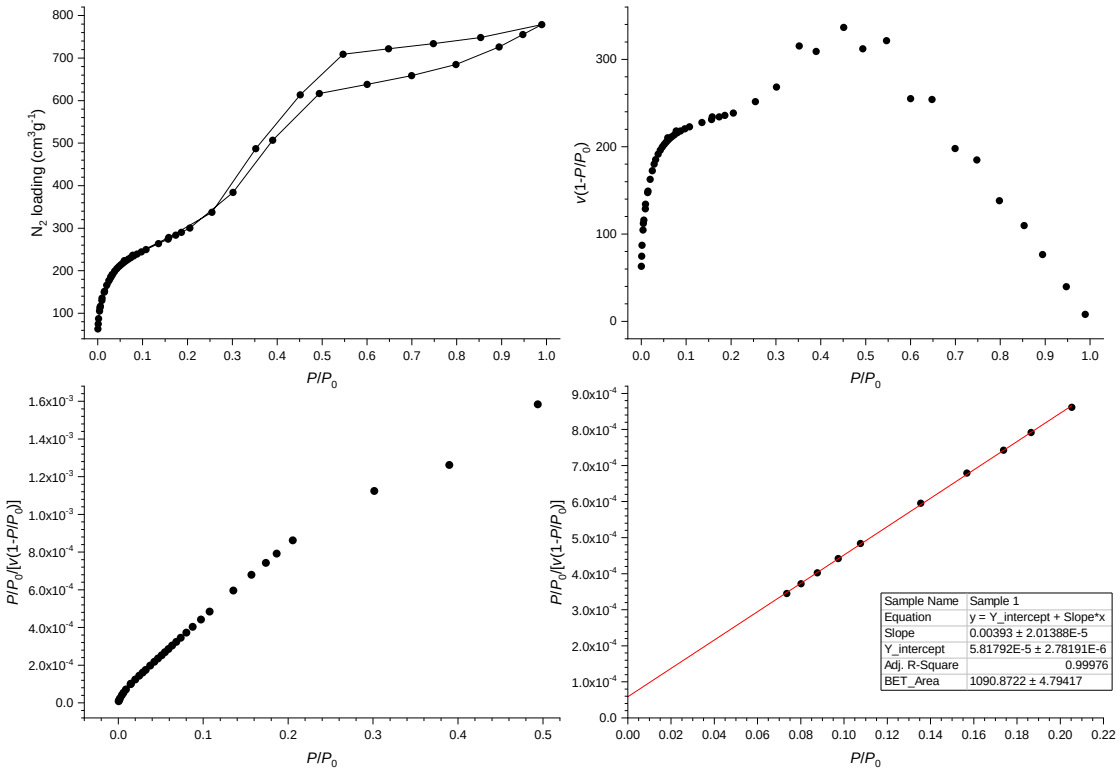

Figure D-4 Nitrogen adsorption isotherm at 77 K and BET surface area plots for PCN-333(Fe) after exposure to Tris HCl at pH 7 for 1 h.

Electrode Preparation

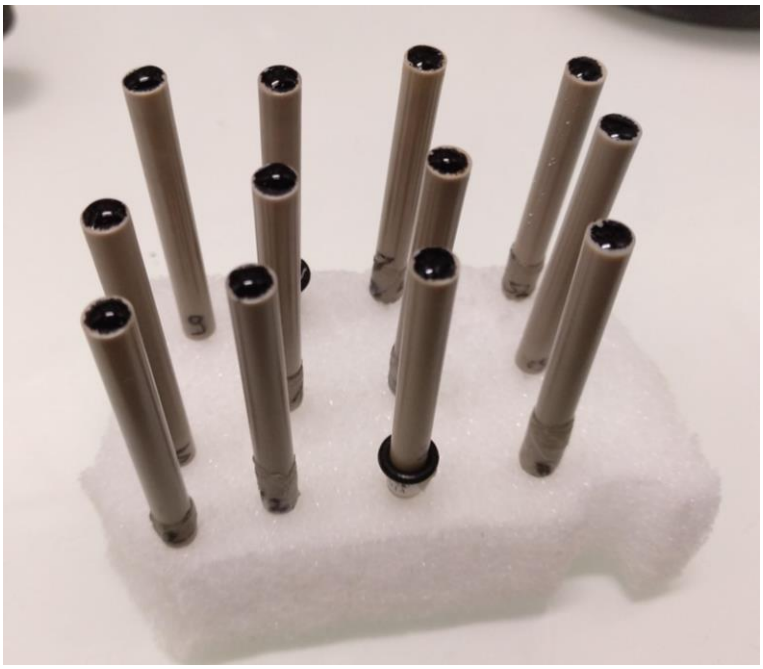

Figure D-5 Picture of the preparation of GC-CNT electrodes by drop-casting.

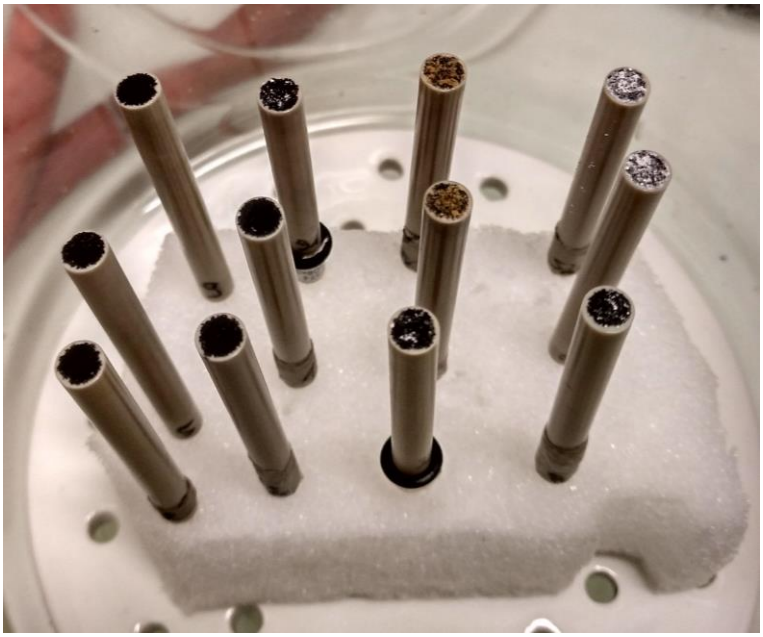

Figure D-6 Picture of prepared modified glassy carbon electrodes upon drying.

Electrochemistry

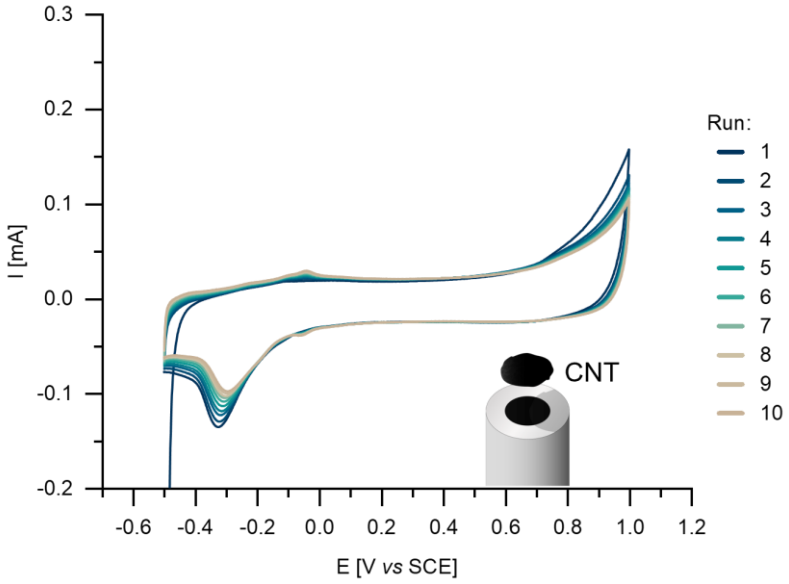

Figure D-7 Cyclic voltammograms of a GC-CNT electrode. Cyclic voltammograms were collected in 0.1 M PB pH 7.0, with a scan rate υ = 20.0 mV/s, using a saturated calomel electrode (SCE) as reference.